

SPECTROSCOPIC MONITORING OF PROTON TRANSFER AND
PROTON-COUPLED ELECTRON TRANSFER REACTIONS

Thomas T. Eisenhart

A dissertation submitted to the faculty at the University of North Carolina at Chapel Hill in
partial fulfillment of the requirements for the degree of Doctorate of Philosophy in the
Department of Chemistry.

Chapel Hill
2016

Approved By:

Jillian Dempsey

James Jorgenson

Gary Glish

John Papanikolas

Joseph Templeton

©2016
Thomas T. Eisenhart
ALL RIGHTS RESERVED

ABSTRACT

Thomas T. Eisenhart: Spectroscopic Monitoring of Proton Transfer and Proton-Coupled
Electron Transfer Reactions
(Under the direction of Jillian Dempsey)

As the need to develop alternative types of energy has become a more pressing issue, the impetus to understand fundamental energy conversion processes like photosynthesis has only increased. One particular facet of photosynthesis that has been identified as crucial to the conversion of H_2O , CO_2 , and light to O_2 and carbohydrates is a proton-coupled electron transfer (PCET) process. Numerous studies have been carried out to gain a broader understanding of PCET processes; however, the traditional tools used to study these reactions have only allowed direct observation of the ET component of PCET. While these are excellent methods for elucidating information about ET, a complete picture involves a study of both the PT and ET components of a PCET process. Our work initially has focused on systems which possess optical handles for both ET and PT, allowing us to gather unique insight into these important reactions. The development of these systems, specifically the probes that can monitor PT reactions, has also allowed us to begin to understand how PT occurs in non-aqueous environments in both the ground state and the electronic excited state.

ACKNOWLEDGMENTS

Jillian: thank you for giving me the opportunity to learn from you. Thank you for making me work hard, for challenging me, and for teaching me how to think critically and creatively. I will carry the lessons I've learned from you into all of my future endeavors.

To the Dempsey lab (especially Brian, Robin, and Eric): thank you for your patience, your caring personalities, your knowledge, and most of all, your friendship. This was certainly a wild journey, and it was made all the better because I got to share it with you.

To my friends in the department, in particular Andrew, Dan, Guy and Melissa: I did not anticipate meeting such incredible, smart, funny, and well-rounded people when I decided to attend UNC, but I could not imagine the past few years without you. Thanks for the laughter, the jokes, the coffee, the beer, and the many, many memories. Here's to a few more in the years to come.

To my parents: thank you for the love, support, and wisdom over the past five years. You both were always quick to listen, slow to give unwanted (but needed) advice, and eager to help in any way possible. From an early age I was given every educational opportunity, and I can't thank you enough for instilling in me a desire to learn. And thank you Emily for being the best sister I could ever ask for!

To my beautiful wife: quite simply, this would not have been possible without you. Your love, support, and laughter have sustained throughout this process, and I am so thankful that we got to start our lives together here in Chapel Hill. Thank you for your patience, kindness, and encouragement. I love you x 3.

TABLE OF CONTENTS

LIST OF FIGURES	vii
LIST OF ABBREVIATIONS.....	xiii
CHAPTER 1: INTRODUCTION	1
1.1. A Challenge to the Scientific Community	1
1.2. A Multifaceted Solution.....	2
1.3. Nature’s Roadmap to a Solar-Powered Future	3
1.4. Proton-Coupled Electron Transfer	5
1.5. PCET of Phenols in Non-Aqueous Solvent Environments.....	7
1.6. New Optical Methods for Monitoring PCET.....	18
1.7. References.....	22
CHAPTER 2: PHOTO-INDUCED PROTON-COUPLED ELECTRON TRANSFER REACTIONS OF ACRIDINE ORANGE: COMPREHENSIVE SPECTRAL AND KINETICS ANALYSIS.....	26
2.1. Introduction.....	26
2.2. Discussion and Results	27
2.3. Experimental Details.....	41
2.4. Thermochemical Analysis	43
2.5. Details of Kinetic Modeling.....	53
2.6. References.....	58

CHAPTER 3: PROTON-COUPLED ELECTRON TRANSFER REACTIONS WITH
PHOTOMETRIC BASES REVEAL FREE ENERGY RELATIONSHIPS FOR PROTON
TRANSFER 61

3.1. Introduction.....	61
3.2. Results.....	64
3.3. Discussion	80
3.4. Conclusions.....	107
3.5. Experimental Details.....	109
3.6. Details of Kinetics Modeling	116
3.7. References.....	123

CHAPTER 4: EXCITED-STATE AND THERMAL PROTON TRANSFER REACTIONS
OF QUINOLINE PHOTOBASES: INFLUENCES OF DRIVING FORCE, ELECTRONIC
STRUCTURE AND HYDROGEN-BONDING 129

4.1. Introduction.....	129
4.2. Electronic Structure of Quinolines.....	131
4.3. Results and Discussion	132
4.4. Conclusions.....	168
4.5. Experimental Details.....	170
4.6. References.....	174

LIST OF FIGURES

Figure 1.1. Keeling Curve.....	2
Figure 1.2. Photosynthetic Scheme.....	4
Figure 1.3. PCET in PSII	5
Figure 1.4. PCET Square Scheme.....	6
Figure 1.5. Mayer PCET Motif.....	8
Figure 1.6. Rhenium (I) tricarbonyl photosensitizers	11
Figure 1.7. Ru(II) photosensitizers linked to hydrogen bonded tyrosine moieties	13
Figure 1.8. Photoexcited rhenium complexes.....	16
Figure 2.1. PCET square scheme incorporating ground and excited state reactivity.	27
Figure 2.2. Spectrophotometric titration of acridine orange.....	28
Figure 2.3. Transient difference spectra of AO.	29
Figure 2.4. Decay of the triplet excited state of AO monitored at 560 nm.....	30
Figure 2.5. Transient difference spectra of AO and ^{ttb} PhOH.....	31
Figure 2.6. Spectroelectrochemistry of AOH ⁺	32
Figure 2.7. Mechanism of reactivity and recombination of ^{3*} AO + ^{ttb} PhOH.	33
Figure 2.8. Mechanism of reactivity for ^{3*} AO and TEMPOH.....	33
Figure 2.9. Decay of the triplet excited state of AOH ⁺ in CH ₃ CN monitored at 560 nm.....	35
Figure 2.10. Kinetics traces of AO with ^{ttb} PhOH at 560 nm	36
Figure 2.11. Kinetics traces of AO with ^{ttb} PhOD at 560 nm	37
Figure 2.12. Kinetics traces of AO with ^{ttb} PhOH at 460 nm.	39
Figure 2.13. Kinetics traces of μM AO with ^{ttb} PhOD at 460 nm.....	40
Figure 2.14. Detailed model of the deactivation and reaction pathways for AO + ^{ttb} PhOH ..	53

Figure 3.1. General schematic of the PCET reaction between NH_2PhOH , Fc^+ , and R-7DMAQ.	64
Figure 3.2. General scheme of R-7DMAQs	65
Figure 3.3. UV-vis absorbance spectrum of TMP-7DMAQ.....	66
Figure 3.4. Absorbance spectrum Ph-7DMAQ.	66
Figure 3.5. Absorbance spectrum of H-7DMAQ.....	67
Figure 3.6. Absorbance spectrum of MeO-7DMAQ	67
Figure 3.7. Absorbance spectrum of .TMP-7DMAQ	68
Figure 3.8. Spectrophotometric titration of TMP-7DMAQ with 2-picoline.	69
Figure 3.9. Spectrophotometric titration of MeO-7DMAQ with 2-picoline	70
Figure 3.10. Spectrophotometric titration of H-7DMAQ with 2-picoline.....	71
Figure 3.11. Spectrophotometric titration of Ph-7DMAQ with 2-picoline.	72
Figure 3.12. Absorbance spectra recorded at various time delays upon rapid mixing of NH_2PhOH and Ph-7DMAQ with Fc^+	74
Figure 3.13. Stopped-flow kinetics traces monitoring the appearance of TMP-7DMAQH^+ at 450 nm and the disappearance of Fc^+ at 620 nm.....	75
Figure 3.14. Stopped-flow kinetics traces monitoring the appearance of Ph-7DMAQH^+ at 460 nm and the disappearance of Fc^+ at 620 nm.....	76
Figure 3.15. Stopped-flow kinetics traces monitoring the appearance of MeO-7DMAQH^+ at 460 nm and the disappearance of Fc^+ at 620 nm.	77
Figure 3.16. Stopped-flow kinetics traces monitoring the appearance of H-7DMAQH^+ at 440 nm and the disappearance of Fc^+ at 620 nm..	78
Figure 3.17. Stopped-flow kinetics traces monitoring the disappearance of Fc^+ at 620 nm as a function of Ph-7DMAQ..	79
Figure 3.18. Cyclic voltammogram of NH_2PhOH	82
Figure 3.19. Cyclic voltammogram of NH_2PhOH upon the addition of 2-picoline	82
Figure 3.20. Mass spectrum obtained from the reaction of Fc^+ , NH_2PhOH , and 2-picoline..	83

Figure 3.21. Spectrophotometric titration of TMP-7DMAQH ⁺ with NH ₂ PhOH	85
Figure 3.22. Spectrophotometric titration of MeO-7DMAQH ⁺ with NH ₂ PhOH	86
Figure 3.23. Spectrophotometric titration of H-7DMAQH ⁺ with NH ₂ PhOH	87
Figure 3.24. Spectrophotometric titration of Ph-7DMAQH ⁺ with NH ₂ PhOH.	88
Figure 3.25. Adduction of MeO-7DMAQ with Fc ⁺	90
Figure 3.26. Adduction of TMP-7DMAQ (with Decamethylferrocenium.....	91
Figure 3.27. Titration of TMP-7DMAQ with Fc ⁺	92
Figure 3.28. Titration of MeO-7DMAQ with Fc ⁺	93
Figure 3.29. Titration of H-7DMAQ with Fc ⁺	94
Figure 3.30. Titration of Ph-7DMAQ with Fc ⁺	95
Figure 3.31. Kinetics and accompanying fit for ET between Fc ⁺ and NH ₂ PhOH.....	97
Figure 3.32. Stopped-flow kinetics traces monitoring the appearance of TMP-7DMAQH ⁺ at 450 nm and the disappearance of Fc ⁺ at 620 nm	99
Figure 3.33. Stopped-flow kinetics traces monitoring the appearance of MeO-7DMAQH ⁺ at 460 nm and the disappearance of Fc ⁺ at 620 nm	100
Figure 3.34. Stopped-flow kinetics traces monitoring the appearance of H-7DMAQH ⁺ at 440 nm and the disappearance of Fc ⁺ at 620 nm	101
Figure 3.35. Stopped-flow kinetics traces monitoring the appearance of Ph-7DMAQH ⁺ at 460 nm and the disappearance of Fc ⁺ at 620 nm	102
Figure 3.36. ΔConcentration profiles from simulated kinetic traces of NH ₂ PhOH, Fc ⁺ , NHPhOH, H-7DMAQ, NH ₃ PhOH ⁺ , and NHPhO..	104
Figure 3.37. Free Energy Relationships.....	106
Figure 4.1. Structure and UV-vis absorbance spectrum of CF ₃ -7DMAQ and its conjugate acid CF ₃ -7DMAQH ⁺	132
Figure 4.2. Spectrophotometric titration of CF ₃ -7DMAQ with aniline.....	134
Figure 4.3. Steady-state luminescence and lifetime of CF ₃ -7DMAQ	136
Figure 4.4. Normalized absorbance and emission spectrum of CF ₃ -7DMAQ	137

Figure 4.5. Normalized absorbance and emission spectrum of CF ₃ -7DMAQH ⁺	137
Figure 4.6. Forster cycle calculations for determining the pK _a [*] of CF ₃ -7DMAQ.	138
Figure 4.7. General reaction scheme of CF ₃ -7DMAQ and HA	139
Figure 4.8. Chemical structures of HA.	140
Figure 4.9. Static and dynamic quenching Pathways	141
Figure 4.10. Steady-state luminescence spectra and Stern-Volmer plot for Collidinium. ...	142
Figure 4.11. Steady-state luminescence spectra and Stern-Volmer plot for 2- Ammoniumbenzimidazole	143
Figure 4.12. Steady-state luminescence and Stern-Volmer plot for Benzylammonium.....	144
Figure 4.13. Steady-state luminescence spectra and Stern-Volmer plot for Isobutylammonium	145
Figure 4.14. Steady-state luminescence and Stern-Volmer plot for Triethylammonium	146
Figure 4.15. Luminescence lifetime decays and Stern-Volmer plot for Collidinium.....	148
Figure 4.16. Luminescence lifetime decays and Stern-Volmer plot for 2- Ammoniumbenzimidazole	149
Figure 4.17. Luminescence lifetime decays and Stern-Volmer plot for Benzylammonium	150
Figure 4.18. Luminescence lifetime decays and Stern-Volmer plot for Isobutylammonium	151
Figure 4.19. Luminescence lifetime decays and Stern-Volmer plot for Triethylammonium	152
Figure 4.20. Determination of K _S with Collidinium	153
Figure 4.21. Determination of K _S with 2-Ammoniumbenzimidazole.....	154
Figure 4.22. Determination of K _S with Benzylammonium	154
Figure 4.23. Determination of K _S with Isobutylammonium	155
Figure 4.24. Hydrogen Bonding Illustration.....	156
Figure 4.25. Titration of collidinium with pyridine.....	157
Figure 4.26. Titration of collidinium with dimethylaniline	157

Figure 4.27. Titration of 2-ammoniumbenzimidazole with pyridine	158
Figure 4.28. Titration of 2-ammoniumbenzimidazole with dimethylaniline.....	158
Figure 4.29. Titration of benzylammonium with pyridine	159
Figure 4.30. Titration of isobutylammonium with pyridine	159
Figure 4.31. Titration of isobutylammonium with dimethylaniline	160
Figure 4.32. Titration of triethylammonium with pyridine.....	160
Figure 4.33. Titration of triethylammonium with dimethylaniline.....	161
Figure 4.34. Transient difference spectrum of CF ₃ -7DMAQ and collidinium	163
Figure 4.35. Recombination of CF ₃ -7DMAQH ⁺ and Isobutylamine.....	164
Figure 4.36. Recombination of CF ₃ -7DMAQH ⁺ and Benzylamine.....	165
Figure 4.37. Recombination of CF ₃ -7DMAQH ⁺ and 2-Aminobenzimidazole	165
Figure 4.38. Recombination of CF ₃ -7DMAQH ⁺ and Collidine.....	166
Figure 4.39. Free Energy Relationships.....	168

LIST OF ABBREVIATIONS

AO	Acridine Orange
AOH ⁺	Acridinium orange
B	Generic Base
bpy	2,2'-bipyridine
bpz	2,2'-bipyrazine
CF ₃ -7DMAQ	2,4-Bis(3,5-trifluoromethyl)phenyl-7-dimethylaminoquinoline
CPET	Concerted proton-electron transfer
DFT	Density Functional Theory
ESPT	Excited-state proton transfer
ET	Electron Transfer
Fc	Ferrocene
Fc ⁺	Ferrocenium
GHG	Green House Gas
H-7DMAQ	7-dimethylaminoquinoline
HA	Generic Acid
KIE	Kinetic isotope effect
MeO-7DMAQ	2,4-Bis(3,4-methoxy)phenyl-7-dimethylaminoquinoline
NH ₂ PhOH	<i>p</i> -aminophenol
NMR	Nuclear magnetic resonance
OEC	Oxygen evolving complex
PCET	Proton-coupled Electron Transfer

Ph-7DMAQ	2,4-Diphenyl-7-dimethylaminoquinoline
PT	Proton Transfer
PV	Photovoltaic
pyr	Pyridine
pyz	Pyrazine
R-7DMAQ	2,4-R-7-dimethylaminoquinoline
TA	Transient Absorption Spectroscopy
TCSPC	Time-correlated single photon counting
TEMPOH	2,2'-6,6'-tetramethylpiperidine-1-ol
TMP-7DMAQ	2,4-Bis(2,3,5,6-tetramethyl)phenyl-7-dimethylaminoquinoline
^{ttb} PhOH	<i>Tri</i> -tertbutylphenol
Yz	Tyrosine Z in Photosystem II

CHAPTER 1: INTRODUCTION

1.1. A Challenge to the Scientific Community

The past century has been a golden age for the scientific community. The development of modern medicine has extended life expectancies to eighty or more years in industrialized nations. The birth of air travel has made it possible to reach every corner of planet Earth in a single day. Advances in agricultural practices continue to help the planet's population of seven billion grow larger every day. In a nutshell, numerous scientific advancements have made the developed world richer, smarter, and more connected than ever before. Instrumental to these developments has been access to cheap and abundant energy sources – most notably fossil fuels like oil, coal, and natural gas. It is no secret that the developed world is heavily reliant on fossil fuels to power vehicles and heat homes, but it also needs these natural resources to develop life-saving medicines, and to fertilize and harvest crops. The demand for fossil fuels has continued to increase over recent decades as the world population grown, and developing countries like China, India, and Brazil crave increasing amounts cheap energy.¹ While cheap energy is beneficial to economic development, the environmental consequences associated with burning unregulated amounts of fossil fuels are becoming apparent. Beginning with the Keeling experiments in Mauna Loa that monitored carbon dioxide levels in the atmosphere of Hawaii (Figure 1.1), scientists have come to realize that the world's continued reliance on fossil fuels is having adverse effects on the natural world through the accumulation of CO₂ and other greenhouse gases (GHGs) in the atmosphere.¹⁻³

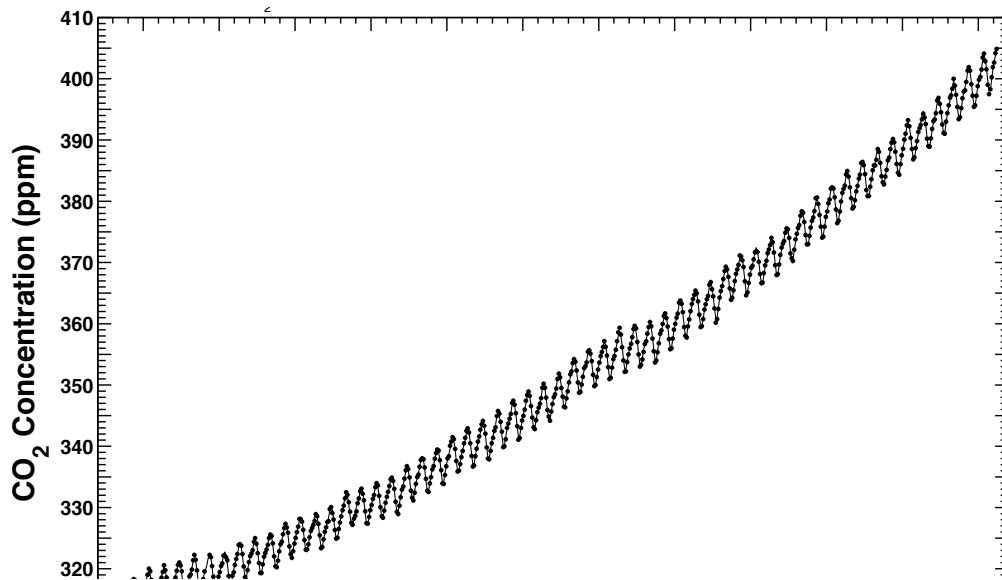


Figure 1.1 Keeling curve showing the monthly average concentration of atmospheric CO₂ at the Mauna Loa Observatory in Hawaii. (Data Source: Scripps Institute of Oceanography, scrippsco2.ucsd.edu).

In just the past decade, atmospheric CO₂ levels have passed the 400 parts per million mark for the first time in a few million years. Scientists are in overwhelming agreement that this increase in concentration of carbon dioxide (among other GHGs) is playing a role in warming the planet.¹⁻³ Compounding this, the world's population is estimated to grow to a level of 9 billion by 2040.¹ Demand for energy, food, transportation, and medicine will only increase with population growth. A continued reliance solely on fossil fuels to meet demand for these needs will result in staggering and unpredictable environmental consequences to society. As such, the scientific community is facing a challenge of historic and unprecedented challenge. Politics and economics will continue to dictate that fossil fuels are widely used, so the time is now for scientists to develop new technologies that force society to rethink how our world is powered – the livelihood of future generations depends on it.

1.2. A Multifaceted Solution

Though the energy and environmental challenges facing society have been well documented, strategies to develop sustainable solutions to address these challenges have been

pursued to limited degrees of success. Wind energy has long been used to carry out work, and advances in turbine technology have allowed for the development of wind turbines that generate appreciable amounts of electricity. The conversion of biomass to useable fuels has long been touted as a potential pathway to synthesize liquid fuels from renewable feedstocks. Geothermal energy can be harvested on both small and large scales to heat water and generate electricity. Most notably, solar photovoltaic cells (PVs), devices that convert solar photons directly to electricity, have rapidly developed in their efficiency. These advances have translated to a steep increase in adoption of this technology amongst developed and developing nations.

The continued adoption of solar technologies is particularly encouraging as the solar flux bombarding the earth each hour (4.3×10^{20} J) is roughly equivalent to the energy consumed by the entire planet in one year.² Solar energy is abundant, free, and while some geographic areas may have a larger influx, there is not a small oligarchy controlling the collection and distribution of this energy source (like the current petroleum economy). However, a downfall of current solar technologies (notably PVs) is that the electricity produced must be utilized immediately. Storage of this energy is not currently viable using traditional battery storage methods. While research is being carried out to develop efficient and robust batteries that can operate on the large scale necessary, another storage approach has developed that draws inspiration from the natural world: storing solar energy in chemical bonds of fuels.

1.3. Nature's Roadmap to a Solar-Powered Future

Conveniently, nature has provided a detailed blueprint on how to harvest and store solar energy in chemical bonds. In green plants, the process of photosynthesis utilizes

sunlight to drive the oxidation of water and reduction of carbon dioxide to produce oxygen and store energy in the form of carbohydrates (Figure 1.2).

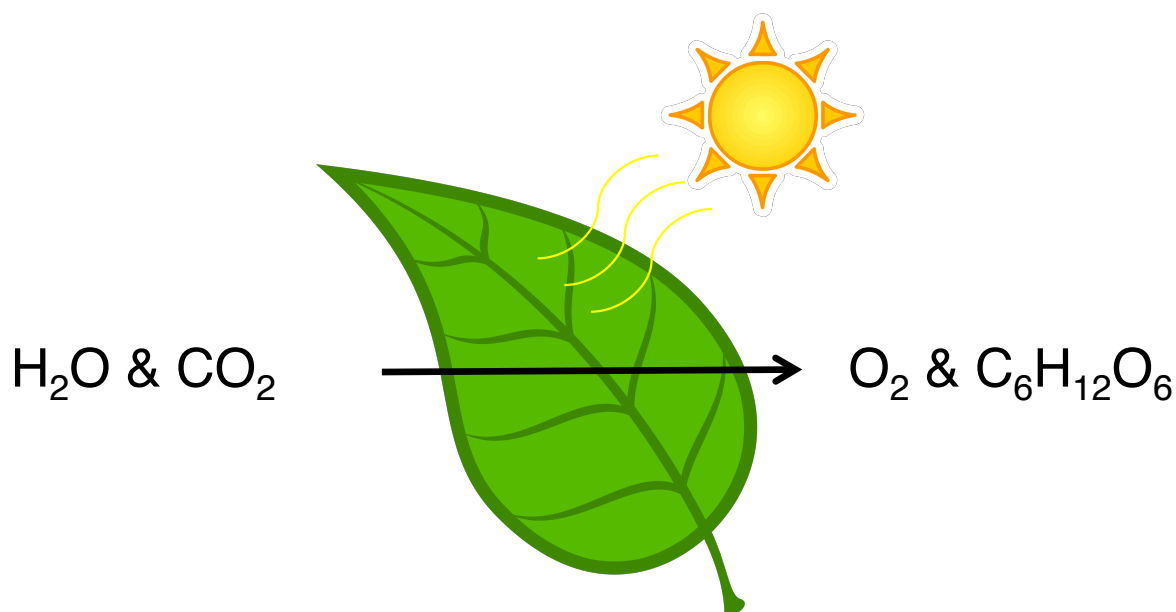
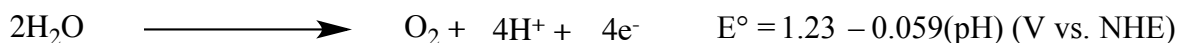


Figure 1.2. Schematic representing green plants' use of solar energy to catalyze the transformation of water and carbon dioxide into oxygen and carbohydrates.

Not only does nature provide insight into storing solar energy in chemical bonds, it demonstrates this process using H_2O and CO_2 as reactants. Both of these inputs are cheap and abundant, thus their utilization as reactants for a renewable fuel process is of great interest to the scientific community.⁴⁻⁹ Both CO_2 and H_2O are highly stable molecules, meaning the photosynthetic reactions involving these substrates do not proceed spontaneously and thus require an input of energy to be carried out. The full equation and thermodynamic potential for water oxidation in aqueous solution is shown below as an example (Equation 1.1).

Equation 1.1



In nature, H_2O oxidation is carried out in Photosystem II (PSII), with the process beginning in chlorophyll P680. Chlorophyll P680 absorbs a photon and quickly undergoes

electron transfer (ET) to a nearby pheophytin molecule to generate a powerful oxidant $P680^{\bullet+}$. A nearby tyrosine (Y_Z) is oxidized by $P680^{\bullet+}$, with proton-transfer (PT) from Y_Z to Histidine 190 (His^{190}) coupled to this ET reaction (Figure 1.3).

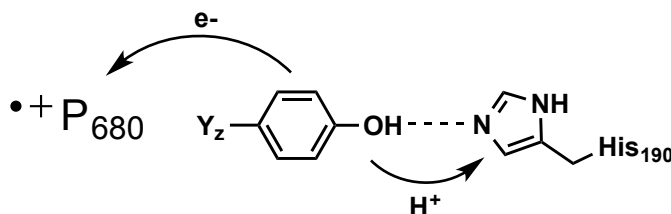


Figure 1.3. ET and PT between Tyrosine_Z, Histidine₁₉₀, and Chlorophyll P680 in Photosystem II. Figure adapted with permission.³¹

Oxidized, deprotonated Y_Z then goes on to oxidize the oxygen evolving complex (OEC), a cluster of four manganese ions and one calcium ion that carries out the actual water oxidation event, regenerating Y_Z upon reprotonation by His^{190} . This process of photon absorption and coupled ET and PT steps must be completed four times before the OEC has the necessary oxidative strength to fully oxidize two equivalents of H_2O . In the case of photosynthesis, the protons released are used to regenerate NADPH; however, in a solar fuels device, these protons could be used for a number of fuel forming reactions. The efficient reduction of protons to H_2 would generate a storable fuel, or the coupling of CO_2 reduction to proton transfer could potentially generate valuable feedstocks like formic acid, methanol, or methane. Developing either of these potential strategies would be a significant achievement in developing new energy technologies.^{10–12}

1.4. Proton-Coupled Electron Transfer

A defining characteristic of water oxidation is the movement of multiple protons and electrons. Reactions of this type, appropriately referred to as *proton-coupled electron transfer* (PCET) reactions, were first described in 1981 by T.J. Meyer, and have been widely

investigated over the past few decades.^{13–16} PCET reactions are generally described using a square scheme (Figure 1.4) where the PCET process can proceed through three different mechanisms. The first two are stepwise mechanisms where either initial ET is followed by PT, or vice versa (edges of the square scheme). Conversely, in a concerted proton-electron transfer (CPET) reaction, both the proton and electron move in a single kinetic step, avoiding possible high-energy, charged intermediates (diagonal).

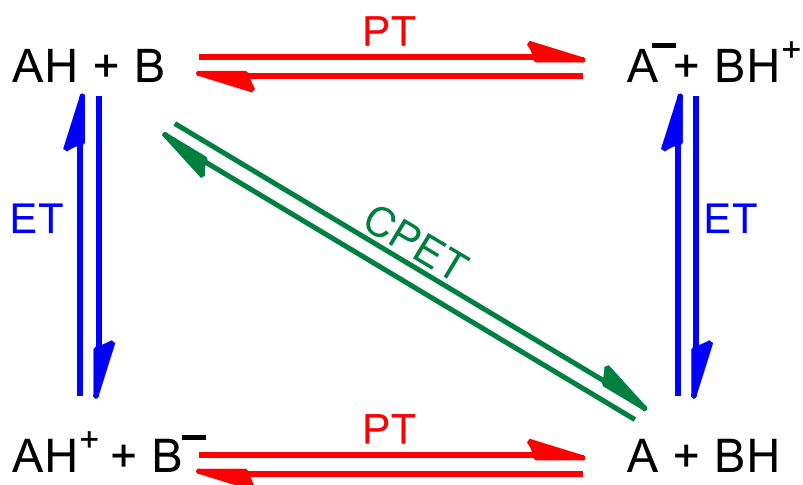


Figure 1.4. Square scheme denoting the three pathways for a single proton-coupled electron transfer event. The outside of the square shows the stepwise pathways, ET-PT or PT-ET, while the diagonal shows the concerted pathway, CPET.

PCET reactions are vital to important reactions like water oxidation and proton reduction, and thus a comprehensive understanding of PCET is desired. For any particular PCET reaction, that understanding involves elucidating the mechanism of reactivity, developing a thermodynamic picture of the system, and extracting relevant kinetic information about the process. Further, using that knowledge to understand which parameters control PCET is vital to the development of technologies relying on these reactions, in particular solar fuel production. However, determining mechanism, rate information, and

parameters governing PCET reactivity are not easy tasks as the current techniques employed to study these reactions rarely give a comprehensive picture of the reaction of interest.^{17,18}

1.5. PCET of Phenols in Non-Aqueous Solvent Environments

PCET is a massive field that covers a variety of substrates and solvent systems (aqueous vs. non-aqueous, for example).^{16,17,19,20} As such, the scope of the studies discussed here includes PCET as it relates to phenols (and phenol derivatives) in non-aqueous solvents. Phenols are often used in PCET studies as they are structural models for biologically relevant PCET reactions that involve tyrosine; Y_Z in PSII is a notable example.⁷ They are also used because the sterics and electronics of phenols can be easily tuned, and phenoxyl radicals (the PCET product of phenols) are moderately stable with spectroscopic signatures in the visible region.^{16,17} These reactions are often coupled to stopped-flow rapid-mixing^{21–25} and laser flash photolysis methods.^{26–32} Electrochemistry is also widely utilized,^{33–38} and can be especially useful as a complementary technique to time-resolved measurements. There are also a few groups making valuable contributions to the field using theoretical and computational methods.^{14,18,39–41} In this subset of PCET, studies have focused on understanding how a few important variables affect both the rate and mechanism of PCET: how does the overall driving force affect the reaction, what effect does hydrogen bonding have on PCET, and how does PT/ET distance affect the overall PCET process?

Mayer *et al.* have pioneered the use of stopped-flow rapid mixing to study the PCET reactivity of substituted phenols, including phenols with pendant amines and N-heterocycles (e.g. pyridines) that hydrogen bonds to the phenolic proton (Figure 1.5).^{22,42–45}

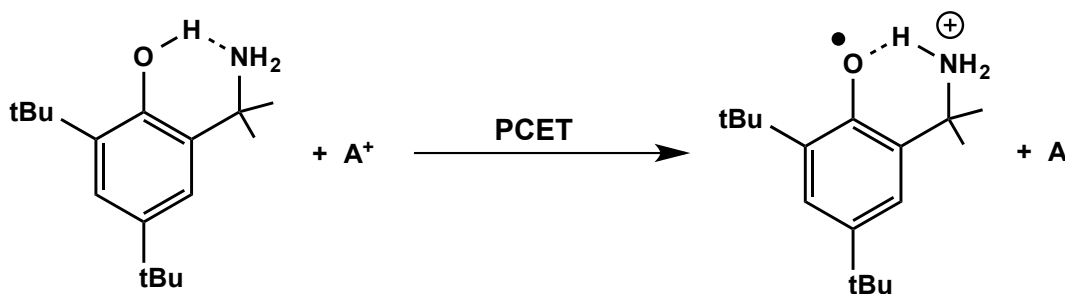


Figure 1.5. General motif used by Mayer to study PCET in phenols hydrogen-bonded to a nearby amine. Oxidation of the phenol, ET, (usually by a chemical oxidant, A^+) generates an acidic phenol radical cation that undergoes PT to the nearby amine. Figure adapted with permission.⁴²

An early publication using this motif examined how driving force affects the PCET reactivity of one of the aforementioned hydrogen bonded phenol-amine compounds.⁴² Five nitrogen-based oxidants of varying strength were used, and kinetic isotope effects (KIEs) and thermochemical arguments suggested a CPET mechanism for all oxidants used. A plot of the rate of ET versus driving force was fit with the adiabatic Marcus equation (Equation 1.2), yielding a large intrinsic barrier of $\lambda = 34 \text{ kcal mol}^{-1}$.

Equation 1.2

$$k = 10^{11} * \exp \left[-\frac{(\lambda + \Delta G^\circ)^2}{4\lambda k_B T} \right]$$

This large barrier is similar to what that observed by Hammarström and co-workers for an aqueous system involving the oxidation of a tyrosine tethered to $\text{Ru}(\text{bpy})_3^{2+}$ ($\lambda = 55 \text{ kcal mol}^{-1}$).⁴⁶ In both cases, this large kinetic barrier is overcome by the fact that the possible stepwise intermediates are charged, high-energy species, favoring the CPET mechanism.

This was followed by one of the first detailed analyses of bi-directional CPET.⁴⁷ Using various chemical oxidants, three substituted-phenols containing differing pendant amines (imidazole, pyridine, primary amine – all of the same general motif in Figure 1.5) exhibited CPET behavior upon mixing (KIEs and thermochemical arguments were used to support this assignment). This reaction was also well-described by the adiabatic Marcus

equation, and it was noted that large intrinsic barriers to CPET cause CPET rate constants to be slower than those for simple ET reactions in organic systems with comparable driving forces. Most interestingly, the authors observed that varying the structure of the proton acceptor had a drastic effect on the rate of CPET, even though the driving force was the same across the three molecules studied.

In another example examining how driving force influences PCET reactivity, Mayer *et al.* synthesized seven phenol-amine compounds, where the amine was an imidazole with various electron donating and withdrawing substituents.⁴⁵ The initial goal was to influence the nature of the hydrogen bond between phenol and amine by varying the electronics of the amine, and to determine whether this affected PCET reactivity. As previously seen, all seven compounds react via CPET upon mixing with a chemical oxidant. However, the rate of CPET correlated only with the driving force for reactivity. This is in contrast to the previously described paper where the driving force was the same, but rate of CPET varied as the structure of the proton acceptor was changed.⁴³ The authors note that comparing reactions at similar driving forces allows one to observe “more subtle effects of structure and substituent effects on other features of CPET.”⁴⁵

Mayer has also used the phenol-amine motif (Figure 1.5) to investigate how varying the proton-donor acceptor distance can affect the rate of PCET.²² Using two amino-phenols with differing proton acceptors – one a traditional primary amine, the other an amino-indanol – PCET occurs in concerted fashion as similarly describe in the aforementioned studies. The amino-indanol has a PT distance between 0.13 – 0.16 Å greater than that of the phenol-amine, and simple tunneling and kinetic models predict this longer donor distance to significantly slow down reactivity. Surprisingly, however, no dependence on the PT distance

is observed for the rate of CPET ($1.4 - 2.8 \times 10^4 \text{ M}^{-1}\text{s}^{-1}$). Because multiple parameters (not just PT distance) are affected by the change in proton acceptor, this study highlights the complexity of PCET reactions and associated challenges of controlling them.

In another example of distance effects in thermal PCET, Mayer *et al.* synthesized a ruthenium terpyridine-4'-carboxylate complex containing 11.2 Å of separation between the carboxylate anion and the ruthenium center.⁴⁸ The oxidized Ru(III) form of this complex was isolated, and stopped-flow rapid-mixing was used to initiate PCET with the hydrogen atom donor TEMPOH. TEMPOH reduced Ru(III) to Ru(II) and transferred a proton to the carboxylate anion in a bidirectional PCET process. Despite the fact that electrochemical experiments show no communication between the ruthenium and carboxylate ligand (the pK_a of the molecule does not change with oxidation state of the ruthenium), this reaction proceeds via CPET mechanism as confirmed by thermodynamic analysis and KIEs. Rates for this reaction were compared to that of a similar ruthenium molecule containing a 6.9 Å distance from metal to carboxylate, and it was found that this shorter molecule, even though it has a smaller driving force for the same PCET reaction with TEMPOH, occurred a thousand times faster than the longer PCET reaction. This study highlights nicely how PCET can be highly distance dependent.

Distance effects can also be measured in excited-state PCET reactions. Wenger *et al.* have used a Re(I) complex with phenol moiety tethered by *p*-xylene linkers to study how varying donor/acceptor distances affect photoinduced PCET (Figure 1.6).³¹

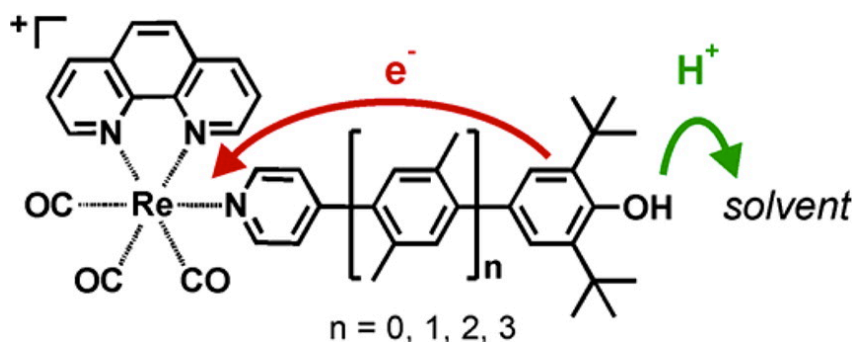


Figure 1.6. Rhenium (I) tricarbonyl photosensitizers with appended 2,6-di-*tert*-butylphenol moieties, linked via *p*-xylylene linkers ($n = 0 - 3$). Upon excitation, the phenol is oxidized by rhenium with proton transfer to solvent (1:1 $\text{H}_2\text{O}/\text{CH}_3\text{CN}$) coupled to the oxidation. Figure used with permission.³¹

When no *p*-xylylene linker is present, excitation induces the release of the phenolic proton, meaning the $n = 0$ dyad behaves like a photoacid, with no ET observed. For the $n = 1$ dyad, the excited complex is quenched via ET from the phenol to rhenium center with no KIE observed for ET. A phenoxyl radical is spectroscopically observed via transient absorption spectroscopy (TA), providing direct evidence for PT (and it was determined this PCET process occurs via stepwise ET-PT. The $n = 2$ dyad exhibits a similar quenching rate via ET as the $n = 1$ dyad, however no phenoxyl radical is observed in this case. This study nicely highlights that strongly coupled donor-acceptor systems exhibit different PCET reactivity as compared to weakly coupled donor-acceptor systems.

Wenger followed this work with a study of the ruthenium(II) analog of the rhenium(I) complex previously highlighted.⁴⁹ In this case, only complexes with $n = 0 - 1$ *p*-xylylene linkers were compared, and the studies were carried out in CH_2Cl_2 with pyridine as an external proton acceptor. No excited-state quenching is observed when pyridine is not present in solution, however, upon the addition of pyridine, both complexes exhibit excited-state quenching with rate constants that differ by two orders of magnitude. TA shows that both complexes form the same photoproducts upon quenching, Ru(II) and phenolate, and it is proposed that these photoproducts are formed via different mechanisms. For the $n = 0$ dyad,

spectral and thermodynamic evidence support this molecule reacting like a photoacid without coupled electron transfer to the ruthenium center. The $n = 1$ dyad is thought to react through initial PCET, forming Ru(I) and phenoxyl radical, with subsequent ET from ruthenium to the phenoxyl moiety. The activation energies for the PCET reactions for these two complexes differ by an order of magnitude, and it is thought that this difference gives rise to the variations in reactivity. This study highlights the difficulties in observing PCET photoproducts while demonstrating again how PCET reactivity can vary when the coupling between donor-acceptor is varied.

Because long-range PCET is an important component of PSII, a thorough understanding of the parameters governing the long-range movement of protons and electrons is an important step in developing a better understanding of PCET.⁵⁰ To begin untangling this problem, a $\text{Ru}(\text{bpz})_3^{2+}$ ($\text{bpz} = 2,2'$ -bipyrazine) complex with a bpz containing one p-xylene spacer bound to a cyanophenol was excited and subsequent PCET reactivity monitored using TA spectroscopy. At first glance this molecule appears to act as a photoacid, as the phenolate anion signal is observed within 2 μs of excitation – this would be consistent with similar studies where no p-xylene linker was present.^{31,49} However, a KIE of 2.0 is determined, and this is used as evidence for initial CPET (too fast to detect photoproducts), followed by rapid back ET (from Ru(I) to phenoxyl radical). This reactivity was compared to that of a similar complex, one containing an unsubstituted phenol moiety, and while the same photoproducts were observed, no KIE was detected. The authors suggest that the unsubstituted phenol dyad undergoes initial rate-determining ET, followed by PT to solvent, before thermal back ET occurs to form the phenolate anion. While not completely conclusive in their assignments of mechanism, this study shows how the presence or absence of an

electron-withdrawing group can affect the mechanism by which an excited-state PCET process occurs, even when the electron-withdrawing group is some distance from the electron acceptor.

Combining some of the work done by Mayer and Wenger, Hammarström synthesized a series of four ruthenium – tyrosine complexes that undergo intramolecular PCET and have varying PT distances (Figure 1.7).⁵¹

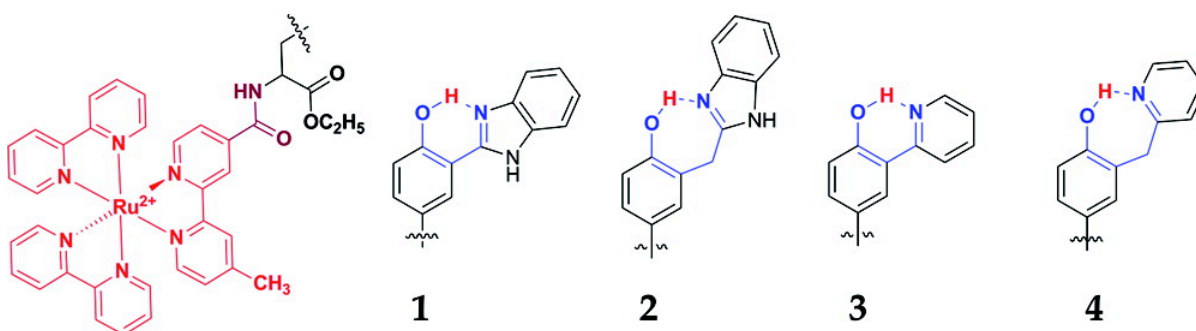


Figure 1.7 Ru(II) photosensitizers linked to hydrogen bonded tyrosine moieties. Upon excitation of Ru(II), methyl viologen is used to oxidatively quench the excited state and generate a Ru(III) species. Ru(III) initiates PCET via ET from tyrosine to Ru(III) and PT to pendant amine. Figure used with permission.⁵¹

Using flash-quench methods to generate a Ru(III) species, PCET occurs via concerted mechanism. Each tyrosyl proton is intramolecularly hydrogen bound to a nearby base, though the strength and distance of this bond differs among complexes due to the difference in bases used and inclusion of methylene spacer. Interestingly, it was determined that CPET occurs faster in the two complexes with lower CPET driving forces (complexes 1 and 3, Figure 1.7). This is due to these two species having shorter hydrogen bond lengths, giving better proton wave function overlap and smaller KIEs. A distance decay constant ($\beta = 27 \text{ \AA}^{-1}$) was also determined, highlighting the sensitivity of the rate of PCET to distance of PT.

Wenger *et al.* follow up on this work by Hammarström with two studies that again use ruthenium compounds containing phenol moieties that are tethered through *p*-xylene linkers. In the first example,⁵² complexes with $n = 1 - 3$ *p*-xylene linkers are used, and upon excitation, the photosensitizer initiates CPET with ET occurring from phenol to ruthenium, and PT occurring to a pyrrolidine base in solution. By varying the number of *p*-xylene linkers, the distance for the ET component of PCET is increased, and TA was used to monitor how varying this distance affects the rate for the PCET process. The overall reaction was determined to proceed via CPET, and the rates were comparable to similar studies of simple ET.⁵² Importantly, a value of $\beta = 0.67 \pm 0.23 \text{ \AA}^{-1}$ for this bidirectional PCET process was determined from this data. This is similar in magnitude to that of simple electron tunneling across oligo-*p*-spacers,⁵³ and provides an initial suggestion that a distance dependence for rates of CPET are not significantly steeper than typical ET rates.

The second study again used a $\text{Ru}(\text{bpy})_3^{2+}$ -phenol dyad linked via *p*-xylene linkers, but now methyl viologen was used as an external quencher and imidazole as a proton acceptor. $\text{Ru}(\text{bpy})_3^{2+}$ is excited and rapidly oxidatively quenched to form a $\text{Ru}(\text{III})$ species. PCET then occurs, with ET occurring from phenol to $\text{Ru}(\text{III})$ and PT to imidazole. This process was determined to occur via CPET, and another distance decay constant was determined for CPET. In this case $\beta = 0.87 \pm 0.09 \text{ \AA}^{-1}$, which is one of the largest values determined for ET across materials of this nature. This provides a second data point regarding the effect distance has on the rate of bidirectional CPET.

A final variable of PCET that has been studied extensively using phenols in non-aqueous environments is hydrogen bonding. While some of the previously described studies

have touched on hydrogen bonding and the role it can play in solution, other studies have solely focused on the role hydrogen bonding can play in PCET.

Mayer and co-workers investigated how the strength of a hydrogen bond in pyridylphenols affects the rate of CPET.⁴⁴ Two phenol-amine compounds were used in this study. The first was a phenol with pendant pyridine directly linked to the phenol, and the second phenol contained a pendant pyridine linked via methylene spacer. This methylene spacer breaks conjugation between pyridine and phenol, and crystallographic evidence suggests the pyridine ring twists out of plane when H-bonding to phenol, making the O--N distance 0.13 Å greater for the compound with the methylene spacer. The CPET reaction for these two compounds was monitored, and the species without a spacer reacts 25-150x faster (depending on the oxidant) than the compound containing the spacer, even though the proton acceptor is the same in both molecules. Rates for the spacer-containing compound were comparable to those of a phenol-primary amine compound (also not conjugated to the phenol), suggesting the nature of the base in this example is not important. The authors conclude that conjugation has a marked effect on the nature of the hydrogen bond, which is reflected in the rates of CPET.

Similar complexes were also utilized by Wenger to begin studying how hydrogen bonding between phenols and pyrazine can affect the favorability of either ET or PT in a PCET reaction. Using two rhenium (I) tricarbonyl diimine complexes, containing a bipyrazine (bpz) and pyridine (pyr) ligands, the other with a bipyridine (bpy) and pyrazine (pyz) ligand, the authors were able to favor either ET or PT from *p*-cyanophenol to the excited rhenium complex (Figure 1.8).³⁰

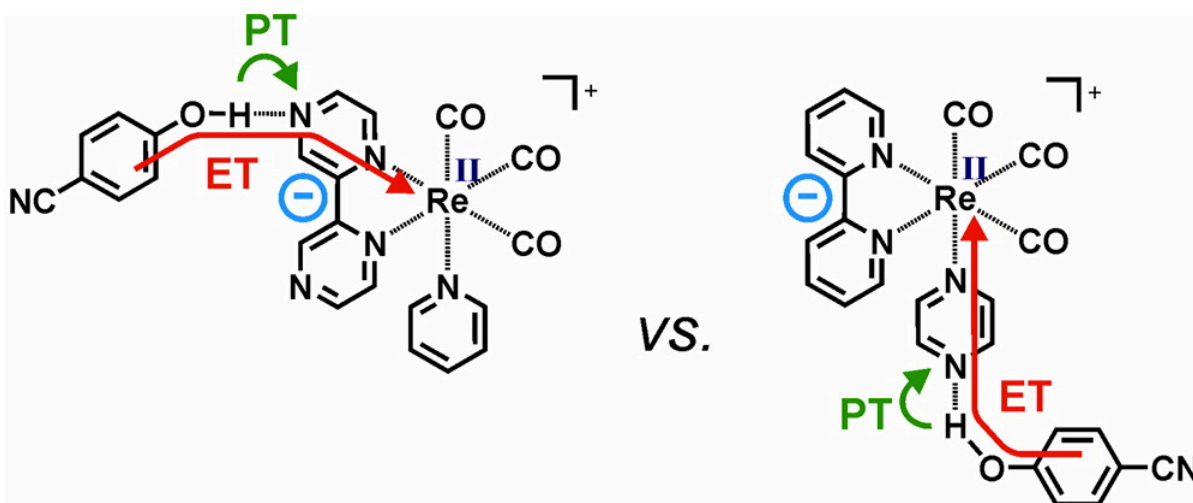


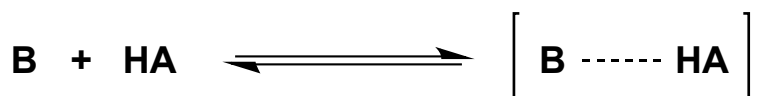
Figure 1.8. Photoexcited rhenium complexes containing (left) a bipyrazine and pyridine ligand (to favor PT, disfavor ET), and (right) a bipyridine and pyrazine ligand (to disfavor PT, favor ET). Figure used with permission.³⁰

In the case of the bpz-py complex, MLCT excitation occurs towards the bpz ligand, to which *p*-cyanophenol is hydrogen bound. The increased electron density on the bpz ring makes PT favorable, but ET to Re(II) less favorable. Conversely, MLCT excitation of the bpy-pyz complex occurs towards the bpy ligand. Because *p*-cyanophenol is hydrogen bonded to pyz in this scenario, ET can more easily occur to the rhenium center, while PT is less favored. TA was used to observe the photoproducts, and in both cases a PCET reaction occurs. Both are most likely to occur via CPET, however, a PT-ET pathway cannot be completely ruled out. The most interesting aspect of this study is the fact that bimolecular rate constants for quenching of the rhenium compounds are on the same order of magnitude. It appears that in this particular case, it does not matter whether the MLCT process occurs towards or away from the protonatable ligand, PCET still occurs at roughly the same rate ($2.0 - 3.6 \times 10^7 \text{ M}^{-1} \text{ s}^{-1}$ depending on the complex analyzed and optical technique used).

Hydrogen bonding in PCET systems is a topic in itself that many researchers have found difficult to quantify and accurately describe, thus it is worth discussing some previous

examples of hydrogen bonding, and what the current best practices are for measuring and accounting for this parameter. Three methods have traditionally been employed to quantify this technique. Consider Equation 1.3 where species HA and B can hydrogen bond in solution.

Equation 1.3



The first method uses UV-vis absorption spectroscopy to quantify the amount of hydrogen bonding. Assuming HA has a strong ground-state absorbance feature in the UV-vis spectrum, species B should either not have any appreciable absorbance features, or it should absorb in a different region of the spectrum from the peak of interest. Beginning with a solution of just HA, UV-vis spectroscopy should be used to monitor the shift of the HA absorbance feature as known concentrations of species B are titrated into solution. This is comparable to a spectrophotometric titration,^{23,32} and is highlighted in a seminal PCET paper by Linschitz *et al.*⁵⁴ This technique becomes challenging however, when peaks overlap or there is no absorbance shift upon addition of HA to B.

The second method uses steady-state luminescence quenching to quantify the amount of hydrogen bonding. This method was first proposed in 2007 to quantify a proposed excited-state hydrogen bonding adduct that was not present in the ground state.⁵⁵ It has subsequently been used in a variety of PCET papers,^{56,57} however this method has recently come under scrutiny.⁵²

The final technique uses nuclear magnetic resonance (NMR) to quantify hydrogen bonding between two species. By monitoring the chemical shift for the acidic proton on HA while adding increasing amounts of B, an association constant can be extracted by plotting

the chemical shift against the concentration of B added. This has been used successfully to quantify the extent of hydrogen bonding and is the recommended method for doing so if experimental conditions allow.^{12,58,59}

1.6. New Optical Methods for Monitoring PCET

Stopped-flow rapid-mixing coupled with optical monitoring, TA spectroscopy, and electrochemistry are all well understood and valuable techniques for studying PCET reactions. They complement one another well and have served as the tools for much of the advancement in the field. However, a shortcoming that prevails throughout these techniques, and the chemistry exploited while using them, is that few PCET processes can be directly monitored in their entirety. That is to say, observing both the ET and PT components of a PCET reaction is no easy task. This is largely due to the fact that electron movement is much easier to monitor than proton movement. With stopped-flow spectroscopy, an electron transfer event is typically observed by monitoring the disappearance of the visible absorbance of a chemical oxidant (ET). In TA, transition metal complexes are employed as photosensitizers for initiating PCET, as a change in oxidation state typically results in an observable spectroscopic change. Electrochemistry was developed to strictly monitor ET by measuring the flow of electrons into and out of an electrode. None of these techniques are inherently useful methods for measuring PT reactions, and this is a problem when PT represents half of the reaction being studied. Instead, researchers have relied on KIEs and thermochemical analysis to rule out various mechanisms, meaning very few studies have directly monitored PT in a PCET reaction. Therefore, developing methods that provide a spectroscopic handle for both ET *and* PT events would be highly beneficial for studying both steps in a PCET reaction. Further, as our goal is to eventually develop a device that uses light

to drive the transformation of small molecules, like H₂O, into energy rich fuels, developing methods that can study excited-state PCET processes would be particularly valuable. Very few of the studies described above (and in the broader context of all PCET research) have been able to study excited-state PCET reactions, leading to a lack of understanding of these processes when comparing what is known about their thermal counterparts. As such, the studies described within seek to develop new methods for studying both ET and PT, particularly in the excited state, in order to gain insight to aid in the development of solar fuels technologies.

In the following chapters, this dissertation will describe the use of a commercially available N-heterocycle to initiate and monitor an excited-state PCET reaction, as well as a series of molecules that have been developed to monitor PT reactions in both the ground-state and excited-state. The first study described centers around acridine orange (AO), a commercially available N-heterocycle that displays a red-shifted visible absorbance feature upon protonation.³² TA was used to monitor the reactivity of AO when excited in the presence of tri-*tert*-butylphenol (^{ttb}PhOH). Spectral evidence, supported by spectroelectrochemistry and thermochemical calculations, clearly showed that excited AO reacts with ^{ttb}PhOH to form acridinium orange radical (AOH[•]) via excited-state CPET. Recombination was observed to occur via ET-PT, and again the spectroscopic evidence was supported by thermochemical calculations. Rates for each of the processes were determined by monitoring kinetics at specific wavelengths, rounding out a comprehensive spectral and kinetic picture of the reaction between AO and ^{ttb}PhOH.

The rest of the dissertation focuses on a series of 2,4-R-7-dimethylaminoquinolines (R-7DMAQ), that have been synthesized, characterized in acetonitrile, and employed as

optical probes for PT reactions. These molecules are particularly useful for this type of reactivity because upon protonation, the UV-visible absorbance of these R-7DMAQs undergoes a significant red-shift, providing an excellent spectroscopic handle for optically monitoring PT. By varying the substituent at the 2- and 4- positions, the electronics of each R-7DMAQ are changed, providing both spectroscopic and pK_a tunability. Dubbed “photometric bases,” four of these molecules were used in stopped-flow studies to monitor PT, while the decay of the absorbance of the chemical oxidant (used to initiate PCET by oxidizing *p*-aminophenol) was used to monitor the ET step. The rate of PT showed a dependence on the pK_a of the conjugate acid of the R-7DMAQ employed, which could be explained by either transition state theory or by Marcus-type nonadiabatic PT.

The fifth of these R-7DMAQs was used as a photosensitizer for excited-state proton transfer (ESPT) reactions. The conjugate acid of 2,4-bis(3,5-trifluoromethyl)-7-dimethylaminoquinoline (CF₃-7DMAQ) has a $pK_a = 11.5$ in acetonitrile. Upon excitation, CF₃-7DMAQ becomes much more basic; its conjugate acid has an excited-state $pK_a = 17.7$. Using two types of time-resolved spectroscopy, CF₃-7DMAQ was excited in the presence of a series of acids with pK_a 's ranging from 15.0 – 17.9, and both the forward and back PT were monitored. The forward PT reaction was observed by monitoring quenching of the fluorescence of CF₃-7DMAQ (30 ns lifetime). TA was also used to monitor forward PT as the growth of the conjugate acid of CF₃-7DMAQ is easily observed at 490 nm. Recombination occurs over longer timescales (~200-300 μ s) and was also monitored using TA. Data show a linear free energy relationship for the thermal back PT, however hydrogen bonding complicates measurements for forward PT. NMR titrations were used to quantify

hydrogen bonding in order to explain the observed rate constants for the forward process, and provide insight into the role hydrogen bonding plays in static quenching processes.

By studying the PT component in all of these systems, a few trends have become clear. In the case of acridine orange, monitoring the PT component of the reaction allowed for direct detection of the PT product in an excited state PCET reaction, and the determination that recombination for this system occurred in stepwise ET-PT fashion. Using photometric bases to monitor PT in stopped-flow studies also provided a complete picture of the mechanism for this PCET process, but also was critical in observing a free energy relationship between the rate of PT and driving force for reactivity. Lastly, monitoring PT in the excited state provided another example of a free energy relationship for PT reactions, and also key insight into the effect hydrogen bonding can have on an excited state process.

This work described in this dissertation aims to develop new methods for monitoring PT and PCET for the purpose of extracting relevant kinetic information regarding PCET reactions. By using N-heterocycles whose optical signatures shift upon a change in protonation state, both excited-state and ground state PT events were monitored by a variety of techniques. As work in this field advances and a better understanding of excited-state PCET is developed, it is hoped that this knowledge will be used to develop catalysts that function efficiently in new, sustainable energy devices.

REFERENCES

- (1) Agency, I. E. *World Energy Outlook 2015*; 2015.
- (2) Lewis, N. S.; Nocera, D. G. *Proc. Nat. Acad. Sci. USA* **2006**, *103* (43), 15729.
- (3) Pales, J. C.; Keeling, C. D. *J. Geophys. Res.* **1965**, *70* (24), 6053.
- (4) Hammarström, L.; Styring, S. *Energy Environ. Sci.* **2011**, *4* (7), 2379.
- (5) Carra, C.; Iordanova, N.; Hammes-Schiffer, S. *J. Am. Chem. Soc.* **2003**, *125* (34), 10429.
- (6) Magnuson, A.; Berglund, H.; Korall, P.; Hammarström, L. *J. Am. Chem. Soc.* **1997**, *119* (II), 10720.
- (7) Mayer, J. M.; Rhile, I. J.; Larsen, F. B.; Mader, E. A.; Markle, T. F.; DiPasquale, A. *G. Photosynth. Res.* **2006**, *87* (1), 3.
- (8) Svensson, B.; Etchebest, C.; Tuffery, P.; van Kan, P.; Smith, J.; Styring, S. *Biochemistry* **1996**, *35* (46), 14486.
- (9) Artero, V.; Fontecave, M. *Chem. Soc. Rev.* **2013**, *42* (6), 2338.
- (10) Rountree, E. S.; McCarthy, B. D.; Eisenhart, T. T.; Dempsey, J. L. *Inorg. Chem.* **2014**, *53* (19), 9983.
- (11) Dempsey, J. L.; Winkler, J. R.; Gray, H. B. *J. Am. Chem. Soc.* **2010**, *132* (47), 16774.
- (12) McCarthy, B. D.; Martin, D. J.; Rountree, E. S.; Ullman, A. C.; Dempsey, J. L. *Inorg. Chem.* **2014**, *53* (16), 8350.
- (13) Robert A. Binstead; Bruce A. Moyer; Samuels, G. J.; Thomas J. Meyer. *J. Am. Chem. Soc.* **1981**, *103*, 2897.
- (14) Hammes-Schiffer, S. *J. Am. Chem. Soc.* **2015**, *137*, 8860.
- (15) Costentin, C. *Chem. Rev.* **2008**, *108* (7), 2145.
- (16) Weinberg, D. R.; Gagliardi, C. J.; Hull, J. F.; Murphy, C. F.; Kent, C. a; Westlake, B. C.; Paul, A.; Ess, D. H.; McCafferty, D. G.; Meyer, T. J. *Chem. Rev.* **2012**, *112* (7), 4016.
- (17) Warren, J. J.; Tronic, T. A.; Mayer, J. M. *Chem. Rev.* **2010**, *110*, 6961.
- (18) Kretchmer, J. S.; Miller, T. F. *Inorg. Chem.* **2016**, *55*, 1022.

- (19) Costentin, C.; Robert, M.; Savéant, J.-M. *Chem. Soc. Rev.* **2010**, *110*.
- (20) Kaila, V. R. I.; Verkhovsky, M. I.; Wikström, M. *Chem. Rev.* **2010**, *110* (12), 7062.
- (21) Manner, V. W.; Dipasquale, A. G.; Mayer, J. M. *J. Am. Chem. Soc.* **2008**, *130*, 7210.
- (22) Markle, T. F.; Rhile, I. J.; Mayer, J. M. *J. Am. Chem. Soc.* **2011**, *133*, 17341.
- (23) Saouma, C. T.; Kaminsky, W.; Mayer, J. M. *J. Am. Chem. Soc.* **2012**, *134*, 10.
- (24) Warren, J. J.; Mayer, J. M. *J. Am. Chem. Soc.* **2008**, *130* (9), 2774.
- (25) Bourrez, M.; Steinmetz, R.; Ott, S.; Gloaguen, F.; Hammarström, L. *Nat. Chem.* **2015**, *7* (2), 140.
- (26) Zhang, M.-T.; Hammarström, L. *J. Am. Chem. Soc.* **2011**, *133* (23), 8806.
- (27) Sjödin, M.; Irebo, T.; Utas, J. E.; Lind, J.; Merényi, G.; Akermark, B.; Hammarström, L. *J. Am. Chem. Soc.* **2006**, *128* (40), 13076.
- (28) Johannissen, L. O.; Irebo, T.; Sjödin, M.; Johansson, O.; Hammarström, L. *J. Phys. Chem. B* **2009**, *113* (50), 16214.
- (29) Gagliardi, C. J.; Westlake, B. C.; Kent, C. A.; Paul, J. J.; Papanikolas, J. M.; Meyer, T. *J. Coord. Chem. Rev.* **2010**, *254* (21-22), 2459.
- (30) Bronner, C.; Wenger, O. S. *Inorg. Chem.* **2012**, *51* (15), 8275.
- (31) Kuss-Petermann, M.; Wolf, H.; Stalke, D.; Wenger, O. S. *J. Am. Chem. Soc.* **2012**, *134* (30), 12844.
- (32) Eisenhart, T. T.; Dempsey, J. L. *J. Am. Chem. Soc.* **2014**, *136* (35), 12221.
- (33) Costentin, C.; Drouet, S.; Passard, G.; Robert, M.; Savéant, J.-M. *J. Am. Chem. Soc.* **2013**, *135*, 9023.
- (34) Costentin, C.; Hajj, V.; Louault, C.; Robert, M.; Savéant, J.-M. *J. Am. Chem. Soc.* **2011**, *133* (47), 19160.
- (35) Savéant, J.-M. *Energy Environ. Sci.* **2012**, *5* (7), 7718.
- (36) Costentin, C.; Robert, M.; Savéant, J.-M.; Teillout, A.-L. *Proc. Natl. Acad. Sci. U. S. A.* **2009**, *106* (29), 11829.
- (37) Alligrant, T. M.; Alvarez, J. C. *J. Phys. Chem. C* **2011**, *115* (21), 10797.

- (38) Alligrant, T. M.; Hackett, J. C.; Alvarez, J. C. *Electrochim. Acta* **2010**, *55* (22), 6507.
- (39) Hammes-Schiffer, S. *Energy Environ. Sci.* **2012**, *5* (7), 7696.
- (40) Hammes-Schiffer, S.; Stuchebrukhov, A. A. *Chem. Rev.* **2010**, *110* (12), 6939.
- (41) Skone, J. H.; Soudackov, A. V; Hammes-schiffer, S. *J. Am. Chem. Soc.* **2006**, *128* (16), 16655.
- (42) Rhile, I. J.; Mayer, J. M. *J. Am. Chem. Soc.* **2004**, *126* (40), 12718.
- (43) Rhile, I. J.; Markle, T. F.; Nagao, H.; Dipasquale, A. G.; Lam, O. P.; Lockwood, M. A.; Rotter, K.; Mayer, J. M. *J. Am. Chem. Soc.* **2006**, *128*, 6075.
- (44) Markle, T. F.; Mayer, J. M. *Angew. Chemie - Int. Ed.* **2008**, *47* (4), 738.
- (45) Markle, T. F.; Markle, T. F.; Rhile, I. J.; Rhile, I. J.; Dipasquale, A. G.; Dipasquale, A. G.; Mayer, J. M.; Mayer, J. M. *Proc. Natl. Acad. Sci.* **2008**, *105*, 8185.
- (46) Sjodin, M.; Hammarström, L. *J. Am. Chem. Soc.* **2000**, *122*, 3932.
- (47) Rhile, I. J.; Markle, T. F.; Nagao, H.; Dipasquale, A. G.; Lam, O. P.; Lockwood, M. A.; Rotter, K.; Mayer, J. M. *J. Am. Chem. Soc.* **2006**, *128*, 6075.
- (48) Manner, V. W.; Mayer, J. M. *J. Am. Chem. Soc.* **2009**, *131* (29), 9874.
- (49) Kuss-Petermann, M.; Wenger, O. S. *J. Phys. Chem. A* **2013**, *117* (28), 5726.
- (50) Bronner, C.; Wenger, O. S. *Phys. Chem. Chem. Phys.* **2014**, *16* (8), 3617.
- (51) Zhang, M.; Irebo, T.; Johansson, O.; Hammarström, L. *J. Am. Chem. Soc.* **2011**, *133* (34), 13224.
- (52) Chen, J.; Kuss-Petermann, M.; Wenger, O. S. *Chem. A Eur. J.* **2014**, *20*, 4098.
- (53) Wenger, O. S. *Chem. Soc. Rev.* **2011**, *40* (7), 3538.
- (54) Biczok, L.; Gupta, N.; Linschitz, H. *J. Am. Chem. Soc.* **1997**, *119* (51), 12601.
- (55) Concepcion, J. J.; Brennaman, M. K.; Deyton, J. R.; Lebedeva, N. V; Forbes, M. D. E.; Papanikolas, J. M.; Meyer, T. J. *J. Am. Chem. Soc.* **2007**, *129*, 6968.
- (56) Bronner, C.; Wenger, O. S. *J. Phys. Chem. Lett.* **2012**, *3*, 70.
- (57) Pizano, A. A.; Yang, J. L.; Nocera, D. G. *Chem. Sci.* **2012**, *3* (8), 2457.

- (58) Nomrowski, J.; Wenger, O. S. *Inorg. Chem.* **2015**, 54 (7), 3680.
- (59) Macomber, R. S. *J. Chem. Educ.* **1992**, 69 (5), 375.

CHAPTER 2: PHOTO-INDUCED PROTON-COUPLED ELECTRON TRANSFER REACTIONS OF ACRIDINE ORANGE: COMPREHENSIVE SPECTRAL AND KINETICS ANALYSIS

Reprinted with permission from Eisenhart, T.T. and Dempsey, J.L. Photo-induced Proton-Coupled Electron Transfer Reactions of Acridine Orange: Comprehensive Spectral and Kinetics Analysis. *J. Am. Chem. Soc.*, **2014**, *136*, 12221-12224. © 2014 American Chemical Society.

2.1. Introduction

Proton-coupled electron transfer (PCET) processes are central to the conversion of small molecules to energy-rich fuels.^{1,2} Harvesting solar energy to achieve these challenging transformations is an increasingly attractive option as the need for alternative energy resources becomes more pressing. Investigation of PCET in biological systems and in molecular models provides a general understanding of PCET processes between molecules in their electronic ground states,¹⁻⁶ but comparatively little is known about PCET reactions of electronically excited molecules.⁷⁻⁹ In response, we are undertaking mechanistic studies to provide a comprehensive understanding of excited-state PCET reactions. Rationalizing how to integrate light absorption and H^+/e^- transfer will facilitate the design of new systems that can effectively couple energy capture and conversion.

A great deal of research has focused on the thermal PCET reactions of phenol substrates, in part because of the importance of tyrosine radicals in biological systems such as photosystem II and ribonucleotide reductase.^{1,2,4,5,10} As a result, the PCET thermochemistry for a great many phenols is well established, including parameters for concerted proton-electron transfer (CPET) and stepwise electron transfer-proton-transfer (ET-PT) and proton-transfer-electron transfer (PT-ET) pathways.¹¹ By coupling this

information to excited-state reduction potentials (obtained via modified Latimer diagrams^{12,13}) and excited-state pK_a values (determined from Förster cycles^{14,15}), a thermochemical picture of excited-state PCET reactions can be developed.⁸

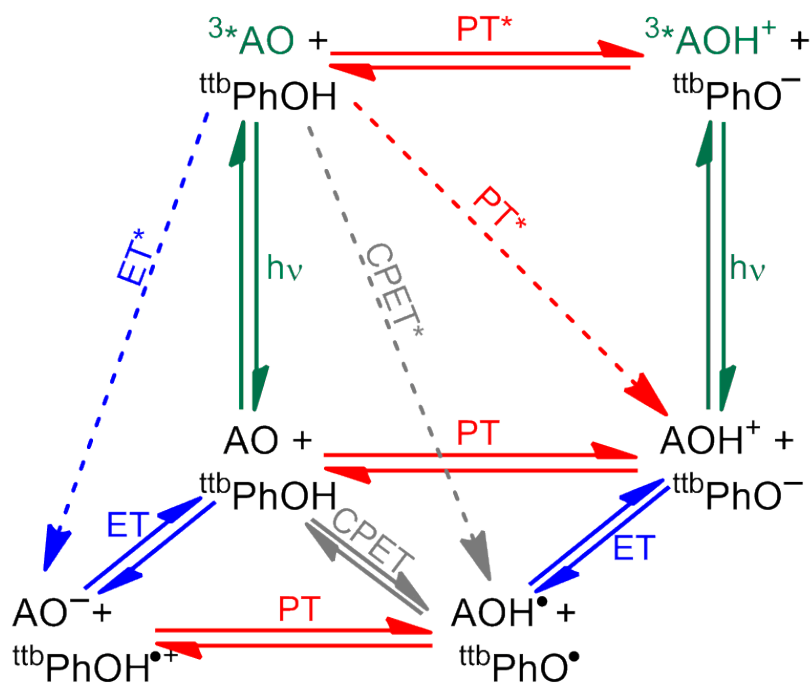


Figure 2.1 PCET square scheme incorporating ground and excited state reactivity.

2.2. Discussion and Results

Here we describe the detailed mechanistic study of a system that undergoes excited-state PCET followed by a thermal PCET reaction that yields the reactants in their electronic ground states. Our model system is based on acridine orange (AO), a Brønsted base and a mild excited-state oxidant¹⁶ that undergoes efficient intersystem crossing to a π - π^* -based triplet state.^{16,17} Employing AO, we phototrigгер the PCET oxidation of tri-*tert*-butylphenol (^{ttb}PhOH) in CH₃CN and track the reaction intermediates with time-resolved spectroscopy.

³*AO can react with ^{ttb}PhOH through a concerted pathway or one of several stepwise PCET reaction pathways (Figure 2.1). The strong absorption features of AO ($\lambda_{\text{max}} = 425 \text{ nm}$, $\epsilon = 25,000 \text{ M}^{-1} \text{ cm}^{-1}$) and the corresponding acridinium (AOH^+ , $\lambda_{\text{max}} = 495 \text{ nm}$, $\epsilon = 62,500 \text{ M}^{-1} \text{ cm}^{-1}$) provide spectroscopic handles for determining the AO protonation states; the oxidation states of these species can also be assessed optically. Analysis of the transient absorption (TA) spectra and corresponding kinetics traces provides a complete picture of the light-induced PCET oxidation of phenol and the subsequent thermal reaction.

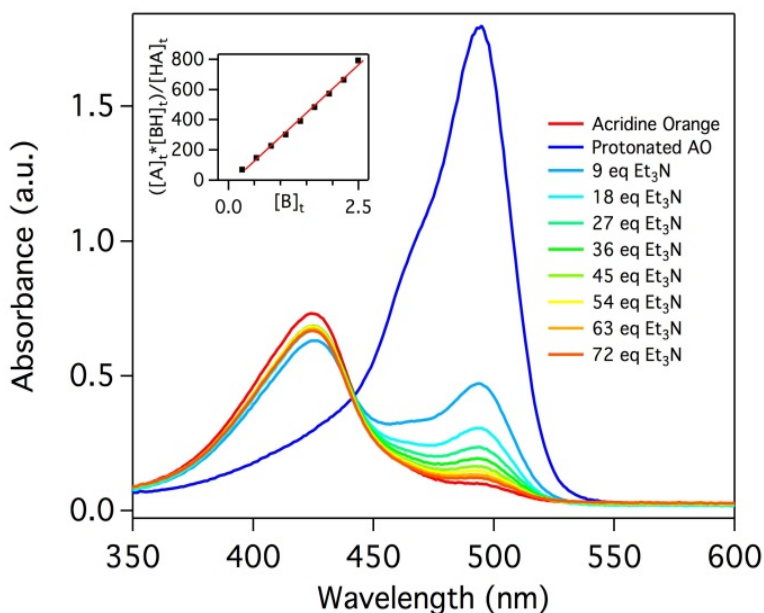


Figure 2.2 Spectrophotometric titration of acridine orange was used to determine the pK_a in CH_3CN . AO was first completely protonated with 1 equivalent of $\text{HBF}_4 \cdot \text{Et}_2\text{O}$ before being titrated with additions of triethylamine ($pK_a = 18.3$). An absorbance spectrum was obtained before and after protonation, and after every addition of Et_3N . The pK_a of AO ($pK_a = 19.3$) was determined using the method of Saouma *et al.*³

In the absence of reactive O–H bonds, TA spectra of AO in CH_3CN (Figure 2.3) were recorded at time intervals between 100 ns and 100 μs following excitation ($\lambda_{\text{ex}} = 425 \text{ nm}$) reveal three features: new absorptions centered at 410 and 540 nm corresponding to the

triplet excited state of ($^3\text{*AO}$) and a bleach centered at 435 nm due to the loss of the ground state AO absorption.

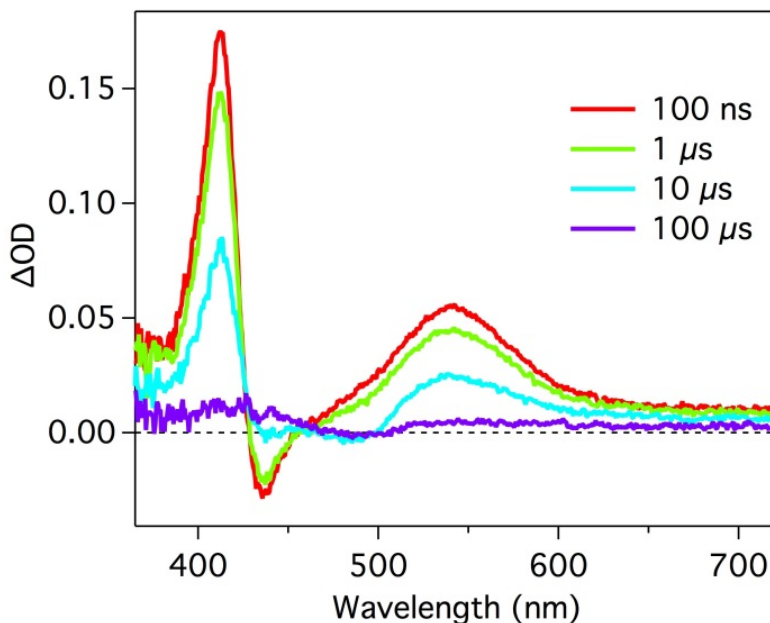


Figure 2.3. Transient difference spectra of 40 μM AO in CH_3CN at selected time delays after laser excitation. $\lambda_{\text{ex}} = 425 \text{ nm}$, 0.1 mM $[\text{Bu}_4\text{N}][\text{PF}_6]$.

These transient features decay non-exponentially: $^3\text{*AO}$ undergoes first-order decay through a nonradiative process (k_{nr}), reacts through a triplet-triplet interaction (k_{TT}) to produce the corresponding radical cation (AO^+) and radical anion (AO^-), and is quenched by ground state AO (k_{s}).^{16–18} Transient features and decay rate constants determined from modeling single wavelength kinetics traces are similar to those reported in water at pH 12 (Figure 2.4).¹⁶

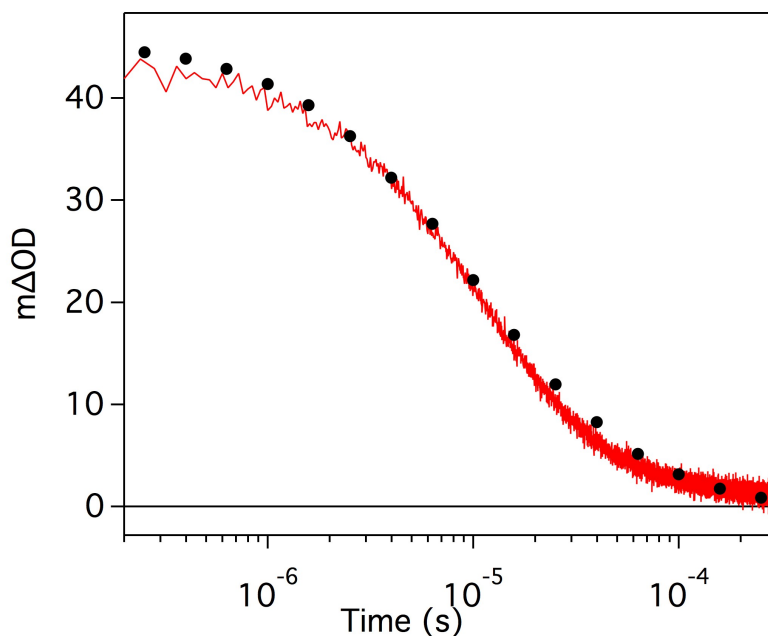


Figure 2.4 Decay of the triplet excited state of AO monitored at 560 nm in CH₃CN (line) and the corresponding simulated spectrum (markers). Rate constants determined from the simulation and the values previously determined in water at pH 12: k_{nr} (300 s⁻¹, lit: 300 s⁻¹), k_{TT} (5.3×10^9 M⁻¹ s⁻¹, lit: 5.5×10^9 M⁻¹ s⁻¹), k_S (1.0×10^8 M⁻¹ s⁻¹, lit: 3×10^8 M⁻¹ s⁻¹). k_{AOH} was determined independently (4.0×10^4 s⁻¹). 40 μ M AO, λ_{ex} = 425 nm, λ_{obs} = 560 nm, 0.1 M [Bu₄N][PF₆].

In the presence of ^{ttb}PhOH, we observe accelerated decay of the ³*AO transient absorption features (410 and 540 nm) (Figure 2.5). Between 100 ns and 10 μ s, the blue absorption feature undergoes a bathochromic shift to 425 nm. This new feature is consistent with the formation of a neutral acridine radical (AOH•), the absorption spectrum (λ_{max} = 425 nm, $\epsilon \geq 6,500$ M⁻¹ cm⁻¹) of which was measured independently via reduction of AOH⁺ in a spectroelectrochemical cell (Figure 2.6). The concurrent growth of a small signal at 400 nm indicates the formation of ^{ttb}PhO• (λ_{max} = 400, ϵ = 2,120 M⁻¹ cm⁻¹).¹⁹ In the time interval 10–100 μ s, the AOH• signal decays and a transient bleach centered at 425 nm, assigned to the loss of AO, appears on the high-energy side of the spectra. Most notably, the spectra

recorded in the time interval 4–100 μs are dominated by the growth of a prominent feature at 495 nm, which is consistent with production of AOH^+ .

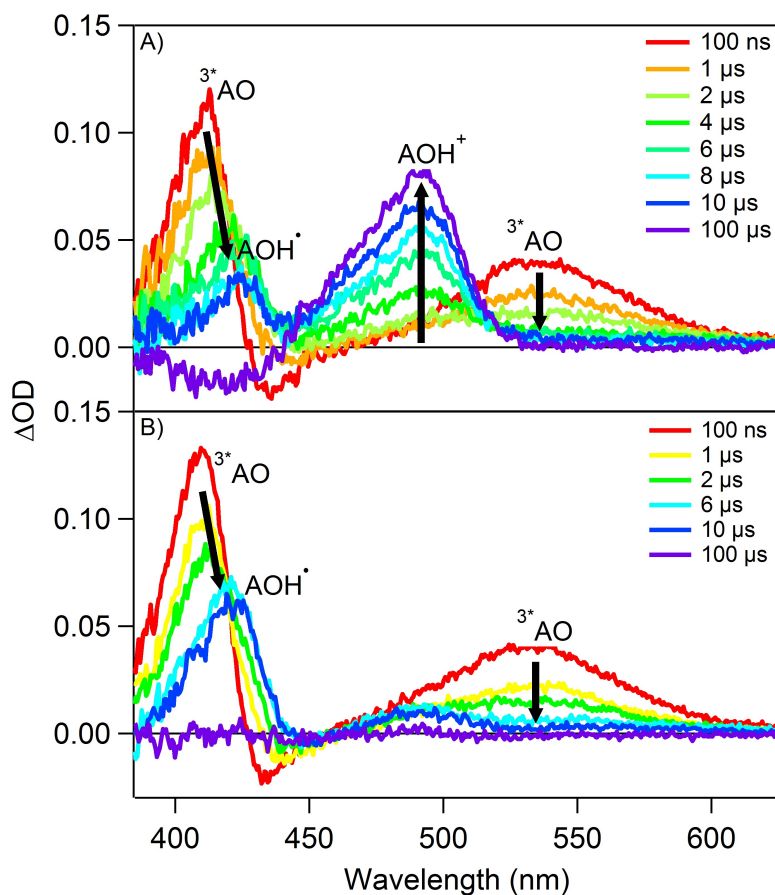


Figure 2.5 Transient difference spectra of A) 40 μM AO and 1 mM ttbPhOH and B) 40 μM AO and 3 mM TEMPOH in CH_3CN at selected time delays after laser excitation. $\lambda_{\text{ex}} = 425 \text{ nm}$, 0.1 mM $[\text{Bu}_4\text{N}][\text{PF}_6]$.

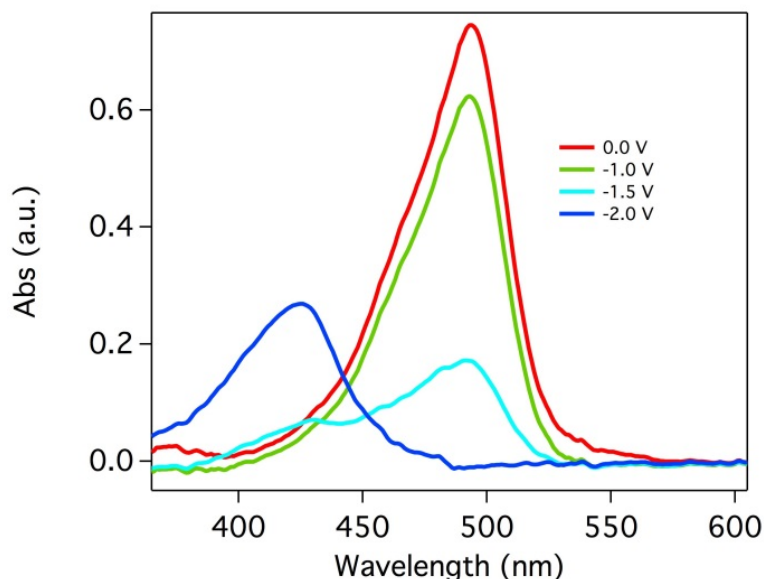


Figure 2.6 Spectroelectrochemistry of 40 μM AOH^+ in CH_3CN . Optical spectra of AOH^+ were recorded in a spectroelectrochemical cell as applied potentials were stepped to increasingly negative values (hold time = 3 s). Bleaching of the characteristic AOH^+ absorption feature ($\lambda_{\text{max}} = 495 \text{ nm}$) is accompanied by growth of a new feature at 425 nm, which we assign to the product of direct reduction, AOH^\bullet .⁵ A clean isosbestic was not observed, suggesting that AOH^+ is not cleanly converted to the acridinium radical, AOH^\bullet . This observation is consistent with the irreversibility observed in CV experiments (Figure S9). Based on the molar extinction coefficient for AOH^+ ($\epsilon = 18,000 \text{ M}^{-1} \text{ cm}^{-1}$), we estimate a lower limit for $\epsilon(\text{AOH}^\bullet)$ of $6,500 \text{ M}^{-1} \text{ cm}^{-1}$. Spectra were recorded with a honeycomb platinum working electrode (Pine Instruments), a platinum counter electrode and a Ag pseudo-reference electrode. We were unable to reference the applied potentials directly to ferrocene with this electrochemical cell. As such, these spectra are referenced only to the silver pseudoreference ($\text{Ag}^{+/0}$) and the results are qualitative, not quantitative.

For comparison, we also explored excited-state PCET reactivity of AO in the presence of 2,2'-6,6'-tetramethylpiperidine-1-ol (TEMPOH), a well-documented PCET reagent that favors CPET over stepwise mechanisms.¹¹ As for $^{\text{ttb}}\text{PhOH}$, added TEMPOH quenches the triplet absorbance features of AO at 410 and 540 nm (Figure 2.5). The appearance of AOH^\bullet (425 nm) is observed on the timescale 100 ns – 10 μs . The concurrent detection of TEMPO^\bullet is not expected ($\lambda_{\text{max}} = 463 \text{ nm}$, $\epsilon = 10 \text{ M}^{-1} \text{ cm}^{-1}$).²⁰ In contrast with the reactivity of $^{\text{ttb}}\text{PhOH}$, no dominant signal at 495 nm appears. The signal corresponding to AOH^\bullet decays on the 100 μs timescale.

Optical detection of discrete intermediates aids evaluation of H^+/e^- transfer

mechanisms for reactions between ^3AO with $^{\text{ttb}}\text{PhOH}$ or TEMPOH. The mechanisms indicated in Figure 2.7 and Figure 2.8 are consistent with the spectral evidence for reaction intermediates. ^3AO is quenched by CPET from both $^{\text{ttb}}\text{PhOH}$ and TEMPOH to form $^{\text{ttb}}\text{PhO}^\bullet$ and TEMPO $^\bullet$, respectively, along with AOH $^\bullet$. This reactivity is presumed to occur through a hydrogen-bonded encounter complex, consistent with previous reports of photo-induced PCET reactions in organic solvents.^{21–23}

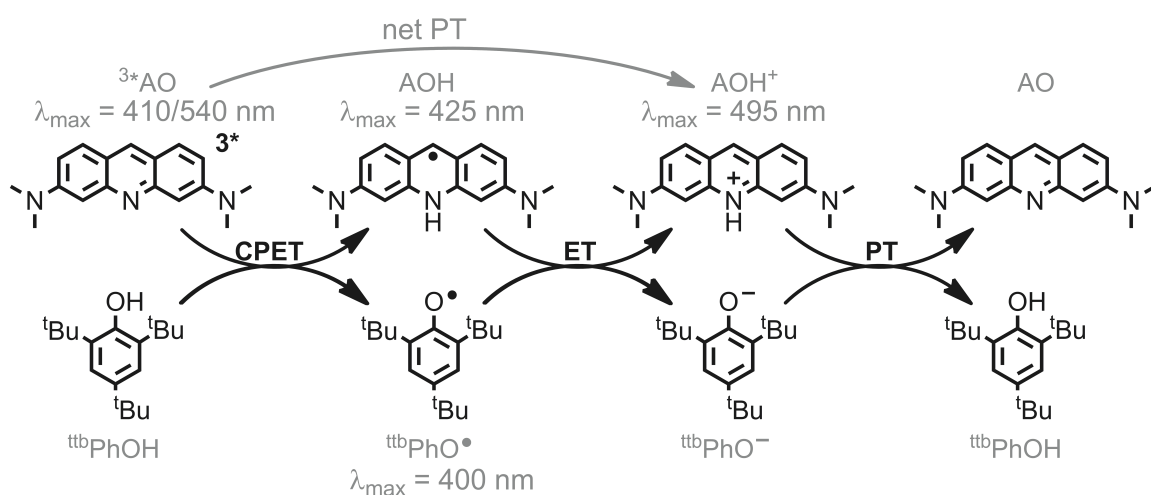


Figure 2.7 Mechanism of reactivity and recombination of $^3\text{AO} + ^{\text{ttb}}\text{PhOH}$.

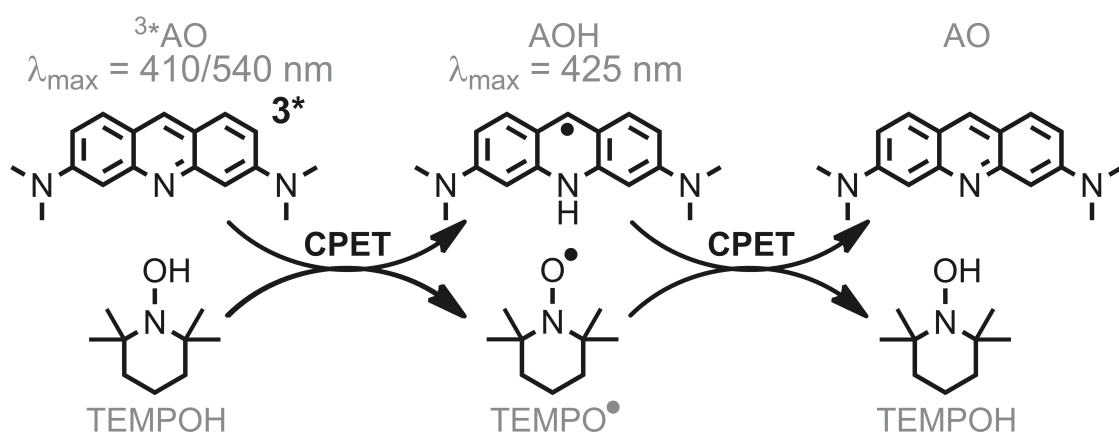


Figure 2.8 Mechanism of reactivity for ^3AO and TEMPOH.

After formation of the excited-state CPET products, thermal back-PCET ensues to yield the ground state reactants. Thermochemical analysis (Section 2.5) indicates that ET-PT and CPET processes are both reasonable pathways for the reaction of ${}^{\text{ttb}}\text{PhO}\bullet$ and $\text{AOH}\bullet$ because they circumvent high energy intermediates (in contrast, initial PT has $\Delta G_{PT}^{\circ} = 49.9$ kcal mol⁻¹).

Spectral observation of the initial ET product (AOH^+) indicates the reaction proceeds via the stepwise ET-PT pathway. Specifically, the $\text{AOH}\bullet$ formed by excited-state CPET is a moderate reductant which can reduce ${}^{\text{ttb}}\text{PhO}\bullet$ ($\Delta G_{ET}^{\circ} = -20.8$ kcal mol⁻¹) and accordingly, ET from $\text{AOH}\bullet$ to ${}^{\text{ttb}}\text{PhO}\bullet$ proceeds to form AOH^+ and ${}^{\text{ttb}}\text{PhO}^-$, detected by the decay of the transient $\text{AOH}\bullet$ signal and the appearance of the AOH^+ absorption feature. Similar reactivity was noted for reactions of phenyl thiyl radical with 9-mesityl-10-methylacridinium; the former acts as an oxidant in a photoredox catalysis scheme.²⁴ The products of this sequential excited-state CPET-thermal ET sequence are equivalent to a net-PT process, reminiscent of reactivity proposed for ruthenium-phenol dyads.^{21,25,26} Subsequently, AOH^+ and ${}^{\text{ttb}}\text{PhO}^-$ recombine via PT to form the ground state reactants, detected by the decay of the AOH^+ signal.

By contrast, the thermal back-PCET reaction of $\text{AOH}\bullet$ and $\text{TEMPO}\bullet$ proceeds via CPET to form the ground state reactants in the time interval 1–100 μs . This assignment is consistent with both spectral observations and the thermochemical preference of $\text{TEMPO}\bullet$ to react via CPET pathways ($\Delta G_{CPET}^{\circ} = -21.7$ kcal mol⁻¹, $\Delta G_{ET}^{\circ} = +8.1$ kcal mol⁻¹, $\Delta G_{PT}^{\circ} = +50.1$ kcal mol⁻¹). The diverging thermal reactivity of $\text{AOH}\bullet$ with ${}^{\text{ttb}}\text{PhO}\bullet$ vs. $\text{TEMPO}\bullet$ is attributed to the different thermochemistry of the two systems.¹¹

The spectral profiles of the AO-derived intermediates allows for detailed kinetics analyses. The quenching of $^3\text{*AO}$ by $^{\text{ttb}}\text{PhOH}$ was monitored by single wavelength TA at 560 nm (Figure 2.10). Quenching is enhanced with increasing concentrations of $^{\text{ttb}}\text{PhOH}$, but the excited-state decay is non-exponential. A kinetics model (based on Figure 2.7) accounting for the intrinsic decay pathways of AO was used to describe the photo-induced PCET reaction scheme between AO and $^{\text{ttb}}\text{PhOH}$ and subsequent thermal reactivity. Intrinsic reactivity of $^3\text{*AO}$ (above) is described by rate constants k_{nr} , k_{TT} , and k_{S} , respectively. The presence of trace amounts of AOH^+ in solution is accounted for by the independently measured rate constant k_{AOH} ($4 \times 10^5 \text{ s}^{-1}$), which describes the relaxation of $^3\text{*AOH}^+$ (Figure 2.9).

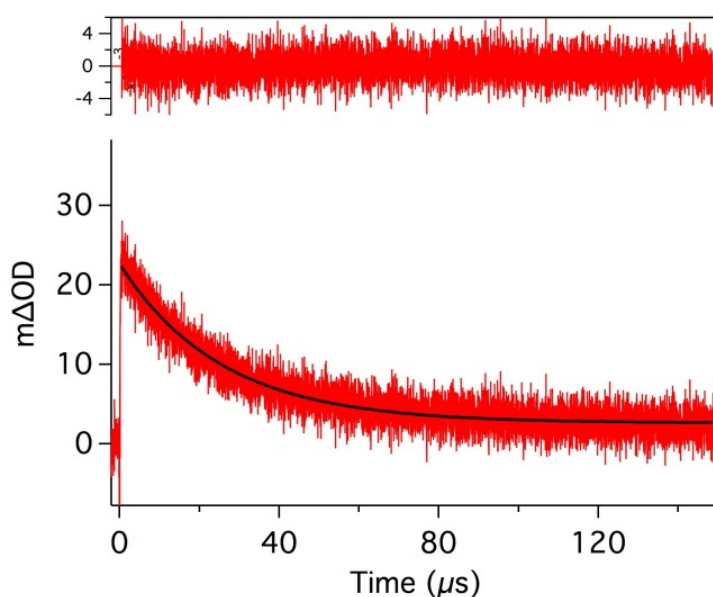


Figure 2.9. Decay of the triplet excited state of AOH^+ in CH_3CN monitored at 560 nm. Kinetics were fit with a single exponential decay to yield $k_{\text{AOH}} = 40,000 \text{ s}^{-1}$. $40 \mu\text{M AOH}^+$, $\lambda_{\text{ex}} = 495 \text{ nm}$, $\lambda_{\text{obs}} = 560 \text{ nm}$, $0.1 \text{ M [Bu}_4\text{N][PF}_6\text{]}$.

Excited-state CPET is described by k_{CPET} . Though not detectable at 560 nm, ET from $\text{AOH}\cdot$ to $^{\text{ttb}}\text{PhO}\cdot$ (k_{ET}) and PT from AOH^+ to $^{\text{ttb}}\text{PhO}^-$ (k_{PT}) complete the model. Rate

constants for these processes were determined from kinetics traces recorded at 460 nm and are discussed below.

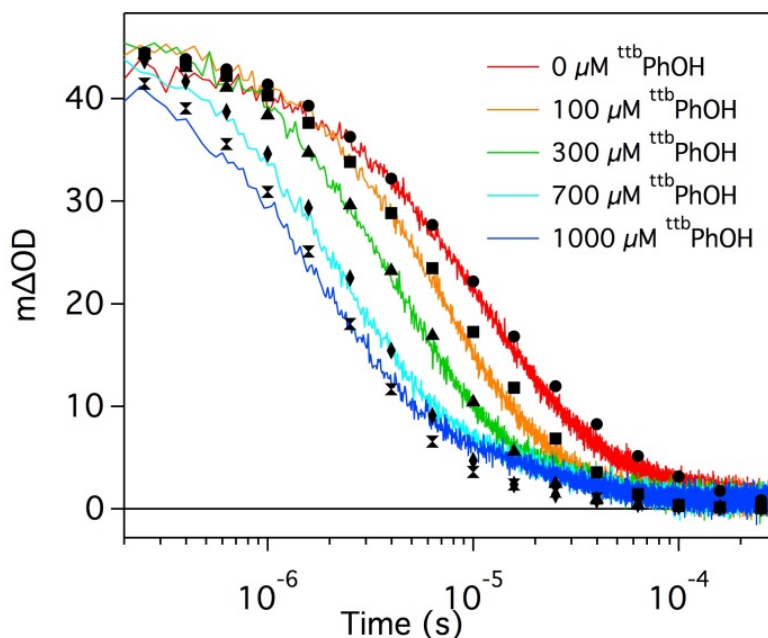


Figure 2.10. Kinetics traces (lines) of 40 μM AO with 0–1000 μM $^{\text{ttb}}\text{PhOH}$ in CH_3CN and the simulated spectra (markers). $\lambda_{\text{ex}} = 425 \text{ nm}$, $\lambda_{\text{obs}} = 560 \text{ nm}$, 0.1 M $[\text{Bu}_4\text{N}][\text{PF}_6]$.

Kinetics simulations were performed with a series of differential equations derived from the kinetics model described in Section 2.6. The rate law for the coupled reactions was solved numerically with an ordinary differential equations solver. Vectors describing initial concentration of reactants, intermediates and products, the time interval for analysis, and rate constants were provided as inputs to solve the initial value problem. The time-dependent concentration profiles produced for each species were translated to simulated TA difference spectra by applying the Beer–Lambert law and summing the absorbance values for each species. Rate constants were adjusted iteratively to simulate the kinetics traces for a series of five samples (0–1000 μM $^{\text{ttb}}\text{PhOH}$) to obtain a self-consistent set of rate constants. Rate

constants independently determined (k_{nr} , k_{TT} , k_S , k_{AOH}) for intrinsic decay processes were fixed at these values in order to give the most accurate rate constants for the other processes.

The second-order rate constant determined for excited-state CPET is $3.7 \times 10^8 \text{ M}^{-1} \text{ s}^{-1}$. The analogous reaction for ^3AO and $^{\text{ttb}}\text{PhOD}$ is slightly slower ($k_{\text{CDET}} = 2.9 \times 10^8 \text{ M}^{-1} \text{ s}^{-1}$, KIE = 1.3) (Figure 2.11).

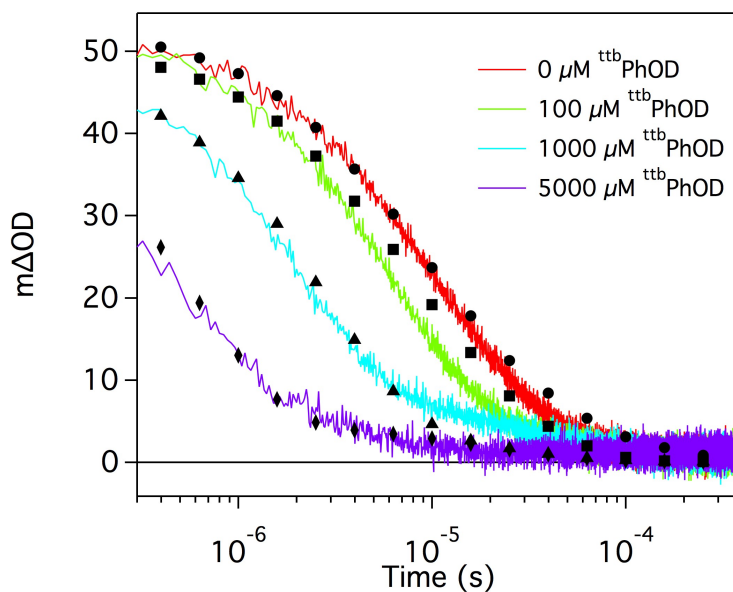


Figure 2.11. Kinetics traces (lines) of 40 μM AO with 0–1000 μM $^{\text{ttb}}\text{PhOD}$ in CH_3CN and the simulated spectra (markers). k_{nr} (300 s^{-1}), k_{TT} ($5.3 \times 10^9 \text{ M}^{-1} \text{ s}^{-1}$), k_S ($1.0 \times 10^8 \text{ M}^{-1} \text{ s}^{-1}$), k_{CDET} ($2.9 \times 10^9 \text{ M}^{-1} \text{ s}^{-1}$), k_{ET} ($5.5 \times 10^9 \text{ M}^{-1} \text{ s}^{-1}$), k_{AOH} ($4.0 \times 10^4 \text{ s}^{-1}$). 40 μM AO, $\lambda_{\text{ex}} = 425 \text{ nm}$, $\lambda_{\text{obs}} = 560 \text{ nm}$, 0.1 M $[\text{Bu}_4\text{N}][\text{PF}_6]$.

This small, but non-negligible KIE is consistent with our assignment of CPET.^{1,27} The second-order rate constant determined through kinetic simulations is a composite of the association constant for the formation of the hydrogen-bonded AO–phenol adduct and the first order rate constant for intra-adduct CPET. Because of the complexity of the system, we cannot directly extract K_A and a first order rate constant as has previously been done in

luminescence quenching experiments.^{21–23} Interpreting hydrogen bonding in the context of kinetics analysis is the focus of ongoing study.

These kinetic details, coupled with thermochemical analysis (Section 2.5), support the proposed forward CPET, reverse ET–PT reaction sequence. An activation energy (ΔG^\ddagger) in the range of +9.9–11.2 kcal mol^{–1} can be estimated from the k_{CPET} (based on the range of [^{ttb}PhOH] investigated).¹¹ Quenching of ³*AO by ^{ttb}PhOH via an ET pathway is inconsistent with this barrier ($\Delta G_{\text{ET}}^\circ = +23.1$ kcal mol^{–1}). If PT from ^{ttb}PhOH to ³*AO is not accompanied by excited-state deactivation (³*AOH⁺ is formed initially, then subsequently relaxes to form AOH⁺), initial PT has a negligible barrier ($\Delta G_{\text{PT}}^\circ = +1.6$ kcal mol^{–1}). Alternatively, if PT is coupled to excited-state deactivation of ³*AO, the free energy change for PT ($\Delta G_{\text{PT}}^\circ = -47.6$ kcal mol^{–1}) indicates this pathway is highly exergonic, though the organic framework does not offer a clear mechanism for coupling relaxation.²⁸ However, for both of these initial PT pathways, the subsequent ET reaction between AOH⁺ and ^{ttb}PhO[–] to form the net PCET products observed spectroscopically is substantially endergonic ($\Delta G_{\text{ET}}^\circ = +20.8$ kcal mol^{–1}), inconsistent with the observed ΔG^\ddagger . Further, the large positive $\Delta G_{\text{ET}}^\circ$ for the PT–ET pathway suggests that the excited-state PT intermediates AOH⁺ and ^{ttb}PhO[–] should be detectable, but they are not observed. Rather, consistent with transient spectral measurements and the estimated barrier, ³*AO is quenched by CPET ($\Delta G_{\text{CPET}}^\circ = -26.8$ kcal mol^{–1}) from ^{ttb}PhOH to form ^{ttb}PhO• and acridine radical AOH•.

The appearance and subsequent reactivity of AOH⁺ was monitored at 460 nm as a function of AO (and in turn, ³*AO) concentration (Figure 2.12).

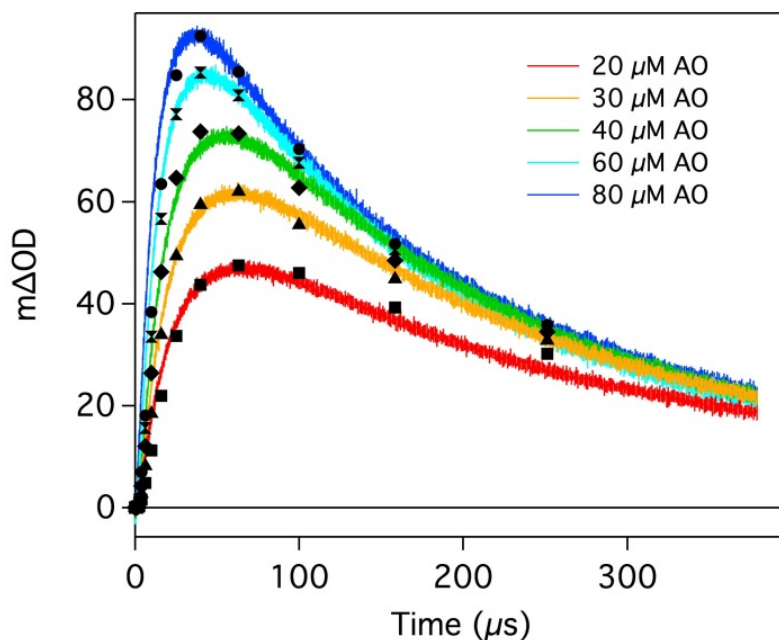


Figure 2.12. Kinetics traces (lines) of 20–80 μM AO with 500 μM $^{\text{ttb}}\text{PhOH}$ in CH_3CN and the simulated spectra (markers). $\lambda_{\text{ex}} = 425 \text{ nm}$, $\lambda_{\text{obs}} = 460 \text{ nm}$, 0.1 M $[\text{Bu}_4\text{N}][\text{PF}_6]$.

Simulations of these kinetics traces per the model described above provides additional insight into the subsequent thermal ET and PT steps – ET from AOH^\bullet to $^{\text{ttb}}\text{PhO}^\bullet$ (k_{ET}) and PT from AOH^+ to $^{\text{ttb}}\text{PhO}^-$ (k_{PT}). In this analysis, rate constants k_{nr} , k_{TT} , k_{S} , k_{AOH} , and k_{CPET} determined from simulations of 560 nm kinetics traces were fixed. The rate constant for k_{ET} is diffusion limited ($5.5 \times 10^9 \text{ M}^{-1} \text{ s}^{-1}$), consistent with the 900 mV driving force for ET ($\Delta G_{\text{ET}}^\circ = -20.8 \text{ kcal mol}^{-1}$), and no KIE is observed, as expected.¹¹ Recombination of AOH^+ and $^{\text{ttb}}\text{PhO}^-$ via PT occurs with a rate constant of $1.0 \times 10^9 \text{ M}^{-1} \text{ s}^{-1}$, consistent with the large driving force (8.7 unit $\text{p}K_{\text{a}}$ difference, $\Delta G_{\text{PT}}^\circ = -11.9 \text{ kcal mol}^{-1}$).¹¹ No KIE is observed, as anticipated for diffusion-controlled bimolecular PT and consistent with related studies (Figure 2.13).²⁹

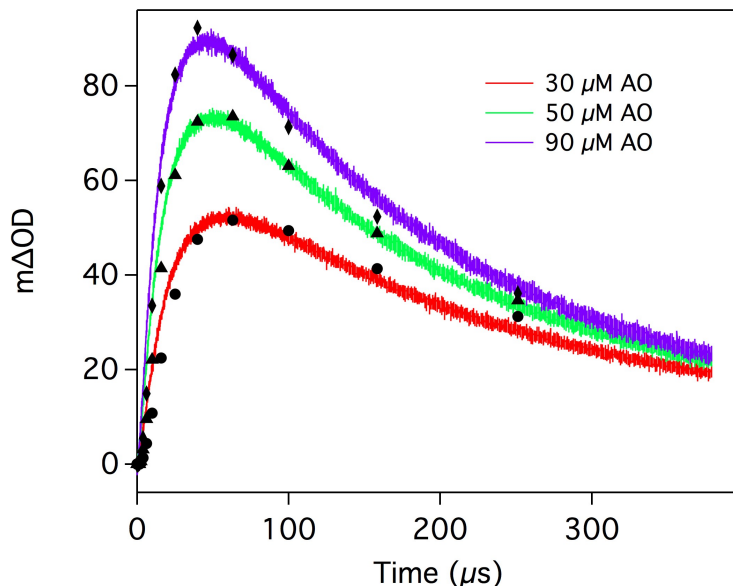


Figure 2.13. Kinetics traces (lines) of 30–90 μM AO with 500 μM $^{\text{tbb}}$ PhOD in CH_3CN and the simulated spectra (markers). k_{nr} (300 s^{-1}), k_{TT} ($5.3 \times 10^9 \text{ M}^{-1} \text{ s}^{-1}$), k_{S} ($1.0 \times 10^8 \text{ M}^{-1} \text{ s}^{-1}$), k_{CDET} ($2.9 \times 10^9 \text{ M}^{-1} \text{ s}^{-1}$), k_{ET} ($5.5 \times 10^9 \text{ M}^{-1} \text{ s}^{-1}$), k_{PT} ($1.0 \times 10^9 \text{ M}^{-1} \text{ s}^{-1}$), k_{AOH} ($4.0 \times 10^4 \text{ s}^{-1}$, see Figure S5). 40 μM AO, $\lambda_{\text{ex}} = 425 \text{ nm}$, $\lambda_{\text{obs}} = 460 \text{ nm}$, 0.1 M $[\text{Bu}_4\text{N}][\text{PF}_6]$.

2.3. Conclusions

In summary, we found that ^3AO reacts with $^{\text{tbb}}$ PhOH and TEMPOH via an excited-state CPET pathway. Excited-state CPET reactions of ^3AO have not, to our knowledge, been previously observed. The ensuing reactivity of the CPET products is dictated by the thermodynamics of the respective systems— $\text{AOH}\cdot$ reduces $^{\text{tbb}}\text{PhO}\cdot$ but is not a potent enough reductant to reduce $\text{TEMPO}\cdot$. Importantly, the unique spectroscopic signatures of the reactants, intermediates and products enabled us to monitor each step of the photo-initiated and subsequent thermal reactions. The spectral evidence for the aforementioned reactivity is supported by kinetics modeling, thermochemical arguments and H/D KIEs. This comprehensive picture of excited-state PCET reactivity provides a first insight into the

intimate coupling of light absorption with both proton and electron transfer. Harnessing this light-driven reactivity will pave new avenues to solar fuel production.

2.4. Experimental Details

All solutions for electrochemical or transient absorption analysis were prepared in a nitrogen-filled glovebox. The acetonitrile used (Fisher Sci, HPLC, >99.9%) was degassed with argon and dried with a Pure Process Technology Solvent System. Reagents were purchased from Aldrich, with the exception of TEMPO[•] (2,2,6,6-Tetramethylpiperidine 1-oxyl, Chem-Impex Intl.). Acridine Orange was purified by dissolving in methanol and precipitating with 0.1 M NaOH before drying *in vacuo* and storing under inert atmosphere. Despite purification, trace amounts of acridinium were still detected in optical spectra. ^{ttb}PhOH was dried *in vacuo* and stored under an inert atmosphere. ^{ttb}PhOD¹ and TEMPOH² were prepared according to literature procedures. Tetrabutylammonium hexafluorophosphate was recrystallized from absolute ethanol, dried *in vacuo*, and stored under inert atmosphere. Triethylamine and tetrafluoroboric acid diethyl ether complex were degassed via the freeze-pump-thaw method (three cycles) and stored under inert atmosphere.

Transient absorption experiments were performed using a commercially available laser flash photolysis system (Edinburgh Instruments LP920) with laser excitation (532 nm, 5–7 ns fwhm, typically 5.0 ± 0.1 mJ/pulse unless stated otherwise, 5 mm beam diameter, 20 mJ/cm²) provided by a pulsed Nd:YAG laser (Spectra-Physics Quanta-Ray LAB-170-10)/optical parametric oscillator (VersaScan-MB) combination. To accommodate the pulsed, 1 Hz intensification of the 450 W Xe probe source of the LP920, the laser system was set such that the flash lamps were fired at 10 Hz yet Q-switched at 1 Hz. The timing of the experiment, including laser and probe pulsing, was PC controlled via Edinburgh software

(L900). The LP920 was equipped with a multigrating detection monochromator outfitted with a Hamamatsu R928 photomultiplier tube (PMT) in a noncooled housing and a gated charge-coupled device (CCD) (Princeton Instruments, PI-MAX3) such that detection was software selectable. Single-wavelength transient absorption kinetics were monitored with the PMT (10 ns fwhm impulse response function, reliable data out to 400 μ s, 300-900 nm) and recorded with a Tektronix TDS-3032C oscilloscope. The gated CCD was used for recording transient spectra covering the entire visible region (400-850 nm, 3 nm spectral bandwidth) at a given time after excitation (10 ns gate width). Data were the result of averaging 40-100 laser shots. Data were collected at room temperature (295 ± 3 K). All samples for transient absorption measurements were prepared in rigorously dry acetonitrile solutions with 100 mM [Bu₄N][PF₆]. Samples were placed into 10 mm path length quartz cuvettes and isolated from atmosphere with a Teflon valve.

Electrochemistry was performed in a nitrogen filled glovebox with a Pine Instruments WaveNow potentiostat using glassy carbon working electrodes, a platinum counter electrode, and a Ag/AgNO₃ (10 mM AgNO₃) reference electrode. All scans were performed in acetonitrile solutions with 100 mM [Bu₄N][PF₆] and referenced to the ferrocene/ferrocenium couple (Fc⁺⁰). Glassy carbon working electrodes (CH Instruments, 3 mm diameter) were polished with 0.3 micron alumina powder and 0.05 micron alumina powder (CH Instruments, contained no agglomerating agents), rinsed and ultrasonicated for one minute in HPLC grade water to remove residual polishing powder. Spectroelectrochemical measurements were performed with a honeycomb platinum working electrode (Pine Instruments), a platinum counter electrode and a Ag pseudo-reference electrode in a thin-layer quartz cuvette.

2.5. Thermochemical Analysis

Table 2.1. Reduction Potentials in CH₃CN

Species	E°' (V vs. Fc ^{+/0})	Reference
AO ^{0/-}	~ -2.4	This work
AOH ^{+•}	~ -1.6	This work
AO ^{3*-/}	0.18	This work
AOH ^{3*+•}	0.53	This work
^{ttb} PhOH ^{•-/}	-0.70	30
^{ttb} PhOH ^{+•/0}	1.18	30
TEMPO ^{•-/}	-1.95	30
TEMPOH ^{+•/0}	0.71	30

Table 2.2. pK_a in CH₃CN

Species	pK _a	Reference
AOH ⁺	19.3	This work
AOH [•]	33.4	This work
^{ttb} PhOH	28	30
^{ttb} PhOH ^{+•}	-3	30
TEMPOH	41	30
TEMPOH ^{+•}	-4	30

Table 2.3. E₀₀ values in CH₃CN

Species	E ₀₀ (eV)	E ₀₀ (kcal/mol)	Reference
AOH ⁺	2.13	49.2	31
AOH [•]	2.58	59.5	This work

E_{00} values for ^3AO and $^3\text{AOH}^+$

The E_{00} ($S_0 \rightarrow T$) for AO has not been measured; but the E_{00} ($S_0 \rightarrow T$) for AOH^+ has been experimentally determined.³¹

$$E_{00}(\text{AOH}^+ \rightarrow ^3\text{AOH}^+) = +2.13 \text{ eV}$$

From this value, the excited state reduction potential of acridinium triplet can be determined from the equation below.^{32,33}

$$E^{\circ'}(\text{AOH}^{3*+/+}) = E^{\circ'}(\text{AOH}^{+/+}) + E_{00}(\text{AOH}^+) = +0.53 \text{ V vs. Fc}^{+/0}$$

By evaluating the electron transfer quenching of the triplet excited states of AO and AOH^+ , Volgelmann has estimated the difference in reduction potentials of ^3AO and $^3\text{AOH}^+$.¹¹

$$\Delta E^{\circ'} = E^{\circ'}(\text{AOH}^{3*+/+}) - E^{\circ'}(\text{AO}^{3*/-}) = +0.35 \text{ eV}$$

From this value, the excited state reduction potential of the acridine orange triplet can be estimated. ^3AO is a very weak excited-state oxidant

$$E^{\circ'}(\text{AO}^{3*/-}) = +0.18 \text{ V vs. Fc}^{+/0}$$

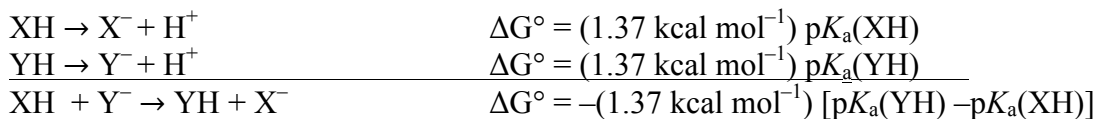
From this value and the experimentally determined $E^{\circ'}(\text{AO}^{0/-})$ value, the acridine orange E_{00} ($S_0 \rightarrow T$) value can be estimated with the equation below.

$$E^{\circ'}(\text{AO}^{3*/-}) = E^{\circ'}(\text{AO}^{0/-}) + E_{00}$$

$$\underline{E_{00}(\text{AO} \rightarrow ^3\text{AO}) = +2.58 \text{ eV}}$$

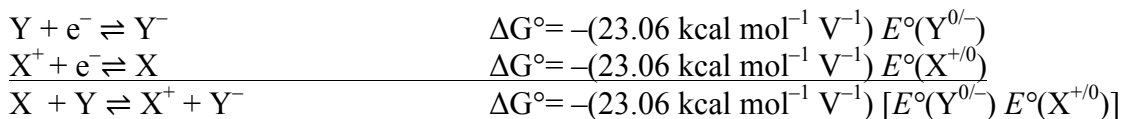
ΔG° for proton transfer reactions³⁰

$$\Delta G_{\text{PT}}^\circ = -RT \ln(K_a) = 2.303RT(\text{p}K_a) = (1.37 \text{ kcal mol}^{-1}) \text{p}K_a \text{ @ 298 K}$$



ΔG° for electron transfer reactions³⁰

$$\Delta G_{\text{ET}}^\circ = -FE^\circ = -(23.06 \text{ kcal mol}^{-1} \text{ V}^{-1})E^\circ$$

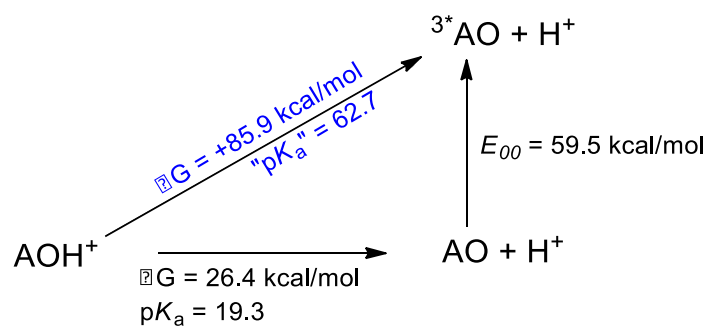
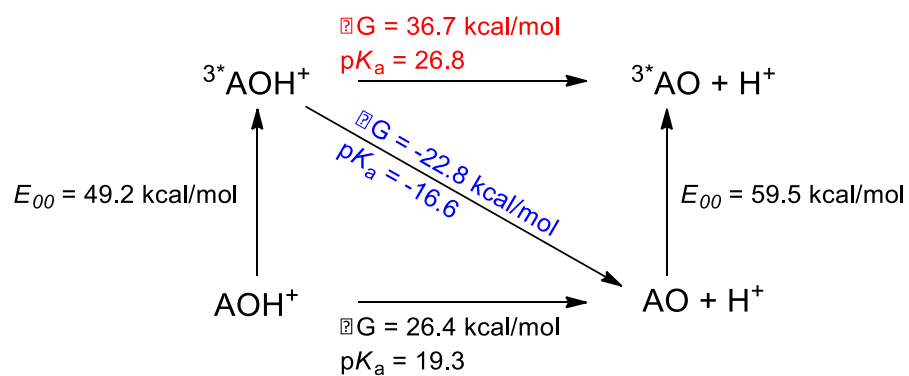
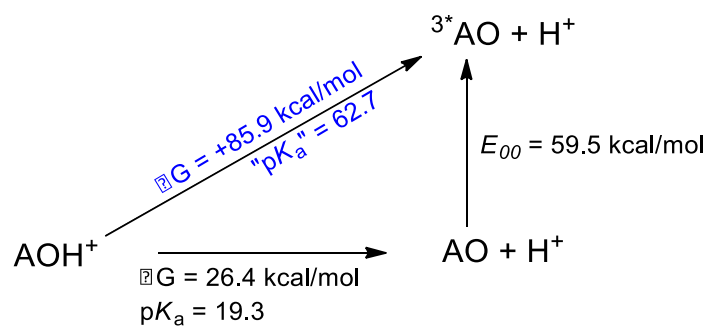
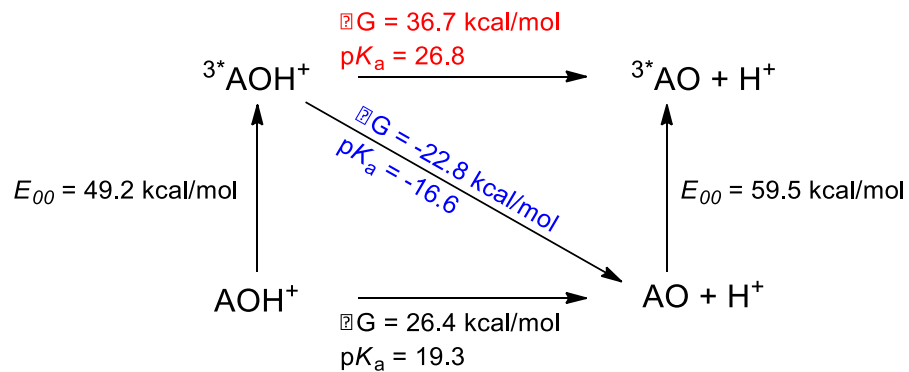


ΔG° for CPET reactions were calculated per Hess's Law, as shown below.

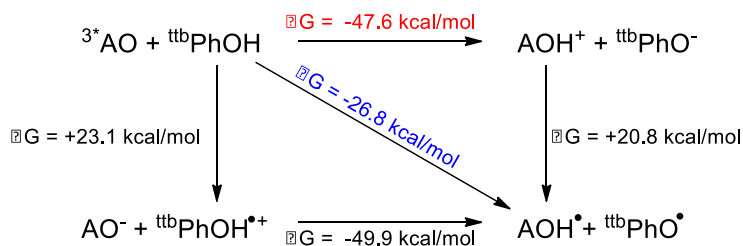
Calculation of Excited State $\text{p}K_a$ for AOH^+

The Förster cycle was utilized to estimate the $\text{p}K_a$ of $^3\text{AOH}^+$ ($\text{p}K_a^*$).³⁵⁻³⁷

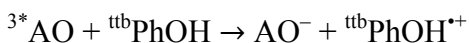
$$\text{p}K_a - \text{p}K_a^* = \frac{E_{00}(\text{AOH}^+) - E_{00}(\text{AO})}{2.303RT} = \frac{E_{00}(\text{AOH}^+) - E_{00}(\text{AO})}{1.37}$$



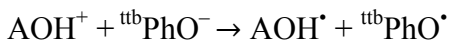
Thermochemical Analysis of Excited State PCET – AO + ^{ttb}PhOH



Electron Transfer

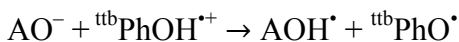


$$\Delta G^\circ = -(23.06 \text{ kcal mol}^{-1} \text{ V}^{-1}) [E^\circ(\text{AO}^{3*/-}) - E^\circ({}^{\text{ttb}}\text{PhOH}^{\bullet+/0})] = +23.1 \text{ kcal mol}^{-1}$$



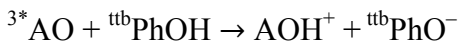
$$\Delta G^\circ = -(23.06 \text{ kcal mol}^{-1} \text{ V}^{-1}) [E^\circ(\text{AOH}^{+/•}) - E^\circ({}^{\text{ttb}}\text{PhO}^{\bullet/-})] = +20.8 \text{ kcal mol}^{-1}$$

Proton Transfer



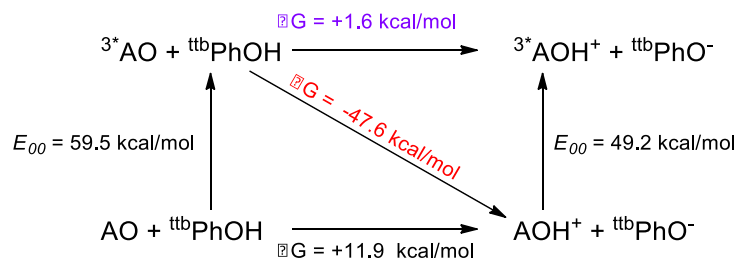
$$\Delta G^\circ = -(1.37 \text{ kcal mol}^{-1}) [\text{p}K_a(\text{AOH}^\bullet) - \text{p}K_a({}^{\text{ttb}}\text{PhOH}^{\bullet+})] = -49.9 \text{ kcal mol}^{-1}$$

See thermal reaction for details

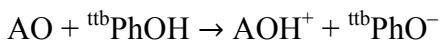


$\Delta G^\circ = -47.6 \text{ kcal mol}^{-1}$ (per Hess's law, with PT coupled to excited-state deactivation, see below)

Thermochemical Analysis of Excited State PT pathways – AO + ^{ttb}PhOH

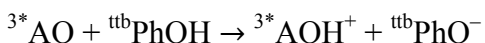


Proton Transfer



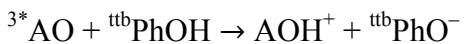
$$\Delta G^\circ = -(1.37 \text{ kcal mol}^{-1}) [\text{p}K_{\text{a}}(\text{AOH}^+) - \text{p}K_{\text{a}}({}^{\text{ttb}}\text{PhOH})] = +11.9 \text{ kcal mol}^{-1}$$

Proton Transfer not coupled to excited state deactivation



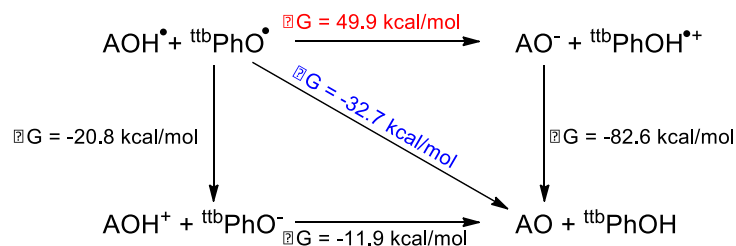
$$\Delta G^\circ = -(1.37 \text{ kcal mol}^{-1}) [\text{p}K_{\text{a}}({}^3\text{AOH}^+) - \text{p}K_{\text{a}}({}^{\text{ttb}}\text{PhOH})] = +1.6 \text{ kcal mol}^{-1}$$

Proton Transfer coupled to excited state deactivation

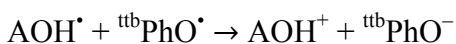


$$\Delta G^\circ = -47.6 \text{ kcal mol}^{-1} \text{ (per Hess's Law)}$$

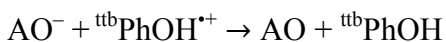
Thermochemical Analysis of Thermal PCET – AO + ^{ttb}PhOH



Electron Transfer

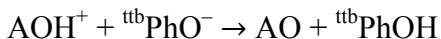


$$\Delta G^\circ = -(23.06 \text{ kcal mol}^{-1} \text{ V}^{-1}) [E^\circ({}^{\text{ttb}}\text{PhO}^{\bullet/-}) - E^\circ(\text{AOH}^{+/ \bullet})] = -20.8 \text{ kcal mol}^{-1}$$

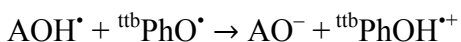


$$\Delta G^\circ = -(23.06 \text{ kcal mol}^{-1} \text{ V}^{-1}) [E^\circ({}^{\text{ttb}}\text{PhOH}^{\bullet+/0}) - E^\circ(\text{AO}^{0/-})] = -82.6 \text{ kcal mol}^{-1}$$

Proton Transfer



$$\Delta G^\circ = -(1.37 \text{ kcal mol}^{-1}) [\text{p}K_a({}^{\text{ttb}}\text{PhOH}) - \text{p}K_a(\text{AOH}^+)] = -11.9 \text{ kcal mol}^{-1}$$

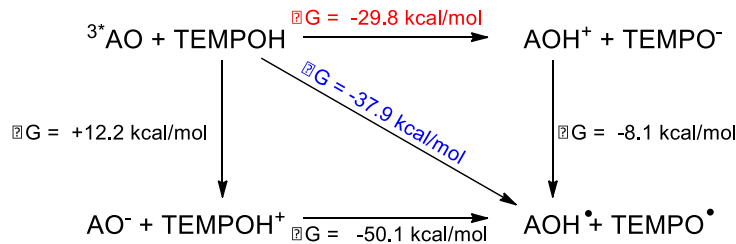


$$\Delta G^\circ = -(1.37 \text{ kcal mol}^{-1}) [\text{p}K_a({}^{\text{ttb}}\text{PhOH}^{\bullet+}) - \text{p}K_a(\text{AOH}^\bullet)] = +49.9 \text{ kcal mol}^{-1}$$

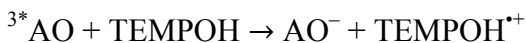
$$[\text{p}K_a({}^{\text{ttb}}\text{PhOH}^{\bullet+}) - \text{p}K_a(\text{AOH}^\bullet)] = -36.4$$

$$\text{p}K_a(\text{AOH}^\bullet) = +33.4$$

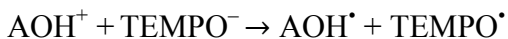
Thermochemical Analysis of Excited State PCET – AO + TEMPOH



Electron Transfer

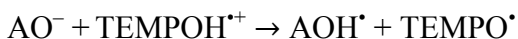


$$\Delta G^\circ = -(23.06 \text{ kcal mol}^{-1} \text{ V}^{-1}) [E^\circ(\text{AO}^{3*/-}) - E^\circ(\text{TEMPOH}^{*+/0})] = +12.2 \text{ kcal mol}^{-1}$$



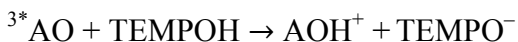
$$\Delta G^\circ = -(23.06 \text{ kcal mol}^{-1} \text{ V}^{-1}) [E^\circ(\text{AOH}^{+/•}) - E^\circ(\text{TEMPO}^{•/-})] = -8.1 \text{ kcal mol}^{-1}$$

Proton Transfer



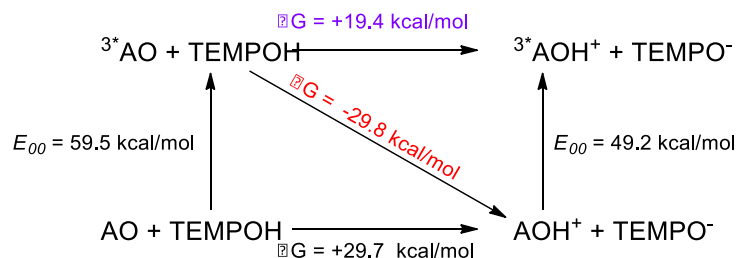
$$\Delta G^\circ = -(1.37 \text{ kcal mol}^{-1}) [\text{p}K_a(\text{AOH}^\bullet) - \text{p}K_a(\text{TEMPOH}^{*+})] = -50.1 \text{ kcal mol}^{-1}$$

See thermal reaction for details

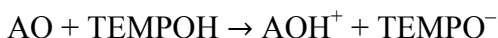


$\Delta G^\circ = -29.8 \text{ kcal mol}^{-1}$ (per Hess's law, with PT coupled to excited-state deactivation, see below)

Thermochemical Analysis of Excited State PT pathways – AO + TEMPOH

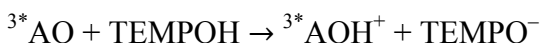


Proton Transfer



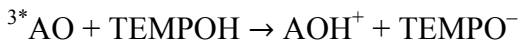
$$\Delta G^\circ = -(1.37 \text{ kcal mol}^{-1}) [\text{p}K_a(\text{AOH}^+) - \text{p}K_a(\text{TEMPOH})] = +29.7 \text{ kcal mol}^{-1}$$

Proton Transfer not coupled to excited state deactivation



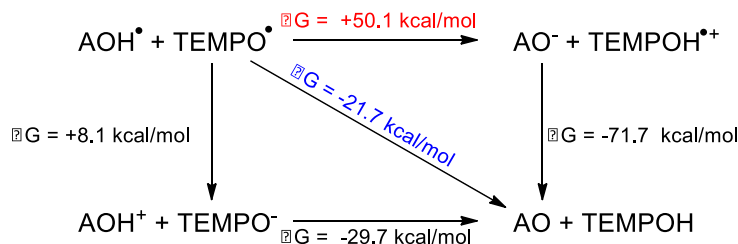
$$\Delta G^\circ = -(1.37 \text{ kcal mol}^{-1}) [\text{p}K_a({}^3\text{AOH}^+) - \text{p}K_a(\text{TEMPOH})] = +19.4 \text{ kcal mol}^{-1}$$

Proton Transfer coupled to excited state deactivation

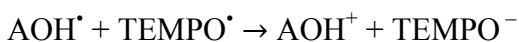


$$\Delta G^\circ = -29.8 \text{ kcal mol}^{-1} \text{ (per Hess's Law)}$$

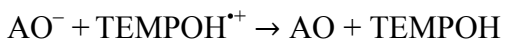
Thermochemical Analysis of Thermal PCET – AO + TEMPOH



Electron Transfer

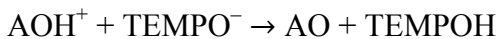


$$\Delta G^\circ = -(23.06 \text{ kcal mol}^{-1} \text{ V}^{-1}) [E^\circ(\text{TEMPO}^{\bullet/-}) - E^\circ(\text{AOH}^{+/ \bullet})] = +8.1 \text{ kcal mol}^{-1}$$

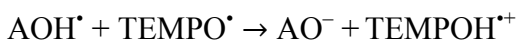


$$\Delta G^\circ = -(23.06 \text{ kcal mol}^{-1} \text{ V}^{-1}) [E^\circ(\text{TEMPOH}^{\bullet+/0}) - E^\circ(\text{AO}^{0/-})] = -71.7 \text{ kcal mol}^{-1}$$

Proton Transfer



$$\Delta G^\circ = -(1.37 \text{ kcal mol}^{-1}) [\text{p}K_a(\text{TEMPOH}) - \text{p}K_a(\text{AOH}^+)] = -29.7 \text{ kcal mol}^{-1}$$



$$\Delta G^\circ = -(1.37 \text{ kcal mol}^{-1}) [\text{p}K_a(\text{TEMPOH}^{\bullet+}) - \text{p}K_a(\text{AOH}^\bullet)] = +50.1 \text{ kcal mol}^{-1}$$

$$[\text{p}K_a(\text{TEMPOH}^{\bullet+}) - \text{p}K_a(\text{AOH}^\bullet)] = -36.5$$

$$\text{p}K_a(\text{AOH}^\bullet) = 32.5 \text{ (33.4 in } ^{\text{ttb}}\text{PhOH cycle)}$$

2.6. Details of Kinetic Modeling

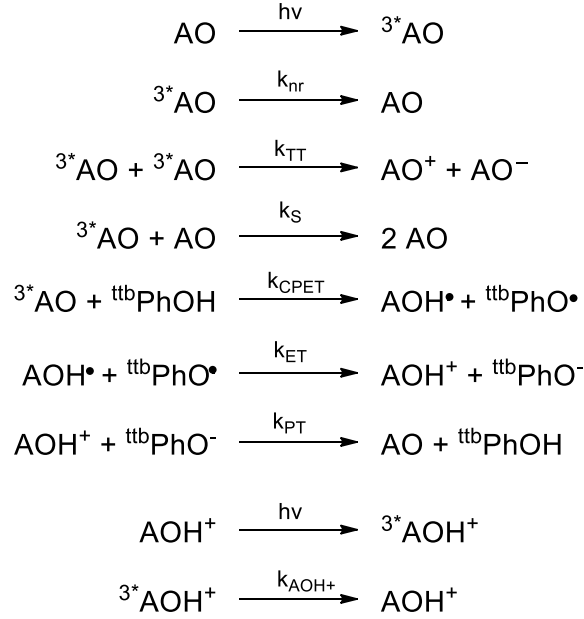


Figure 2.14. Detailed kinetics model of the deactivation and reaction pathways for $\text{AO} + {}^{ttb}\text{PhOH}$

Differential equations employed for kinetic models

$$\frac{d[{}^3\text{AO}]}{dt} = -k_{nr}[{}^3\text{AO}] - k_{TT}[{}^3\text{AO}]^2 - k_S[{}^3\text{AO}](\text{AO} - [{}^3\text{AO}]) - k_{CPET}[{}^3\text{AO}][{}^{ttb}\text{PhOH}]$$

$$\frac{d[{}^{ttb}\text{PhOH}]}{dt} = -k_{CPET}[{}^3\text{AO}][{}^{ttb}\text{PhOH}]$$

$$\frac{d[{}^{ttb}\text{PhO}^\bullet]}{dt} = k_{CPET}[{}^3\text{AO}][{}^{ttb}\text{PhOH}] - k_{ET}[\text{AOH}^\bullet][{}^{ttb}\text{PhO}^\bullet]$$

$$\frac{d[\text{AOH}^\bullet]}{dt} = k_{CPET}[{}^3\text{AO}][{}^{ttb}\text{PhOH}] - k_{ET}[\text{AOH}^\bullet][{}^{ttb}\text{PhO}^\bullet]$$

$$\frac{d[{}^3\text{AOH}^+]}{dt} = -k_{AOH^+}[{}^3\text{AOH}^+]$$

$$\frac{d[\text{AOH}^+]}{dt} = k_{ET}[\text{AOH}^\bullet][{}^{ttb}\text{PhO}^\bullet] - k_{PT}[\text{AOH}^+][{}^{ttb}\text{PhO}^-] \text{ (included only for 460 nm model)}$$

$$\frac{d[\text{AO}]}{dt} = k_{PT}[\text{AOH}^+][{}^{ttb}\text{PhO}^-] \text{ (included only for 460 nm model)}$$

To simulate the kinetics traces, this series of differential equations was solved numerically with an ordinary differential equations solver. We utilized ode23 in MATLAB. The details of the simulations and the MATLAB *.m files employed are provided below.

Kinetics at 560 nm

Input needed to complete simulated fits:

Timescale: logtimespan = -8:0.2:-3; timespan = 10.^logtimespan;

Molar extinction coefficients for ^3AO , $^3\text{AOH}^+$, $^{\text{ttb}}\text{PhO}\cdot$ (in units of $\text{M}^{-1} \text{cm}^{-1}$): eps3AO = 4800; eps3AOH+=3500; epsttbPhO = 250

Vector defining rate constants k_{nr} , k_{TT} , k_{CPET} , k_{ET} , k_{S} and k_{AOH} in this order: k = [knr; kTT; kCPET; kET; kS; kAOH];

Vector defining initial concentrations of ^3AO , $^{\text{ttb}}\text{PhOH}$, $^{\text{ttb}}\text{PhO}\cdot$, $\text{AOH}\cdot$, $^3\text{AOH}^+$: y0 = [3AO; ttbPhOH; ttbPhOrad; AOHrad; 3AOH+];

TripAO_v4.m (script below) describes the various rate expressions associated with kinetics at a given wavelength, in this case 560 nm. y(x) values represent concentrations, and k(x) values represent rate constants.

```
function [yprime]=TripAO_v4(t,y,k)

%y(1)=3AO, y(2)=ttbPhOH, y(3)=ttbPhOrad, y(4)=AOHrad, y(5)=3AOH+ present
due to trace impurity

%k(1)=knr, k(2)=kTT, k(3)=kCPET, k(4)=kET

%k(5)=kS,k(6)=kAOH;

%decay of 3AO
```

```

yprime(1)=-k(1).*y(1)-k(2).*y(1).*y(1)-k(3).*y(1).*y(2)-k(5).*y(1).*(40e-
6-y(1));

%ttbPhOH: loss of ttbPhOH due to CPET quenching of 3AO
yprime(2)=-k(3).*y(1).*y(2);

% ttbPhOradical: formation and loss of ttbPhOradical
yprime(3)=k(3).*y(1).*y(2)-k(4).*y(3).*y(4);

% AOHrad:formation and loss of AOHradical – formed in equal concentration
with ttbPhOradical
yprime(4)=k(3).*y(1).*y(2)-k(4).*y(3).*y(4);

%decay of 3AOH+
yprime(5)=-k(6).*y(5);

yprime=yprime(:);

```

TripAO_Simulated_dOD_v4.m (script below) is used to numerically solve the differential equations provided in TripAO_v4.m based on the initial value inputs. The time-dependent concentration profiles produced for each species are multiplied by the appropriate molar absorptivity coefficients at the wavelength of interest (for species absorbing at 560 nm, see above) and the optical pathlength (defined by the pump probe overlap, 0.5 cm). These absorbance values are summed to yield the simulated transient absorption spectra. The simulated spectra can then be plotted and compared to experimental data.

```

[Tcalc,Ycalc]=ode23s(@(t,y)TripAO_v4(t,y,k),timespan,y0);

%Differential equation solver used to compute a simulated concentration
%profile based on the differential equations describing the electron
%transfer reactions (see TripAO.m)

```

```

dOD_calc23_560=Ycalc(:,1)*eps3AO*0.5+Ycalc(:,3)*epsttbPhO*0.5+Ycalc(:,5)*e
psAOH*0.5

%converts calculated concentration profile into a simulated TA spectrum by
%multiplying the concentration profile by the vector of epsilon values
%dOD_calc23_560 is used for the data at 560 nm.
%Plot Simulated Data
plot(Tcalc,dOD_calc23_560','ko');

```

Kinetics at 460 nm

Input needed to complete simulated fits:

Timescale: logtimespan = -8:0.2:-3; timespan = 10.^logtimespan;

Molar absorptivity coefficients for AOH^+ at 460 nm (in units of $\text{M}^{-1} \text{cm}^{-1}$): epsAOH=18100

Vector defining rate constants k_{nr} , k_{TT} , k_{CPET} , k_{ET} , k_{S} , k_{AOH} , k_{PT} in this order: k = [knr; kTT; kCPET; kET; kS; kAOH; kPT];

Vector defining initial concentrations of ^3AO , $^{\text{ttb}}\text{PhOH}$, $^{\text{ttb}}\text{PhO}\cdot$, $\text{AOH}\cdot$, $^3\text{AOH}^+$, $^{\text{ttb}}\text{PhO}^-$ or AOH^+ (equal conc.), AO and $^{\text{ttb}}\text{PhOH}$ (equal conc): y0 = [3AO; ttbPhOH; ttbPhOrad; AOHrad; 3AOH+; AOH+; AO and ttbPhOH reformed];

TripAO_v4.m describes the various rate expressions associated with kinetics at a given wavelength, in this case 460 nm. y(x) values represent concentrations, and k(x) values represent rate constants.

```
function [yprime]=TripAO_v4(t,y,k)
```

```

%y(1)=3AO, y(2)=ttbPhOH, y(3)=ttbPhOrad, y(4)=AOHrad, y(5)=AOH+ present
due to trace impurity, y(6)=ttbPhO- and AOH+ formed in solution, y(7)=AO
and ttbPhOH

%k(1)=knr, k(2)=kTT, k(3)=kCPET, k(4)=kET

%k(5)=kS

%k(6)=kAOH; k(7)=kPT

%decay of 3AO
yprime(1)=-k(1).*y(1)-k(2).*y(1).*y(1)-k(3).*y(1).*y(2)-k(5).*y(1).*(40e-
6-y(1));

%ttbPhOH: loss of ttbPhOH due to CPET quenching of 3AO
yprime(2)=-k(3).*y(1).*y(2);

% ttbPhOradical: formation and loss of ttbPhOradical
yprime(3)=k(3).*y(1).*y(2)-k(4).*y(3).*y(4);

%AOHrad:formation and loss of AOHradical – formed in equal concentration
with ttbPhOradical
yprime(4)=k(3).*y(1).*y(2)-k(4).*y(3).*y(4);

%3AOH+ decay
yprime(5)=-k(6).*y(5);

%Formation and reactivity of AOH+ and ttbPhO- – equal concentrations
yprime(6)=k(4).*y(3).*y(4)-k(7).*y(6).*y(6);

%Recombination of AOH+ and ttbPhO-;
yprime(7)=k(7).*y(6).*y(6);

yprime=yprime(:);

```

TripAO_Simulated_dOD_v4.m (script below) is used to numerically solve the differential equations provided in TripAO_v4.m based on the initial value inputs. The time-dependent concentration profiles produced for each species are multiplied by the appropriate molar absorptivity coefficients at the wavelength of interest (see above) and the optical pathlength (defined by the pump probe overlap, 0.5 cm). These absorbance values are summed to yield the simulated transient absorption spectra. The simulated spectra can then be plotted and compared to experimental data.

```
[Tcalc,Ycalc]=ode23s(@(t,y)TripAO_v4(t,y,k),timespan,y0);  
%Differential equation solver used to compute a simulated concentration  
%profile based on the differential equations describing the electron  
%transfer reactions (see TripAO.m)  
  
dOD_calc23_460=Ycalc(:,6)*epsAOH*0.5;  
%converts calculated concentration profile into a simulated TA spectrum by  
%multiplying the concentration profile of AOH+ by the epsilon value  
%dOD_calc23_560 is used for the data at 460  
plot(Tcalc,dOD_calc23_460','ko');
```

REFERENCES

- (1) Weinberg, D. R.; Gagliardi, C. J.; Hull, J. F.; Murphy, C. F.; Kent, C. A.; Westlake, B. C.; Paul, A.; Ess, D. H.; McCafferty, D. G.; Meyer, T. J. *Chem. Rev.* **2012**, *112*, 4016–4093.
- (2) Costentin, C.; Robert, M.; Savéant, J.-M. *Chem. Rev.* **2010**, *110*, PR1–PR40.
- (3) Mayer, J. M.; Rhile, I. J.; Larsen, F. B.; Mader, E. A.; Markle, T. F.; DiPasquale, A. G. *Photosynth. Res.* **2006**, *87*, 3–20.
- (4) Dempsey, J. L.; Winkler, J. R.; Gray, H. B. *Chem. Rev.* **2010**, *110*, 7024–7039.
- (5) Costentin, C.; Robert, M.; Savéant, J.-M. *Acc. Chem. Res.* **2010**, *43*, 1019–1029.
- (6) Stubbe, J.; Nocera, D. G.; Yee, C. S.; Chang, M. C. Y. *Chem. Rev.* **2003**, *103*, 2167–2201.
- (7) Wenger, O. S. *Acc. Chem. Res.* **2013**, *46*, 1517–1526.
- (8) Wenger, O. S. *Coord. Chem. Rev.* **2014**, *ASAP*.
- (9) Gagliardi, C. J.; Westlake, B. C.; Kent, C. A.; Paul, J. J.; Papanikolas, J. M.; Meyer, T. J. *Coord. Chem. Rev.* **2010**, *254*, 2459–2471.
- (10) Hammarström, L.; Styring, S. *Energy Environ. Sci.* **2011**, *4*, 2379.
- (11) Warren, J. J.; Tronic, T. A.; Mayer, J. M. *Chem. Rev.* **2010**, *110*, 6961–7001.
- (12) Rehm, D.; Weller, A. *Isr. J. Chem.* **1970**, *8*, 259.
- (13) Juris, A.; Balzani, V.; Barigelletti, F.; Campagna, S.; Belser, P.; Von Zelewsky, A. *Coord. Chem. Rev.* **1988**, *84*, 85–277.
- (14) Forster, T. *Zeitschrift für Elektrochemie* **1950**, *54*, 531–535.
- (15) Grabowski, Z. R.; Rubaszewska, W. *J. Chem. Soc. Faraday Trans. 1 Phys. Chem. Condens. Phases* **1977**, *73*, 11–28.
- (16) Kellmann, A. *Photochem. Photobiol.* **1971**, *14*, 85–93.
- (17) Chan, M. S.; Bolton, J. R. *Photochem. Photobiol.* **1981**, *34*, 537–547.
- (18) Kellmann, A. *Photochem. Photobiol.* **1974**, *20*, 103–108.

- (19) Manner, V. W.; Markle, T. F.; Freudenthal, J. H.; Roth, J. P.; Mayer, J. M. *Chem. Commun.* **2008**, 256–258.
- (20) Nakahara, K.; Iwasa, S.; Iriyama, J.; Morioka, Y.; Suguro, M.; Satoh, M.; Cairns, E. *J. Electrochim. Acta* **2006**, *52*, 921–927.
- (21) Kuss-Petermann, M.; Wenger, O. S. *J. Phys. Chem. A* **2013**, *117*, 5726–5733.
- (22) Pizano, A. a.; Yang, J. L.; Nocera, D. G. *Chem. Sci.* **2012**, *3*, 2457.
- (23) Concepcion, J. J.; Brennaman, M. K.; Deyton, J. R.; Lebedeva, N. V; Forbes, M. D. E.; Papanikolas, J. M.; Meyer, T. J. *J. Am. Chem. Soc.* **2007**, *129*, 6968–6969.
- (24) Nguyen, T. M.; Nicewicz, D. A. *J. Am. Chem. Soc.* **2013**, *135*, 9588–9591.
- (25) Bronner, C.; Wenger, O. S. *Phys. Chem. Chem. Phys.* **2014**, *16*, 3617–3622.
- (26) Chen, J.; Kuss-Petermann, M.; Wenger, O. S. *Chem. - A Eur. J.* **2014**, 4098–4104.
- (27) Alligrant, T. M.; Alvarez, J. C. *J. Phys. Chem. C* **2011**, *115*, 10797–10805.
- (28) Dempsey, J. L.; Winkler, J. R.; Gray, H. B. *J. Am. Chem. Soc.* **2010**, *132*, 16774–16776.
- (29) Irebo, T.; Zhang, M.-T.; Markle, T. F.; Scott, A. M.; Hammarström, L. *J. Am. Chem. Soc.* **2012**, *134*, 16247–16254.
- (30) Warren, J.J.; Mayer, J.M. *Chem Rev.* **2010**, *110*, 6961-7001.
- (31) Chambers, R.W.; Kearns, D.R. *Photochem. Photobiol.* **1969**, *10*, 215-219.
- (32) Rehm, D.; Weller, A. *Isr. J. Chem.* **1970**, *8*, 259.
- (33) Juris, A.; Balzani, V.; Barigelletti, F.; Campagna, S.; Belser, P.; Von Zelewsky, A. *Coord. Chem. Rev.* **1988**, *84*, 85–277.
- (34) Vogelmann, E.; Rauscher, W.; Krameer, H. E. a. *Photochem. Photobiol.* **1979**, *29*, 771–776.
- (35) Forster, T. *Zeitschrift fur Elektrochemie* **1950**, *54*, 531–535.
- (36) Grabowski, Z. R.; Rubaszewska, W. *J. Chem. Soc. Faraday Trans. 1 Phys. Chem. Condens. Phases* **1977**, *73*, 11–28.
- (37) Dempsey, J. L.; Winkler, J. R.; Gray, H. B. *J. Am. Chem. Soc.* **2010**, *132*, 16774–16776.

CHAPTER 3: PROTON-COUPLED ELECTRON TRANSFER REACTIONS WITH PHOTOMETRIC BASES REVEAL FREE ENERGY RELATIONSHIPS FOR PROTON TRANSFER

3.1. Introduction

Proton-coupled electron transfer (PCET) reactions involve the transfer of both a proton and electron, and can proceed through either stepwise or concerted mechanisms. In stepwise reactions, initial electron transfer (ET) is followed by proton transfer (PT) (ET-PT) or vice versa (PT-ET). By contrast, in a concerted proton-electron transfer (CPET) both the electron and proton move in a single kinetic step, circumventing charged, high-energy intermediates. These types of reactions are found throughout chemistry and biology and play an important role in the activation of small, energy-poor molecules, like H₂O and CO₂, into energy-rich fuels.^{1,2} As such, PCET processes underpin emerging energy technologies based on photon-to-fuel conversion strategies, and thus understanding and controlling PCET reactions is a high priority for the scientific community. However, elucidating the operating mechanism of a given PCET process can be quite difficult.^{3,4} Extracting relevant kinetic information about proton and electron transfers and interpreting the reaction parameters controlling the PCET reaction is an even greater challenge. Therefore, in order to advance our understanding of PCET reactions, more effective and versatile methods for monitoring PCET processes must be developed.

Spectroscopic monitoring of ET processes is enabled by the fact that transition metals often have unique optical signatures for each of their oxidation states. As such, time-resolved spectroscopic techniques like optical spectroscopy coupled to stopped-flow rapid mixing⁵⁻⁹

and transient absorption^{10–17} spectroscopy have been widely employed to monitor the ET component of PCET reactions. Electrochemistry has also been used to monitor the ET component of a PCET event.^{18–21} However, it is significantly more difficult to monitor the PT component of a PCET reaction through conventional methods. There are few methods available by which proton movement can be monitored on appropriate time scales; time-resolved infrared spectroscopy has been successfully employed to monitor PT,^{22–28} but when there is an accompanying ET reaction, electron transfer kinetics must generally be determined in a separate experiment. Our lab has recently reported the comprehensive optical monitoring of an excited-state PCET reaction and the subsequent thermal PCET recombination, but this is a rare example of concurrent spectroscopic monitoring of the electron and proton transfer components of a PCET process.¹⁷ As a result, PCET reaction mechanisms are generally inferred from reaction products, KIE studies of the ET component, and thermodynamic analyses.^{3,6,11,18,29,30} This approach has inherent shortcomings; as a result, little information is typically gleaned about the role PT plays in a PCET reaction, and this has further ramifications in the broader context of PT reactions.

Recognizing the integral role PT plays in PCET reactions, control over PT processes may offer a clear pathway to orchestrate and manipulate PCET reaction pathways and provide avenues for the development of catalysts that can, for instance, activate inert, energy poor molecules for fuel synthesis. However, in order to control PT, the parameters that govern a PT event need to be well understood. For instance, can we develop clear correlations between the driving force ($-\Delta G_{PT}$) and rate constant (k_{PT}) for PT within in a PCET process? While there have been some experimental investigations into the relationships between thermochemical parameters and reaction kinetics of PCET reaction, a

unified understanding, especially one that includes concerted reaction mechanisms and non-aqueous solvents, is not yet available.^{3,4,7,9,31–39} To advance our understanding of PCET reactions, a technique to effectively monitor PT must be developed.

Borrowing concepts from pH indicators and acid/base chemistry, we have identified, synthesized, and characterized a series of ‘photometric bases’ and further demonstrate that these molecules can be used to optically monitor PT processes in PCET reactions. In this work, we present a series of 7-dimethylaminoquinoline derivatives that have optical signatures in the visible region that shift upon protonation. This red shift in absorbance upon protonation provides an excellent handle to optically monitor a PT event. While similar approaches have been utilized to study pure PT reactions (thermal and excited state, both in water and non-aqueous solvents), these studies have relied on indicator dyes, many of which are carbon-based acids/bases and have limited tunability for PT driving force, and thus were not readily extendable to the PCET studies of interest here.^{40–44}

In the series of 2,4-R-7-dimethylaminoquinoline derivatives studied here, variation of the R-group at the 2,4-positions of the quinoline allows the optical properties and pK_a (in CH_3CN) to be systematically tuned. This allows (1) direct access to a variety of optical windows across the visible region in which PT reactions can be monitored and (2) an opportunity to vary PT driving force. The latter presents a unique opportunity to systematically examine the relationship between $-\Delta G_{\text{PT}}$ and k_{PT} within in a PCET process. With these tools in hand, we have explored the PCET reaction between ferrocenium (Fc^+), these photometric bases and *p*-aminophenol (NH_2PhOH) using optical spectroscopy and stopped-flow rapid-mixing (Figure 3.1). Both PT and ET processes were monitored

independently of one another, revealing free energy relationships between the proton transfer rate constants and the pK_a of the photometric base.

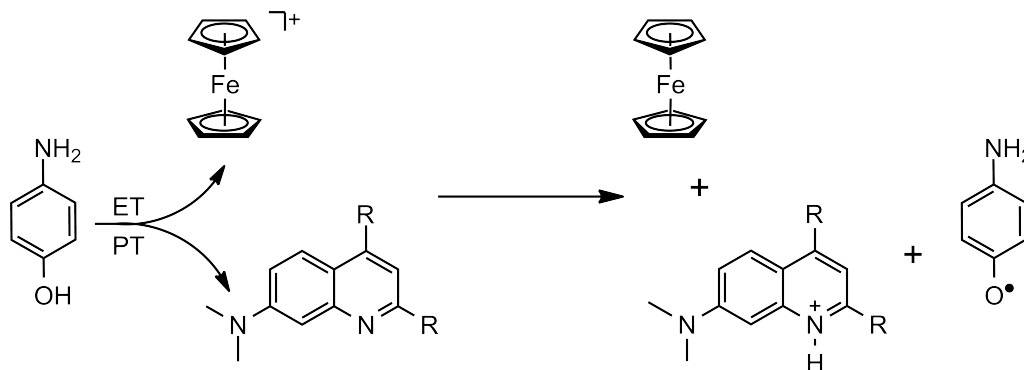


Figure 3.1. General schematic of the PCET reaction between NH_2PhOH , Fc^+ , and R-7DMAQ. NH_2PhOH is oxidized by Fc^+ , generating $\text{NH}_2\text{PhOH}^{\bullet+}$, which is then deprotonated by R-7DMAQ. Products of this initial PCET reaction are ferrocene, *p*-iminephenol, and R-7DMAQH⁺.

3.2.Results

Synthesis and Characterization of 2,4-R-7-Dimethylaminoquinoline Derivatives

The aryl substituted 2,4-R-7-dimethylaminoquinoline derivatives (R-7DMAQ, R=aryl) were synthesized via the procedure outlined in Figure 3.2a. N,N-dimethyl-3-phenylenediamine was refluxed with diethyl malonate to form 2,4-hydroxy-7-dimethylaminoquinoline. Bromination of the hydroxyl groups was carried out by refluxing the isolated reaction product in dry acetonitrile with phosphorus oxybromide and potassium carbonate. The final R-7DMAQ was obtained via a Suzuki coupling; a wide variety of commercially available boronic acids permits access to a range of aryl-substituted 7-DMAQs. 7-dimethylaminoquinoline (H-7DMAQ) was synthesized in one step via a Skraup reaction (Figure 3.2b).

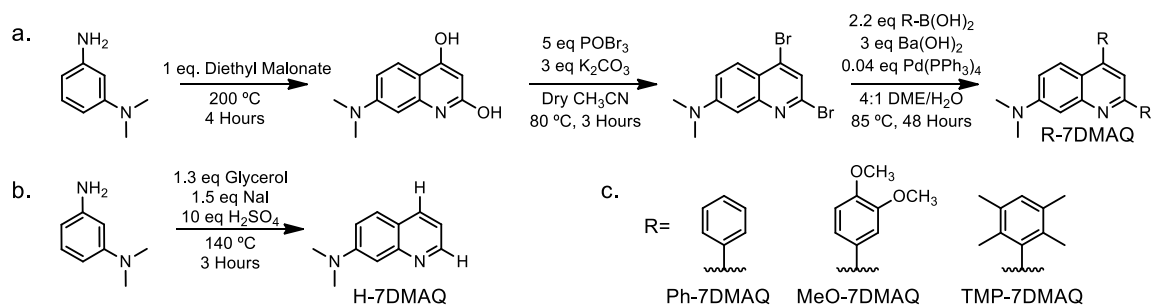


Figure 3.2 a) General scheme for the synthesis of the R-7DMAQs containing aryl-substituents (Ph, MeO, and TMP-7DMAQ). The substituents at the 2,4 positions of the quinoline backbone are determined by the identity of the boronic acid employed in the third step. b) H-7DMAQ was synthesized in one step via a Skraup reaction. Details of these reactions are included in the experimental section. c) Substituents of the R-7DMAQs and the nomenclature used throughout this manuscript.

Absorbance spectra of all the 7DMAQ derivatives exhibit a broad absorption feature centered 370–390 nm that tails into the visible region (Table 3.1, Figure 3.3 - Figure 3.7). Protonation of this 7DMAQ species to form 7DMAQH⁺ results in a bathochromic shift of this absorbance feature of ca. 71 nm, and an increase in the extinction coefficient (λ_{max} = 432–465 nm, Table 3.1, Figure 3.3 - Figure 3.7). Of note, MeO-7DMAQH⁺ has two pronounced absorbance features (λ_{max} = 375, 465 nm).

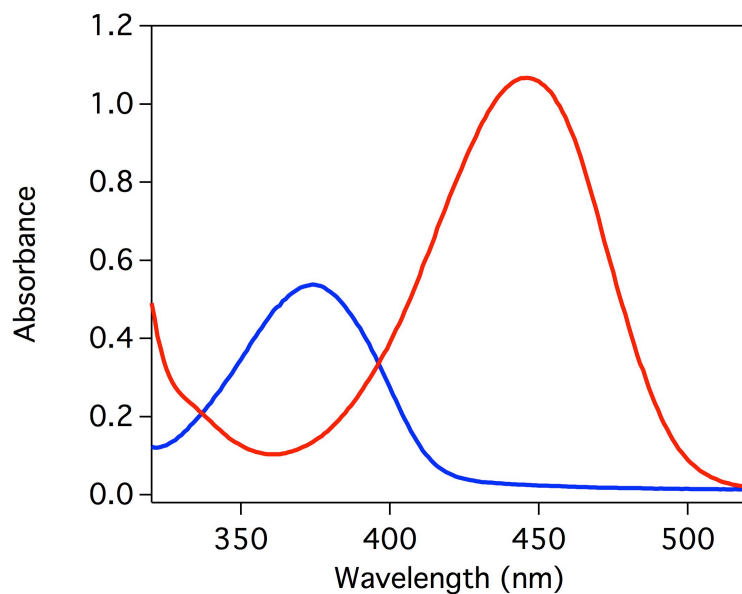


Figure 3.3. UV-vis absorbance spectrum of TMP-7DMAQ in acetonitrile (78 μM) and its conjugate acid TMP-7DMAQH⁺ (formed *in situ* upon the addition of 1 equiv. of HBF₄).

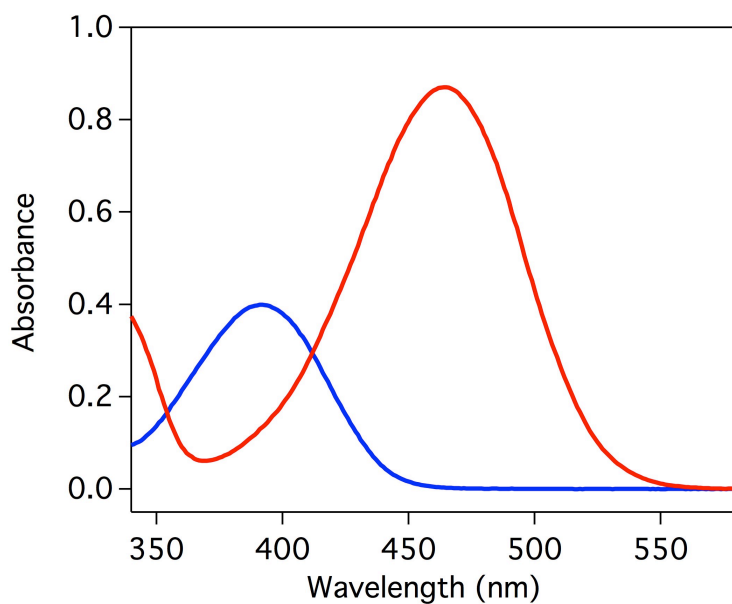


Figure 3.4 Absorbance spectrum 92 μM of Ph-7DMAQ (blue) and its conjugate acid Ph-7DMAQH⁺ (red) in CH₃CN.

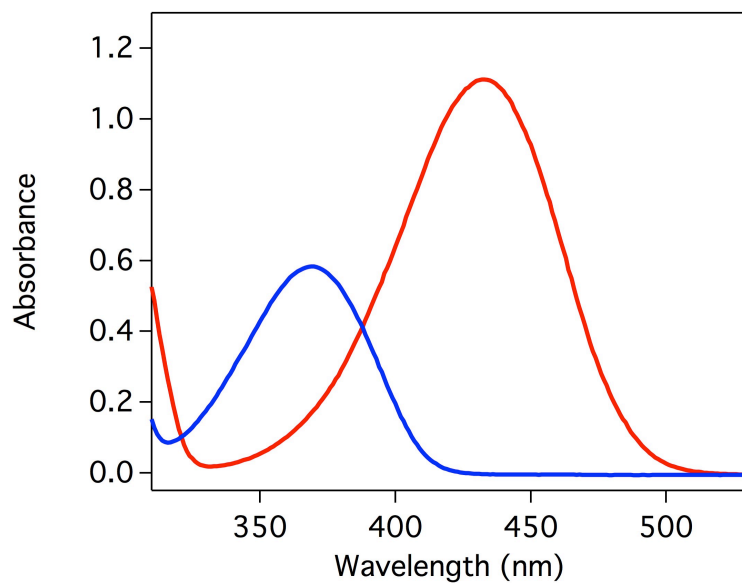


Figure 3.5 Absorbance spectrum of 183 μM H-7DMAQ (blue) and its conjugate acid H-7DMAQH⁺ (red) in CH₃CN.

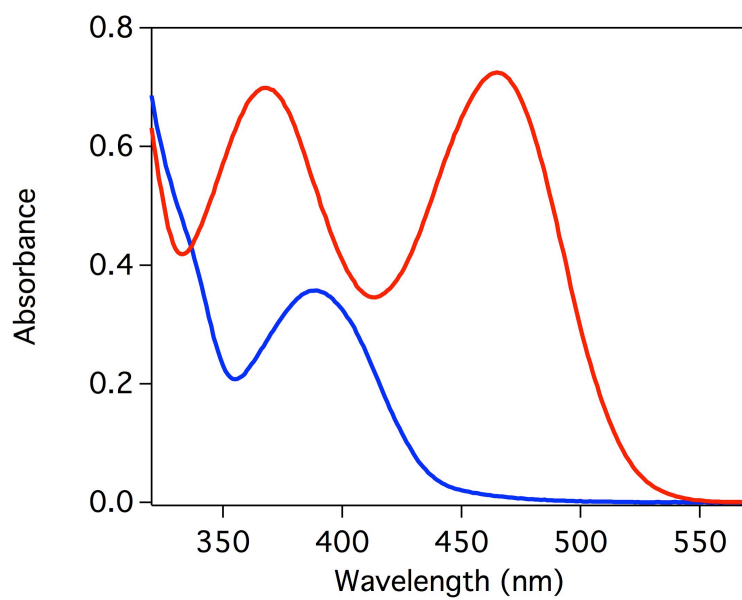


Figure 3.6. Absorbance spectrum of 37 μM MeO-7DMAQ (blue) and its conjugate acid MeO-7DMAQH⁺ (red) in CH₃CN.

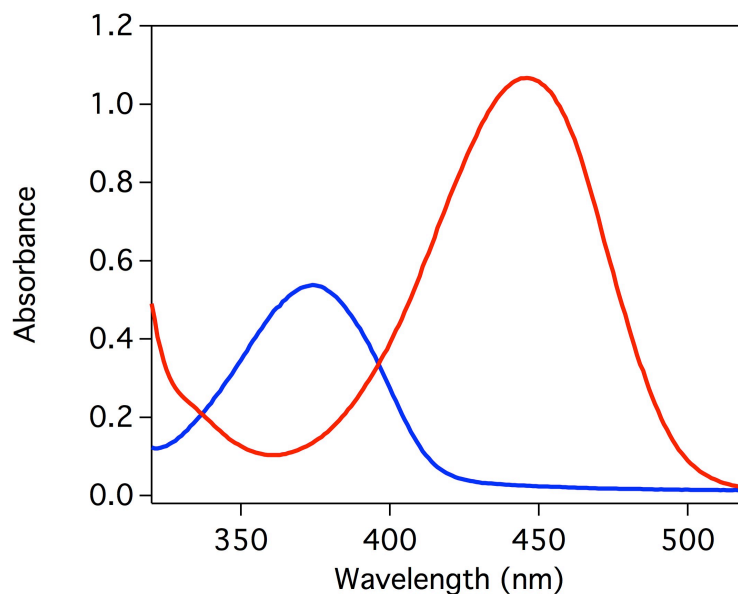


Figure 3.7 Absorbance spectrum of 83 μM TMP-7DMAQ (blue) and its conjugate acid TMP-7DMAQH⁺ (red) in CH₃CN.

Table 3.1

Base	pK _a (CH ₃ CN)	λ_{max} B (nm)	λ_{max} BH ⁺ (nm)	ϵ , B/BH ⁺ (M ⁻¹ cm ⁻¹)	E _{p,a} (V vs. Fc ^{+/0})
Ph-7DMAQ	14.2	392	464	4,300/9,800	0.45
H-7DMAQ	15.0	370	432	3,300/6,000	0.39
MeO- 7DMAQ	15.0	389	375, 465	389 nm: 10,000 375/465 nm: 20,000/20,500	0.44
TMP- 7DMAQ	15.2	374	446	6,600/13,200	0.51

Spectrophotometric titrations were carried out to determine the pK_a values for these compounds; values ranged from 14.2-15.2, with more electron donating aryl substituents giving rise to higher pK_a values (Details in Section 3.5, Table 3.1, Figure 3.8 - Figure 3.11).^{7,17,45}

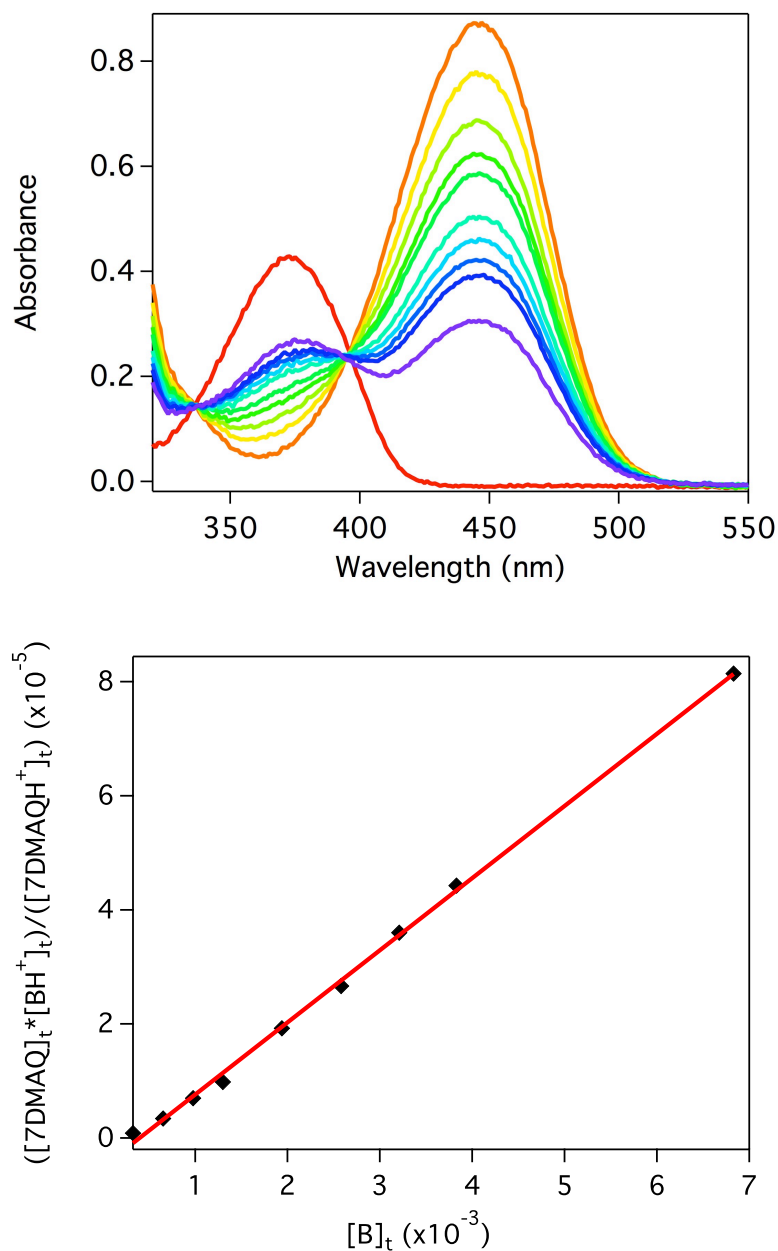


Figure 3.8. (top) Spectrophotometric titration of 64 μ M TMP-7DMAQ with 2-picoline (B) ($pK_a = 13.32$). 2-picoline and 2 picolinium (BH^+) are transparent in the region recorded and do not contribute to the overall signal. (bottom) The slope of $([7DMAQ][BH^+])/([7MAQH^+])$ vs. $[B]$, determined by monitoring the absorbance at 450 nm, can be used to determine the pK_a of TMP-7DMAQ ($pK_a = 15.2$ in CH_3CN).

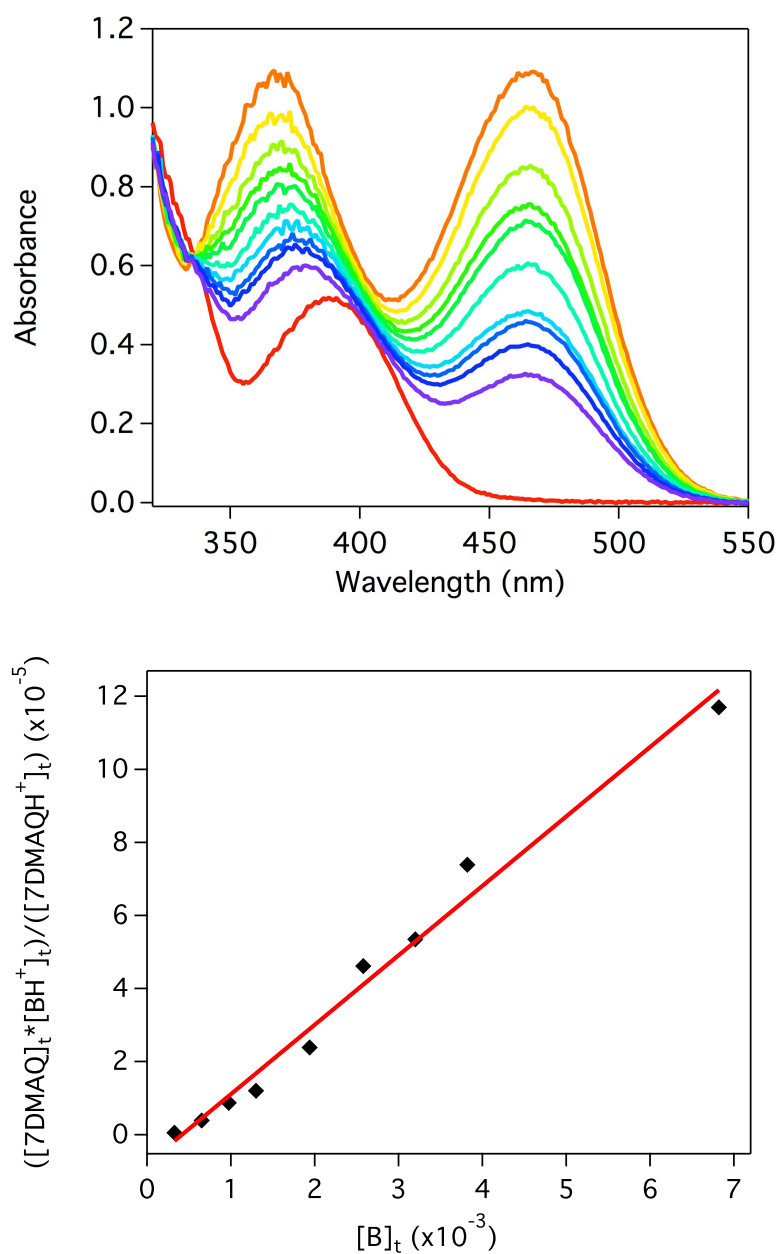


Figure 3.9. (top) Spectrophotometric titration of 54 μM MeO-7DMAQ with 2-picoline (B) ($\text{p}K_{\text{a}} = 13.32$). 2-picoline and 2 picolinium (BH^+) are transparent in the region recorded and do not contribute to the overall signal. (bottom) The slope of $([\text{7DMAQ}][\text{BH}^+])/[\text{7DMAQH}^+]$ vs. $[\text{B}]$, determined by monitoring the absorbance at 460 nm, can be used to determine the $\text{p}K_{\text{a}}$ of MeO-7DMAQ ($\text{p}K_{\text{a}} = 15.0$ in CH_3CN).

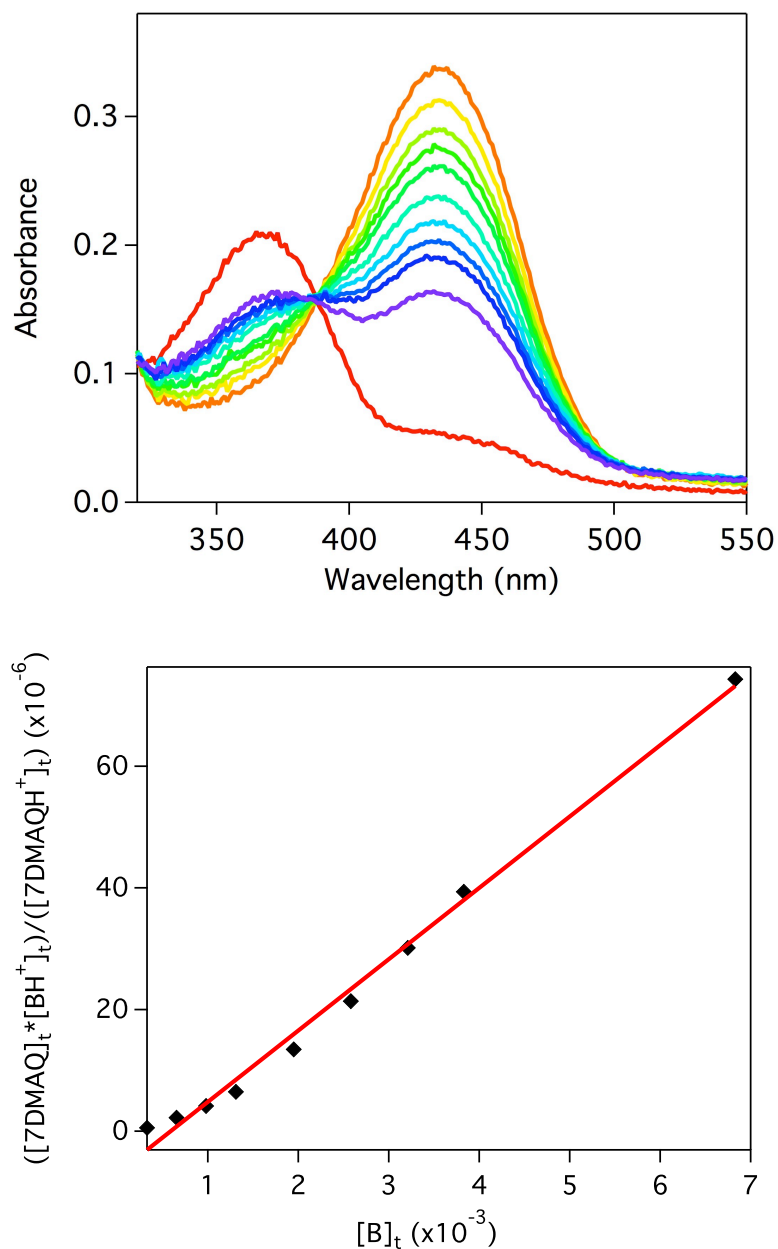


Figure 3.10. (top) Spectrophotometric titration of 58 μM H-7DMAQ with 2-picoline (B) ($pK_a = 13.32$). 2-picoline and 2 picolinium (BH^+) are transparent in the region recorded and do not contribute to the overall signal. (bottom) The slope of $([7\text{DMAQ}]_t [\text{BH}^+]_t) / ([7\text{DMAQH}^+]_t)$ vs. $[\text{B}]_t$, determined by monitoring the absorbance at 440 nm, can be used to determine the pK_a of H-7DMAQ ($pK_a = 15.0$ in CH_3CN).

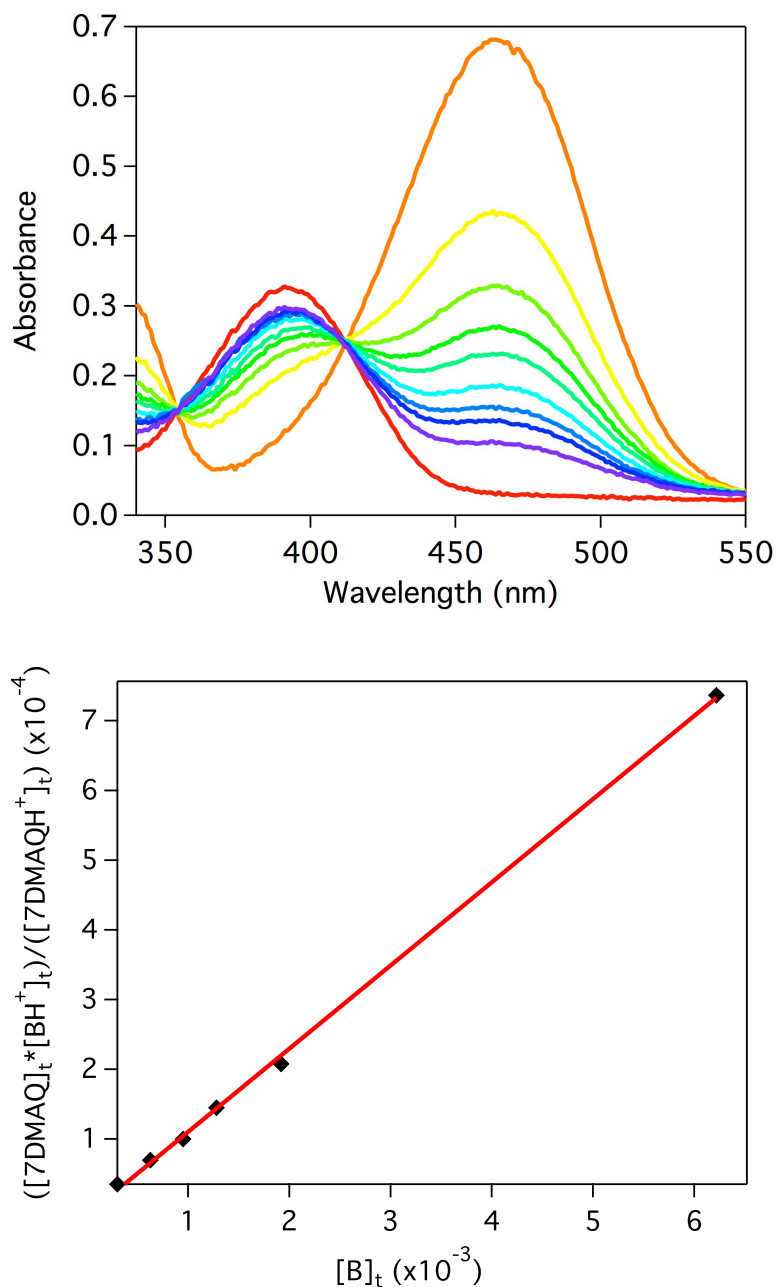


Figure 3.11. (top) Spectrophotometric titration of 69 μ M Ph-7DMAQ with 2-picoline (B) ($pK_a = 13.32$). 2-picoline and 2 picolinium (BH^+) are transparent in the region recorded and do not contribute to the overall signal. (bottom) The slope of $([7DMAQ][BH^+])/[7MAQH^+]$ vs. $[B]$, determined by monitoring the absorbance at 460 nm, can be used to determine the pK_a of Ph-7DMAQ ($pK_a = 14.2$ in CH_3CN).

Time-Resolved Optical Monitoring of PCET Reactions

The termolecular PCET reaction between NH_2PhOH , R-7DMAQ, and Fc^+ was initiated by stopped-flow rapid mixing of a solution of NH_2PhOH (100-500 μM) and R-7DMAQ (30 μM) with a solution of ferrocenium hexafluorophosphate (60 μM) and monitored via optical spectroscopy. Upon mixing, Fc^+ oxidizes NH_2PhOH , generating the aminophenol radical cation. This radical cation is much more acidic and is readily deprotonated by basic species in solution,^{3,46,47} including R-7DMAQ, to generate R-7DMAQH⁺ and $\text{NH}_2\text{PhO}^\bullet$.

This PCET reaction was first explored with Ph-7DMAQ. Absorbance spectra recorded at various time delays have prominent features corresponding to Fc^+ ($\lambda_{\text{max}} = 620$ nm), Ph-DMAQ ($\lambda_{\text{max}} = 392$ nm) and Ph-DMAQH⁺ ($\lambda_{\text{max}} = 464$ nm) (Figure 3.12). The peaks corresponding to Fc^+ and Ph-7DMAQ decay over the 0-100 ms timescale, while a new feature consistent with Ph-DMAQH⁺ grows in on a similar timescale as the reaction proceeds. Clean conversion of Ph-7DMAQ to its conjugate acid is indicated by the well-defined isosbestic point at 415 nm.

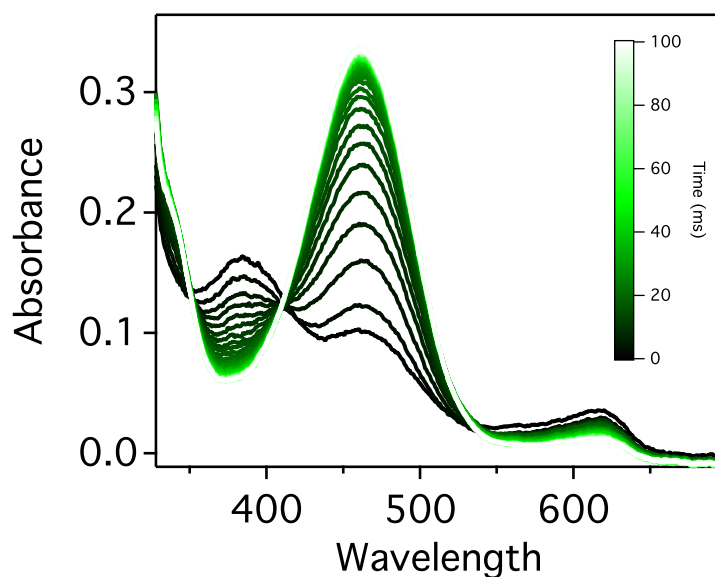


Figure 3.12. Absorbance spectra recorded at various time delays (0–100 ms, 6 ms intervals) upon rapid mixing of NH_2PhOH (100 μM) and Ph-7DMAQ (30 μM) with Fc^+ (150 μM) in CH_3CN .

For each R-7DMAQ, single wavelength reaction kinetics were recorded for both the appearance of the 7DMAQH^+ peak ($\lambda_{\text{obs}} = 440\text{--}460\text{ nm}$) and the loss of the Fc^+ peak ($\lambda_{\text{obs}} = 620\text{ nm}$). Below, general observations of these kinetics traces are described for the series of four R-7DMAQs explored (Figure 3.13 - Figure 3.16).

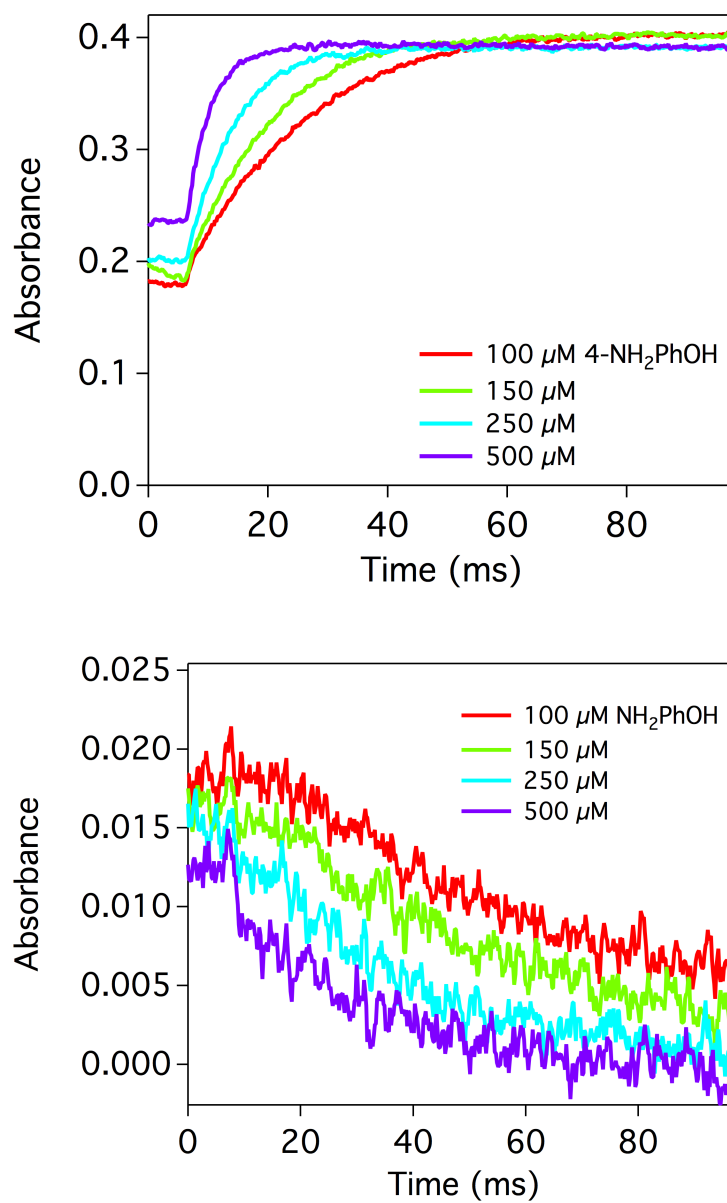


Figure 3.13 Stopped-flow kinetics traces monitoring the appearance of TMP-7DMAQH⁺ at 450 nm (top) and 620 nm (bottom). Present in each reaction are 60 μM Fc⁺, 30 μM TMP-7DMAQ, and 100 - 500 μM NH₂PhOH.

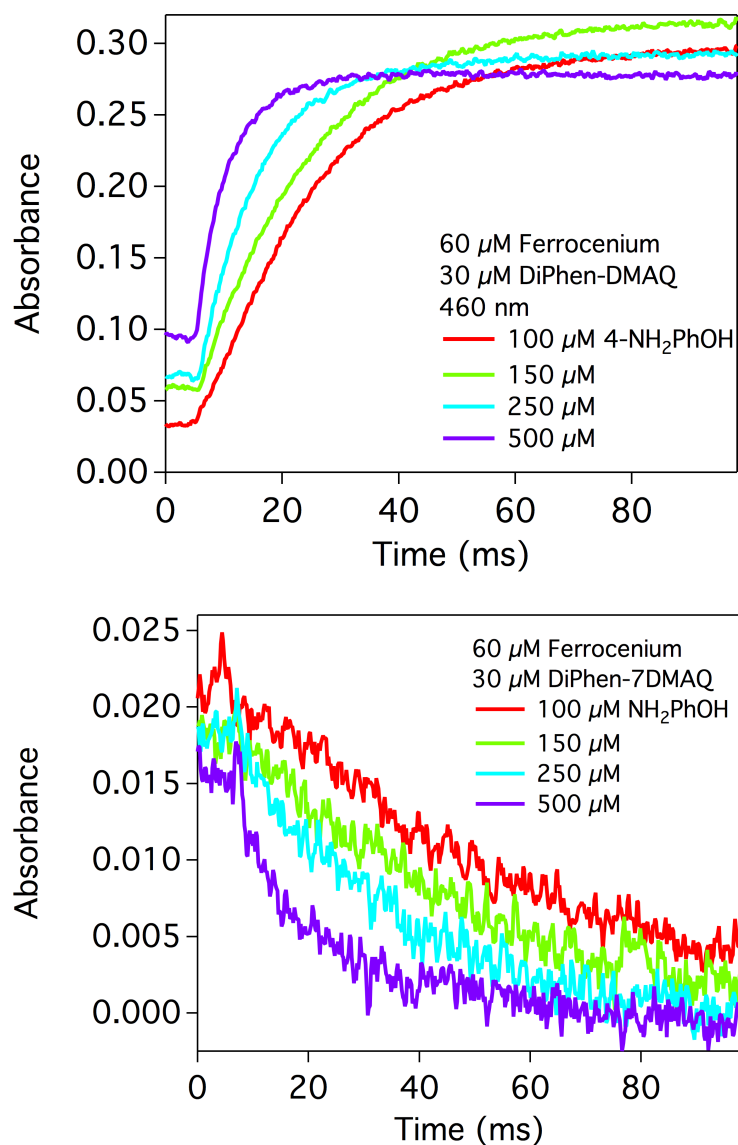


Figure 3.14 Stopped-flow kinetics traces monitoring (top) the appearance of Ph-7DMAQH⁺ at 460 nm and (bottom) the disappearance of Fc⁺ at 620 nm. Present in each reaction are 60 μM Fc⁺, 30 μM Ph-7DMAQ, and 100 – 500 μM NH₂PhOH.

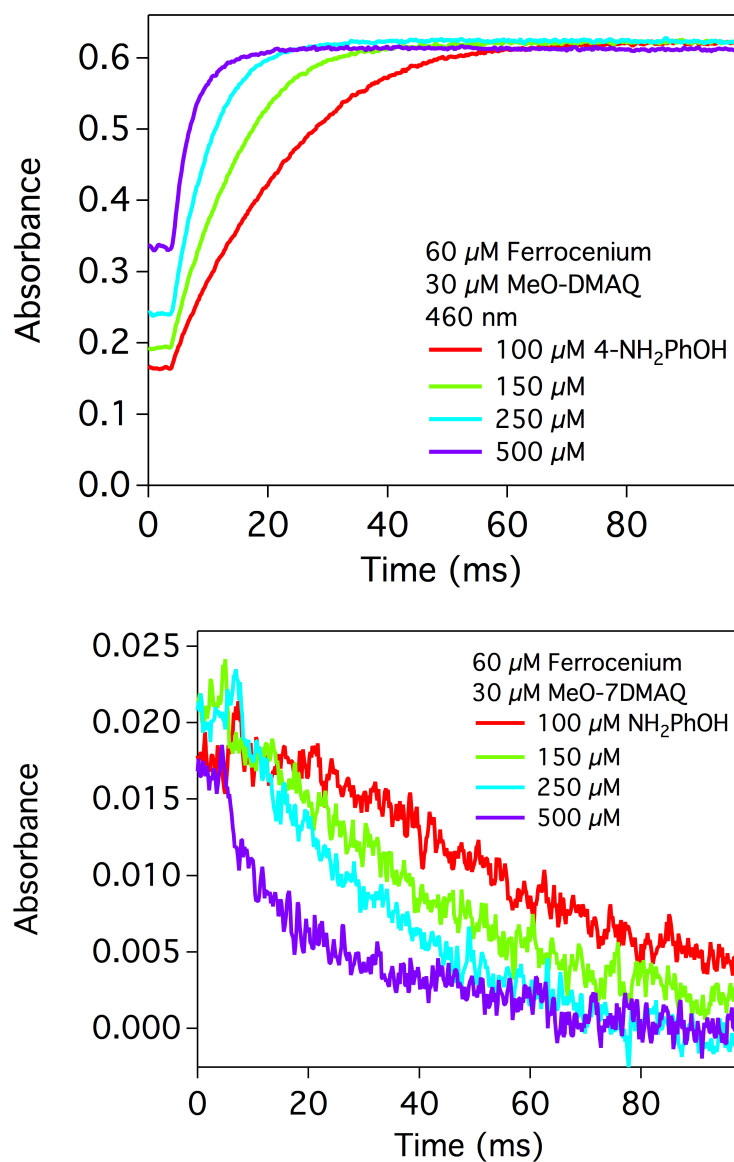


Figure 3.15. Stopped-flow kinetics traces monitoring (top) the appearance of MeO-7DMAQH⁺ at 460 nm and (bottom) the disappearance of Fc⁺ at 620 nm. Present in each reaction are 60 μM Fc⁺, 30 μM MeO-7DMAQ, and 100 – 500 μM NH₂PhOH.

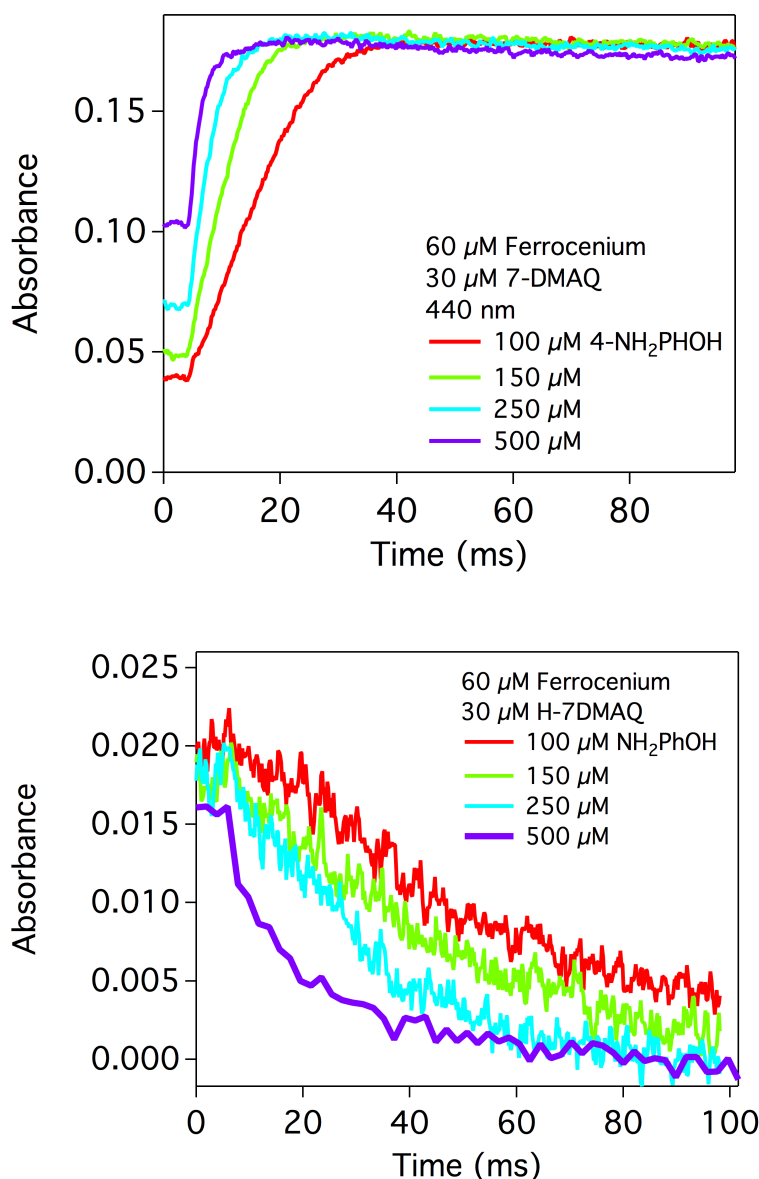


Figure 3.16. Stopped-flow kinetics traces monitoring (top) the appearance of H-7DMAQH^+ at 440 nm and (bottom) the disappearance of Fc^+ at 620 nm. Present in each reaction are 60 μM Fc^+ , 30 μM H-7DMAQ, and 100 – 500 μM NH_2PhOH .

Kinetics traces at 460 nm and 620 nm, reflecting the formation of R-7DMAQH^+ and decay of Fc^+ , respectively, were recorded as a function of NH_2PhOH concentration for the four photometric bases (Figure 3.13 - Figure 3.16). At both wavelengths, the rates of reaction accelerated as the concentration of NH_2PhOH was increased. In a separate experiment, the

kinetics of Fc^+ reduction were monitored ($\lambda_{\text{obs}} = 620 \text{ nm}$) as a function of R-7DMAQ concentration (with constant concentrations of NH_2PhOH and Fc^+). Notably, changes in the concentration of the photometric base did not affect the decay kinetics of the Fc^+ signal (Figure 3.17).

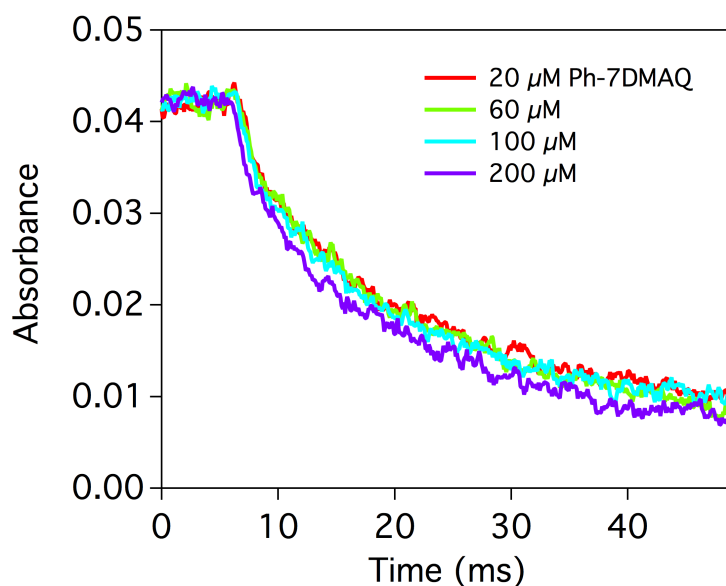


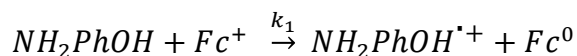
Figure 3.17. Stopped-flow kinetics traces monitoring the disappearance of Fc^+ at 620 nm as a function of Ph-7DMAQ concentration. Present in each reaction are Fc^+ (100 μM), NH_2PhOH (1.0 mM), and 0 – 200 μM Ph-7DMAQ.

3.3. Discussion

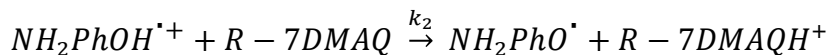
Proton-Coupled Electron Transfer Reactivity

The stopped-flow experiments described above provide kinetics data about both PT and ET processes in the oxidation of NH_2PhOH by the oxidant/base combination of Fc^+ and R-7DMAQ (the formal bond dissociation free energy^{3,36} ranges from 74.4 to 75.7 kcal mol⁻¹ for the R-7DMAQ compounds employed). The observation that higher concentrations of NH_2PhOH correlate with increases in both the observed rates of PT and ET suggests that the PT and ET components are coupled. Qualitatively, however, these two processes do not appear to occur with the same reaction kinetics. Further, for samples in which the concentration of R-7DMAQ was varied as the concentrations of NH_2PhOH and Fc^+ were held constant, kinetics traces reveal that the decay of the Fc^+ signal is not sensitive to base concentration. These observations indicate that this reaction is not operating under a concerted proton-electron transfer (CPET) mechanism. The viability of both stepwise PT-ET and ET-PT pathways was considered. PT-ET would require an initial deprotonation event, yet the differences between $\text{p}K_{\text{a}}$ values of NH_2PhOH (~30) and the 7DMAQH^+ species (14.2–15.2) suggest that protonation of R-7DMAQ by NH_2PhOH is highly endergonic. By contrast, an ET-PT process (Equation 3.1 - Equation 3.2) involves a slightly endergonic ET process ($\Delta G_{\text{ET}} \approx 60$ mV) followed by PT from the NH_2PhOH radical cation ($\text{NH}_2\text{PhOH}^{\bullet+}$) to R-7DMAQ (rough estimation of the $\text{p}K_{\text{a}}$ of $\text{NH}_2\text{PhOH}^{\bullet+}$ in CH_3CN from the $\text{p}K_{\text{a}}$ reported in DMSO yields a value of 15.8;^{3,48} however, observations of deprotonation by R-7DMAQ in this work suggests the value is in fact lower as PT to R-7DMAQ appears facile).

Equation 3.1



Equation 3.2



While our data qualitatively supports an initial ET-PT mechanism for the reaction of NH_2PhOH , Fc^+ , and $R-7DMAQ$ to form NH_2PhO^{\bullet} , $R-7DMAQH^+$ and Fc , kinetics analysis must account for reactivity of these unstable products. NH_2PhO^{\bullet} is a reactive radical species; extensive studies exploring the electrochemical oxidation of aniline and its derivatives (including NH_2PhOH), much of which has focused on the electropolymerization of poly(aniline) films have been carried out. Upon oxidation, anilines and their derivatives are initially deprotonated, but the products formed are highly favored to undergo a second one-electron, one-proton oxidation,^{49–53} and their two-electron, two-proton chemistry is well preceded.^{54–60} Our own electrochemical and mass spectrometric investigations of NH_2PhOH support this hypothesis and suggest that in the presence of base, the one-electron oxidized product can be readily deprotonated before undergoing a second oxidation and deprotonation (Figure 3.18 - Figure 3.20).

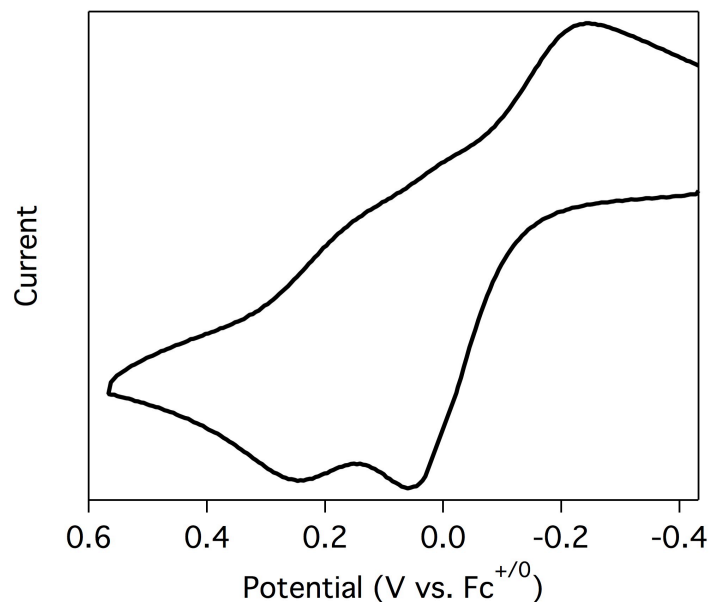


Figure 3.18. Cyclic voltammogram of 650 μM NH_2PhOH recorded at 300 mV/s in a 250 mM $[\text{Bu}_4\text{N}][\text{PF}_6]$ CH_3CN solution. Two irreversible oxidations are observed at 0.06 V and 0.23 V vs. $\text{Fc}^{+/0}$.

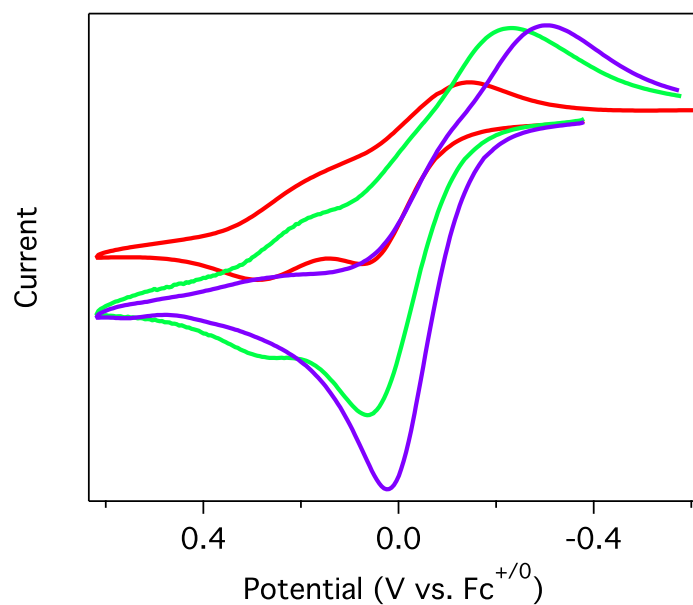


Figure 3.19. Cyclic voltammogram of 530 μM NH_2PhOH recorded at 300 mV/s in a 250 mM $[\text{Bu}_4\text{N}][\text{PF}_6]$ CH_3CN solution (red trace). Two irreversible oxidations are observed at 0.06 V and 0.23 V vs. $\text{Fc}^{+/0}$. Upon the addition of 1 equivalent 2-picoline ($\text{pK}_a = 13.32$), the first oxidation becomes more pronounced, however, the second oxidation is still present. Upon the addition of 5 equivalents of 2-picoline, only one oxidation is observed, indicative of a $2\text{e}^-/2\text{H}^+$ process in the presence of a proton acceptor.

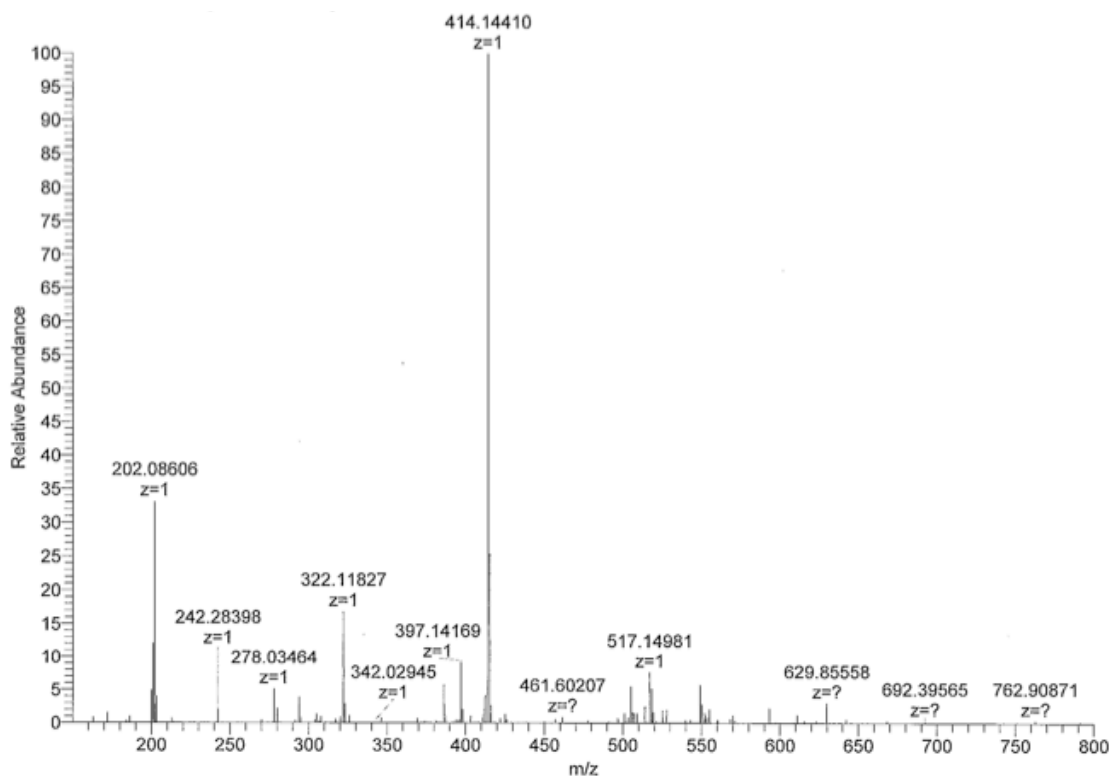
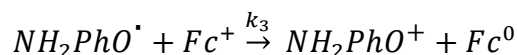


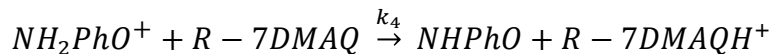
Figure 3.20. Mass spectrum obtained from the reaction of Fc^+ (440 μM), NH_2PhOH (3.0 mM), and 2-picoline (220 μM) in dry CH_3CN . In a nitrogen glovebox, the three reactants were mixed together in a scintillation vial and stirred for 5 minutes, after which the mixture was analyzed via mass spectrometry. The signals at $m/z = 414.14$ ⁵⁸ and 322.12 ⁵⁹ correspond to known products formed from the reaction of NHPhO , the $2e^-/2\text{H}^+$ oxidation product of NH_2PhOH . The signal at $m/z = 414.14$ ($\text{C}_{24}\text{H}_{19}\text{O}_4\text{N}_3$, expected $m/z = 413.10$ in its neutral form) is an oligomer formed from the reaction of four NHPhO molecules. The signal at $m/z = 322.12$ ($\text{C}_{18}\text{H}_{15}\text{O}_3\text{N}_3$, expected $m/z = 321.10$ in its neutral form) is the oligomer formed from three molecules of NHPhO .

This observation, combined with previous reports of two-electron, two-proton reactions involving NH_2PhOH , provides compelling evidence that stopped-flow kinetics data contain details of the secondary PCET reactivity of NHPhOH^\bullet to form *p*-benzoquinone imine NHPhO (Equation 3.3 - Equation 3.4).

Equation 3.3



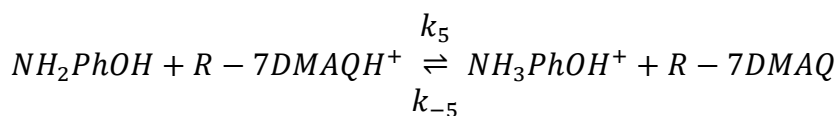
Equation 3.4



Equation 3.1 - Equation 3.4 together describe two sequential stepwise PCET reactions. A complete picture of the reactivity, and a full kinetics analysis, however, must also account for additional reactivity.

While NH_2PhOH is a weaker base than R-7DMAQ, the high concentration of NH_2PhOH in these experiments requires that we take into account an equilibrium between R-7DMAQH⁺ and NH_2PhOH (Equation 3.5). Spectrophotometric titrations (Figure 3.21 - Figure 3.24), indicate a weak equilibrium between these two reagents ($K_5 = 1 \times 10^{-2}$ to 5×10^{-4}). These titrations provide an estimation of the $\text{p}K_{\text{a}}$ of NH_3PhOH^+ in acetonitrile (12.5, see Section 3.5).

Equation 3.5



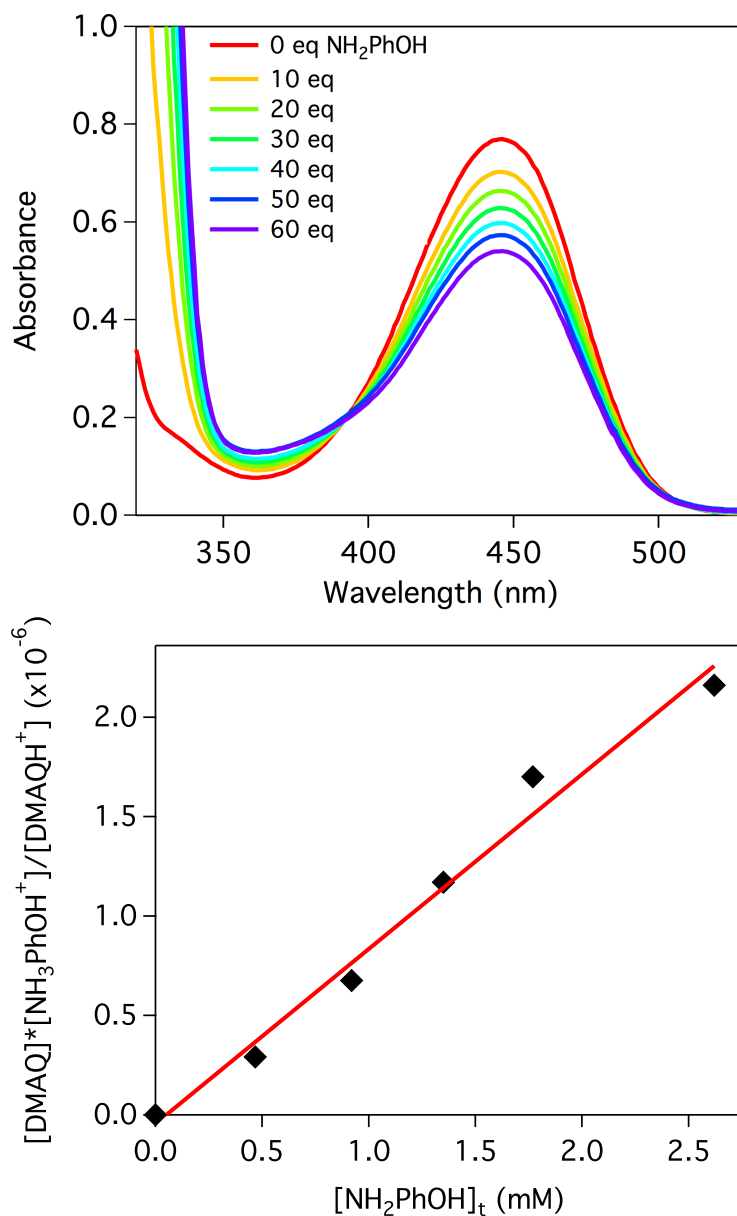


Figure 3.21. (top) Spectrophotometric titration of 60 μM TMP-7DMAQH⁺ with NH₂PhOH in CH₃CN. The weak proton-transfer equilibrium between these two molecules, combined with the absorbance of excess NH₂PhOH, cause minimal TMP-7DMAQ to be observed spectroscopically. (bottom) The slope of $([\text{7DMAQ}][\text{BH}^+])/[\text{7MAQH}^+]$ vs. [NH₂PhOH], determined by monitoring the absorbance of TMP-7DMAQH⁺ at 450 nm, can be used to determine both K_{eq} for the interaction between TMP-7DMAQ and NH₂PhOH ($K_{\text{eq}} = 9.1 \times 10^{-4}$), and the pK_{a} of NH₃PhOH⁺ ($pK_{\text{a}} = 12.2$ in CH₃CN).

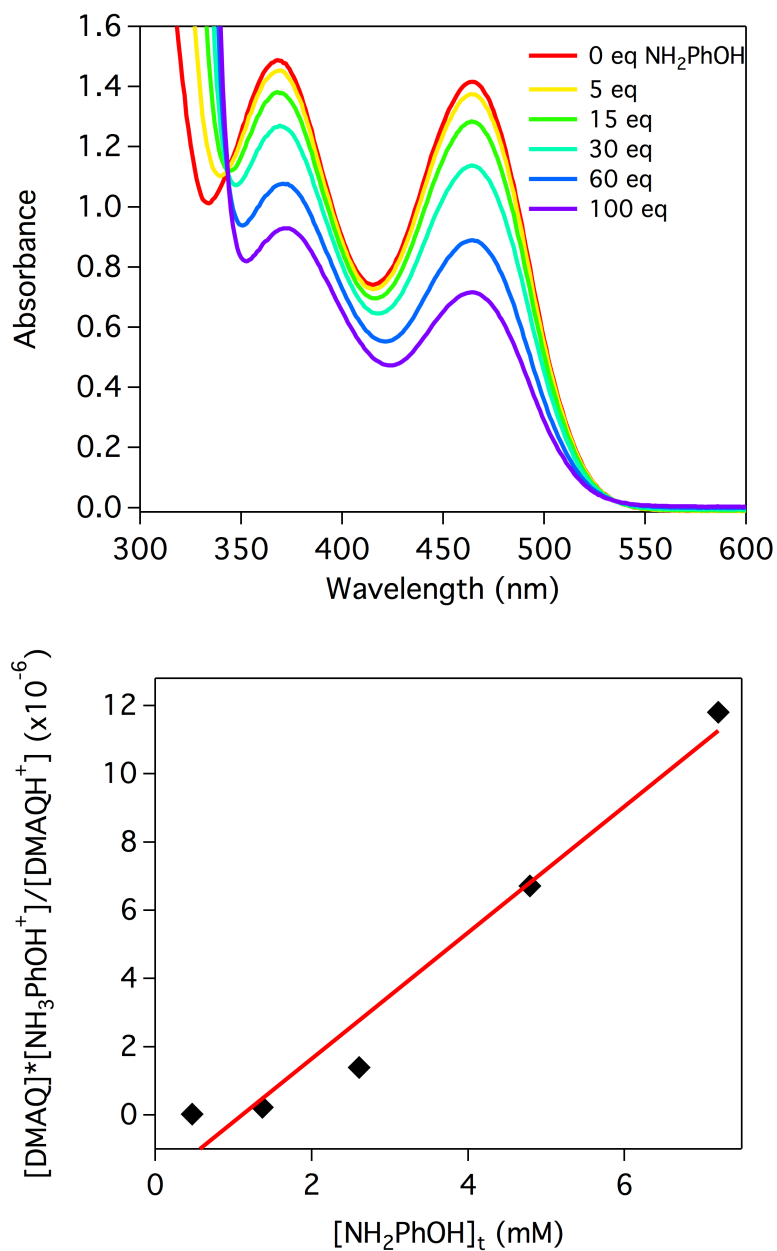


Figure 3.22. (top) Spectrophotometric titration of 70 μM MeO-7DMAQH⁺ with NH_2PhOH in CH_3CN . The weak proton-transfer equilibrium between these two molecules, combined with the absorbance of excess NH_2PhOH , cause minimal MeO-7DMAQ to be observed spectroscopically. (bottom) The slope of $([\text{7DMAQ}][\text{BH}^+]/[\text{7MAQH}^+])$ vs. $[\text{NH}_2\text{PhOH}]$, determined by monitoring the absorbance of MeO-7DMAQH⁺ at 460 nm, can be used to determine both K_{eq} for the interaction between MeO-7DMAQ and NH_2PhOH ($K_{\text{eq}} = 1.9 \times 10^{-3}$), and the $\text{p}K_{\text{a}}$ of NH_3PhOH^+ ($\text{p}K_{\text{a}} = 12.3$ in CH_3CN).

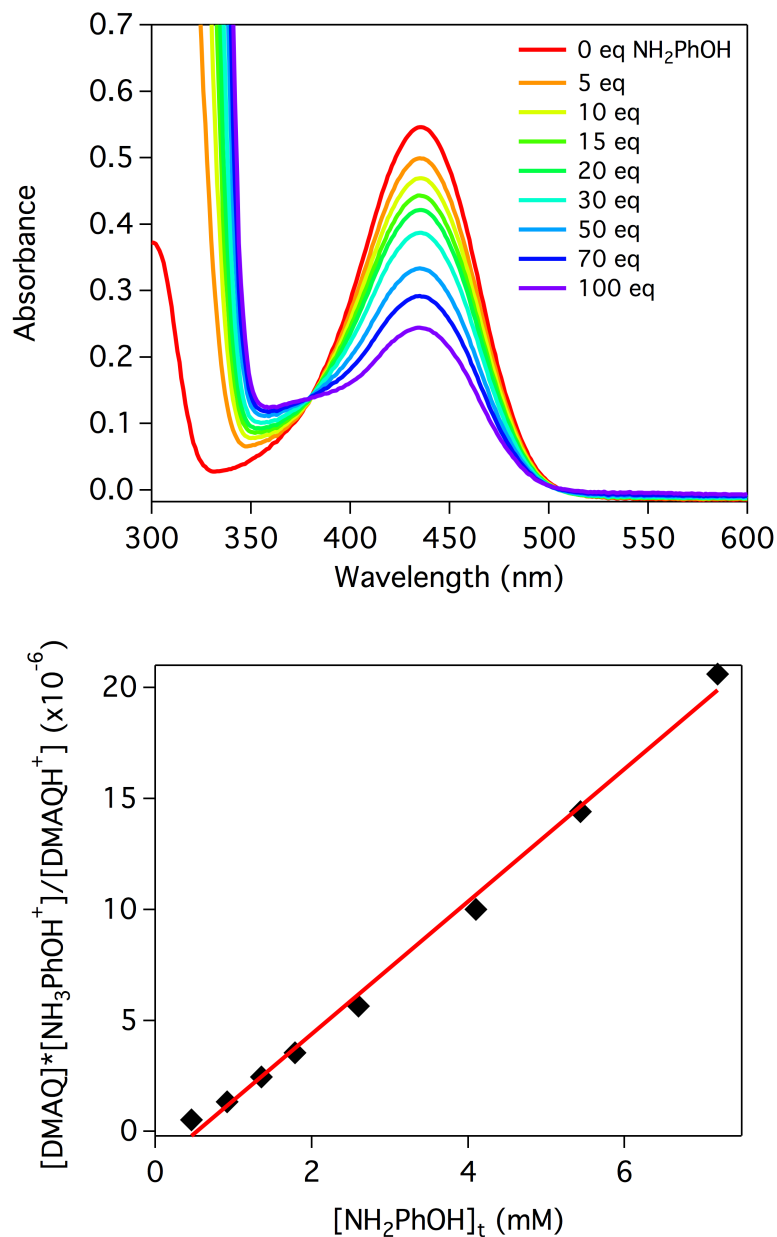


Figure 3.23. (top) Spectrophotometric titration of $54 \mu\text{M}$ H-7DMAQH^+ with NH_2PhOH in CH_3CN . The weak proton-transfer equilibrium between these two molecules, combined with the absorbance of excess NH_2PhOH , cause minimal H-7DMAQ to be observed spectroscopically. (bottom) The slope of $([\text{7DMAQ}][\text{BH}^+])/[\text{7MAQH}^+]$ vs. $[\text{NH}_2\text{PhOH}]$, determined by monitoring the absorbance of H-7DMAQH^+ at 440 nm, can be used to determine both K_{eq} for the interaction between H-7DMAQ and NH_2PhOH ($K_{\text{eq}} = 3.0 \times 10^{-3}$), and the $\text{p}K_{\text{a}}$ of NH_3PhOH^+ ($\text{p}K_{\text{a}} = 12.5$ in CH_3CN).

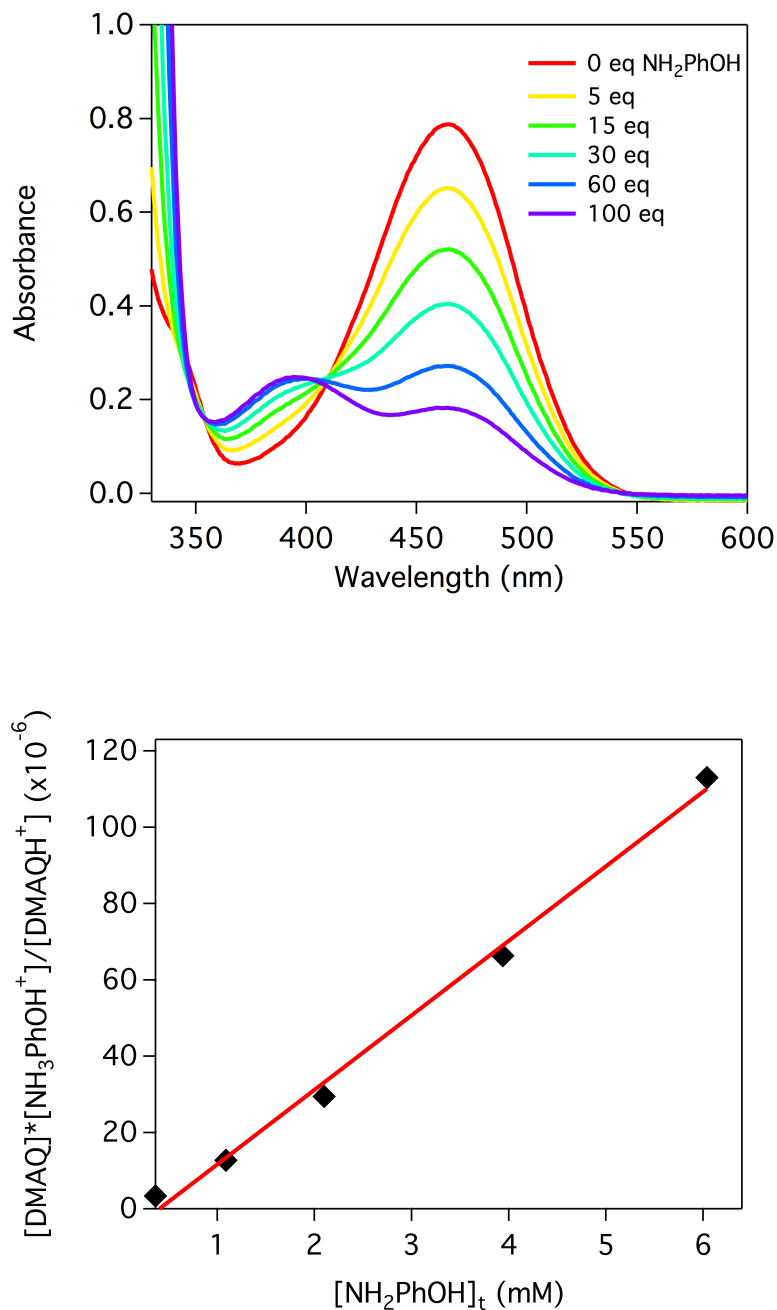
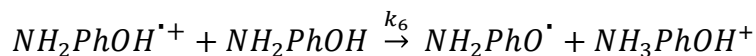


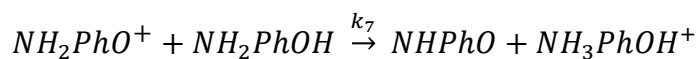
Figure 3.24. (top) Spectrophotometric titration of 82 μM Ph-7DMAQH⁺ with NH_2PhOH in CH_3CN . The weak proton-transfer equilibrium between these two molecules, combined with the absorbance of excess NH_2PhOH , cause minimal Ph-7DMAQ to be observed spectroscopically. (bottom) The slope of $([\text{7DMAQ}][\text{BH}^+])/[\text{7MAQH}^+]$ vs. $[\text{NH}_2\text{PhOH}]$, determined by monitoring the absorbance of Ph-7DMAQH⁺ at 460 nm, can be used to determine both K_{eq} for the interaction between Ph-7DMAQ and NH_2PhOH ($K_{\text{eq}} = 2.0 \times 10^{-2}$), and the $\text{p}K_{\text{a}}$ of NH_3PhOH^+ ($\text{p}K_{\text{a}} = 12.5$ in CH_3CN).

The amine group of unreacted NH_2PhOH can also serve as a proton acceptor for either of the radical cations generated in Equation 3.2 and Equation 3.4 (Equation 3.6 - Equation 3.7). Based on the relative basicities of the proton acceptors in solution, we posit that PT to NH_2PhOH will be slower than PT to R-7DMAQ. However, because the concentration of DMAQ is half that of the oxidant Fc^+ , and NH_2PhOH in excess, NH_2PhOH must serve as a proton acceptor from both a stoichiometric and kinetic perspective.

Equation 3.6

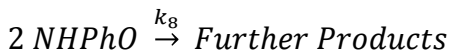


Equation 3.7



As discussed above, the product NHPhO reacts further to form oligomeric structures; we simplistically represent this complex terminal reactivity with Equation 3.8.^{58,59}

Equation 3.8



Lastly, when Fc^+ is titrated into a solution of R-7DMAQ, the absorbance of R-7DMAQ decreases, and a new peak appears at 460 nm, suggesting an adduct between R-7DMAQ and Fc^+ (Figure 3.25). However, upon addition of a stronger base (that doesn't absorb in the visible region), 1,8-diazabicycloundec-7ene (DBU, $\text{pK}_a = 24$),⁶¹ the original absorbance spectrum of basic R-7DMAQ is recovered. Quinolines are Lewis bases⁶² and can thus form adducts with Lewis acids, like Fc^+ .⁶³

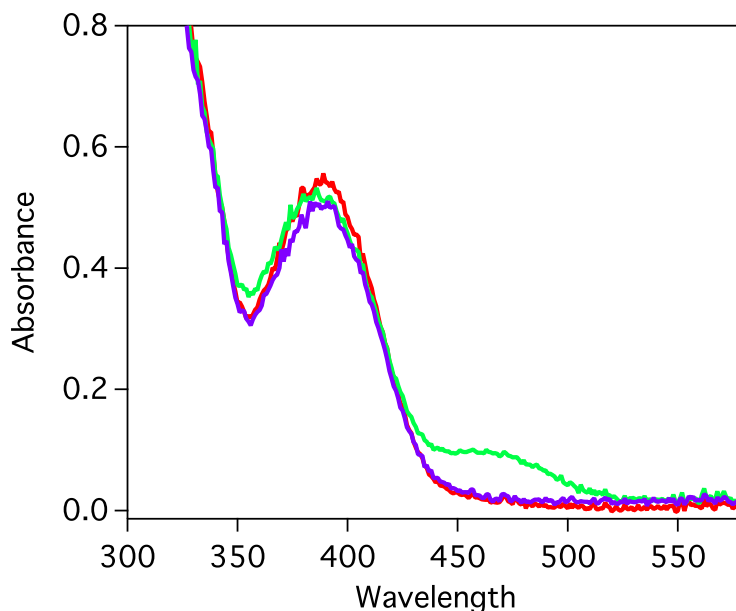
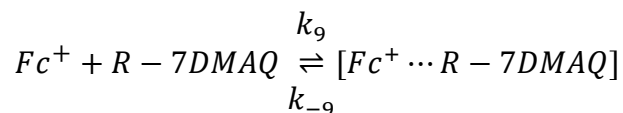


Figure 3.25. Adduction of MeO-7DMAQ with Fc^+ . Red = 60 μM MeO-7DMAQ, Green = addition of 1 equivalent Fc^+ , Purple = addition of 1 equivalent of DBU ($\text{p}K_{\text{a}} = 24$). Addition of DBU recovers the initial absorbance of MeO-7DMAQ as the Lewis acid-base interaction between DBU and Fc^+ is stronger than that of Fc^+ with MeO-7DMAQ.

To further confirm that the absorbance shifts arise from a Lewis acid-base interaction, and ensure the reactivity was not resulting from an endergonic electron transfer reaction, the interaction of Ph-7DMAQ with decamethylferrocenium (a 507 mV weaker oxidant)⁶³ was tested. Upon titration with $\text{Me}_{10}\text{Fc}^+$, a similar change in absorbance of Ph-7DMAQ is observed (Figure 3.26). This Lewis acid-base interaction between the R-7DMAQs and Fc^+ (Eq. 9) was quantified using a modified Benesi-Hildebrand analysis⁶⁴ (see Figure 3.27 - Figure 3.30, Section 3.5), and taken into account when modeling the kinetics of the described PCET system (*vide infra*).

Equation 3.9



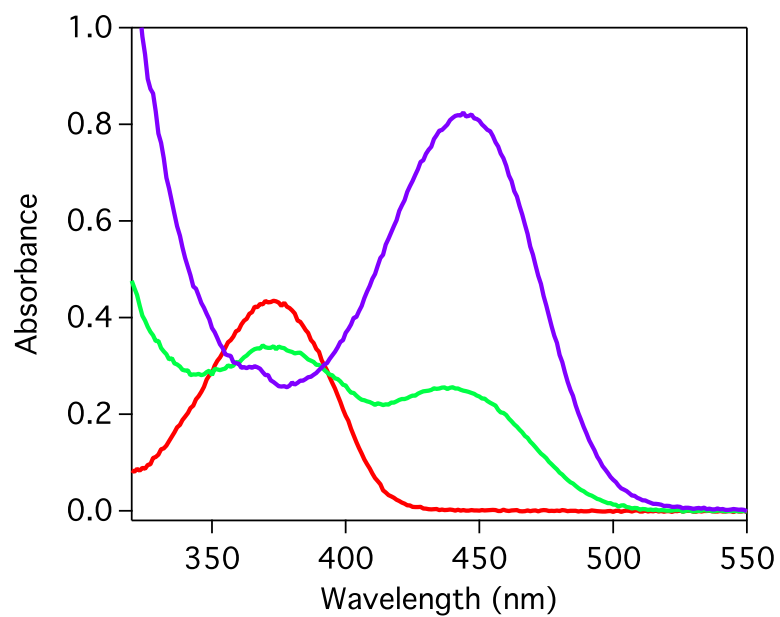


Figure 3.26. Adduction of TMP-7DMAQ (35 μ M) with Decamethylferrocenium ($\text{Me}_{10}\text{Fc}^+$), which is 0.507 V weaker of an oxidant than Fc^+ . Red = TMP-7DMAQ only, Green = addition of 1 equivalent of $\text{Me}_{10}\text{Fc}^+$, Purple = addition of 5 equivalents of $\text{Me}_{10}\text{Fc}^+$.

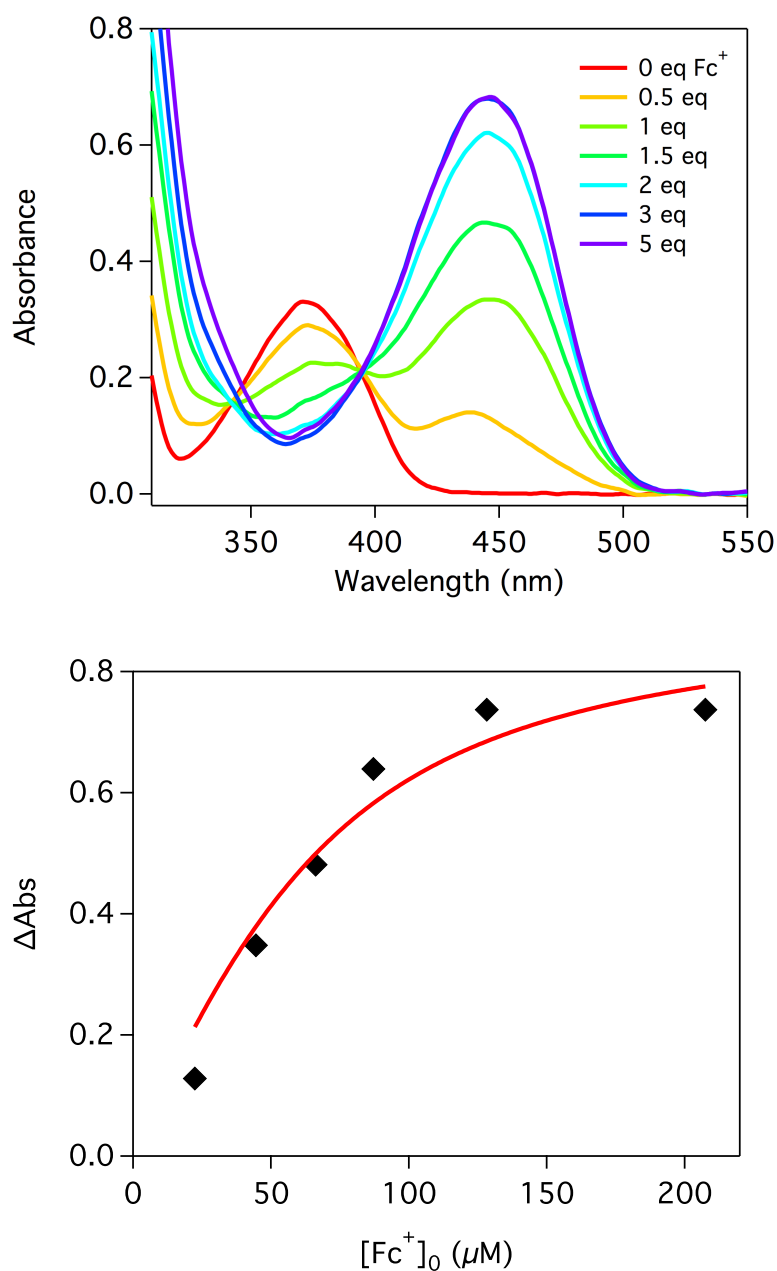


Figure 3.27. (top) Titration of 53 μM TMP-7DMAQ with Fc^+ in CH_3CN . These two species form a Lewis Acid-Base adduct in solution that gives rise to a signal similar to that of TMP-7DMAQH^+ . (bottom) Plot of $\Delta\text{Absorbance}$ versus $[\text{Fc}^+]$; absorbance was monitored at 450 nm. The data was fit using a modified Benesi-Hildebrand analysis (described above), resulting in $K_{\text{eq}} = 3.6 \times 10^4 \text{ M}^{-1}$ and $\Delta\epsilon = 1.5 \times 10^4 \text{ M}^{-1} \text{ cm}^{-1}$. Experimentally $\Delta\epsilon$ is 1.3×10^4 , this was calculated from the difference of the adduct absorbance (when fully adducted) and that of free TMP-7DMAQ at 450 nm. This value is in good agreement with the value determined through fitting.

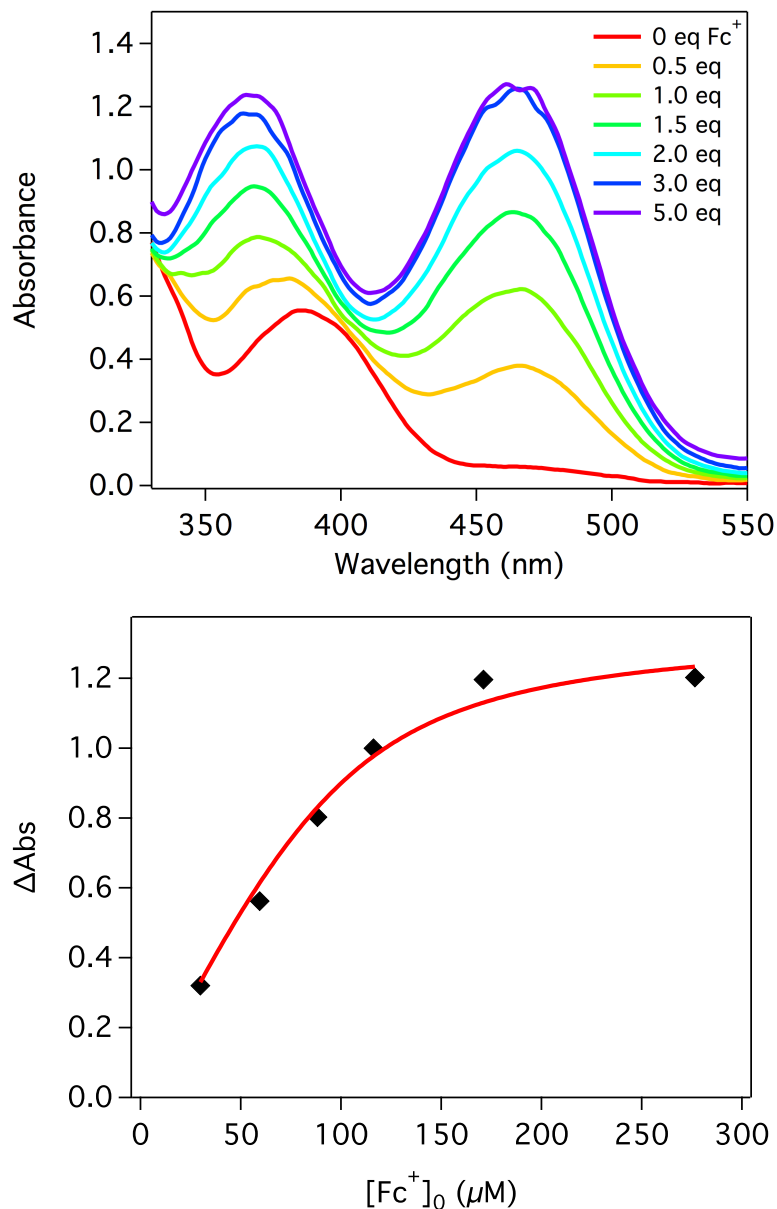


Figure 3.28. (top) Titration of 63 μM MeO-7DMAQ with Fc⁺ in CH₃CN. These two species form a Lewis Acid-Base adduct in solution that gives rise to a signal similar to that of MeO-7DMAQH⁺. (bottom) Plot of ΔAbsorbance versus [Fc⁺]₀; absorbance was monitored at 460 nm. The data was fit using a modified Benesi-Hildebrand analysis (described above), resulting in $K_{eq} = 6.2 \times 10^4 \text{ M}^{-1}$ and $\Delta\epsilon = 1.3 \times 10^4 \text{ M}^{-1} \text{ cm}^{-1}$. Experimentally $\Delta\epsilon$ is 2.0×10^4 , this was calculated from the difference of the adduct absorbance (when fully adducted) and that of free MeO-7DMAQ at 450 nm. This value is in good agreement with the value determined through fitting.

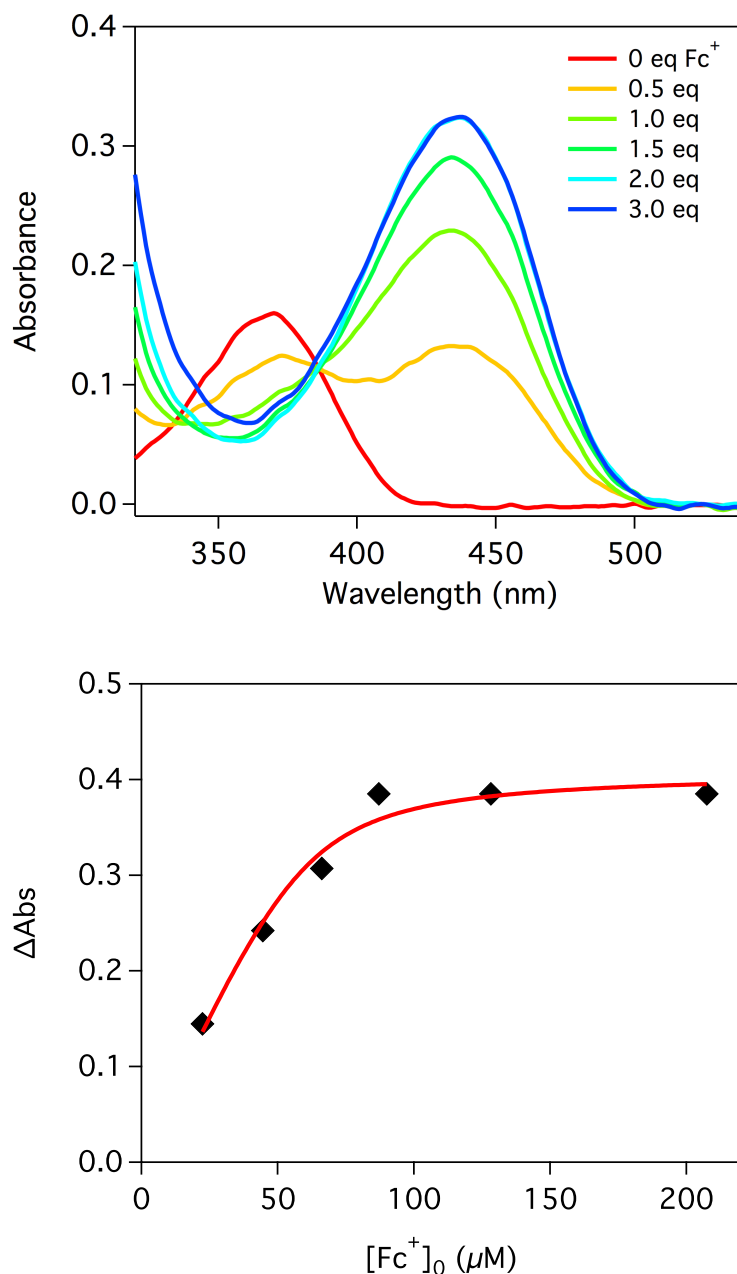


Figure 3.29. (top) Titration of 55 μM H-7DMAQ with Fc^+ in CH_3CN . These two species form a Lewis Acid-Base adduct in solution that gives rise to a signal similar to that of H-7DMAQH^+ . (bottom) Plot of $\Delta\text{Absorbance}$ versus $[\text{Fc}^+]_0$; absorbance was monitored at 440 nm. The data was fit using a modified Benesi-Hildebrand analysis (described above), resulting in $K_{\text{eq}} = 2.1 \times 10^5 \text{ M}^{-1}$ and $\Delta\varepsilon = 6.8 \times 10^3 \text{ M}^{-1} \text{ cm}^{-1}$. Experimentally $\Delta\varepsilon$ is 6.0×10^3 , this was calculated from the difference of the adduct absorbance (when fully adducted) and that of free H-7DMAQ at 450 nm. This value is in good agreement with the value determined through fitting.

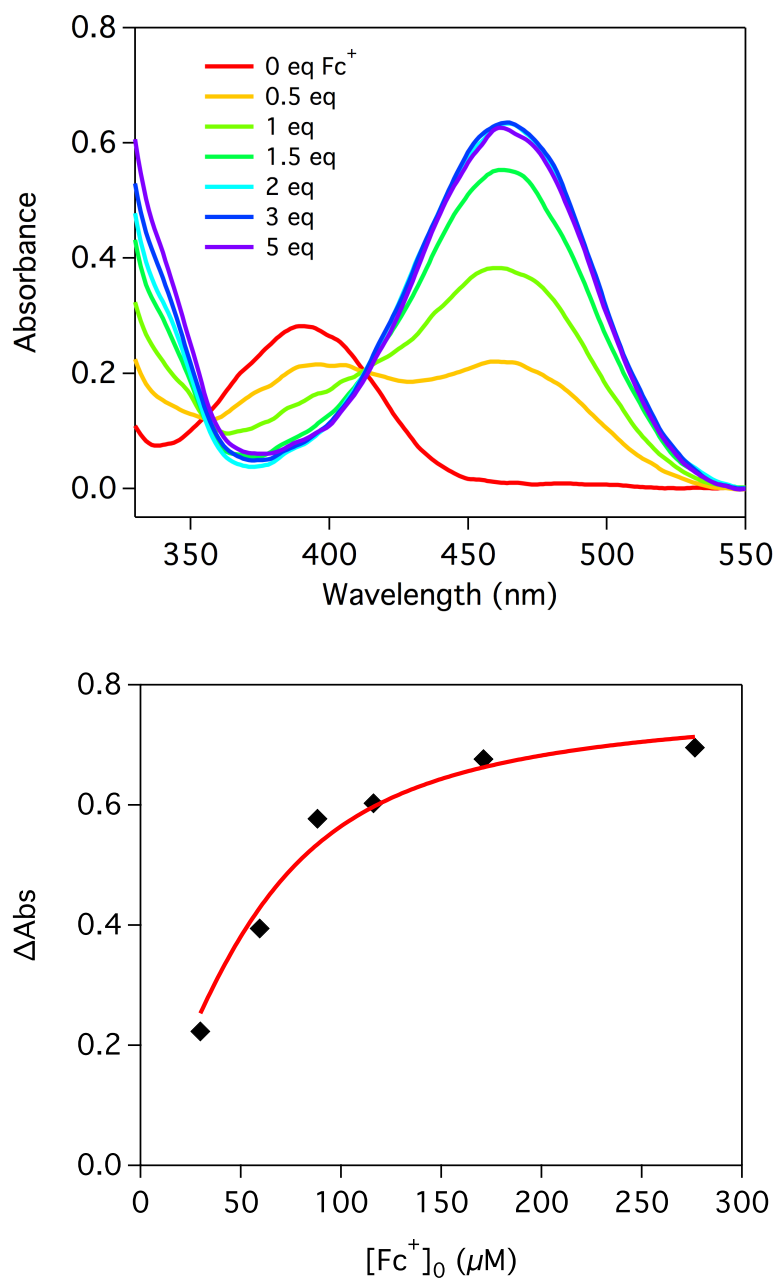


Figure 3.30. (top) Titration of 65 μM Ph-7DMAQ with Fc^+ in CH_3CN . These two species form a Lewis Acid-Base adduct in solution that gives rise to a signal similar to that of Ph-7DMAQH^+ . (bottom) Plot of ΔAbs versus $[\text{Fc}^+]$; absorbance was monitored at 460 nm. The data was fit using a modified Benesi-Hildebrand analysis (described above), resulting in $K_{\text{eq}} = 4.5 \times 10^4 \text{ M}^{-1}$ and $\Delta\epsilon = 1.3 \times 10^4 \text{ M}^{-1} \text{ cm}^{-1}$. Experimentally $\Delta\epsilon$ is 9.8×10^3 , this was calculated from the difference of the adduct absorbance (when fully adducted) and that of free Ph-7DMAQ at 450 nm. This value is in good agreement with the value determined through fitting.

Kinetic Model for PCET

Kinetics simulations were performed with a series of differential equations (see Supporting Information) derived from the kinetics model described in Equation 3.1 - Equation 3.9 to determine rate constants for elementary reaction steps. The rate law for the coupled series of reactions was solved numerically using an ordinary differential equation solver. Initial concentrations of reactants, intermediates, and products, as well as the time interval of the reaction and rate constants were provided as inputs. Solving these equations resulted in time-dependent concentration profiles for each species – known molar extinction coefficients were used to convert time-dependent concentration profiles into simulated stopped-flow kinetics traces.

In order to minimize floating parameters, kinetics traces monitoring the loss of the Fc^+ absorbance at 620 nm upon rapid mixing with NH_2PhOH in the absence of R-7DMAQ were simulated to quantify the rates of ET between Fc^+ and NH_2PhOH (Equation 3.1) and $\text{NH}_2\text{PhO}^\bullet$ (Equation 3.3) (Figure 3.31).

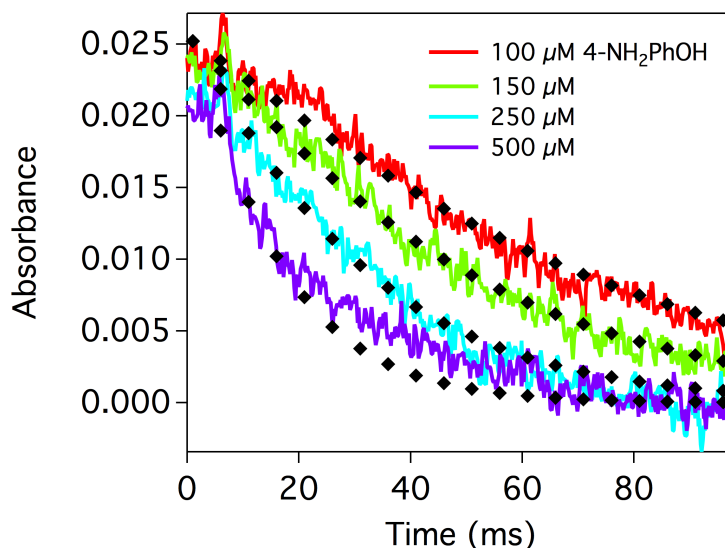


Figure 3.31. Kinetics and accompanying fit for ET between Fc^+ (60 μM) and NH_2PhOH (100 - 500 μM). The reaction was monitored at 620 nm and the rate constants input were $k_1 = 1.2 \times 10^5 \text{ M}^{-1} \text{ s}^{-1}$, $k_3 = 5 \times 10^5 \text{ M}^{-1} \text{ s}^{-1}$, $k_7 = 3 \times 10^6 \text{ M}^{-1} \text{ s}^{-1}$, $k_8 = 1 \times 10^5 \text{ M}^{-1} \text{ s}^{-1}$, and $k_9 = 1 \times 10^5 \text{ M}^{-1} \text{ s}^{-1}$.

To describe reactivity in the absence of R-7DMAQ, rate constants $k_2, k_4, k_5, k_{-5}, k_9, k_{-9}$ were set to zero in the kinetics model and the remaining rate constants were adjusted iteratively to simulate the kinetics traces. Simulations were extremely sensitive to both k_1 and k_3 and yielded values of $1.2 \times 10^5 \text{ M}^{-1} \text{ s}^{-1}$ and $5.0 \times 10^5 \text{ M}^{-1} \text{ s}^{-1}$, respectively, for these two rate constants. These rate constants are consistent with those predicted by the Marcus cross relation based on the self-exchange rate constants for ferrocene/ferrocenium and phenoxyl/phenoxide (the $\text{PhOH}^{\bullet+/0}$ self-exchange rate constant is not known).^{65,66}

Simulations also provided rate constants for proton transfer from the oxidation products to NH_2PhOH ($k_6 = 3.0 \times 10^6 \text{ M}^{-1} \text{ s}^{-1}$, $k_7 = 1.0 \times 10^5 \text{ M}^{-1} \text{ s}^{-1}$, see below for further discussion). The rate constant depicting terminal oligomerization reactivity of para-quinoneimine ($k_8 = 1 \times 10^5 \text{ M}^{-1} \text{ s}^{-1}$) falls in the range estimated for oligomer formation.⁵⁹ The value of this parameter had minimal influence on the kinetic fits, but was necessary to model the consumption of the *p*-benzoquinone imine.^{58,59}

To model kinetics data for samples incorporating the photometric bases ($\lambda_{\text{obs}} = 440\text{-}460\text{ nm}$ and 620 nm), the five rate constants determined above in the absence of R-7DMAQ were held constant. Values for K_5 and K_9 , which describe the equilibria of R-7DMAQ with NH_2PhOH and Fc^+ , respectively, were used to determine the ratios of $k_5:k_{-5}$ and $k_9:k_{-9}$. The forward rate constants k_5 and k_9 were determined through iterative simulation while the reverse rate constants k_{-5} and k_{-9} were fixed by maintaining $K_{\text{eq}} = k_5/k_{-5}$ (k_9/k_{-9}). As a result, the only remaining variables in the complete kinetics model described by Equation 3.1 - Equation 3.9 were the rate constants for proton transfer from the initial oxidation products $\text{NH}_2\text{PhOH}^{\bullet+}$ and NH_2PhO^+ to R-7DMAQ (k_2 and k_4 respectively). Rate constants k_2 and k_4 were iteratively adjusted, together with k_5 and k_9 , to achieve satisfactory simulation of the single wavelength kinetics traces at both $\lambda_{\text{obs}} = 440\text{--}460\text{ nm}$ and $\lambda_{\text{obs}} = 620\text{ nm}$ (Figure 3.32 - Figure 3.35). Simulations were repeated across a set of samples that contained varying concentrations of NH_2PhOH to obtain a self-consistent set of rate constants for each R-7DMAQ. k_2 values from these simulations fall in the range $1.5 - 7.5 \times 10^8\text{ M}^{-1}\text{ s}^{-1}$ while the corresponding k_4 values are smaller; in the range $5.5 \times 10^6 - 3.0 \times 10^7\text{ M}^{-1}\text{ s}^{-1}$.

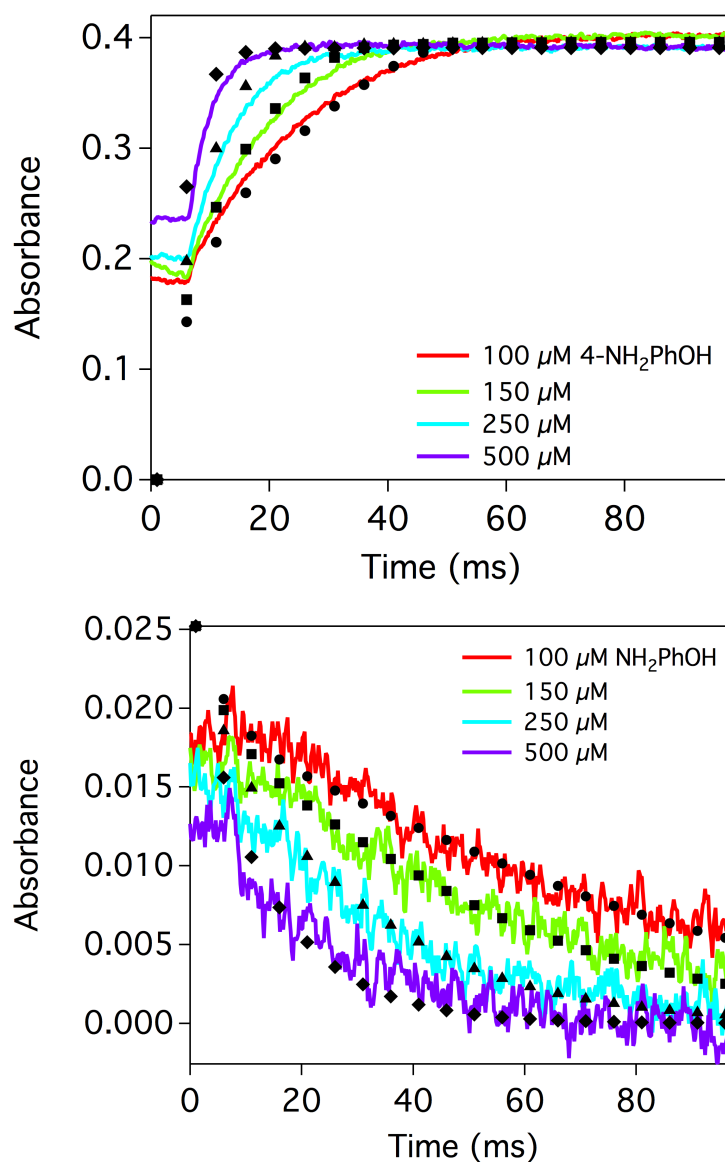


Figure 3.32. Stopped-flow kinetics traces monitoring (top) the appearance of TMP-7DMAQH⁺ at 450 nm and (bottom) the disappearance of Fc⁺ at 620 nm for the reaction between 100–500 μM NH₂PhOH, 60 μM Fc⁺, and 30 μM TMP-7DMAQ. Dotted lines represent the kinetics simulation based on the kinetics model described by Eq. 1–9. Rate constants used in the simulation: k_1 , $1.2 \times 10^5 \text{ M}^{-1} \text{ s}^{-1}$; k_2 , $7.5 \times 10^8 \text{ M}^{-1} \text{ s}^{-1}$; k_3 , $5.0 \times 10^5 \text{ M}^{-1} \text{ s}^{-1}$; k_4 , $3.0 \times 10^7 \text{ M}^{-1} \text{ s}^{-1}$; k_5 , $2.7 \times 10^3 \text{ M}^{-1} \text{ s}^{-1}$; k_{-5} , $3.0 \times 10^6 \text{ M}^{-1} \text{ s}^{-1}$; k_6 , $3.0 \times 10^6 \text{ M}^{-1} \text{ s}^{-1}$; k_7 , $1.0 \times 10^5 \text{ M}^{-1} \text{ s}^{-1}$; k_8 , $1.0 \times 10^5 \text{ M}^{-1} \text{ s}^{-1}$; k_9 , $1.4 \times 10^6 \text{ M}^{-1} \text{ s}^{-1}$; k_{-9} , $38.9 \text{ M}^{-1} \text{ s}^{-1}$.

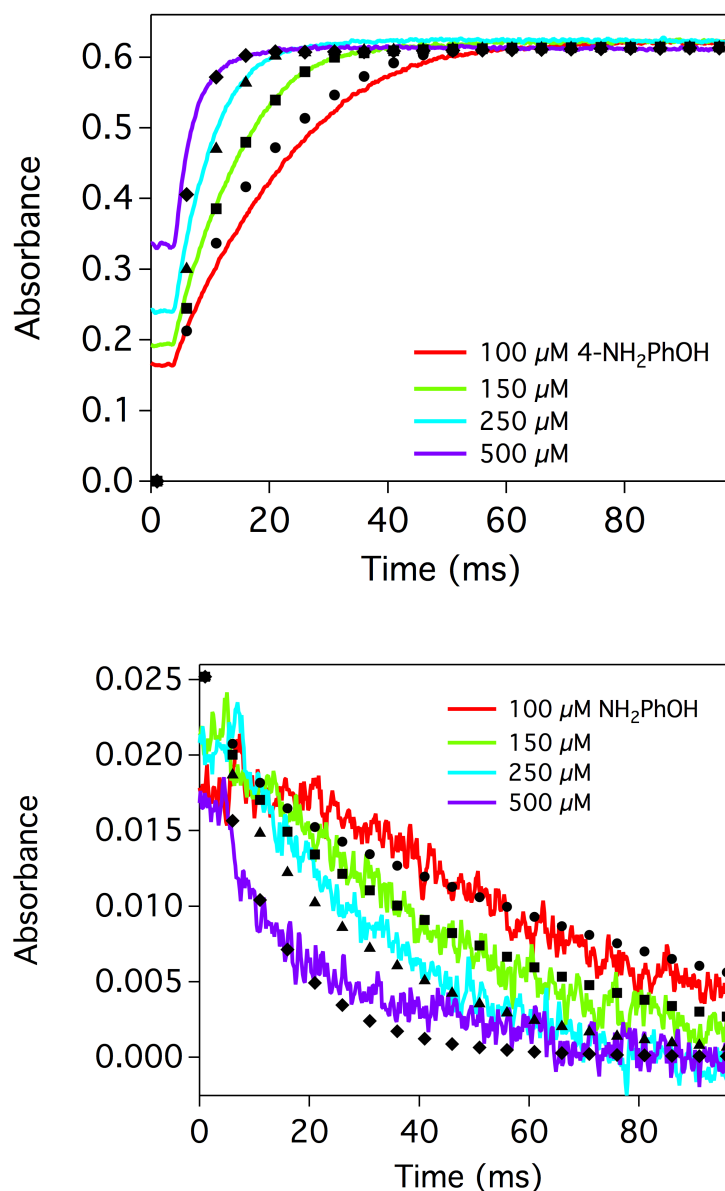


Figure 3.33. Stopped-flow kinetics traces monitoring (top) the appearance of MeO-7DMAQH⁺ at 460 nm and (bottom) the disappearance of Fc⁺ at 620 nm for the reaction between 100–500 μM NH₂PhOH, 60 μM Fc⁺, and 30 μM MeO-7DMAQ. Dotted lines represent the kinetics simulation based on the kinetics model described by Eq. 3.1 – 3.9. See Table 3.2 for rate constants used in the simulation.

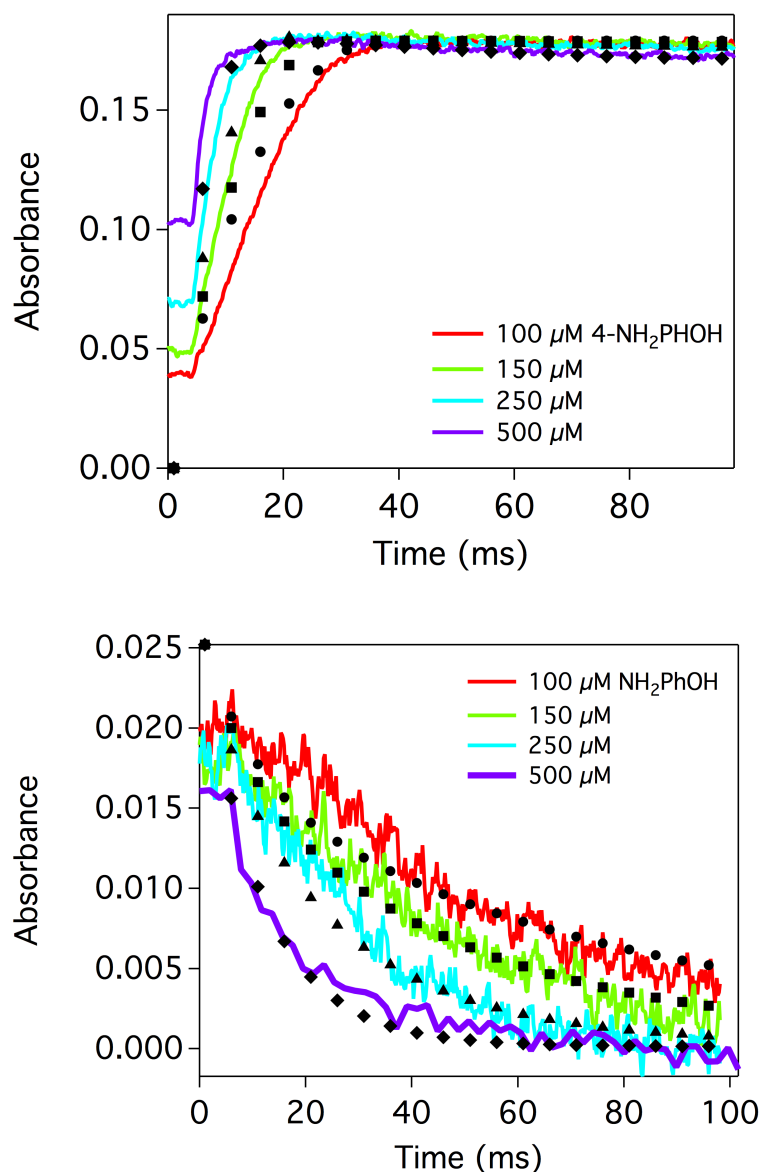


Figure 3.34. Stopped-flow kinetics traces monitoring (top) the appearance of H-7DMAQH^+ at 440 nm and (bottom) the disappearance of Fc^+ at 620 nm for the reaction between 100–500 μM NH_2PhOH , 60 μM Fc^+ , and 30 μM H-7DMAQ . Dotted lines represent the kinetics simulation based on the kinetics model described by Eq. 3.1 – 3.9. See Table 3.2 for rate constants used in the simulation.

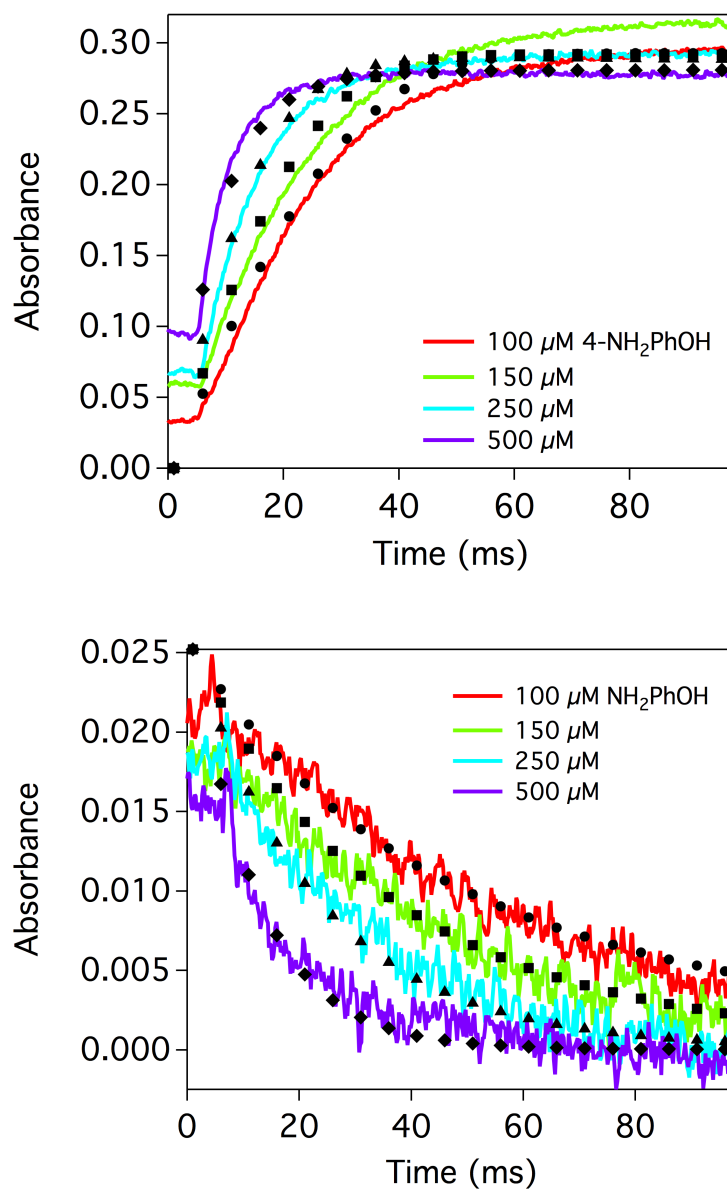


Figure 3.35. Stopped-flow kinetics traces monitoring (top) the appearance of Ph-7DMAQH⁺ at 460 nm and (bottom) the disappearance of Fc⁺ at 620 nm for the reaction between 100–500 μM NH₂PhOH, 60 μM Fc⁺, and 30 μM Ph-7DMAQ. Dotted lines represent the kinetics simulation based on the kinetics model described by Eq. 3.1 – 3.9. See Table 3.2 for rate constants used in the simulation.

Table 3.2. Rate constants determined through kinetic modeling.

Rate Constants	Phen-7DMAQ (M ⁻¹ s ⁻¹)	H-7DMAQ (M ⁻¹ s ⁻¹)	MeO-7DMAQ (M ⁻¹ s ⁻¹)	TMP-7DMAQ (M ⁻¹ s ⁻¹)
k_1	1.2×10^5	1.2×10^5	1.2×10^5	1.2×10^5
k_2	1.5×10^8	6.0×10^8	6.0×10^8	7.5×10^8
k_3	5.0×10^5	5.0×10^5	5.0×10^5	5.0×10^5
k_4	5.5×10^6	2.0×10^7	2.0×10^7	3.0×10^7
k_5	2.0×10^4	3.0×10^3	5.7×10^3	2.7×10^3
k_{-5}	1.0×10^6	1.0×10^6	3.0×10^6	3.0×10^6
k_6	3.0×10^6	3.0×10^6	3.0×10^6	3.0×10^6
k_7	1.0×10^5	1.0×10^5	1.0×10^5	1.0×10^5
k_8	1.0×10^5	1.0×10^5	1.0×10^5	1.0×10^5
k_9	3.0×10^5	1.2×10^6	1.0×10^6	1.4×10^6
k_{-9} (s ⁻¹)	6.7	5.7	16.1	38.9

To more closely examine the influence of individual rate constants on simulations of single-wavelength kinetics traces, the concentration profiles of individual reactants and intermediates underpinning the kinetics simulations were examined. In the studies described in this work, the concentration of Fc^+ is held constant (60 μM) while the initial concentrations of NH_2PhOH range from 100 – 500 μM . These near pseudo-first order conditions might suggest that all of the Fc^+ would be consumed through the oxidation of NH_2PhOH to $\text{NH}_2\text{PhOH}^{\bullet+}$, and thus the subsequent oxidation of $\text{NH}_2\text{PhO}^\bullet$ would not occur as the Fc^+ would rapidly decay to zero. However, concentration profiles of Fc^+ , NH_2PhOH , $\text{NH}_2\text{PhO}^\bullet$ and NHPhO show that with the rate constants determined from the kinetics simulations, Fc^+ is not immediately and completely consumed by reaction with NH_2PhOH ; $\text{NH}_2\text{PhO}^\bullet$ forms rapidly and Fc^+ oxidizes both NH_2PhOH and $\text{NH}_2\text{PhO}^\bullet$ on the ms timescale (Figure 3.36). Incorporating the oxidation of $\text{NH}_2\text{PhO}^\bullet$ by Fc^+ is critical for accurately describing the reaction of interest and obtaining good kinetics simulations.

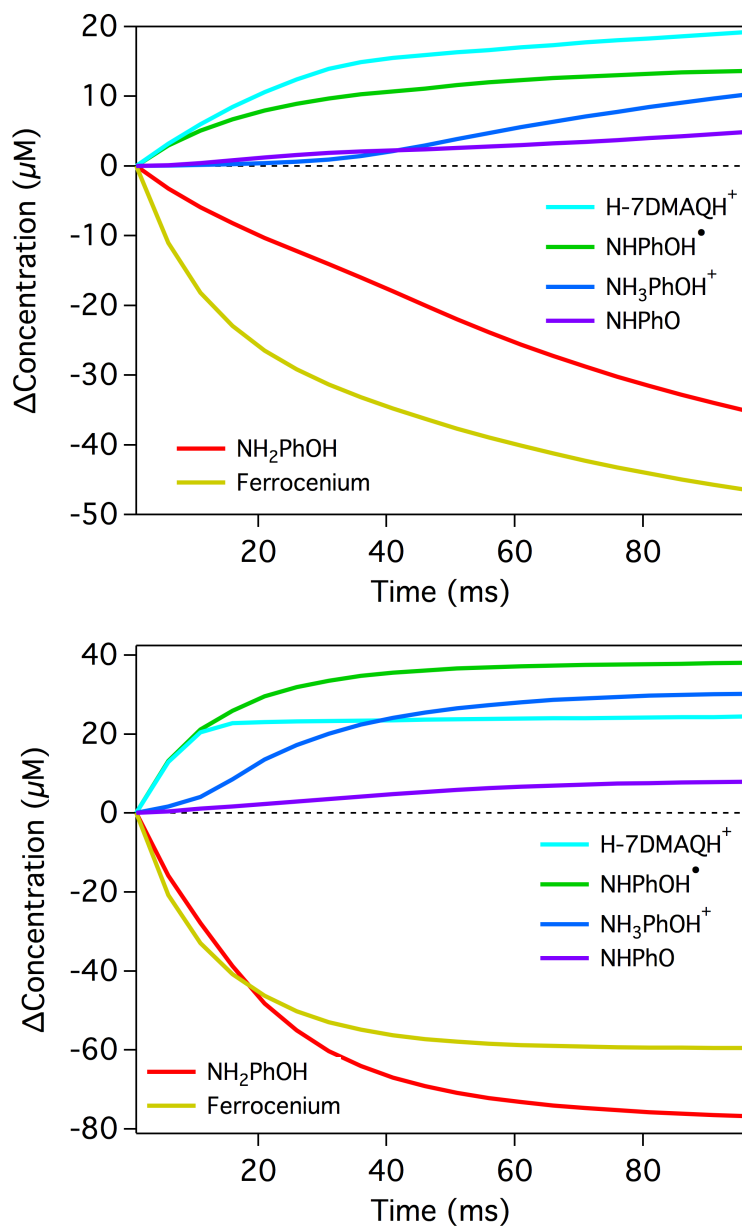


Figure 3.36. $\Delta\text{Concentration}$ profiles from simulated kinetic traces of NH_2PhOH , Fc^+ , $\text{NH}_2\text{PhO}^\bullet$, H-7DMAQ, NH_3PhOH^+ , and NHPhO . In both samples, initial concentrations were $60 \mu\text{M Fc}^+$ and $30 \mu\text{M H-7DMAQ}$. For the sample shown in the top panel, the initial concentration of NH_2PhOH was $100 \mu\text{M}$ while for the sample shown in the bottom panel had an initial concentration of $500 \mu\text{M NH}_2\text{PhOH}$. In both traces it is clear that Fc^+ (shown in green) is not rapidly and completely consumed by the first oxidation process. This is further evidence that the second oxidation (and subsequent proton transfer) does occur as described above. Note that NH_2PhOH reacts to form both $\text{NH}_2\text{PhO}^\bullet$ (and subsequently NHPhO) and NH_3PhOH^+ .

Driving Force Dependent Rate Constants for Proton Transfer

For the rate constants obtained from kinetics simulations for proton transfer from $\text{NH}_2\text{PhOH}^{\bullet+}$ (k_2) and NH_2PhO^+ (k_4) to R-7DMAQ, linear correlations are observed between $\ln(k_{\text{PT}})$ and the $\text{p}K_{\text{a}}$ values for the conjugate acids of the R-7DMAQ proton acceptors (Figure 6). While the two trend lines have identical slopes (slope = 1.65) their vertical offset reflects the difference in the unknown $\text{p}K_{\text{a}}$ values of $\text{NH}_2\text{PhOH}^{\bullet+}$ and NH_2PhO^+ . As such, the $\text{p}K_{\text{a}}$ values on the x-axis only linearly correlate with $-\Delta G_{\text{PT}}$ within each set of data.³ The free energy relationships observed are consistent with what is predicted by the Brønsted relation for acid-base reactivity, as well as theory developed by Bell based on the transition state model.^{41,67–69} Indeed, linear correlations between rate and driving force have been observed in many examples of proton transfer, and Brønsted slopes have been traditionally used to characterize reaction mechanisms and compare proton transfer processes.^{33,34,41–43,67,69–73}

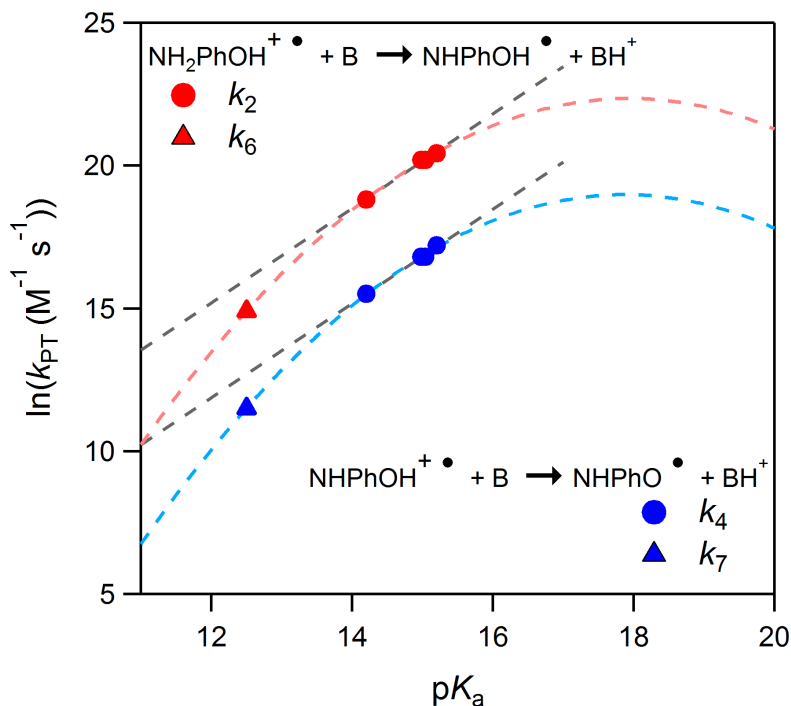


Figure 3.37. For proton transfer reactions from aminophenol oxidation products, free energy relationships are observed between the rate constants and the pK_a value for the conjugate acid of the proton acceptor, which is proportional to the driving force for proton transfer within each set of reactions. Included on this plot are the values for k_2 and k_4 , the rates of PT to R-7DMAQ derivatives (●, $pK_a(\text{R-7DMAQH}^+) = 14.2\text{--}15.2$), as well as k_6 and k_7 , the rates of PT to NH_2PhOH (▲, $pK_a(\text{NH}_3\text{PhOH}^+) = 12.5$). Across the R-7DMAQ derivatives, linear free energy relationships (gray dashed lines) are observed for proton transfer from $\text{NH}_2\text{PhOH}^{\bullet+}$ (slope = 1.66) and from $\text{NH}_2\text{PhO}^{\bullet+}$ (slope = 1.65). Including proton transfer from these radical cations to NH_2PhOH , the data fit best to a quadratic relationship (blue and red dashed lines).

When the rate constants for proton transfer from $\text{NH}_2\text{PhOH}^{\bullet+}$ (k_6) and $\text{NH}_2\text{PhO}^{\bullet+}$ (k_7) to NH_2PhOH are added to the plot ($pK_a(\text{NH}_3\text{PhOH}^+) = 12.5$), these data points fall off the linear trend lines defined by the four R-7DMAQ bases, lending distinct curvature to the $\ln(k_{\text{PT}})$ – pK_a relationship (Figure 3.37). While NH_2PhOH is a structurally distinct base from the R-7DMAQ class of compounds, examples of free energy relationships in proton transfer reactions involving nitrogen and oxygen acids and bases have been shown to hold across a range of proton donors/acceptors.⁷⁴ The data sets (k_2 and k_6 , k_4 and k_7) fit well to parabolas,

consistent with the quadratic correlation between ΔG^\ddagger (the free energy of activation) and $-\Delta G_{PT}$ predicted by Marcus for proton transfer reactions.^{41,67,69,75,76} In this context, the linear relation observed for proton transfer to the R-7DMAQ bases could simply result from the small ΔpK_a range that these data points span, across which the higher order terms of the quadratic can be neglected to give an apparent linear relationship for $d\Delta G^\ddagger/d\Delta G_{PT}$.^{31,69,77} While parabolic free energy relationships have long been theorized for proton transfer,^{75,76,78,79} limited experimental examples revealing these relationships are available, especially in either non-aqueous solvents or as part of a PCET process.^{69,74,76,80} Unfortunately, the system studied in this work limits the range of driving forces that can be examined, preventing a more definitive assessment of the free energy relationship for proton transfer. Nevertheless, these data enhance our understanding of free energy relationships for proton transfer processes in PCET reactions.

3.4. Conclusions

Utilizing a series of 7-dimethylamino quinoline derivatives as photometric bases, both the PT and ET components of the PCET oxidation of NH_2PhOH were optically monitored upon rapid-mixing via stopped-flow. Analysis of this complex multi-electron, multi-proton reaction was enabled by spectroscopic handles for both proton transfer and electron transfer. A comprehensive kinetics model was constructed, from which rate constants for elementary reaction steps were determined. These data reveal free energy relationships between PT rate constants and the pK_a values for the conjugate acids of the proton acceptors over the driving force range examined that suggest a Marcus relationship for proton transfer. Notably, linear free energy relationships for PT components of PCET reactions have recently been reported by our group for elementary proton transfer steps

involved in hydrogen evolution catalyzed by transition metal complexes.^{33,34} Taken together, these experimentally determined relationships enhance our understanding of PT processes in PCET reactions, and provide a framework to continue studying these types of reactions in a more comprehensive fashion.

3.5. Experimental Details

All solutions for electrochemical and stopped-flow analyses were prepared in a nitrogen-filled glovebox. The acetonitrile used (Fisher Scientific, HPLC, >99.9%) was degassed with argon and dried with a Pure Process Technology Solvent System. Reagents were purchased from Sigma Aldrich with the exception of 3,4-dimethoxyphenylboronic acid (VWR), 3,5-bis(trifluoromethyl)phenylboronic acid (Matrix), and phenylboronic acid (Chem-Impex). 2-picoline, tetrafluoroboric acid diethyl ether complex, and aniline were degassed via the freeze-pump-thaw method (3+ cycles) and stored under inert atmosphere. UV-vis spectra were collected on an Agilent Cary 60 spectrometer. Spectrophotometric titrations were carried out in a nitrogen-filled glovebox using fiber optics that feed through the glovebox and couple to the Cary 60 spectrometer. Molar extinction coefficients were determined spectroscopically using the Cary 60 Spectrometer and the Beer-Lambert relationship. Mass spectrometry was carried out with a LTQ FT (ICR 7T) (ThermoFisher, Bremen, Germany) mass spectrometer. Measurements were made on complexes dissolved in methanol. Samples were introduced via a microelectrospray source at a flow rate of 3 $\mu\text{L}/\text{min}$. Xcalibur (ThermoFisher, Bremen, Germany) was used to analyze the data.

Synthesis of 7-dimethylaminoquinoline Derivatives

7-dimethylaminoquinoline (H-7DMAQ)

Unsubstituted 7-dimethylaminoquinoline (H-7DMAQ) was obtained via Skraup reaction as described by Picken⁸¹ with a modification from Ozerov.⁸² 1.0 g (4.8 mmol) 3-(N,N-dimethylamino)aniline dihydrochloride was dissolved in 10 mL of H_2O and to it 20 mL of 1.0 M sodium hydroxide was added. Dichloromethane (4 x 25 mL) was used to extract the basic aniline, and the combined organic layers were concentrated in vacuo to a brown oil in a

round bottom flask. Glycerol (0.5 mL, 6.8 mmol) and sodium iodide (1.08 g, 7.2 mmol) were added. The reaction flask was put on ice and concentrated sulfuric acid (2.7 mL) was added dropwise. The mixture was heated to reflux (140° - 150° C) for a period of 3 hours. After cooling, equal volumes (40 mL) of H₂O and CH₂Cl₂ were used to transfer the mixture to a 250 mL Erlenmeyer flask. The Erlenmeyer flask was placed in an ice bath, and the mixture was basified with aqueous sodium hydroxide (1.0 M) until pH paper confirmed the solution was alkaline. Sodium sulfite was added to quench any remaining I₂, and the reaction mixture was filtered. CH₂Cl₂ (4 x 25 mL) was used to extract the organic product. The organic layer was dried (MgSO₄), filtered, concentrated to an oil, and purified on silica gel (eluent, chloroform/methanol 99.5/0.5 to 95/5) yielding H-7DMAQ as a yellow oil (0.39 g, 47% yield). ¹H NMR (400 MHz, CDCl₃) δ (ppm): 8.74 (d, 1H), 7.96 (d, 1H), 7.64 (d, 1H), 7.19 (dd, 1H), 7.16 (d, 1H), 7.10 (dd, 1H), 3.10 (s, 6H, s).

General Procedures for Aryl-Substituted 2,4-R-7-dimethylaminoquinoline derivatives

The four aryl-substituted 2,4-R-7-dimethylaminoquinoline derivatives (R-7DMAQ) were synthesized in three steps.

2,4-Dihydroxy-7-dimethylaminoquinoline

The synthesis of 2,4-dihydroxy-7-dimethylaminoquinoline was adapted from Knierzinger and Wolfbeis.⁸³ 3-(N,N-dimethylamino)aniline dihydrochloride (2.0 g, 9.6 mmol) was dissolved in 10 mL of H₂O and to it 40 mL of 1.0 M sodium hydroxide was added. The solution was poured into a separation funnel and CH₂Cl₂ (4 x 50 mL) was used to extract the basic aniline. The combined organic layers were concentrated in vacuo. Diethylmalonate (1.5 mL, 9.6 mmol) was added to the round bottom containing the aniline, a Dean-Stark apparatus was fitted to the flask (to distill off ethanol produced *in situ*), and the

mixture was refluxed between 180-200°C for three hours. Upon cooling, grayish solids were left behind in the reaction flask. The solids were transferred to a Buchner funnel and washed thoroughly with H₂O. Solids retained by the funnel were placed in a beaker and stirred with acetone. This mixture was then filtered, and the resulting solids collected are 2,4-dihydroxy-7-dimethylaminoquinoline (2,4-OH-7DMAQ) (1.4 g, 75% yield). ¹H NMR (400 MHz, CD₂Cl₂) δ (ppm): 10.83 (s, 1H, -OH), 10.70 (s, 1H, -OH), 7.54 (d, 1H, Ar-H), 6.60 (dd, 1H, Ar-H), 6.40 (d, 1H, Ar-H), 5.42 (s, 1H, Ar-H), 2.95 (s, 6H, CH₃).

2,4-Dibromo-7-dimethylaminoquinoline

The synthesis of 2,4-dibromo-7-dimethylaminoquinoline (2,4-Br-7DMAQ) was adapted from Janin *et al.*⁸⁴ To a round bottom containing a teflon-coated stir bar, 2,4-OH-7DMAQ (1.0 g, 4.9 mmol), POBr₃ (7.0 g, 24.5 mmol) and K₂CO₃ (2.0 g, 14.7 mmol) were added. This mixture was dissolved in dry acetonitrile (60 mL) and refluxed for three hours at 80°C. After the mixture cooled, water was slowly added to the reaction vessel until the solution stopped bubbling. Aqueous sodium hydroxide (2 M) was then added until the solution reached neutral pH and a precipitate formed. CH₂Cl₂ (4 x 50 mL) was then used to extract the organic product. A simple silica column with CH₂Cl₂ mobile phase separated the product mixture (typically the second yellow band to elute). 2,4-Br-7DMAQ was obtained as a green-yellow crystalline powder (0.53 g, 33%). ¹H NMR (400 MHz, CD₂Cl₂) δ (ppm): 7.89 (d, 1H, Ar-H), 7.44 (s, 1H, Ar-H), 7.14 (dd, 1H, Ar-H), 6.99 (d, 1H, Ar-H), 3.09 (s, 6H, CH₃).

2,4-R-7-dimethylaminoquinoline

The procedure for the Suzuki coupling of 2,4-dibromo-7-dimethylaminoquinoline with aryl-boronic acid to yield aryl-substituted 2,4-R-7-dimethylaminoquinoline (R-7DMAQ) was adapted from Watanabe⁸⁵ and Suzuki.⁸⁶ In a nitrogen-filled glove box, 2,4-Br-7-DMAQ (1 eq), an aryl boronic acid (2.2 eq), Pd(PPh₃)₄ (0.04 equiv.), and a teflon-coated stir bar were added to a Schlenk flask. The flask was removed from the glovebox in a sealed vessel and placed under nitrogen flow on a Schlenk line. Ba(OH)₂ (3 equiv.) was degassed and cannula transferred to the Schlenk flask along with a mixture of degassed dimethoxyethane/H₂O (4:1, also added via cannula transfer). The mixture was refluxed at 85°C under a N₂ atmosphere for 48 hours. Upon cooling of the reaction mixture, water was added to the flask to aid in transfer to a separatory funnel. The mixture was then extracted with CH₂Cl₂ and purified further using column chromatography. These details, along with further characterization for each R-7DMAQ, are included in the Supporting Information.

Stopped-Flow Experiments

Stopped-Flow rapid mixing experiments were performed on a HI-TECH SF-61DX2 double-mixing stopped-flow spectrophotometer in single mixing mode with Kinetic Studio data acquisition software (v2.33). For single wavelength kinetics measurements, a tungsten light source and dual-beam photomultiplier tube (Hamamatsu R928) were used. For spectral analysis, a xenon light source and single-beam photodiode array were used. Stopped-flow measurements were all performed under a nitrogen atmosphere. Samples were prepared inside of an inert-atmosphere glovebox in septum-sealed bottles. PEEK tubing was used to transfer solutions directly from sealed bottles to the stopped-flow syringes. To ensure purity of samples analyzed, each syringe was purged three times prior to each measurement. In a typical experiment, one syringe was loaded with ferrocenium hexafluorophosphate (60 μM)

while the other was loaded with R-7DMAQ (30 μM) and varying concentrations of NH_2PhOH (100-500 μM). Upon injection, absorbance vs. time was monitored at various wavelengths for kinetics traces. Fitting of the data was carried out in MATLAB (The MathWorks, Inc.) and is described elsewhere in the text.

Electrochemistry

All electrochemical measurements were performed in a nitrogen-filled glovebox, using electrode leads that were fed through a custom port and connected to a Pine Instruments WaveDriver potentiostat. A three-electrode cell was used for all experiments, utilizing platinum working electrodes, a glassy carbon counter electrode (CH Instruments, 3 mm diameter), and a silver wire pseudo-reference that had been immersed in a glass tube fitted with a porous Vycor tip and filled with a 0.25 M $[\text{Bu}_4\text{N}][\text{PF}_6]$ acetonitrile solution. The glassy carbon electrodes were polished using a Milli-Q water slurry of 0.05 micron polishing powder (CH instruments, containing no agglomerating agents), rinsed and sonicated in Milli-Q water, and rinsed with acetone. Working electrodes were electrochemically pretreated with two cyclic scans between 1.5 and -2.5 V at 200 mV/s in 0.25 mM $[\text{Bu}_4\text{N}][\text{PF}_6]$ solution. Background voltammograms of electrolyte-only solutions were collected for every electrode at the appropriate scan rate. All voltammograms were recorded in 0.25 M $[\text{Bu}_4\text{N}][\text{PF}_6]$ acetonitrile solutions and internally referenced to ferrocene.

Spectrophotometric Titrations

The pK_a of each of the R-7DMAQs in acetonitrile was determined by spectrophotometric titration. First, an acetonitrile solution of each R-7DMAQ was prepared

and an absorbance spectrum recorded. One equivalent of $\text{HBF}_4 \cdot \text{Et}_2\text{O}$ was then added to form R-7DMAQH^+ *in situ*, and another spectrum recorded. 2-picoline ($\text{pK}_a = 13.32$) was titrated into the R-7DMAQH^+ solution, and the change in absorbance was monitored by UV-vis spectroscopy. Concentrations of R-7DMAQH^+ , R-7DMAQ , and 2-picoline were calculated based on the absorption of R-7DMAQH^+ and the initial concentration of each reagent. Linear regression plots (shown below) were used to determine the pK_a of each R-7DMAQ .^{7,17}

Quantification of Equilibria and Rate Constants

The proton transfer equilibrium existing between R-7DMAQH^+ and NH_2PhOH in CH_3CN was investigated spectroscopically. An acetonitrile solution of each R-7DMAQH^+ was prepared by adding one equivalent of $\text{HBF}_4 \cdot \text{Et}_2\text{O}$ to R-7DMAQ and an absorbance spectrum recorded. NH_2PhOH was titrated into the R-7DMAQH^+ solution, and the change in absorbance was monitored by UV-vis absorbance spectroscopy after each successive addition. Concentrations of each species in solution were calculated based on the change in absorption of R-7DMAQH^+ and the initial concentrations of each reagent. Plotting $([\text{R-7DMAQ}] * [\text{NH}_3\text{PhOH}^+]) / [\text{R-7DMAQH}^+]$ versus $[\text{NH}_2\text{PhOH}]$ should give a straight line with a slope equal to K_{eq} for this interaction. The pK_a of $\text{R-7DMAQH}^+ + \log(K_{\text{eq}})$ then provides the pK_a of NH_3PhOH^+ .^{7,17}

Modified Benesi-Hildebrand Analysis

In order to determine the equilibrium constant for the associated of R-7DMAQ with Fc^+ , a modified Benesi-Hildebrand analysis was performed. The Benesi-Hildebrand method requires that one of the species be present in large excess, however, these conditions are not possible for this system. The analysis described below was modified from the original report,⁸⁷ and this modified equation has been previously utilized.⁶⁴ Equation S1 is a

rearrangement of the equilibrium expression (Equation 3.9), solved for the concentration of adduct, $[R-7DMAQ \cdots Fc^+]$. $R-7DMAQ_0$ is the initial concentration of R-7DMAQ in solution, Fc_0^+ is the concentration of ferrocenium added, and K_{obs} is the equilibrium constant for adduction (k_9/k_{-9}). Equation 3.10 allows the Benesi-Hildebrand equation to be rearranged per Equation 3.11. ΔA is the change in absorbance at a given wavelength, $\Delta \epsilon$ describes the difference in extinction coefficients between the adducted and free R-7DMAQ at the observed wavelength, and l represents the pathlength (1 cm in this analysis). The change in absorbance of R-7DMAQ (in this case, a new peak appears at lower energies than the R-7DMAQ absorbance) was monitored as a function of added Fc^+ , and the resulting data was plotted as ΔAbs vs. Total $[Fc^+]$ added. The data was then fit to Equation 3.11, substituting in Equation 3.10 for $[Fc^+ \cdots R-7DMAQ]$, leaving both K_{obs} and $\Delta \epsilon$ to float. Values for K_{eq} and $\Delta \epsilon$ are reported and discussed in Section 3.3.

Equation 3.10

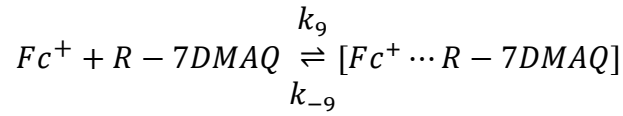
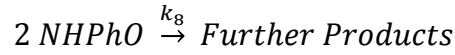
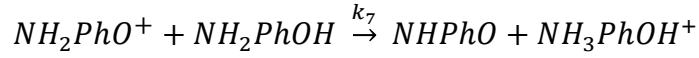
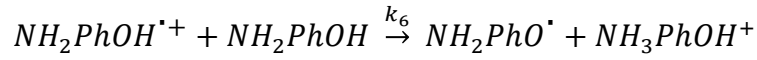
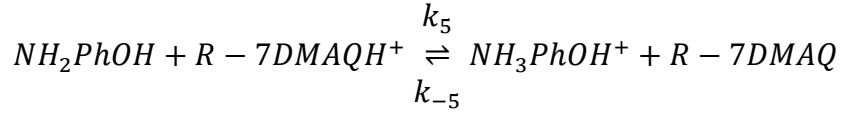
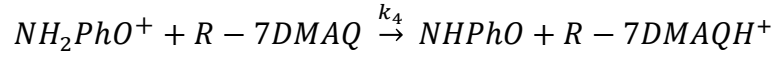
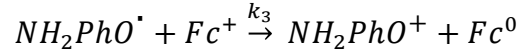
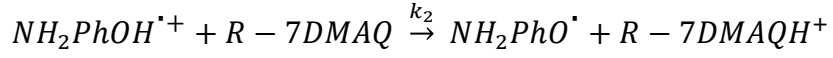
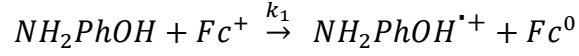
$$\begin{aligned}
 & [Fc^+ \cdots R-7DMAQ] \\
 &= \frac{1}{2} \left(Fc_0^+ + R-7DMAQ_0 + \frac{1}{K_{obs}} \right) \\
 &\pm \sqrt{\frac{1}{4} (Fc_0^+ + R-7DMAQ_0 + \frac{1}{K_{obs}})^2 - (Fc_0^+ * R-7DMAQ_0)}
 \end{aligned}$$

Equation 3.11

$$\Delta Abs = l \Delta \epsilon [Fc^+ \cdots R-7DMAQ]$$

3.6.Details of Kinetics Modeling

Detailed Kinetics Model



Differential equations employed for kinetic models

$$\begin{aligned}
\frac{d[NH_2PhOH]}{dt} &= -k_1[NH_2PhOH][Fc^+] - k_5[NH_2PhOH][R7DMAQH^+] \\
&\quad + k_{-5}[R7DMAQ][NH_3PhOH^+] - k_6[NH_2PhOH][NH_2PhOH^{+■}] \\
&\quad - k_7[NH_2PhOH][NHPHOH^{+■}] \\
\frac{d[Fc^+]}{dt} &= -k_1[NH_2PhOH][Fc^+] - k_3[Fc^+][NHPHOH] - k_9[Fc^+][R7DMAQ] + k_{-9}[Fc^+ \\
&\quad - R7DMAQ] \\
\frac{d[NH_2PhOH^{+■}]}{dt} &= k_1[NH_2PhOH][Fc^+] - k_2[NH_2PhOH^{+■}][R7DMAQ] \\
&\quad - k_6[NH_2PhOH][NH_2PhOH^{+■}] \\
\frac{d[Fc^0]}{dt} &= k_1[NH_2PhOH][Fc^+] + k_3[Fc^+][NHPHOH] \\
\frac{d[R7DMAQ]}{dt} &= -k_2[NH_2PhOH^{+■}][R7DMAQ] - k_4[NHPHOH^{+■}][R7DMAQ] \\
&\quad + k_5[NH_2PhOH][R7DMAQH^+] - k_{-5}[R7DMAQ][NH_3PhOH^+] \\
&\quad - k_9[Fc^+][R7DMAQ] + k_{-9}[Fc^+ - R7DMAQ] \\
\frac{d[NHPHOH]}{dt} &= k_2[NH_2PhOH^{+■}][R7DMAQ] - k_3[Fc^+][NHPHOH] \\
&\quad + k_6[NH_2PhOH][NH_2PhOH^{+■}] \\
\frac{d[R7DMAQH^+]}{dt} &= k_2[NH_2PhOH^{+■}][R7DMAQ] + k_4[NHPHOH^{+■}][R7DMAQ] \\
&\quad - k_5[NH_2PhOH][R7DMAQH^+] + k_{-5}[R7DMAQ][NH_2PhOH^+] \\
\frac{d[NHPHOH^{+■}]}{dt} &= k_3[Fc^+][NHPHOH] - k_4[R7DMAQ][NHPHOH^{+■}] \\
&\quad - k_7[NH_2PhOH][NHPHOH^{+■}] \\
\frac{d[NHPHO]}{dt} &= k_4[R7DMAQ][NHPHOH^{+■}] + k_7[NH_2PhOH][NHPHOH^{+■}] \\
&\quad - k_8[NHPHO][NHPHO] \\
\frac{d[Fc^+ - R7DMAQ]}{dt} &= k_9[Fc^+][R7DMAQ] - k_{-9}[Fc^+ - R7DMAQ]
\end{aligned}$$

$$\frac{d[\textit{Further Products}]}{dt} = k_8[\textit{NHPhO}][\textit{NHPhO}]$$

To simulate the kinetics traces, this series of differential equations was solved numerically with an ordinary differential equations solver. We utilized ode23 in MATLAB. The details of the simulations and the MATLAB *.m files employed are provided below.

*Note that the rate constants described below are not numbered in the same fashion as described above and in the main text. More specifically, the equilibrium expressions are not in the same order as above, and the forward and reverse steps for these expressions are also given individual numbers (i.e. k_5 and k_6 instead of $k_{5/-5}$). Please refer to the annotations below (in green) for an accurate description of each of the reagents and rate constants used in this analysis.

Input needed to complete simulated fits:

Timescale: logtimespan = [0.001:0.005:0.1]; timespan = logtimespan;

Molar extinction coefficients for DMAQ, Fc^+ -DMAQ adduct, and Fc^+ :

epsDMAQ = X; X = 6000, 9800, 13200, or 20500 depending on the DMAQ being modeled

epsFcDMAQ = X; X = 6000, 9800, 13200, or 20500 depending on the DMAQ being modeled

epsFc = 420;

Vector defining rate constants $k_I - k_{II}$: k = [k_1 ; k_2 ; k_3 ; k_4 ; k_5 ; k_6 ; k_7 ; k_8 ; k_9 ; k_{10} ; k_{11}];

Vector defining initial concentrations of all reactants, intermediates, and products: $y_0 = [\text{NH}_2\text{PhOH}; \text{Fc}^+; \text{NH}_2\text{PhOH radical cation}; \text{Fc}^0; \text{R-7DMAQ}; \text{NHPhOH}; \text{R-7DMAQH}^+; \text{NHPhOH radical cation}; \text{NHPhO}; \text{Fc}^+-\text{DMAQ}; \text{NH}_3\text{PhOH}^+; \text{product of } 2\text{NHPhO}]$; this typically would be entered as $y_0 = [x; 60\text{e-}6; 0; 0; 30\text{e-}6; 0; 0; 0; 0; 0; 0; 0]$; where $x = 100\text{-}500\text{e-}6$ depending on the concentration of NH_2PhOH being modeled.

StepWise_ECEC_v2(t,y,k) (script below) describes the various rate expressions associated with kinetics of the reactions described in Scheme S2. $y(x)$ values represent concentrations, and $k(x)$ values represent rate constants.

```
function [yprime] = StepWise_ECEC_v2(t,y,k)

%y(1) = NH2PhOH
%y(2) = Fc+
%y(3) = NH2PhOHradcat
%y(4) = Fc0
%y(5) = R-7DMAQ
%y(6) = NHPhOH
%y(7) = R-7DMAQH+
%y(8) = NHPhOHradcat
%y(9) = NHPhO
%y(10) = Fc+-DMAQ
%y(11) = NH3PhOH+
%y(12) = Product of 2 NHPhO

%k(1) = rate of ET from NH2PhOH to Fc+
%k(2) = rate of PT from NH2PhOHradcat to R-7DMAQ
%k(3) = rate of ET from NHPhOH to Fc+
```

%k(4) = rate of PT from NHPHOHradcat to R-7DMAQ

%k(5) = forward equilibrium for Fc+-DMAQ adduct

%k(6) = reverse equilibrium for Fc+-DMAQ adduct

%k(7) = rate of PT from NH₂PhOHradcat to NH₂PhOH

%k(8) = rate of PT from NHPHOHradcat to NH₂PhOH

%k(9) = forward equilibrium of PT from R-7DMAQH⁺ to NH₂PhOH

%k(10) = reverse equilibrium of PT from R-7DMAQH⁺ to NH₂PhOH

%k(11) = further product formation

%d[NH₂PhOH]/dt

yprime(1) = -k(1).*y(1).*y(2) - k(7).*y(1).*y(3) - k(8).*y(1).*y(8) - k(9).*y(1).*y(7) + k(10).*y(5).*y(11);

%d[Fc⁺]/dt

yprime (2) = -k(1).*y(1).*y(2)- k(3).*y(2).*y(6) - k(5).*y(2).*y(5) + k(6).*y(10);

%d[NH₂PhOHradcat]/dt

yprime(3) = k(1).*y(1).*y(2) - k(2).*y(3).*y(5) - k(7).*y(1).*y(3);

%d[Fc⁰]/dt

yprime(4) = k(1).*y(1).*y(2) + k(3).*y(2).*y(6);

%[R-7DMAQ]/dt

yprime(5) = -k(2).*y(3).*y(5) - k(4).*y(5).*y(8) - k(5).*y(2).*y(5) + k(6).*y(10) + k(9).*y(1).*y(7) -
k(10).*y(5).*y(11);

%[NHPHOH]/dt

yprime(6) = k(2).*y(3).*y(5) - k(3).*y(2).*y(6) + k(7).*y(1).*y(3);

%[R-7DMAQH⁺]/dt

yprime(7) = k(2).*y(3).*y(5) + k(4).*y(5).*y(8) - k(9).*y(1).*y(7) + k(10).*y(5).*y(11);

%[NHPHOH]/dt

```

yprime(8) = k(3).*y(2).*y(6) - k(4).*y(5).*y(8) - k(8).*y(1).*y(8);
%[NHPhO]/dt
yprime(9) = k(4).*y(5).*y(8) + k(8).*y(1).*y(8)-k(11).*y(9).*y(9);
%[Fc-DMAQ]/dt
yprime(10) = k(5).*y(2).*y(5) - k(6).*y(10);
%[NH3PhOH+]/dt
yprime(11) = k(7).*y(1).*y(3) + k(8).*y(1).*y(8) + k(9).*y(1).*y(7) - k(10).*y(5).*y(11);
%[FurtherProds]/dt
yprime(12) = k(11).*y(9).*y(9);

yprime=yprime(:);

```

PT Kinetics (440-460 nm)

Solver_StepWise_ECEC_v2.m (script below) is used to numerically solve the differential equations provided in StepWise_ECEC_v2.m based on the initial value inputs. The time-dependent concentration profiles for each species are multiplied by the appropriate molar absorptivity coefficients at the wavelength of interest (440-460 depending on the R-7DMAQ being analyzed) and the optical pathlength (1 cm). These absorbance values are summed to generate the simulated stopped-flow traces, which are then plotted and compared to experimental data.

```

[Tcalc,Ycalc]=ode23s(@(t,y)StepWise_ECEC_v2(t,y,k),timespan,y0);
%Differential equation solver used to compute a simulated concentration
%profile based on the differential equations describing the electron
%transfer reactions

```

```
dOD_calc_460=(Ycalc(:,7)*epsDMAQ + Ycalc(:,10)*epsFcDMAQ);
%+Ycalc(:,9)*epsFcDMAQ);
%converts calculated concentration profile into a simulated SF spectrum by
%the vector of epsilon values
%dOD_calc_460 is used for the data at 460 nm with DP7DMAQ
```

```
plot(Tcalc,dOD_calc_460,'ko');
hold on;
```

ET Kinetics (620 nm)

Solver_StepWise_Fc_ECEC_v2.m (script below) is used to numerically solve the differential equations provided in StepWise_ECEC_v2.m based on the initial value inputs. The time-dependent concentration profiles for each experiment are multiplied by the appropriate molar absorptivity coefficient (at 620 nm) and the optical pathlength (1 cm). This absorbance value is used to generate simulated stopped-flow spectra, which are then plotted and compared to experimental data.

```
[Tcalc,Ycalc]=ode23s(@ (t,y)StepWise_ECEC_v2(t,y,k),timespan,y0);
%Differential equation solver used to compute a simulated concentration
%profile based on the differential equations describing the electron
%transfer reactions
```

```
dOD_calc_620=(Ycalc(:,2)*epsFc);
%converts calculated concentration profile into a simulated SF spectrum by
%the vector of epsilon values
%dOD_calc_460 is used for the data at 460 nm with DP7DMAQ
```

```
plot(Tcalc,dOD_calc_620,'ko');  
hold on;
```

REFERENCES

- (1) Weinberg, D. R.; Gagliardi, C. J.; Hull, J. F.; Murphy, C. F.; Kent, C. a; Westlake, B. C.; Paul, A.; Ess, D. H.; McCafferty, D. G.; Meyer, T. J. *Chem. Rev.* **2012**, *112* (7), 4016.
- (2) Costentin, C.; Robert, M.; Savéant, J.-M. *Chem. Soc. Rev.* **2010**, *110*.
- (3) Warren, J. J.; Tronic, T. A.; Mayer, J. M. *Chem. Rev.* **2010**, *110*, 6961.
- (4) Kretchmer, J. S.; Miller, T. F. *Inorg. Chem.* **2016**, *55*, 1022.
- (5) Manner, V. W.; Dipasquale, A. G.; Mayer, J. M. *J. Am. Chem. Soc.* **2008**, *130*, 7210.
- (6) Markle, T. F.; Rhile, I. J.; Mayer, J. M. *J. Am. Chem. Soc.* **2011**, *133*, 17341.
- (7) Saouma, C. T.; Kaminsky, W.; Mayer, J. M. *J. Am. Chem. Soc.* **2012**, *134*, 10.
- (8) Warren, J. J.; Mayer, J. M. *J. Am. Chem. Soc.* **2008**, *130* (9), 2774.
- (9) Bourrez, M.; Steinmetz, R.; Ott, S.; Gloaguen, F.; Hammarström, L. *Nat. Chem.* **2015**, *7* (2), 140.
- (10) Zhang, M.-T.; Hammarström, L. *J. Am. Chem. Soc.* **2011**, *133* (23), 8806.
- (11) Sjödin, M.; Irebo, T.; Utas, J. E.; Lind, J.; Merényi, G.; Akermark, B.; Hammarström, L. *J. Am. Chem. Soc.* **2006**, *128* (40), 13076.
- (12) Johannissen, L. O.; Irebo, T.; Sjödin, M.; Johansson, O.; Hammarström, L. *J. Phys. Chem. B* **2009**, *113* (50), 16214.
- (13) Gagliardi, C. J.; Westlake, B. C.; Kent, C. A.; Paul, J. J.; Papanikolas, J. M.; Meyer, T. J. *Coord. Chem. Rev.* **2010**, *254* (21-22), 2459.
- (14) Bronner, C.; Wenger, O. S. *Inorg. Chem.* **2012**, *51* (15), 8275.
- (15) Kuss-Petermann, M.; Wolf, H.; Stalke, D.; Wenger, O. S. *J. Am. Chem. Soc.* **2012**, *134* (30), 12844.
- (16) Wenger, O. S. *Acc. Chem. Res.* **2013**, *46* (7), 1517.
- (17) Eisenhart, T. T.; Dempsey, J. L. *J. Am. Chem. Soc.* **2014**, *136* (35), 12221.
- (18) Costentin, C.; Drouet, S. *J. Am. Chem. Soc.* **2013**, *135*, 9023-9031.
- (19) Costentin, C.; Hajj, V.; Louault, C.; Robert, M.; Savéant, J.-M. *J. Am. Chem. Soc.* **2011**, *133* (47), 19160.

- (20) Savéant, J.-M. *Energy Environ. Sci.* **2012**, 5 (7), 7718.
- (21) Costentin, C.; Robert, M.; Savéant, J.-M.; Teillout, A.-L. *Proc. Natl. Acad. Sci. U. S. A.* **2009**, 106 (29), 11829.
- (22) Kombarova, S. V.; Il'ichev, Y. V. *Langmuir* **2004**, 20 (15), 6158.
- (23) Mohammed, O. F.; Pines, D.; Pines, E.; Nibbering, E. T. J. *Chem. Phys.* **2007**, 341 (1-3), 240.
- (24) Mohammed, O. F.; Pines, D.; Dreyer, J.; Pines, E.; Nibbering, E. T. J. *Science*. **2005**, 310 (5745), 83.
- (25) Psciuk, B. T.; Prémont-Schwarz, M.; Koeppe, B.; Keinan, S.; Xiao, D.; Nibbering, E. T. J.; Batista, V. S. *J. Phys. Chem. A* **2015**, 119 (20), 4800.
- (26) Prémont-Schwarz, M.; Barak, T.; Pines, D.; Nibbering, E. T. J.; Pines, E. *J. Phys. Chem. B* **2013**, 117 (16), 4594.
- (27) Mohammed, O. F.; Xiao, D.; Batista, V. S.; Nibbering, E. T. J. *J. Phys. Chem. A* **2014**, 118, 3090.
- (28) Genosar, L.; Cohen, B.; Huppert, D. *J. Phys. Chem. A* **2000**, 104 (29), 6689.
- (29) Chen, J.; Kuss-Petermann, M.; Wenger, O. S. *Chem. A Eur. J.* **2014**, 20, 4098.
- (30) Bronner, C.; Wenger, O. S. *J. Phys. Chem. Lett.* **2012**, 3, 70.
- (31) Fecenko, C. J.; Thorp, H. H.; Meyer, T. J. *J. Am. Chem. Soc.* **2007**, 129 (49), 15098.
- (32) Mayer, J. M. *Acc. Chem. Res.* **2011**, 44, 36.
- (33) Martin, D. J.; Rountree, E. S.; McCarthy, B. D.; Dempsey, J. L. *Submitted* **2016**.
- (34) Rountree, E. S.; Dempsey, J. L. *Submitted* **2016**.
- (35) Mayer, J. M. *J. Phys. Chem. Lett.* **2011**, 2, 1481.
- (36) Waidmann, C. R.; Miller, A. J. M.; Ng, C. A.; Scheuermann, M. L.; Porter, T. R.; Tronic, T. A.; Mayer, J. M. *Energy Environ. Sci.* **2012**, 5 (7), 7771.
- (37) Hammes-Schiffer, S.; Stuchebrukhov, A. A. *Chem. Rev.* **2010**, 110 (12), 6939.
- (38) Hammes-Schiffer, S. *Energy Environ. Sci.* **2012**, 5 (7), 7696.
- (39) Hammes-Schiffer, S. *J. Am. Chem. Soc.* **2015**, 137, 8860.
- (40) Gutman, M.; Huppert, D. *J. Biochem. Biophys. Methods* **1979**, 1 (1), 9.

- (41) Jarczewski, A.; Hubbard, C. D. *J. Mol. Struct.* **2003**, 649 (3), 287.
- (42) Sen Gupta, S. K.; Arvind, U. *J. Phys. Org. Chem.* **1997**, 10 (6), 466.
- (43) Hojatti, M.; Leffek, K. T. *Can. J. Chem.* **1984**, 62 (12), 2653.
- (44) Crooks, J. E.; Robinson, B. H. *Faraday Symp. Chem. Soc.* **1975**, 10, 29.
- (45) McCarthy, B. D.; Martin, D. J.; Rountree, E. S.; Ullman, A. C.; Dempsey, J. L. *Inorg. Chem.* **2014**, 53 (16), 8350.
- (46) Bordwell, F. G.; Zhang, X. M.; Cheng, J. P. *J. Org. Chem.* **1993**, 58 (23), 6410.
- (47) Bordwell, F. G.; Cheng, J. *J. Am. Chem. Soc.* **1991**, 113 (5), 1736.
- (48) Kütt, A.; Leito, I.; Kaljurand, I.; Sooväli, L.; Vlasov, V. M.; Yagupolskii, L. M.; Koppel, I. a. *J. Org. Chem.* **2006**, 71 (7), 2829.
- (49) Yamada, K.; Teshima, K.; Kobayashi, N.; Hirohashi, R. *J. Electroanal. Chem.* **1995**, 394 (1-2), 71.
- (50) Miras, M.; Barbero, C. *Synth. Met.* **1991**, 43, 3081.
- (51) Miras, M.; Barbero, C.; Kotz, R. *J. Electrochem. Soc.* **1991**, 138, 335.
- (52) Wei, Y.; Jaag, G.-W.; Chan, C.-C.; Hsueh, K. F.; Hariharan, R.; Patel, S. a.; Whitecar, C. K. *J. Phys. Chem.* **1990**, 94 (6), 7716.
- (53) MacDiarmid, A. G.; Epstein, A. J. *Faraday Discuss. Chem. Soc.* **1989**, 88, 317.
- (54) Snead, W.; Remick, A. *J. Am. Chem. Soc.* **1957**, 79 (5), 6121.
- (55) Taj, S.; Ahmed, M.; Sankarapavinasam, S. *J. Electroanal. Chem.* **1992**, 338, 347.
- (56) Kwon, S. J.; Yang, H.; Jo, K.; Kwak, J. *Analyst* **2008**, 133 (11), 1599.
- (57) Heras, A. M.; Avila, J. L.; Ruiz, J. J.; Garcia-Blanco, F. *Electrochim. Acta* **1984**, 29 (4), 541.
- (58) Sun, W.; Jiao, K.; Zhang, S.; Zhang, C.; Zhang, Z. *Anal. Chim. Acta* **2001**, 434 (1), 43.
- (59) Brown, K. C.; Corbett, J. F. *J. Chem. Soc. Perkin Trans. 2* **1979**, No. 3, 308.
- (60) Corbett, J. F. *J. Chem. Soc. B Phys. Org.* **1969**, 213.
- (61) Kaljurand, I.; Ku, A.; Soova, L. *J. Org. Chem.* **2005**, 70 (4), 1019.
- (62) Raston, C. L.; Skelton, B. W.; Whitaker, C. R.; White, A. H. *Aust. J. Chem.* **1988**, 41, 409.

- (63) Noviandri, I.; Brown, K. N.; Fleming, D. S.; Gulyas, P. T.; Lay, P. A.; Masters, A. F.; Phillips, L. *J. Phys. Chem. B* **1999**, *103* (32), 6713.
- (64) Ward, W. M.; Farnum, B. H.; Siegler, M.; Meyer, G. J. *J. Phys. Chem. A* **2013**, *117*, 8883.
- (65) Meyer, T. J.; Taube, H. In *Comprehensive Coordination Chemistry*; Pergamon Press: New York, 1987.
- (66) Neta, P. *J. Phys. Chem. Ref. Data* **2005**, *34* (1), 109.
- (67) Arnaut, L. G.; Formosinho, S. J. *Chem. - A Eur. J.* **2008**, *14* (22), 6578.
- (68) Bell, R. P. *The Proton in Chemistry*; Chapman and Hall: London, 1973.
- (69) Silverman, D. N. *Biochim. Biophys. Acta - Bioenerg.* **2000**, *1458* (1), 88.
- (70) Gamiz-Hernandez, A. P.; Magomedov, A.; Hummer, G.; Kaila, V. R. I. *J. Phys. Chem. B* **2015**, *119* (6), 2611.
- (71) Kaila, V. R. I.; Hummer, G. *J. Am. Chem. Soc.* **2012**, *244*, 19040.
- (72) Elgrishi, N.; McCarthy, B. D.; Rountree, E. S.; Dempsey, J. L. *ACS Catal.* **2016**, 3644.
- (73) Pearson, R. G.; Dillon, R. L. *J. Am. Chem. Soc.* **1953**, *75* (10), 2439.
- (74) Andrieux, C. P.; Gamby, J.; Hapiot, P.; Savéant, J. M. *J. Am. Chem. Soc.* **2003**, *125* (33), 10119.
- (75) Marcus, R. A. *J. Phys. Chem.* **1968**, *72* (3), 891.
- (76) Peters, K. S. *Acc. Chem. Res.* **2009**, *42* (1), 89.
- (77) Reece, S. Y.; Seyedsayamdost, M. R.; Stubbe, J.; Nocera, D. G. *J. Am. Chem. Soc.* **2006**, *128* (42), 13654.
- (78) Kiefer, P. M.; Hynes, J. T. *J. Phys. Chem. A* **2004**, *108* (52), 11793.
- (79) Borgis, D.; Hynes, J. T. *J. Phys. Chem.* **1996**, *100* (4), 1118.
- (80) Peters, K. S.; Cashin, A.; Timbers, P. **2000**, No. 17, 107.
- (81) Berg, O. Van Den; Jager, W. F.; Cangialosi, D.; Turnhout, J. Van; Verheijen, P. J. T.; Wu, M.; Picken, S. J. *Macromolecules* **2006**, *39*, 224.
- (82) Lee, C.; Zhou, J.; Ozerov, O. V. *J. Am. Chem. Soc.* **2013**, *135* (9), 3560.
- (83) Knierzinger, A.; Wolfbeis, O. S. *J. Heterocycl. Chem.* **1980**, *17* (2), 225.

- (84) Janin, Y. L.; Roulland, E.; Beurdeley-thomas, A.; Decaudin, D.; Monneret, C.; Poupon, M.-F. *J. Chem. Soc. Perkin Trans. 1* **2002**, 1, 529.
- (85) Watanabe, T.; Miyaura, N.; Suzuki, A. *Synlett* **1992**, 1992 (03), 207.
- (86) Suzuki, A. *Proc. Japan Acad. Ser. B*, **2004**, 80 (8), 359.
- (87) Benesi, H. A.; Hildebrand, J. H. *J. Am. Chem. Soc.* **1949**, 71 (8), 2703.

CHAPTER 4: EXCITED-STATE AND THERMAL PROTON TRANSFER REACTIONS OF QUINOLINE PHOTOBASES: INFLUENCES OF DRIVING FORCE, ELECTRONIC STRUCTURE AND HYDROGEN-BONDING

4.1. Introduction

Proton Transfers (PT) are an important class of fundamental reactions that are pervasive in all aspects of chemistry.¹⁻³ These processes play a vital role in acid-base catalysis⁴, enzymatic catalysis⁵, photosynthesis⁶⁻⁹, and the development of new energy technologies¹⁰⁻¹² among other areas. Therefore, studying PT to better understand how these reactions operate and how to control them can have far reaching applications across the chemical landscape. One subset of PT that is particularly interesting is excited state proton transfer (ESPT). Coupling PT to light absorption is of great interest to those developing energy technologies based on light-driven fuel production.¹³⁻¹⁶ As the production of fuels like hydrogen and methanol from water and carbon dioxide involve coupling PT and electron transfer, we posit that a stronger fundamental understanding of ESPT will result in a better understanding of how to promote more complex PCET reactions with light. However, developing systems that allow for precise study of ESPT is no simple task.

In the field of ESPT, photoacids — molecules whose electronic excited state is more acidic than ground state — have been studied much more comprehensively than photobases — molecules observed to become more basic upon excitation.¹⁷⁻¹⁹ Not only have the photophysics behind the phenomenon of photoacidity been more thoroughly examined, but there are extensive studies in the literature investigating the behavior of photoacids.^{17,18,20} Naphthol^{10,20,21} and pyrene¹⁹ derivatives are some of the most well-studied photoacids, with

these structures offering tunability in the absorbance, emission, and pK_a of the photoacid. As such, they have been used to study everything from hydrogen evolution catalysis¹⁰ to donor-acceptor distance relationship in proton-coupled electron transfer reactions.^{22–24} Photobases, on the other hand, are less well studied with fewer known examples in the literature, with acridines,^{13,25–27} quinolines,^{14,28–30} and coumarins^{31,32} being some of the better-known structures exhibiting photobasic behavior.

Quinolines are a particularly attractive motif for studying ESPT with photobases, as our lab has previous experience synthesizing and characterizing 2,4-aryl-7-dimethylaminoquinolines (R-7DMAQ). In a recently reported study, a series of R-7DMAQS were employed as optical probes for the PT step in a thermal PCET reaction.³³ R-7DMAQs undergo a red shift in their ground state absorbance upon protonation of the quinoline nitrogen, providing an optical handle for PT events. By varying the substituent at the 2- and 4-positions, the pK_a , and thus driving force for PT can be varied. These molecules were only used to study ground state PT processes, however, and because it has long been known that quinolines exhibit an enhanced basicity upon excitation, the R-7DMAQ platform also provides an excellent opportunity to more deeply explore ESPT.^{14,28,29} In the present work we investigate the excited-state and thermal PT reactions of the photobase 2,4-Bis(3,5-trifluoromethyl)phenyl-7-dimethylaminoquinoline (CF₃-7DMAQ), and reveal that PT driving force, hydrogen bonding and electronic structure all influence the reaction kinetics of elementary proton transfer processes.

4.2. Electronic Structure of Quinolines

The electronic origins of quinoline photobasicity were recently detailed eloquently by Dawlaty and coworkers.¹⁴ Quinolines have two accessible electronic states in the UV-visible range, 1L_a and 1L_b , where 1L_a represents increased atomic centered charge density and 1L_b represents increased charge density centered on bonds. As such, excitation to the lower lying 1L_a state results in increased charge density on the quinoline nitrogen, resulting in an enhanced pK_a of the N-heterocycle.¹⁴ Further evidence for this electronic assignment has been observed in 3- and 6-aminoquinolines.^{28,29} In these instances, excitation of the quinoline moves electron density away from the amino group, making it more acidic, while the quinoline nitrogen becomes more basic; a similar phenomenon is also observed in amino-substituted coumarins.^{31,32} These same electronic structure factors are key to the photo-induced reactivity of R-7DMAQs, but what makes them especially unique for the study of PT reactions is the ground-state absorbance features imparted by the dimethylamino substituent on the quinoline ring. This group alters the electronics of R-7DMAQs, giving them a broad absorbance feature in the visible region (~400 nm) corresponding to an intramolecular charge transfer from the dimethylamino to the quinoline ring.²⁸ While strong visible light absorption is useful for carrying out photophysical and chemical measurements, R-7DMAQs also undergo a large red shift (~70 nm) in optical absorbance upon protonation of the quinoline nitrogen. This absorbance shift provides an excellent optical handle for monitoring PT reactions in the visible region, complementing the photoluminescence measurements typically employed in the study of photoacids and photobases.

4.3. Results and Discussion

CF₃-7DMAQ was synthesized according to a previously reported procedure.³³ The absorbance spectrum of CF₃-7DMAQ in acetonitrile has a maximum absorbance at 410 nm ($\lambda_{\text{abs}} = 415 \text{ nm}$, $\varepsilon = 5,190 \text{ M}^{-1} \text{ cm}^{-1}$, Figure 4.1), and upon protonation to form its conjugate base, the absorbance feature shifts $\sim 70 \text{ nm}$ while also increasing in molar absorptivity ($\lambda_{\text{abs}} = 490 \text{ nm}$, $\varepsilon = 11,270 \text{ M}^{-1} \text{ cm}^{-1}$, Figure 4.1).

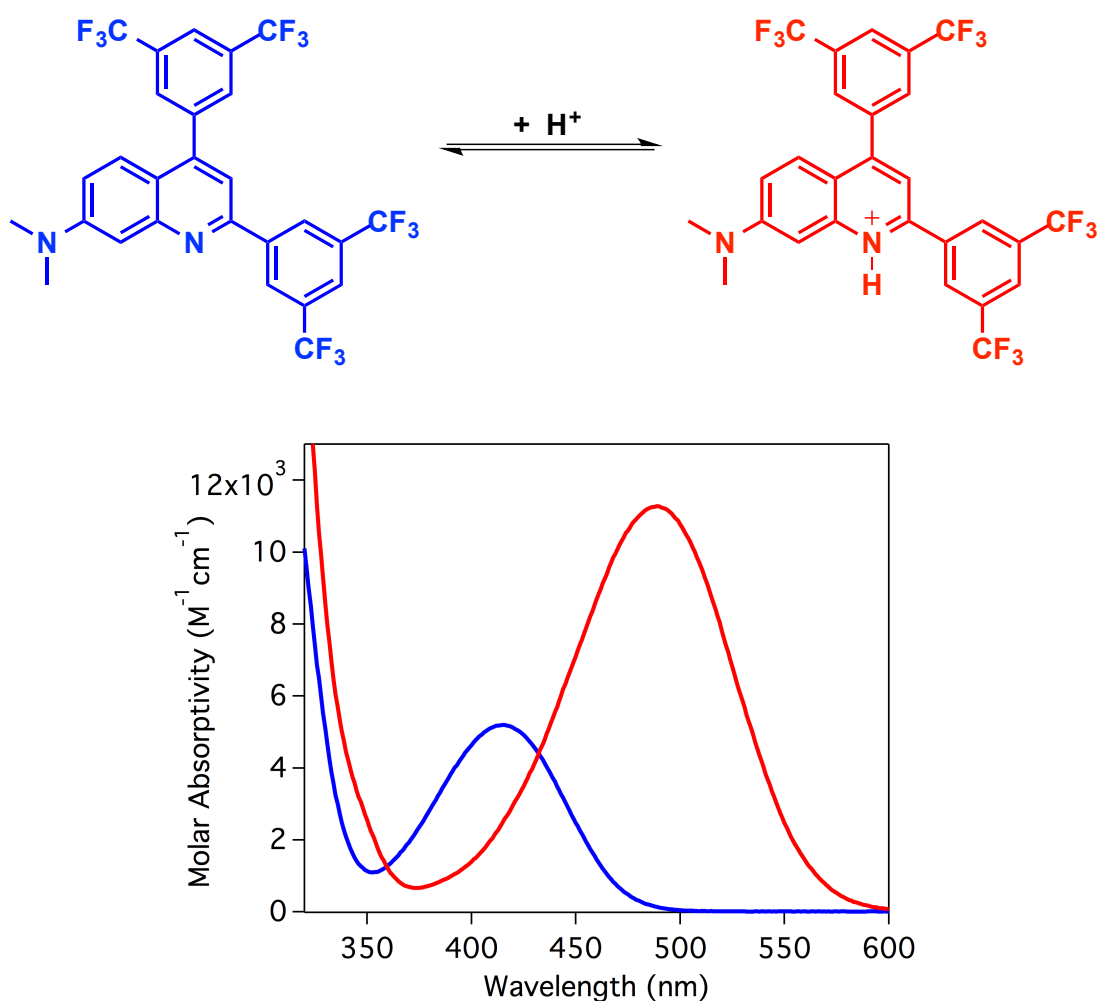


Figure 4.1. (Top) Structure and (bottom) corresponding UV-vis absorbance spectrum of CF₃-7DMAQ (blue) in acetonitrile (87 μM) and its conjugate acid CF₃-7DMAQH⁺ (red, formed *in situ* upon the addition of 1 equivalent of HBF₄).

The pK_a of the conjugate acid of CF₃-7DMAQ was determined in acetonitrile via spectrophotometric titration with aniline ($pK_a = 11.5$, Figure 4.2). Of note, this R-7DMAQ derivative is 2.7-3.7 pK_a units lower than previously reported derivatives with electron-donating aryl substituents at the 2,4-positions.³³

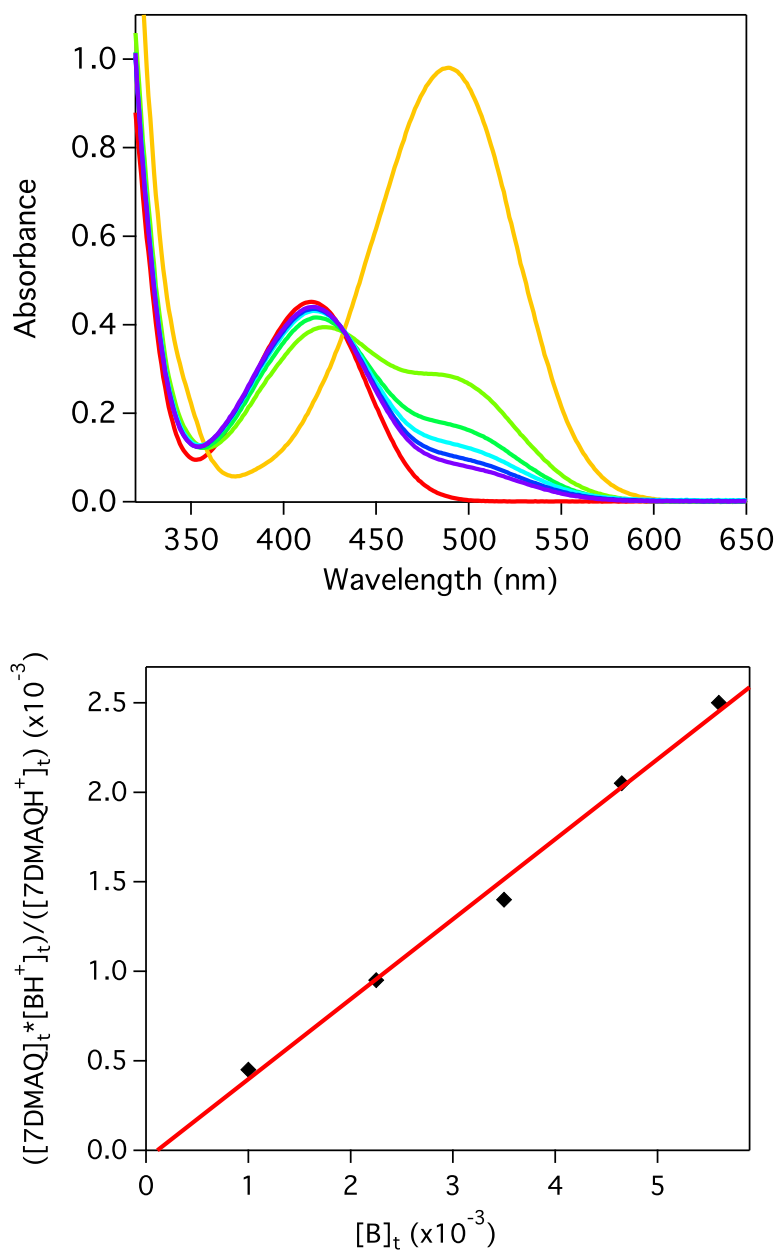
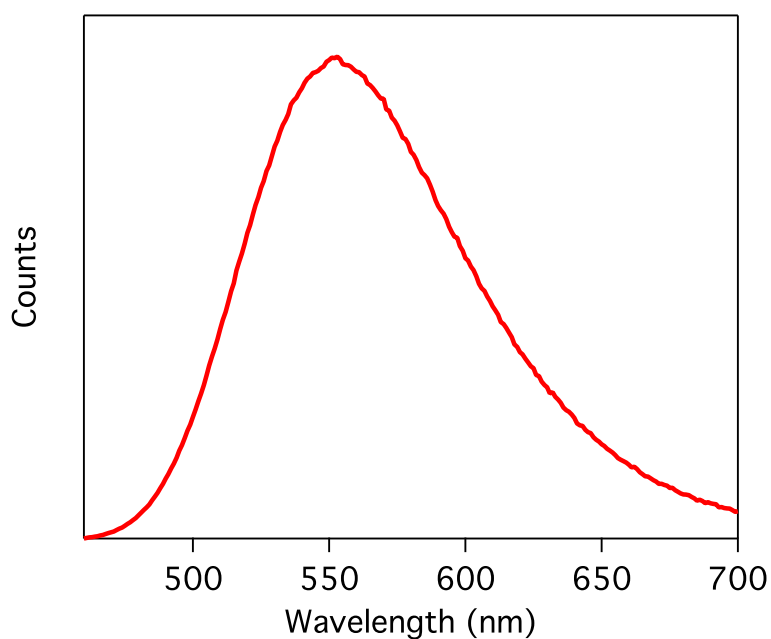


Figure 4.2. (top) Spectrophotometric titration of 87 μM CF_3 -7DMAQ with aniline (B) ($\text{pK}_a = 10.62$). Aniline and anilinium (BH^+) are transparent in the region recorded and do not contribute to the overall signal. (bottom) The slope of $([7DMAQ][\text{BH}^+])/[7DMAQH^+]$ vs. $[\text{B}]$, determined by monitoring the absorbance at 480 nm, can be used to determine the pK_a of CF_3 -7DMAQ ($\text{pK}_a = 11.5$ in CH_3CN).

The emissive properties of CF₃-7DMAQ in acetonitrile were also examined; it exhibits a strong fluorescence signal upon excitation, with $\lambda_{\text{max}} = 552$ nm and a lifetime of $\tau = 30$ ns (Figure 4.3). The conjugate acid, CF₃-7DMAQH⁺, also fluoresces when excited, albeit with much less intensity, and has a $\lambda_{\text{max}} = 670$ nm and lifetime of $\tau < 150$ ps; similar to the ground state absorbance spectrum, this emission is red shifted compared to that of the basic species.



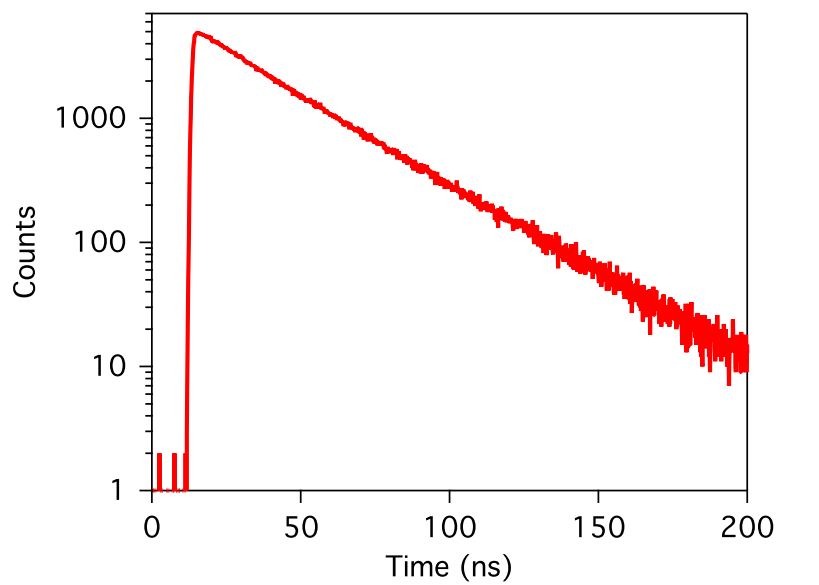


Figure 4.3. Steady-state luminescence (top) and lifetime (bottom) of CF₃-7DMAQ in acetonitrile (50 μM). Maximum $\lambda_{\text{em}} = 553$ nm and the measured lifetime of CF₃-7DMAQ $\tau = 30$ ns ($\lambda_{\text{obs}} = 560$ nm).

The values of E_{00} for CF₃-7DMAQ (Figure 4.4) and its conjugate acid (Figure 4.5) were estimated from the overlap between normalized absorbance and emission spectra. From these values, the Förster cycle was used to calculate the excited-state pK_a of CF₃-7DMAQ.^{13,14,18,34}

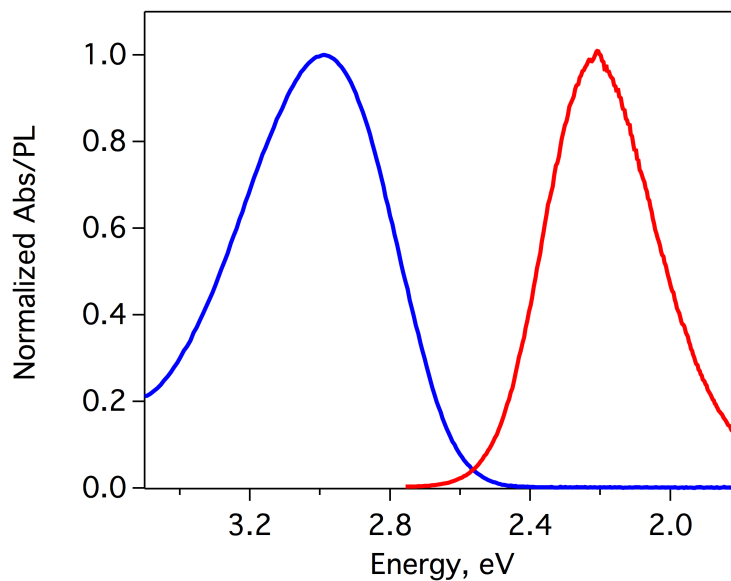


Figure 4.4. Normalized absorbance (blue) and emission (red) spectrum of $\text{CF}_3\text{-7DMAQ}$ in acetonitrile ($87\ \mu\text{M}$). The 0 – 0 energy gap can be estimated from the overlap of these two spectra (or the average of the maximum of the absorbance/emission) and was calculated to be $E_{00} = 2.56\ \text{eV}$.

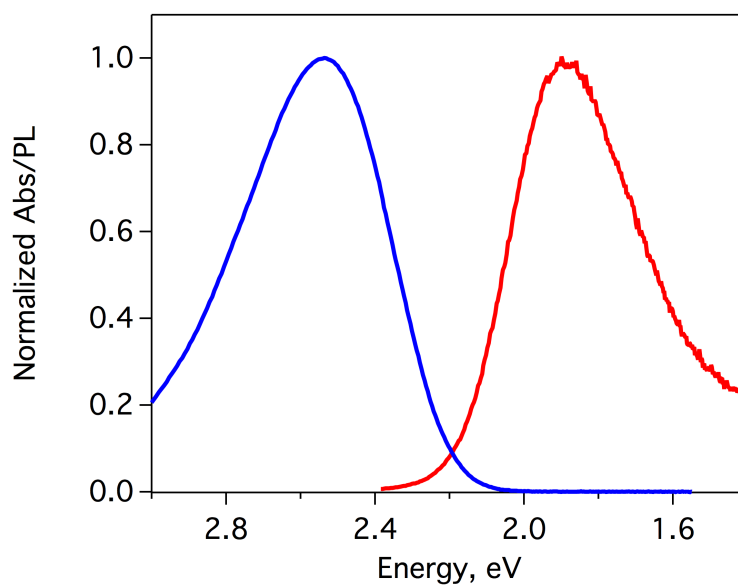


Figure 4.5. Normalized absorbance (blue) and emission (red) spectrum of $\text{CF}_3\text{-7DMAQH}^+$ in acetonitrile ($87\ \mu\text{M}$). The 0 – 0 energy gap can be estimated from the overlap of these two spectra (or the average of the maximum of the absorbance/emission) and was calculated to be $E_{00} = 2.19\ \text{eV}$.

From the E_{00} values and the ground-state pK_a , the excited-state pK_a of CF_3 -7DMAQH⁺ was determined (17.7). The six unit increase in pK_a is consistent with what has been measured for other N-heterocycles (Figure 4.6, Section 4.5).^{13,14,29}

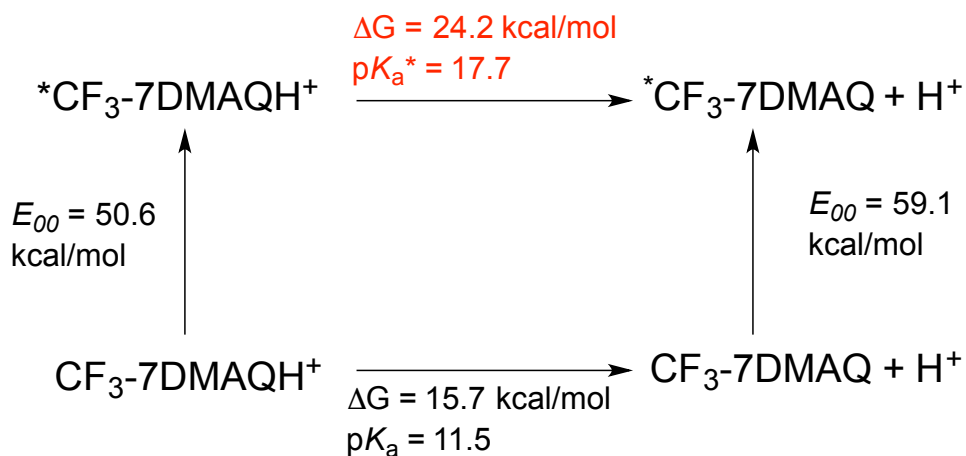


Figure 4.6. Square scheme detailing Forster cycle calculations for determining the pK_a of CF_3 -7DMAQ*.

Photoluminescence measurements to experimentally validate the photobasic properties of CF_3 -7DMAQ were subsequently undertaken using a series of five acids with pK_a values ranging from 15.0 – 18.8 in acetonitrile (Figure 4.7, acids and corresponding pK_a are shown in Table 4.1).^{35–37}

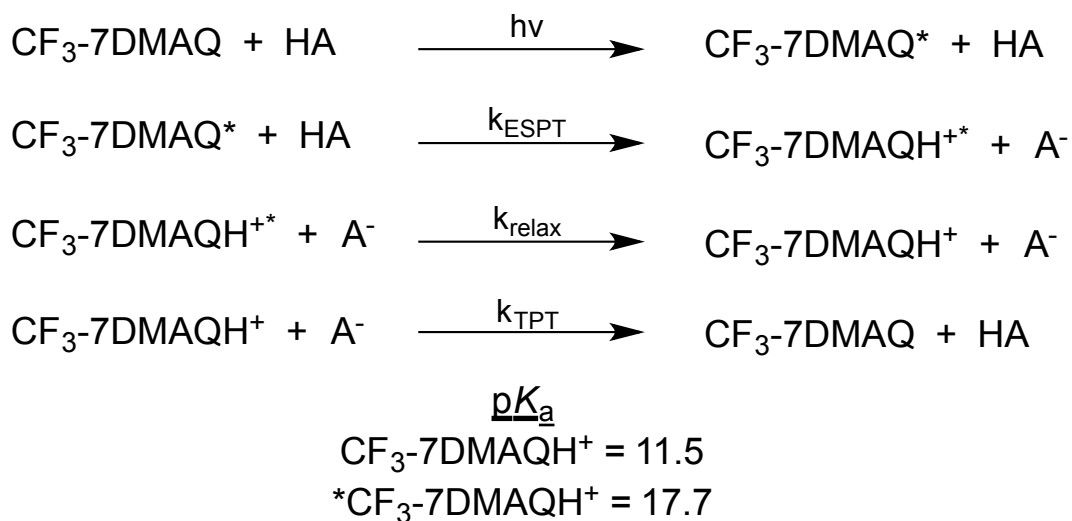


Figure 4.7. Scheme detailing reactions being monitored in this study. Excitation of CF₃-7DMAQ results in ESPT from an acid to the quinoline. Thermal recombination occurs quickly thereafter.

Table 4.1. Experimentally measured parameters and rate constants for quenching, hydrogen bonding, and proton transfer between CF₃-7DMAQ and a series of five acids.

Acid	pK _a	K _{SV} ¹	k _q (M ⁻¹ s ⁻¹) ²	K _D (M ⁻¹) ²	K _S (M ⁻¹) ³	H _{PYR} (M ⁻¹) ⁴	H _{DMA} (M ⁻¹) ⁴	k _{BPT} (M ⁻¹ s ⁻¹) ⁵
Collidinium	15.0	40.4	7.97 x 10 ⁸	23.9	24.1	8.8	1.2	7.8 x 10 ⁸
2-Ammoniumbenzimidazole	16.1	50.5	1.42 x 10 ⁹	42.7	2.6	2.3	0.1	2.1 x 10 ⁹
Benzylammonium	16.9	35.4	1.21 x 10 ⁹	36.3	1.2	3.7	--	2.5 x 10 ⁹
Isobutylammonium	17.9	18.8	6.40 x 10 ⁸	19.2	0.2	0.8	0.2	3.3 x 10 ⁹
Triethylammonium	18.8	14.8	--	--	14.8	1.6	38	--

¹K_{SV} determined from Stern-Volmer fits of steady-state quenching. ²k_q and K_D determined from TCSPC quenching measurements. ³K_S determined by fitting steady-state quenching data with a modified Stern-Volmer equation using experimentally determined K_D. ⁴Values determined through NMR titration. ⁵k_{BPT} determined via transient absorption spectroscopy.

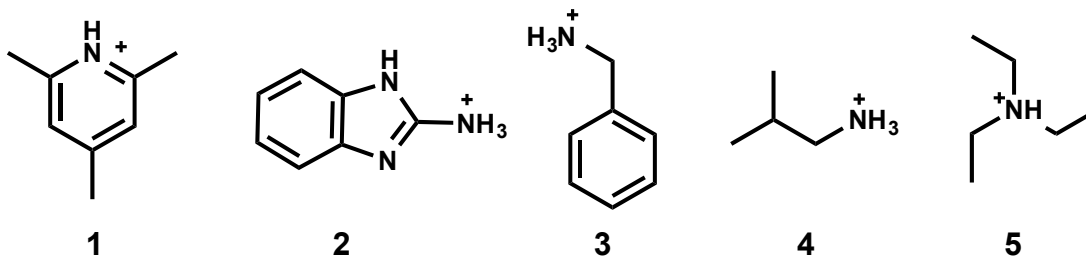


Figure 4.8. Chemical structures of the acids used in this study – all contain a tetrafluoroborate counterion. (1) Collidinium, (2) 2-Ammoniumbenzimidazole, (3) Benzylammonium, (4) Isobutylammonium, (5) Triethylammonium.

Quenching was monitored using two different methods, steady-state luminescence and time-resolved luminescence (via time-correlated single photon counting ,TCSPC). Steady-state luminescence is useful for determining Stern-Volmer quenching constants, K_{SV} (Equation 4.1, where I is the intensity at a given wavelength and Q is the concentration of quencher present), but this technique does not provide information on the nature of the quenching process (i.e. static vs. dynamic quenching, Equation 4.2 where τ represents the measured lifetime). TCSPC does provide information about the quenching process, as the luminescence lifetime of a species will only change if dynamic (diffusional) quenching is present; no static quenching is observed with this technique (Figure 4.9).³⁸

Equation 4.1

$$\frac{I_0}{I} = 1 + K_{SV}[Q]$$

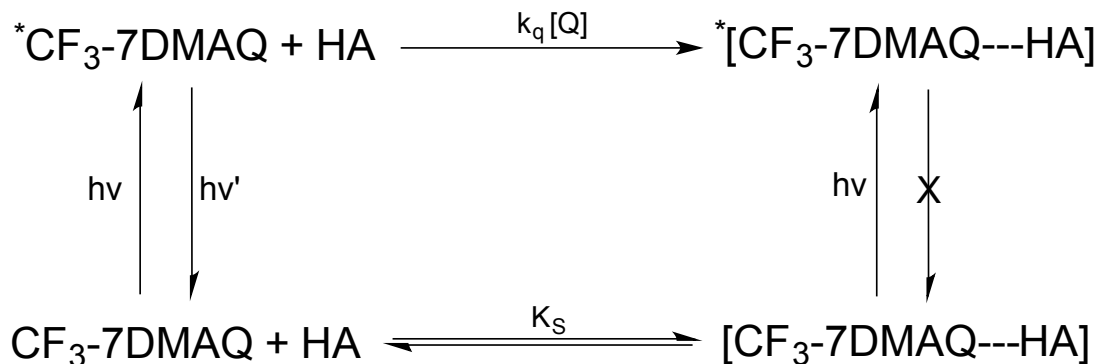


Figure 4.9. Square scheme depicting the various quenching pathways for excited $\text{CF}_3\text{-7DMAQ}$ with acid. The left side of the square represents excitation and emission. This emission can be quenched dynamically (top reaction, $k_q[\text{Q}] = K_D$) or statically (bottom).

The steady state luminescence of $\text{CF}_3\text{-7DMAQ}$ (50 μM) was monitored from 460 – 700 nm while varying the concentration of acid present (0.5 – 5.0 mM). A Stern-Volmer analysis was performed and quenching of the steady-state PL was observed with all five acids, with Stern-Volmer constants ranging from $K_{SV} = 14.7 - 51.0$ (Figure 4.10 - Figure 4.14).

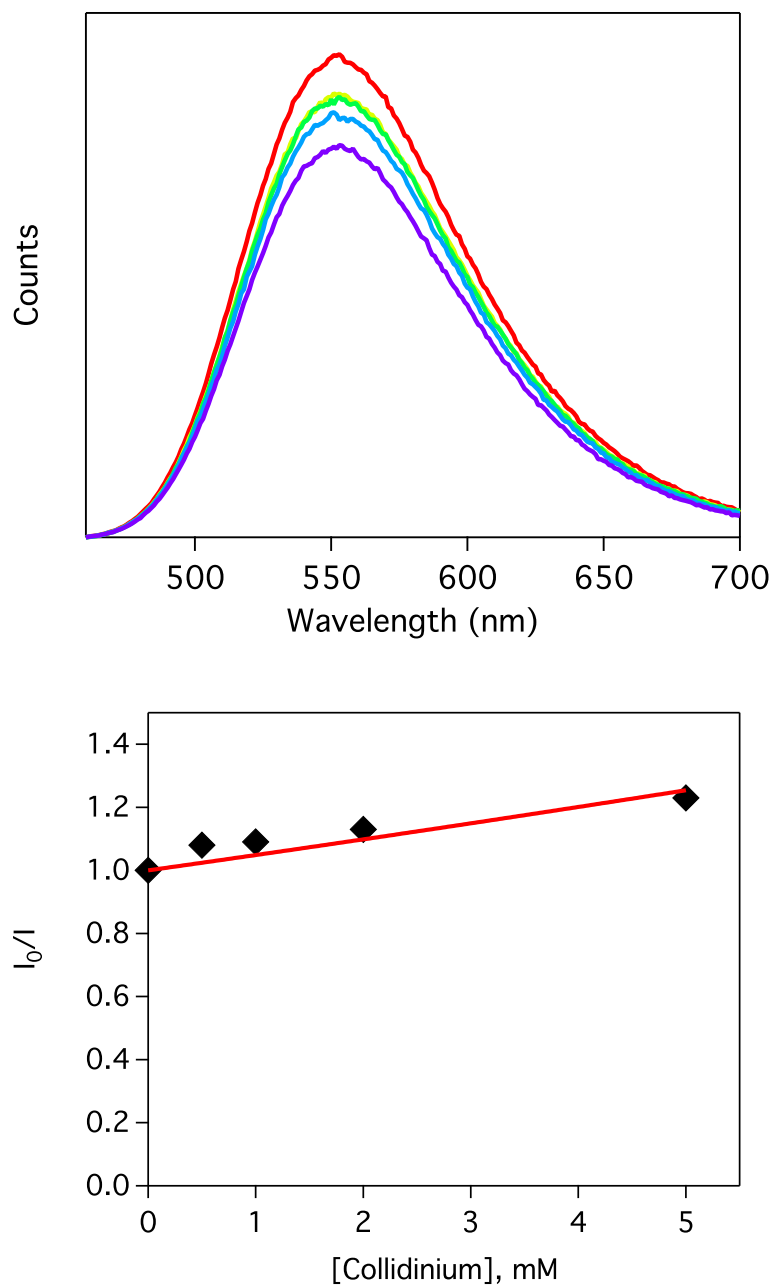


Figure 4.10. (Top) Steady-state luminescence spectra obtained from acetonitrile solutions of CF₃-7DMAQ (50 μ M) and 0 mM (red), 0.5 mM (yellow), 1.0 mM (green), 2.0 mM (blue), and 5.0 mM (purple) collidine. (Bottom) Corresponding Stern-Volmer plot measured at 560 nm; $K_{SV} = 40.4$.

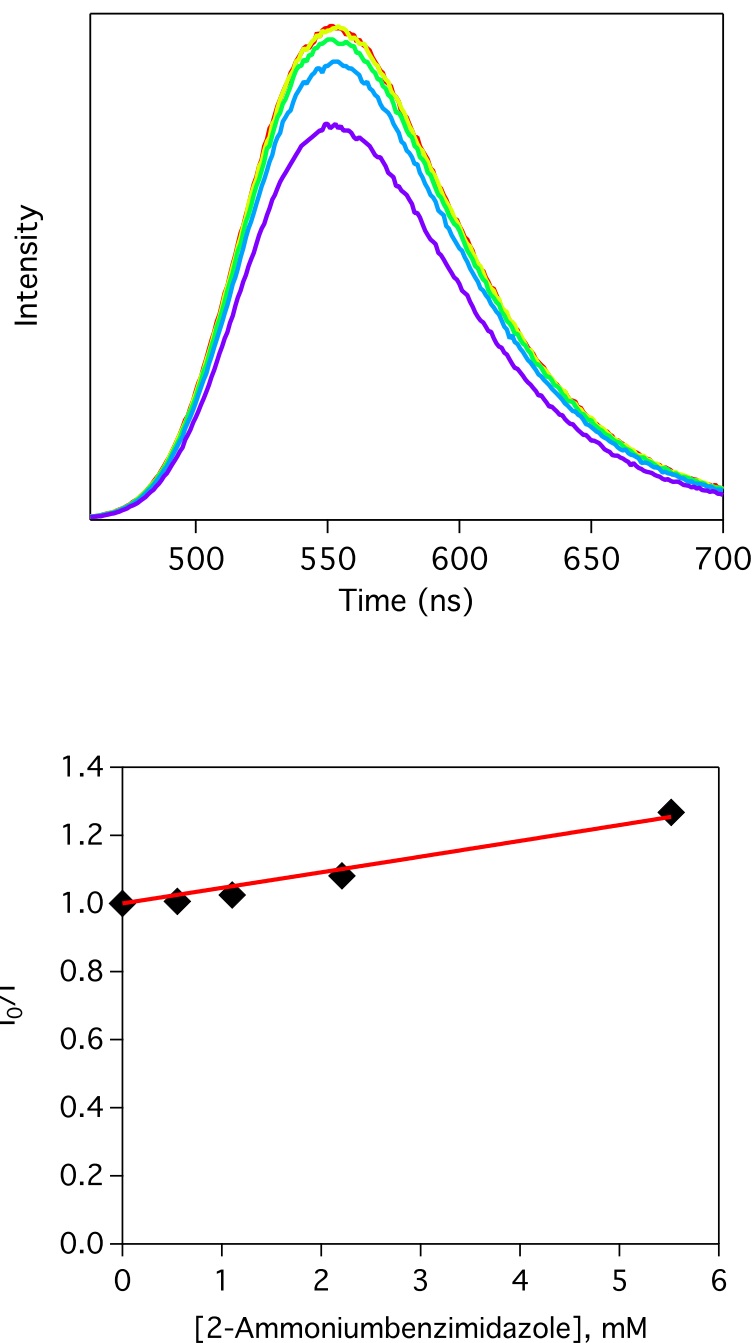


Figure 4.11. (Top) Steady-state luminescence spectra obtained from acetonitrile solutions of CF₃-7DMAQ (50 μM) and 0 mM (red), 0.55 mM (yellow), 1.1 mM (green), 2.2 mM (blue), and 5.5 mM (purple) 2-ammoniumbenzimidazole. (Bottom) Corresponding Stern-Volmer plot measured at 560 nm; $K_{SV} = 50.5$.

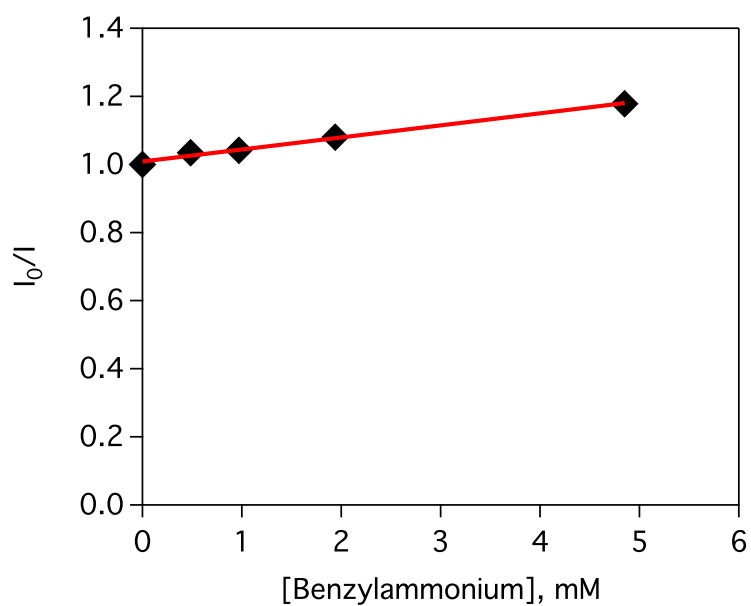
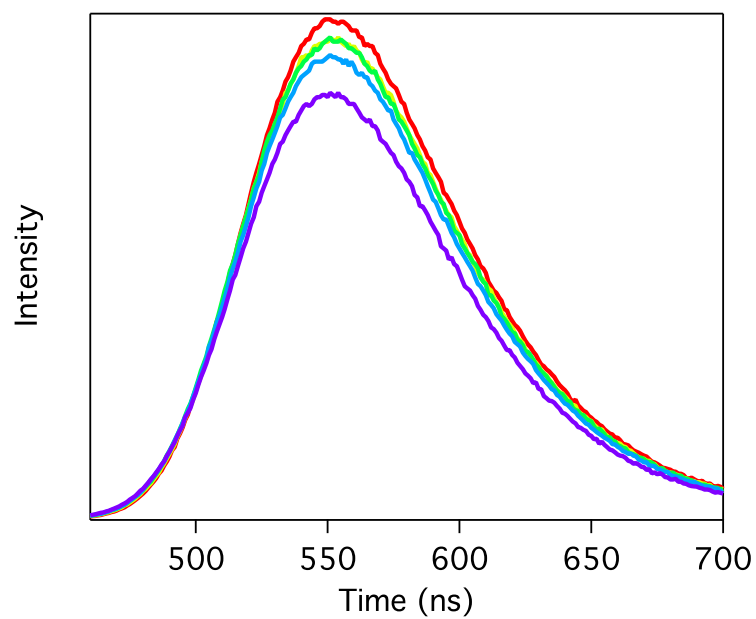


Figure 4.12. (Top) Steady-state luminescence spectra obtained from acetonitrile solutions of CF₃-7DMAQ (50 μ M) and 0 mM (red), 0.49 mM (yellow), 0.97 mM (green), 1.94 mM (blue), and 4.85 mM (purple) benzylammonium. (Bottom) Corresponding Stern-Volmer plot measured at 560 nm; $K_{SV} = 35.4$.

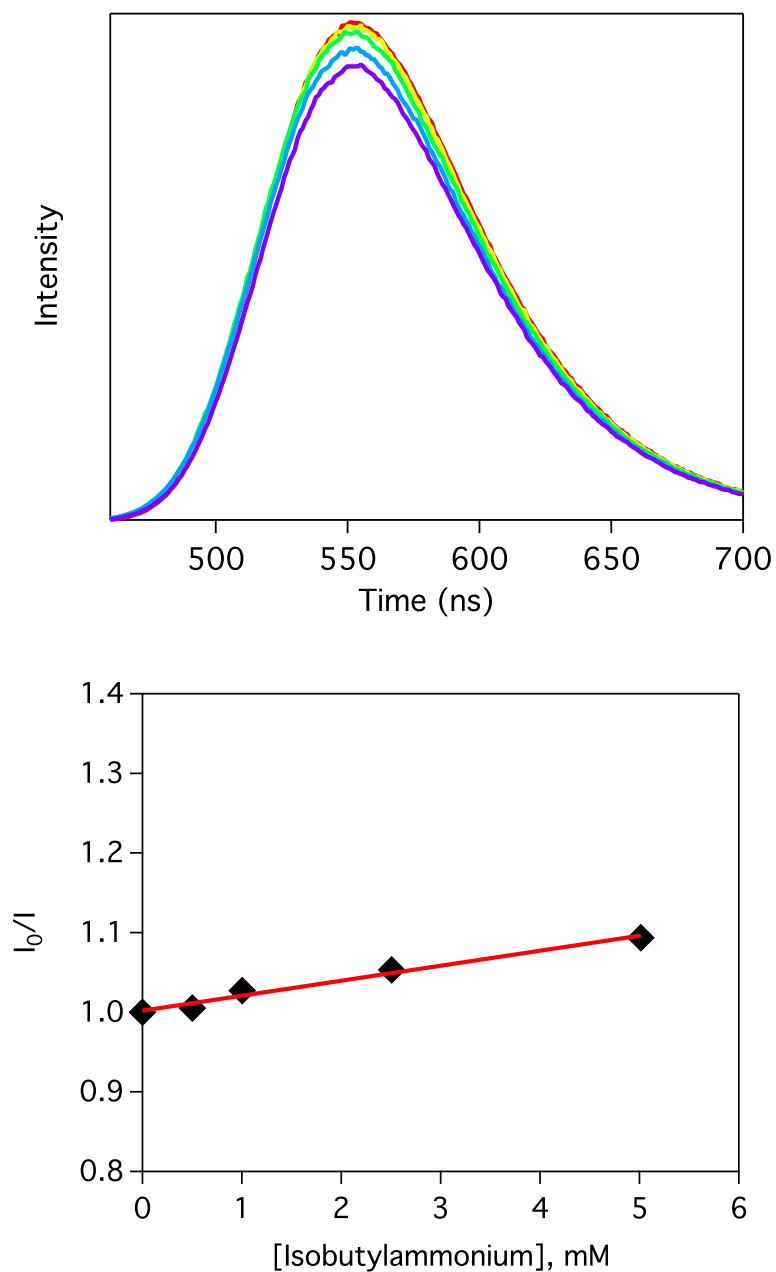


Figure 4.13. (Top) Steady-state luminescence spectra obtained from acetonitrile solutions of CF₃-7DMAQ (50 μM) and 0 mM (red), 0.5 mM (yellow), 1.0 mM (green), 2.5 mM (blue), and 5.0 mM (purple) isobutylammonium. (Bottom) Corresponding Stern-Volmer plot measured at 560 nm; $K_{SV} = 18.8$.

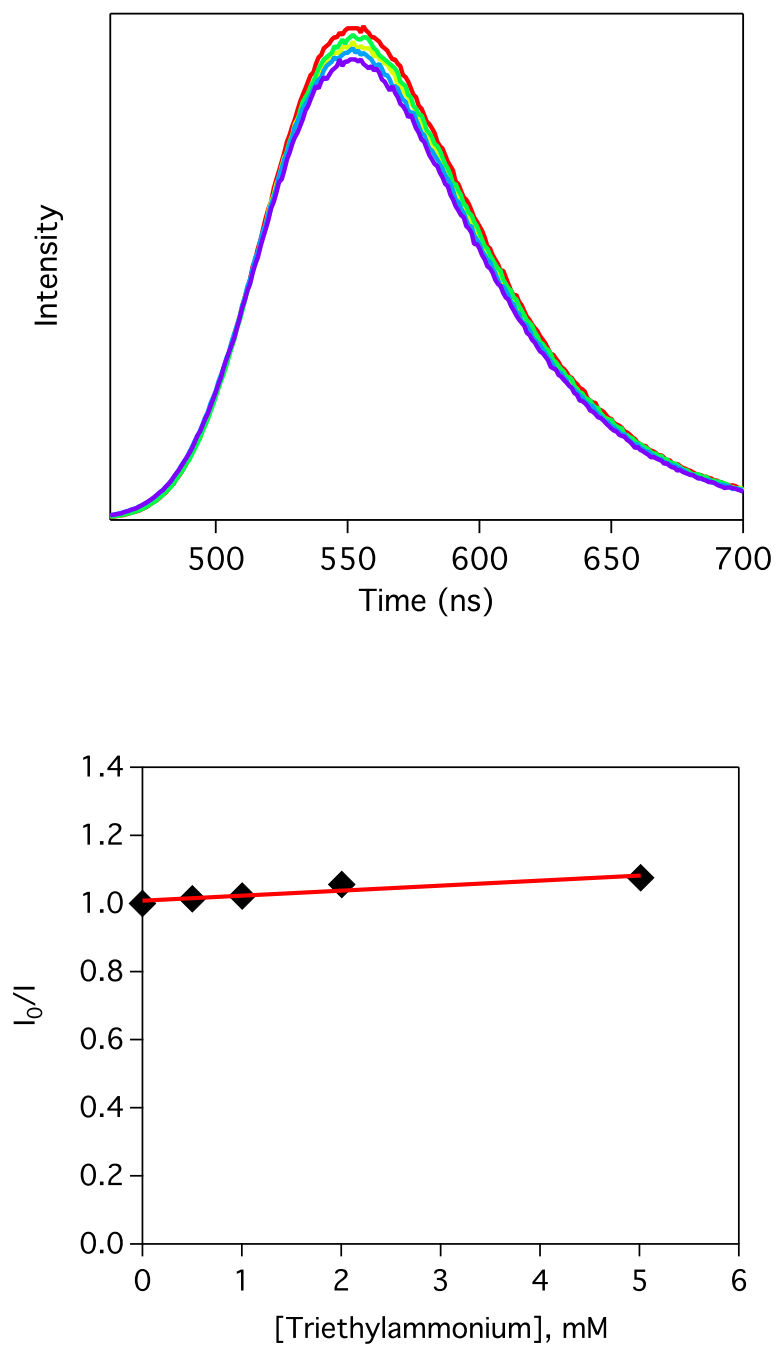


Figure 4.14. (Top) Steady-state luminescence spectra obtained from acetonitrile solutions of CF₃-7DMAQ (50 μM) and 0 mM (red), 0.5 mM (yellow), 1.0 mM (green), 2.0 mM (blue), and 5.0 mM (purple) triethylammonium. (Bottom) Corresponding Stern-Volmer plot measured at 560 nm; $K_{SV} = 14.8$.

TCSPC was employed to quantify quenching of the lifetime of CF₃-7DMAQ in the presence of varying concentrations of acid (Figure 4.15 - Figure 4.19). From this data, the Stern-Volmer constant for diffusional quenching (K_D) was determined (Equation 4.2); from this value the rate constant for dynamic quenching could be calculated.

Equation 4.2

$$\frac{\tau_0}{\tau} = 1 + K_D[Q] = 1 + k_q\tau_0[Q]$$

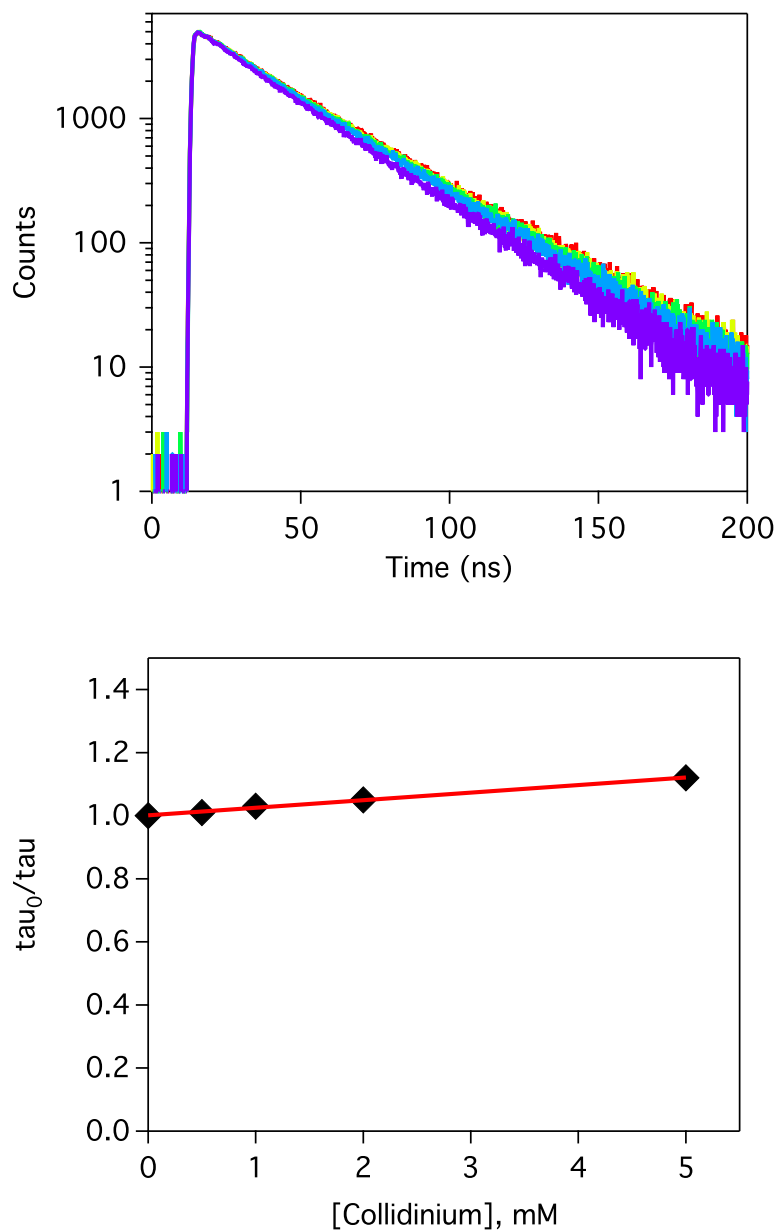


Figure 4.15. (Top) Luminescence lifetime decays detected at 560 nm from acetonitrile solutions of CF₃-7DMAQ (50 μ M) and 0 mM (red), 0.5 mM (yellow), 1.0 mM (green), 2.0 mM (blue), and 5.0 mM (purple) collidine. (Bottom) Corresponding Stern-Volmer plot; $K_D = 23.9$, $k_q = 7.97 \times 10^8 \text{ M}^{-1} \text{ s}^{-1}$.

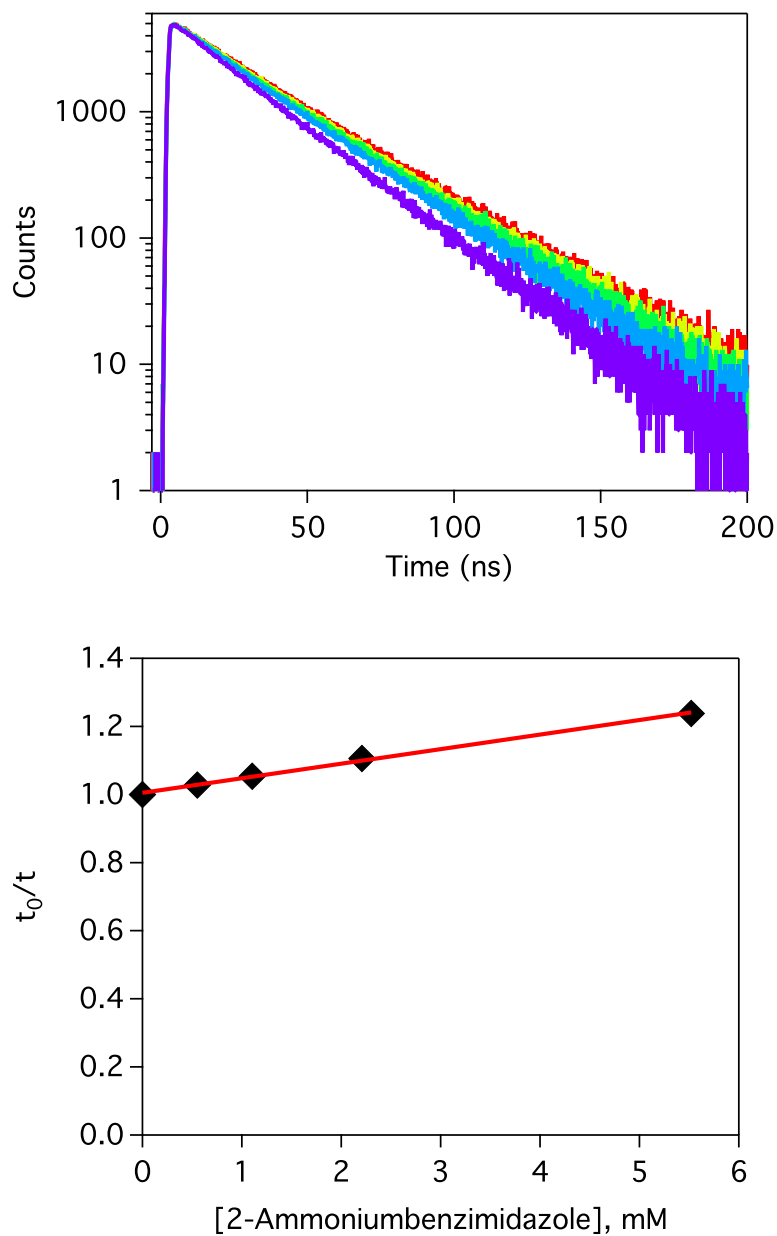


Figure 4.16. (Top) Luminescence lifetime decays detected at 560 nm from acetonitrile solutions of CF_3 -7DMAQ (50 μM) and 0 mM (red), 0.55 mM (yellow), 1.1 mM (green), 2.2 mM (blue), and 5.5 mM (purple) 2-ammoniumbenzimidazole. (Bottom) Corresponding Stern-Volmer plot; $K_D = 42.7$, $k_q = 1.42 \times 10^9 \text{ M}^{-1} \text{ s}^{-1}$.

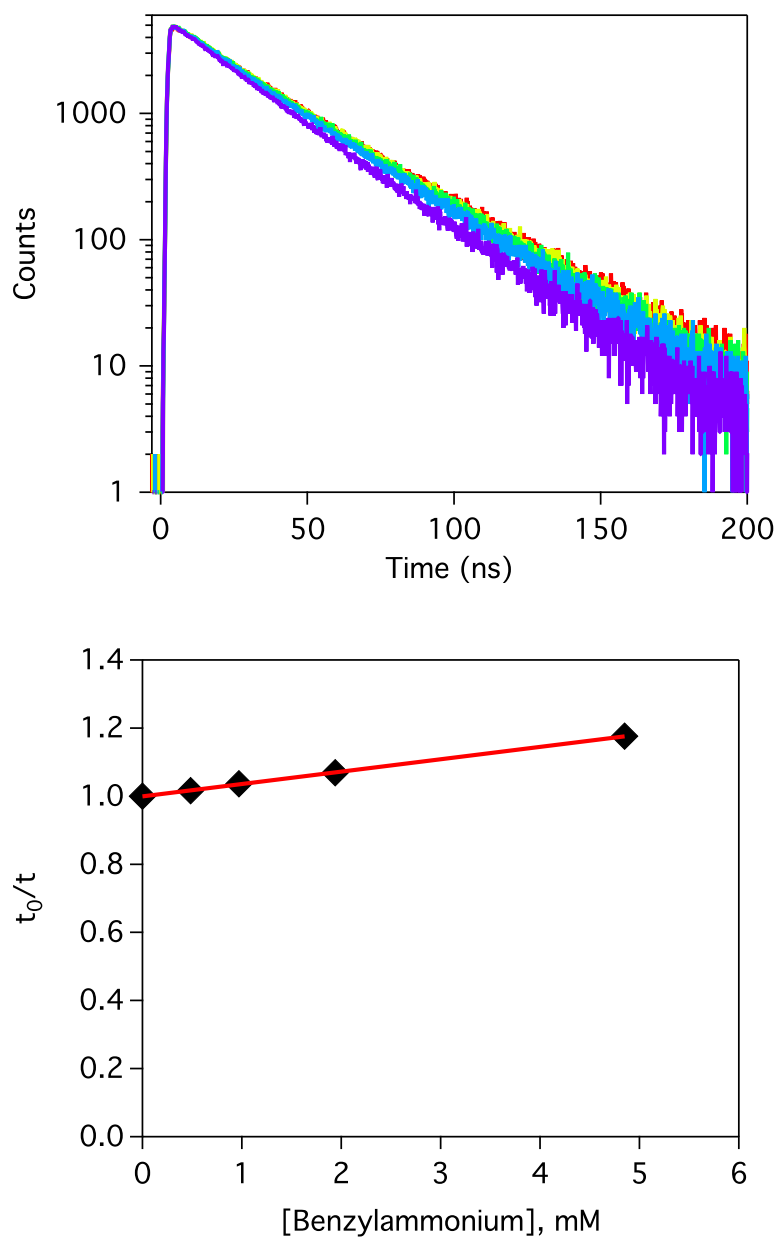


Figure 4.17. (Top) Luminescence lifetime decays detected at 560 nm from acetonitrile solutions of CF₃-7DMAQ (50 μ M) and 0 mM (red), 0.49 mM (yellow), 0.97 mM (green), 1.94 mM (blue), and 4.85 mM (purple) benzylammonium. (Bottom) Corresponding Stern-Volmer plot; $K_D = 36.3$, $k_q = 1.21 \times 10^9 \text{ M}^{-1} \text{ s}^{-1}$.

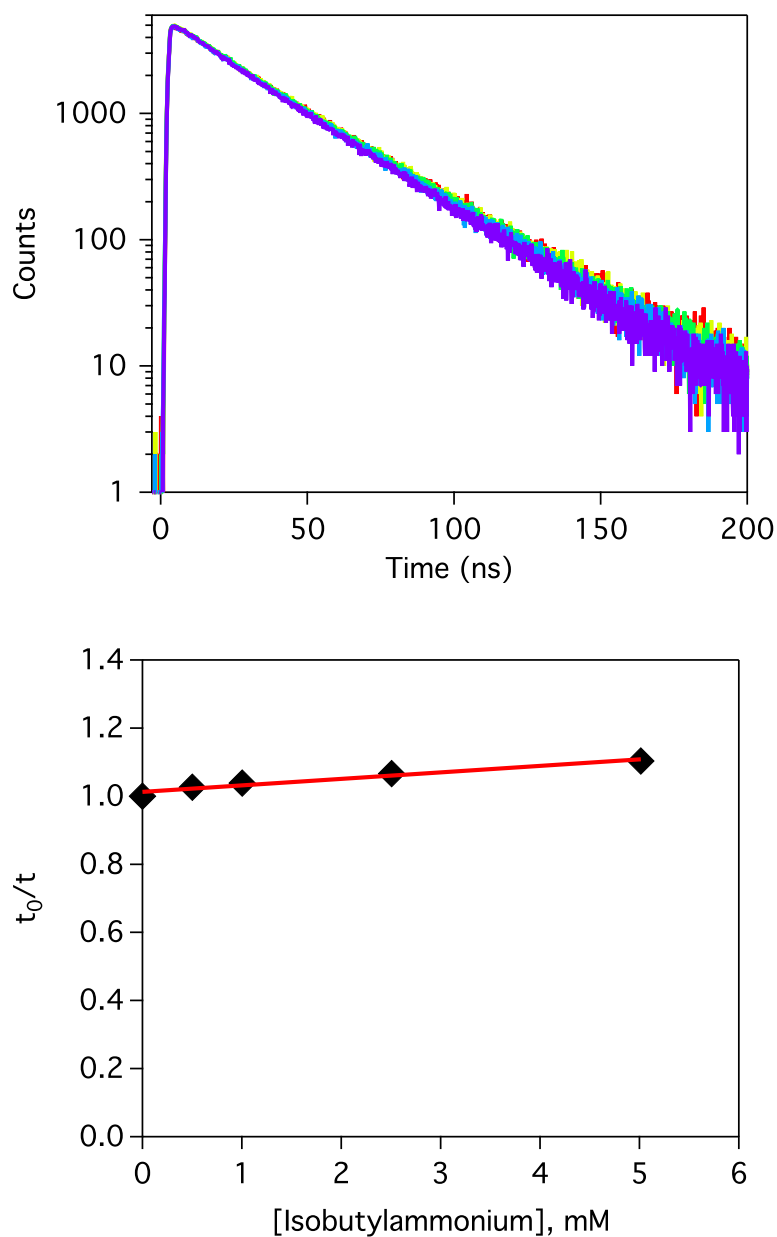


Figure 4.18. (Top) Luminescence lifetime decays detected at 560 nm from acetonitrile solutions of CF_3 -7DMAQ (50 μM) and 0 mM (red), 0.5 mM (yellow), 1.0 mM (green), 2.5 mM (blue), and 5.0 mM (purple) isobutylammonium. (Bottom) Corresponding Stern-Volmer plot; $K_D = 19.2$, $k_q = 6.40 \times 10^8 \text{ M}^{-1} \text{ s}^{-1}$.

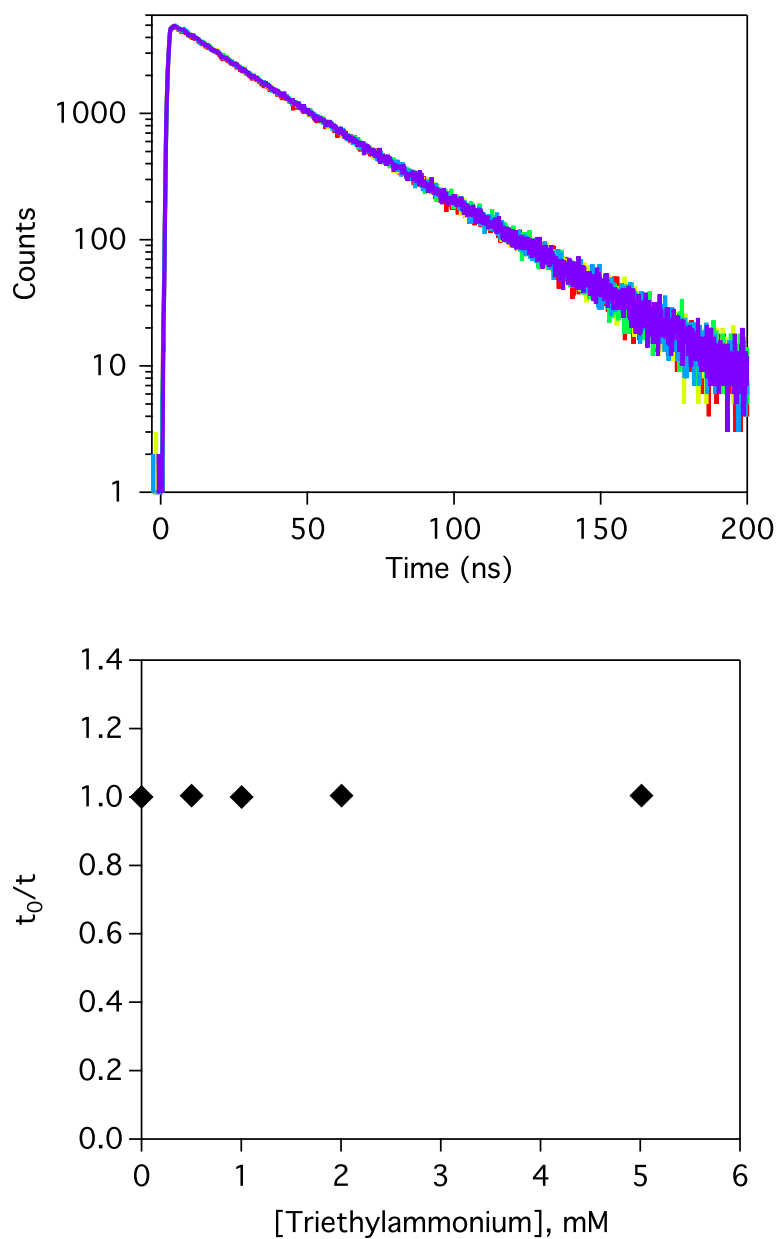


Figure 4.19. (Top) Luminescence lifetime decays detected at 560 nm from acetonitrile solutions of CF₃-7DMAQ (50 μ M) and 0 mM (red), 0.5 mM (yellow), 1.0 mM (green), 2.5 mM (blue), and 5.0 mM (purple) triethylammonium. (Bottom) Corresponding Stern-Volmer plot showing no change in the lifetime (or τ_0/τ) as a function of [triethylammonium], indicating all quenching seen in the steady state is due to static quenching processes.

Interestingly, the K_{SV} values determined from the steady-state do not match the values of K_D determined from TCSPC, most notably for collidinium and triethylammonium acids. In

fact, no diffusional quenching is observed for triethylammonium – the lifetime does not change as a function of acid present. Having determined K_D from TCSPC measurements and K_{SV} from steady-state experiments, K_S (Stern-Volmer constant representing the static component of the overall quenching process) was also determined by fitting a modified Stern-Volmer equation to the steady-state quenching data (Equation 4.3, Figure 4.20 - Figure 4.23, Table 4.1).

Equation 4.3

$$\frac{I_0}{I} = (1 + K_D[Q])(1 + K_S[Q])$$

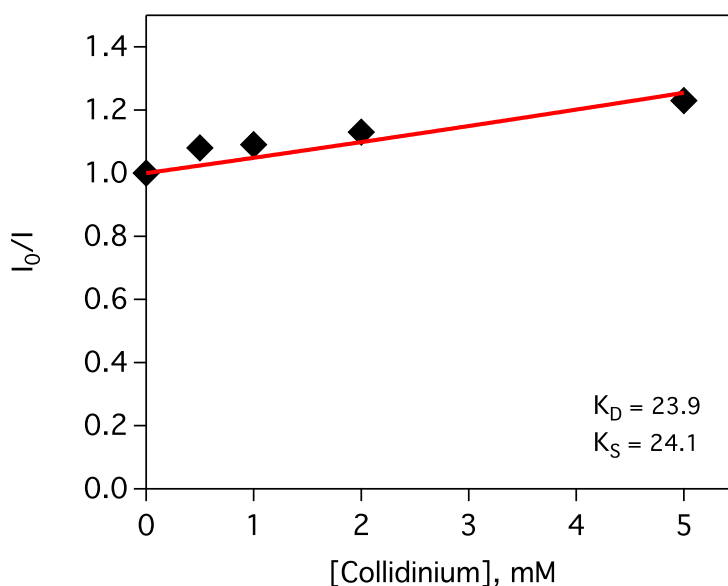


Figure 4.20. Determination of Stern-Volmer static quenching constant, $K_S = 24.1$ from steady-state luminescence data using K_D determined from lifetime quenching experiments.

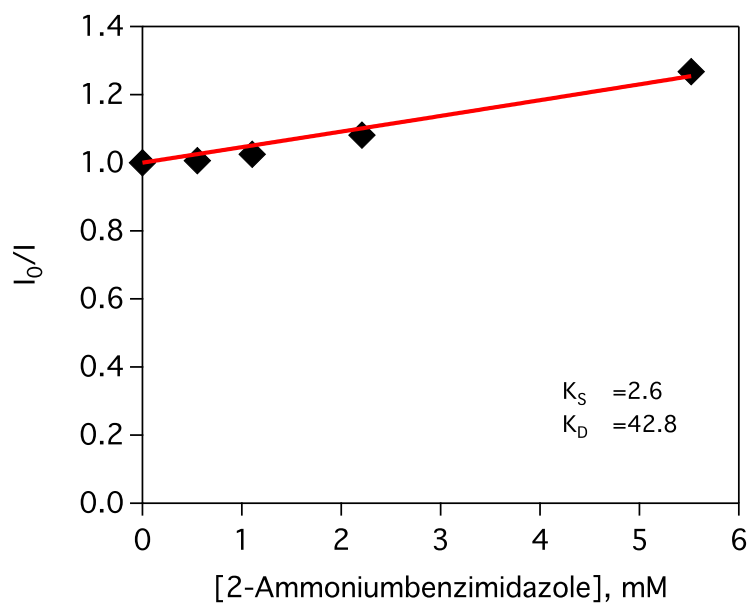


Figure 4.21. Determination of Stern-Volmer static quenching constant, $K_S = 2.6$ from steady-state luminescence data using K_D determined from lifetime quenching experiments.

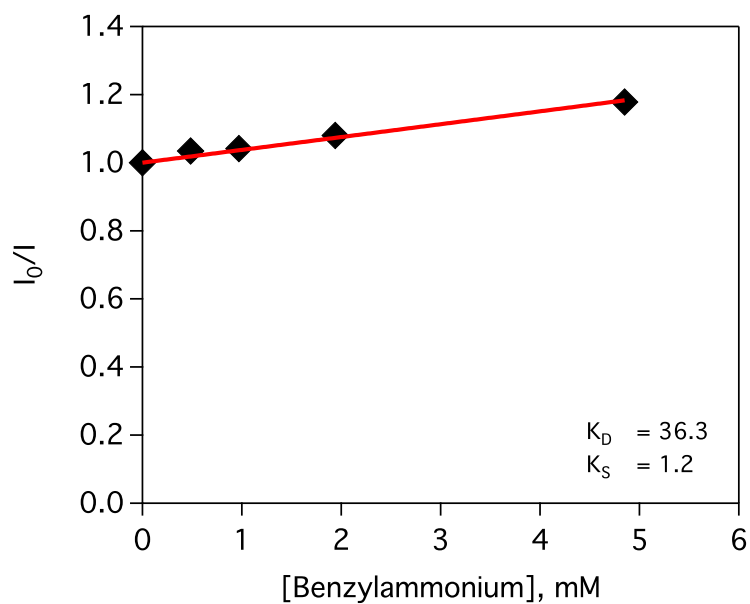


Figure 4.22. Determination of Stern-Volmer static quenching constant, $K_S = 1.2$ from steady-state luminescence data using K_D determined from lifetime quenching experiments.

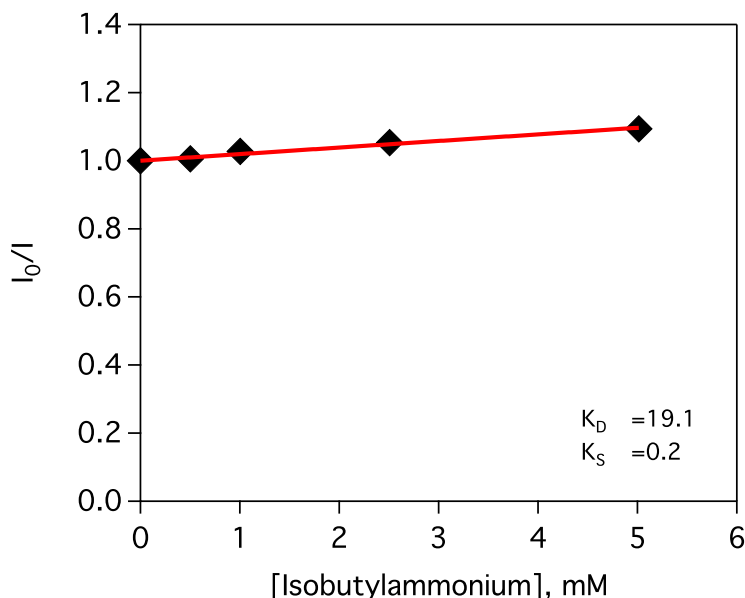


Figure 4.23. Determination of Stern-Volmer static quenching constant, $K_S = 0.2$ from steady-state luminescence data using K_D determined from lifetime quenching experiments.

Given that the excited state pK_a of CF_3 -7DMAQH⁺ is 17.7, thermodynamics would predict that acids with lower pK_a (i.e. collidinium) would undergo the fastest quenching. However, no trend between rate constant and driving force is observed for this ESPT reaction. Notably, collidinium and triethylammonium have much larger values of K_S than the other three acids used. In the case of triethylammonium, all of the quenching observed is static in nature, no diffusional quenching was observed with this acid. This is not surprising as ESPT from triethylammonium to CF_3 -7DMAQ* is expected to be endergonic ($\Delta pK_a = 1.1$), however, it is surprising that static quenching is observed.

The observation of static quenching led us to hypothesize both on the nature of this quenching process (i.e. what is causing it), and exactly how a static process could affect PT rates observed. Hydrogen bonding is prevalent among acids and bases in acetonitrile, and it has been shown to play an important role in PT reactions (along with proton-coupled electron transfer reactions).^{28,32,39–42} Therefore, we chose to examine the extent of hydrogen bonding

occurring in solution between CF₃-7DMAQ and acid via NMR. By monitoring the shift of the acidic proton peak of each acid as a function of the concentration of base added, an estimation of the association between the two molecules can be determined (see Section 4.5 for details). Because CF₃-7DMAQ has two protonatable sites, a dimethylamino group and a quinolinic nitrogen (Figure 4.24), separate experiments were carried out using either dimethylaniline or pyridine as models for the two H-bonding sites in CF₃-7DMAQ to better understand how each acid interacts with the two nitrogens on CF₃-7DMAQ (Figure 4.25 - Figure 4.33, Table 4.1).

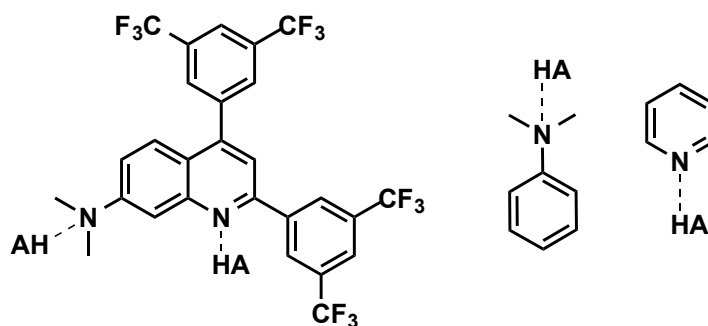


Figure 4.24. (Left) Depiction of hydrogen bonding between CF₃-7DMAQ and HA at the dimethylamino and quinoline nitrogen groups. (Right) Hydrogen bonding between HA and model complexes used in NMR titrations, dimethylaniline and pyridine.

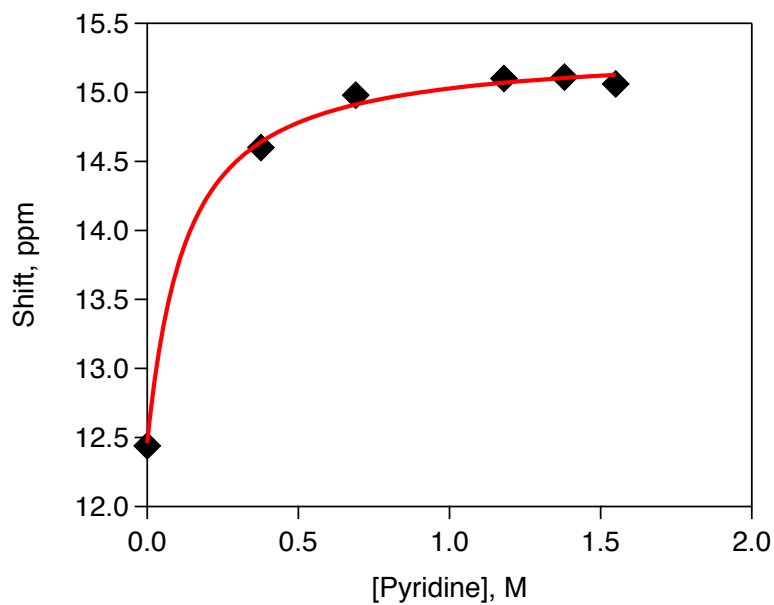


Figure 4.25. Titration of collidinium (20.7 mM) with pyridine in deuterated acetonitrile. The fit is represented by **Equation 4.4** (Section 4.5). K_{HB} was determined to be $8.8 \pm 1.5 \text{ M}^{-1}$.

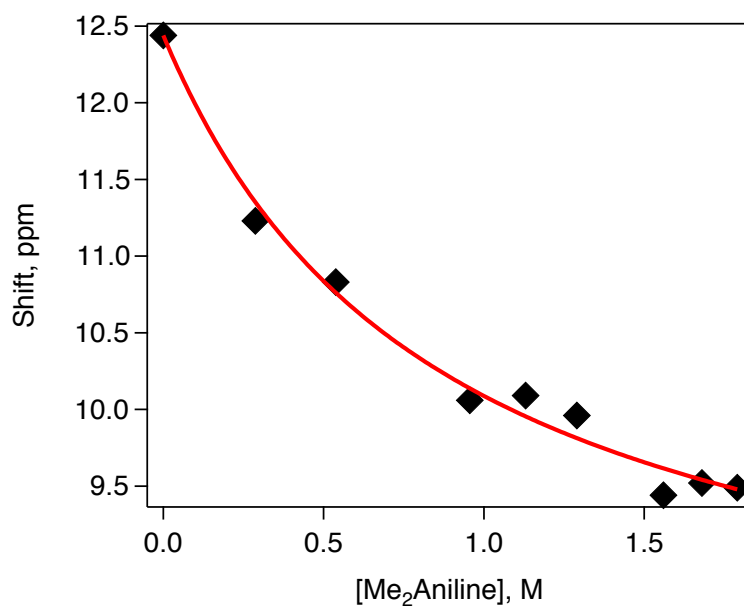


Figure 4.26. Titration of collidinium (18.0 mM) with dimethylaniline in deuterated acetonitrile. The fit is represented by **Equation 4.4** (Section 4.5). K_{HB} was determined to be $1.2 \pm 0.2 \text{ M}^{-1}$.

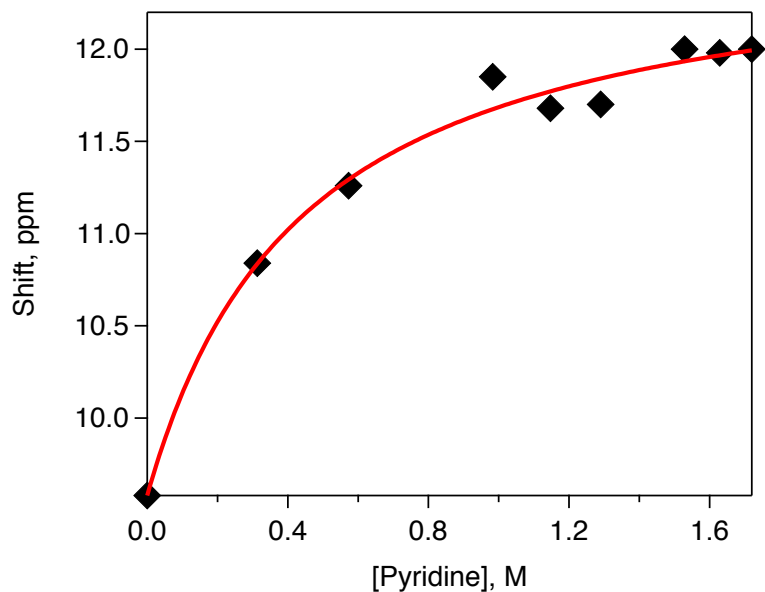


Figure 4.27. Titration of 2-ammoniumbenzimidazole (17.2 mM) with pyridine in deuterated acetonitrile. The fit is represented by **Equation 4.4** (Section 4.5). K_{HB} was determined to be $2.3 \pm 0.4 \text{ M}^{-1}$.

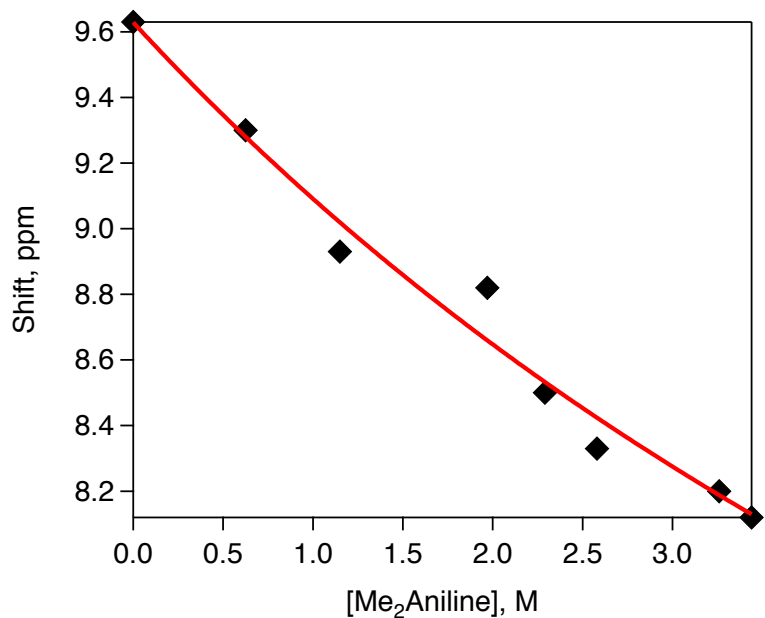


Figure 4.28. Titration of 2-ammoniumbenzimidazole (34.4 mM) with dimethylaniline in deuterated acetonitrile. The fit is represented by **Equation 4.4** (Section 4.5). K_{HB} was determined to be $0.1 \pm 0.09 \text{ M}^{-1}$.

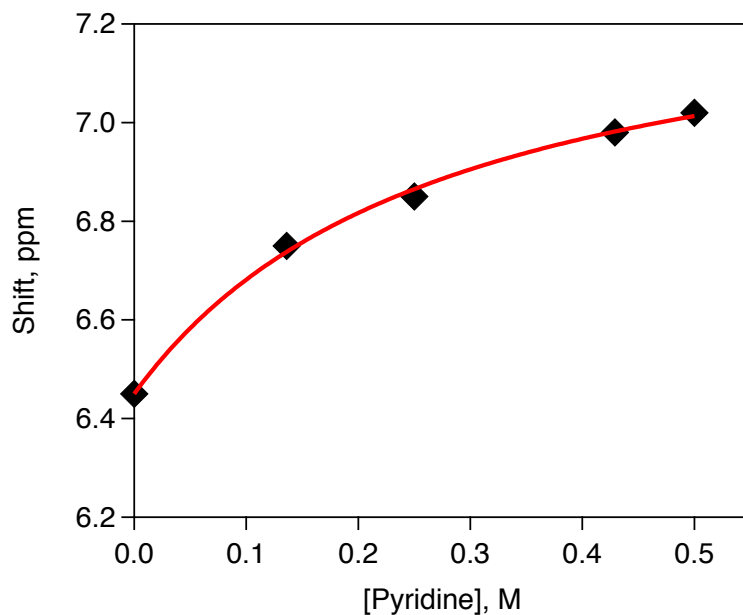


Figure 4.29. Titration of benzylammonium (7.5 mM) with pyridine in deuterated acetonitrile. The fit is represented by **Equation 4.4** (Section 4.5). K_{HB} was determined to be $3.6 \pm 0.5 \text{ M}^{-1}$.

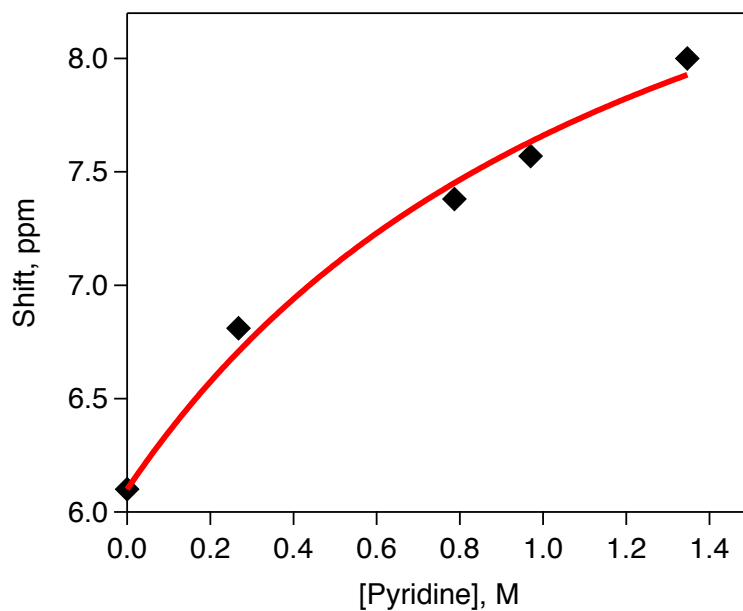


Figure 4.30. Titration of isobutylammonium (17.2 mM) with pyridine in deuterated acetonitrile. The fit is represented by **Equation 4.4** (Section 4.5). K_{HB} was determined to be $0.8 \pm 0.3 \text{ M}^{-1}$.

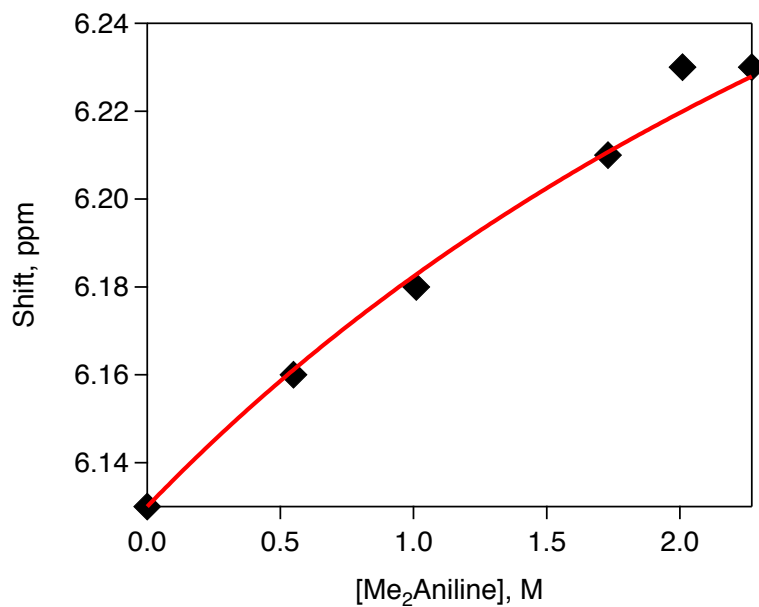


Figure 4.31. Titration of isobutylammonium (30.2 mM) with dimethylaniline in deuterated acetonitrile. The fit is represented by **Equation 4.4** (Section 4.5). K_{HB} was determined to be $0.2 \pm 0.1 \text{ M}^{-1}$.

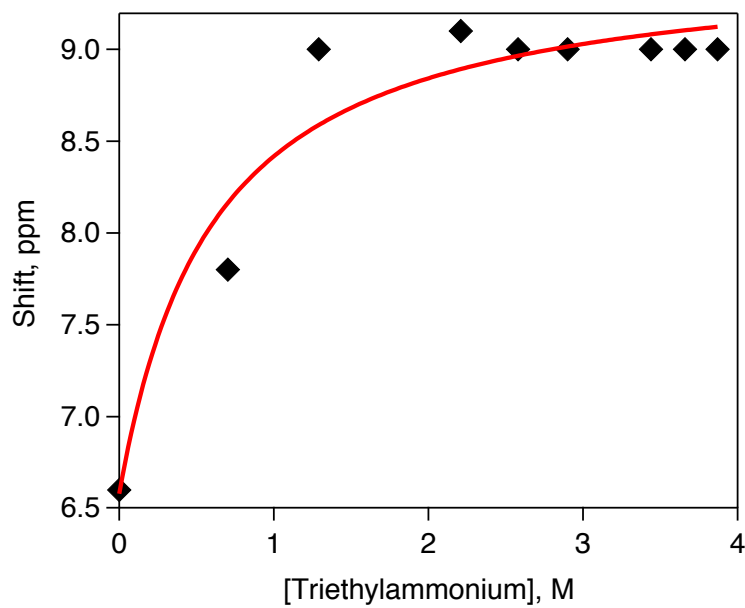


Figure 4.32. Titration of triethylammonium (38.7 mM) with pyridine in deuterated acetonitrile. The fit is represented by **Equation 4.4** (Section 4.5). K_{HB} was determined to be $1.7 \pm 0.7 \text{ M}^{-1}$.

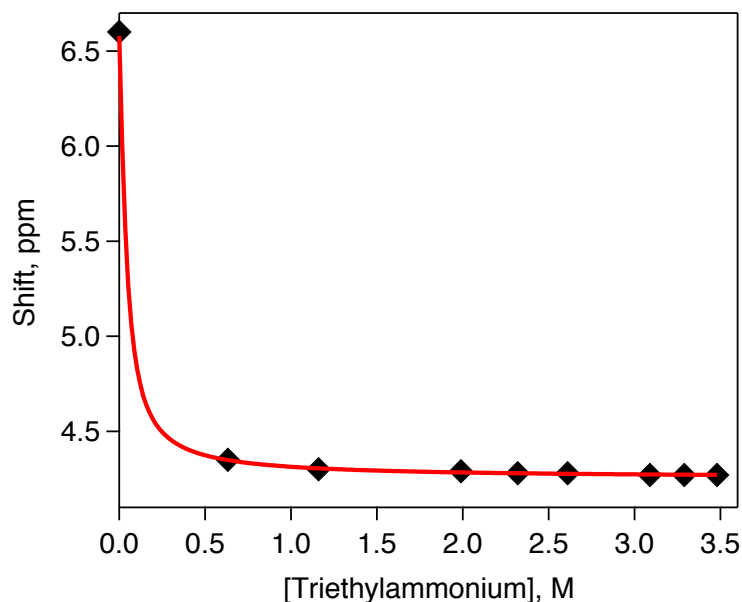


Figure 4.33. Titration of triethylammonium (34.8 mM) with dimethylaniline in deuterated acetonitrile. The fit is represented by **Equation 4.4** (Section 4.5). K_{HB} was determined to be $39.2 \pm 4.8 \text{ M}^{-1}$.

For the acids whose diffusional and steady state quenching rates were comparable (large K_{D} , small K_{S}), it is not surprising to observe little hydrogen bonding to either pyridine or dimethylaniline (Table 4.1). However, in the case of collidinium, significant hydrogen bonding is observed to pyridine ($K_{\text{HB}} = 8.8 \text{ M}^{-1}$). Substantial hydrogen bonding at the proton accepting nitrogen of CF_3 -7DMAQ would account for the large static quenching component determined for this acid, as the excited, hydrogen-bound complex is likely to undergo quantitative PT and be non-emissive (Figure 4.24).

Conversely, triethylammonium exhibits a large hydrogen bonding constant for dimethylaniline. PT between triethylammonium and the quinolinic nitrogen of CF_3 -7DMAQ is $1.5 \text{ kcal mol}^{-1}$ uphill. As such, the observation of quenching, static or dynamic, is surprising, but hydrogen bonding between the acid and dimethylaniline helps explain this phenomenon. Excitation of CF_3 -7DMAQ involves intramolecular charge transfer from the

dimethylamino group and into the quinoline ring, with localization on the quinoline nitrogen.^{14,28,29} Strong hydrogen bonding between triethylammonium and the dimethylamino group distorts the electronic structure of CF₃-7DMAQ and affects the intramolecular charge transfer (ICT) upon light absorption, resulting in static quenching. This has previously been observed in 3-aminoquinolines, as a hydrogen bond donor interacting with the amine substituent results in a decrease in the occurrence of ICT, and thus static quenching.^{28,29} In contrast to the static quenching between hydrogen-bonded quinoline and acid (at the quinoline nitrogen), this quenching is due not to PT, but to a disruption of the electronic structure of CF₃-7DMAQ.²⁸⁻³⁰ Hydrogen bonding between the dimethylamino group and triethylammonium decreases the availability of the lone pair to participate in the transition, thus resulting in static quenching. It is surprising that this hydrogen bonding is not reflected in absorption spectrum; a shift in the optical absorbance would be expected.³⁹ The lack of diffusional quenching for this can be accounted for by the endergonic nature of this PT reaction, though it is worth noting that diffusional quenching is observed with isobutylammonium, which is also an endergonic process albeit much less so ($\Delta pK_a = 0.2$ units uphill compared to 1.1). Because hydrogen bonding complicates the forward PT process, conclusions about the free energy relationship between proton transfer and driving force cannot be made. While a trend between K_D and driving force for PT would still be expected, hydrogen bonding at the dimethylamino nitrogen (specifically for collidinium) also seems to complicate this measurement.

Next, the thermal back PT reaction was examined (k_{TPT} , Figure 4.7). Normally this recombination is spectroscopically silent, but CF₃-7DMAQ provides an optical handle for PT that can be observed with transient absorption spectroscopy. In the presence of collidinium,

TA spectra of CF₃-7DMAQ ($\lambda_{\text{exc}} = 430 \text{ nm}$) in CH₃CN were recorded at various wavelength intervals (450 – 570 nm) over a range of 100 μs . Within a few microseconds of excitation, a broad, positive feature centered around 490 nm is observed to grow in (Figure 4.34); this feature is not present when CF₃-7DMAQ is excited in the absence of acid. Normalization of this transient spectrum to the ground-state absorbance spectrum of CF₃-7DMAQH⁺ shows two absorbance features with striking similarities, providing strong evidence that PT is indeed occurring as the excited state of the quinoline is quenched.

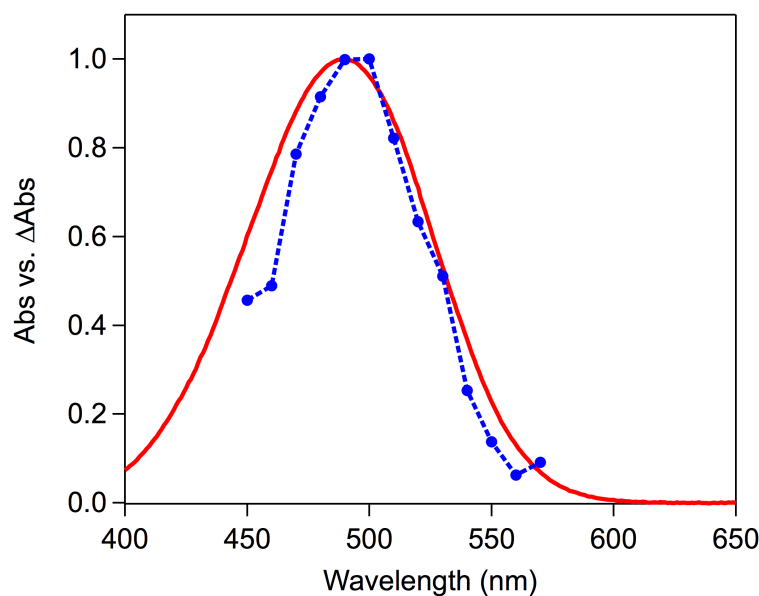


Figure 4.34. Transient difference spectrum (blue) of CF₃-7DMAQ (50 μM) and collidinium (20 mM) taken 4 μs after laser excitation ($\lambda_{\text{exc}} = 440 \text{ nm}$). The spectrum is normalized and compared to the ground state absorbance spectrum of CF₃-7DMAQH⁺ (red).

The thermal back PT reaction (k_{TPT} , Figure 4.7) was monitored via single wavelength kinetics traces ($\lambda_{\text{obs}} = 490 \text{ nm}$) for each of the acid-base reactions. Because CF₃-7DMAQH⁺ and conjugate base (of the acid) are formed in a 1:1 ratio upon ESPT, the recombination reaction should follow a second-order equal concentration kinetics. Plotting one over the change in absorbance versus time results in a linear relationship, and the second-order rate

constants for back PT were determined from these plots (representative plots shown in Figure 4.35 – Figure 4.38, Table 4.2). Note that no PT product was observed when triethylammonium was used as the acid source, hence no back PT is observed.

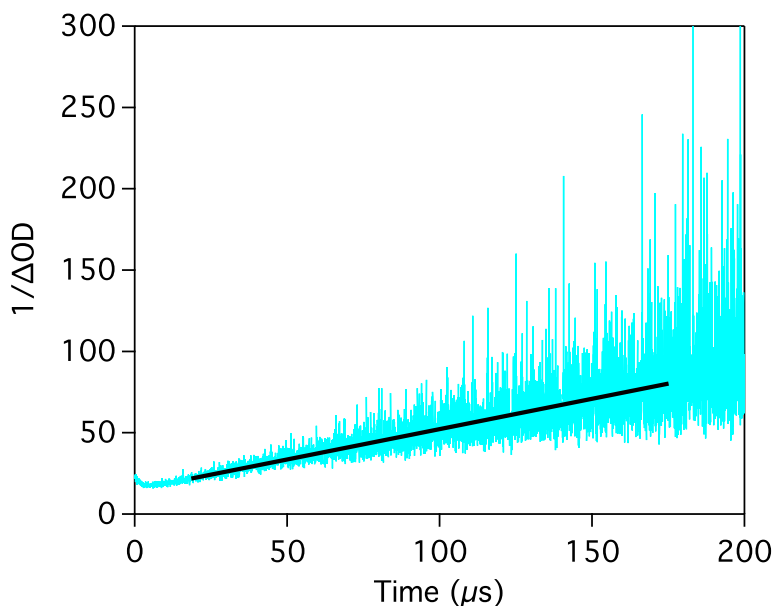


Figure 4.35. Recombination (back PT) of $\text{CF}_3\text{-7DMAQH}^+$ and Isobutylamine in CH_3CN monitored at 490 nm and plotted as $1/\Delta\text{OD}$. Kinetics were fit with a linear fit and multiplied by $\epsilon = 11,000$ to yield $k_{\text{BPT}} = 3.3 \times 10^9 (\pm 1.4 \times 10^9) \text{ M}^{-1} \text{ s}^{-1}$. 50 μM $\text{CF}_3\text{-7DMAQ}$, 1.76 mM Isobutylammonium, $\lambda_{\text{ex}} = 430 \text{ nm}$, $\lambda_{\text{obs}} = 490 \text{ nm}$, 0.1 M $[\text{Bu}_4\text{N}][\text{PF}_6]$.

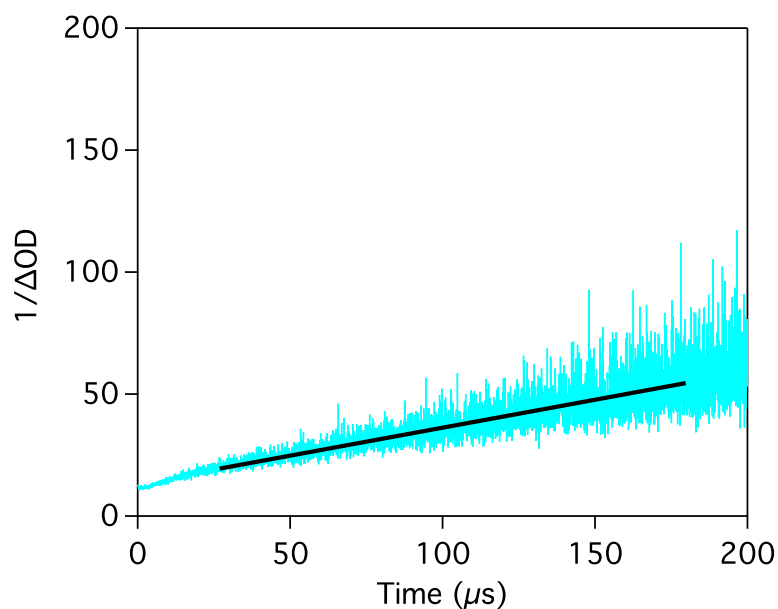


Figure 4.36. Recombination (back PT) of $\text{CF}_3\text{-7DMAQH}^+$ and Benzylamine in CH_3CN monitored at 490 nm and plotted as $1/\Delta\text{OD}$. Kinetics were fit with a linear fit and multiplied by $\epsilon = 11,000$ to yield $k_{\text{BPT}} = 2.5 \times 10^9 (\pm 7.0 \times 10^8) \text{ M}^{-1} \text{ s}^{-1}$. 50 μM $\text{CF}_3\text{-7DMAQ}$, 1.91 mM 2-Benzylammonium, $\lambda_{\text{ex}} = 430 \text{ nm}$, $\lambda_{\text{obs}} = 490 \text{ nm}$, 0.1 M $[\text{Bu}_4\text{N}][\text{PF}_6]$.

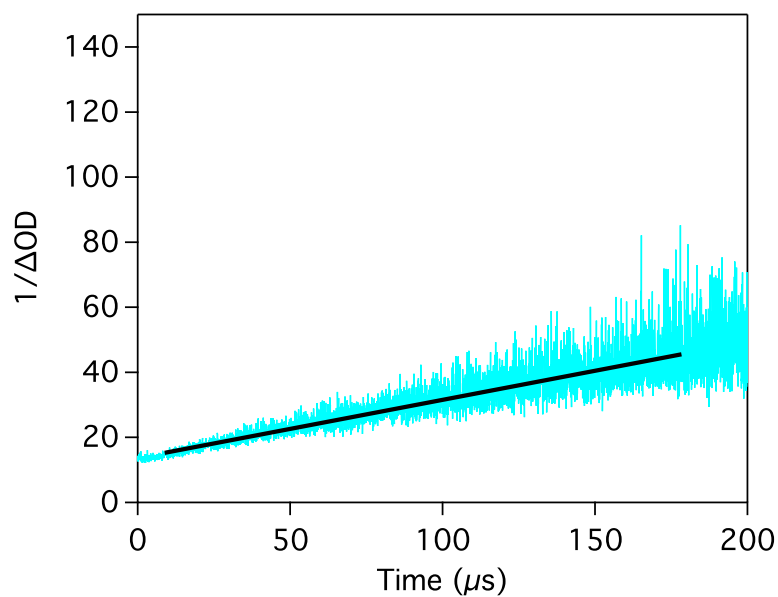


Figure 4.37. Recombination (back PT) of $\text{CF}_3\text{-7DMAQH}^+$ and 2-Aminobenzimidazole in CH_3CN monitored at 490 nm and plotted as $1/\Delta\text{OD}$. Kinetics were fit with a linear fit and multiplied by $\epsilon = 11,000$ to yield $k_{\text{BPT}} = 2.1 \times 10^9 (\pm 3.8 \times 10^8) \text{ M}^{-1} \text{ s}^{-1}$. 50 μM $\text{CF}_3\text{-7DMAQ}$, 2.00 mM 2-Ammoniumbenzimidazole, $\lambda_{\text{ex}} = 430 \text{ nm}$, $\lambda_{\text{obs}} = 490 \text{ nm}$, 0.1 M $[\text{Bu}_4\text{N}][\text{PF}_6]$.

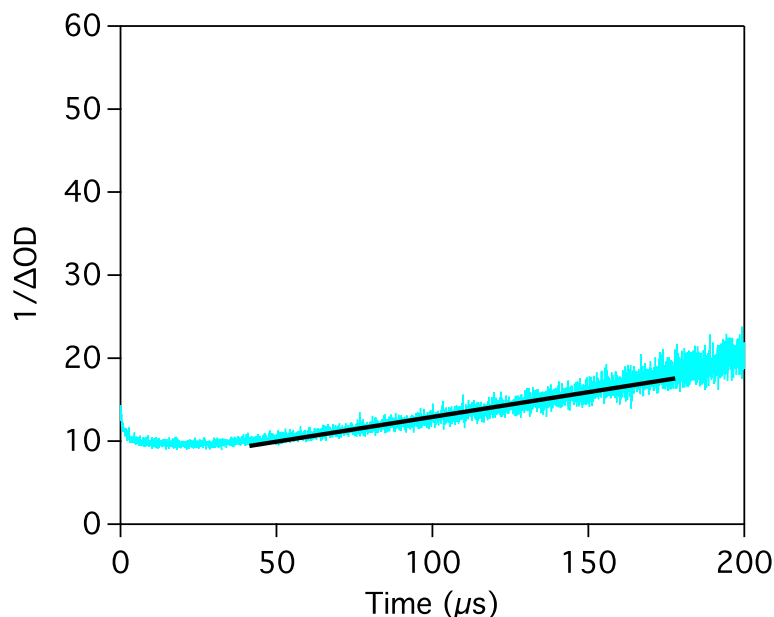


Figure 4.38. Recombination (back PT) of $\text{CF}_3\text{-7DMAQH}^+$ and Collidine in CH_3CN monitored at 490 nm and plotted as $1/\Delta\text{OD}$. Kinetics were fit with a linear fit and multiplied by $\epsilon = 11,000$ to yield $k_{\text{BPT}} = 7.8 \times 10^8 (\pm 3.3 \times 10^8) \text{ M}^{-1} \text{ s}^{-1}$. 50 μM $\text{CF}_3\text{-7DMAQ}$, 2.01 mM Collidine, $\lambda_{\text{ex}} = 430 \text{ nm}$, $\lambda_{\text{obs}} = 490 \text{ nm}$, 0.1 M $[\text{Bu}_4\text{N}][\text{PF}_6]$.

Table 4.2. Rates of back PT between $\text{CF}_3\text{-7DMAQH}^+$ and the conjugate base of each acid investigated.

Acid	pK_{a}	$-\Delta G_{\text{BPT}} (\text{kcal mol}^{-1})$	$k_{\text{BPT}} (\text{M}^{-1} \text{s}^{-1})$
Collidine	15.0	4.8	7.8×10^8
2-Ammoniumbenzimidazole	16.1	6.3	2.1×10^9
Benzylammonium	16.9	7.4	2.5×10^9
Isobutylammonium	17.9	8.8	3.3×10^9
Triethylammonium	18.8	10.0	-

Contrasting the rate constants determined for the forward PT step, there is a noticeable trend for the rate constants for back PT reaction. One would expect faster recombination between $\text{CF}_3\text{-7DMAQH}^+$ ($\text{pK}_{\text{a}} = 11.5$) and conjugate bases of acids with

higher pK_a (i.e. isobutylamine); this is reflected in the calculated driving force for back PT. Plots of $\ln(k_{\text{BPT}})$ vs. $-\Delta G_{\text{PT}}$ show clear correlation between these parameters. The data can be fit to a linear relationship (slope = 0.35, Figure 4.39, top), consistent with Brønsted theory and the Bell transition-state model for PT.^{3,5,43,44} A similar relationship has been observed in a previous study using other aryl-substituted 7-dimethylaminoquinolines, as well as in many other experimental systems.^{5,12,43–49} However, the data can also be fit with a quadratic function, consistent with a Marcus relationship for PT (Figure 4.39, bottom).^{1,5,43,44,50} There is a large body of theoretical work support this type of relationship, and though few examples have been observed experimentally there are a few available.^{1,5,51,52} While it qualitatively appears that the data could be plateauing or approaching the Marcus inverted region, large driving forces for PT cannot be accessed in this system: stronger acids ($pK_a < 15$) lead to ground state protonation of CF₃-7DMAQ ($pK_a = 11.5$), and weaker acids ($pK_a > 18.8$) cannot protonated the excited-state of CF₃-7DMAQ ($pK_a = 17.7$). As such, stronger conclusions cannot be made about the nature of the free energy relationship between k_{PT} and $-\Delta G_{\text{PT}}$.

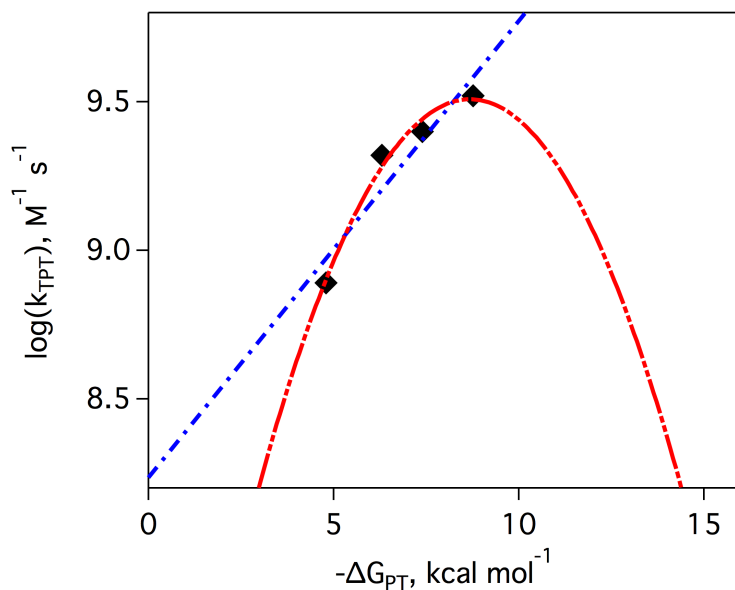


Figure 4.39. Plot of the log of the rate of thermal back PT versus driving force for back PT fit linearly (blue) and to a quadratic (red). The linear fit gives a Brønsted slope = 0.15 with an $r^2 = 0.89$. From the limited amount of data points (and driving force region), it is difficult to draw conclusions about the nature of this PT event.

4.4. Conclusions

This study examined the photobasic properties of substituted-quinoline, CF₃-7DMAQ, and exploited the unique spectral properties of this molecule to monitor both forward ESPT and thermal recombination. Steady state and time-resolved luminescence measurements were used to analyze the ESPT reaction between CF₃-7DMAQ and a series of acids with varying pK_a . Due to complex hydrogen bonding at both the quinolinic nitrogen and dimethylamino group, static and dynamic quenching processes were present, contributing to convoluted rates of PT in the forward direction. As such, no free energy trend was observed for this reaction. However, transient absorption spectroscopy was used to

analyze the recombination reaction, and a free energy relationship between the rate of PT and driving force for recombination was observed. This data could be fit to both a linear and quadratic function, though a lack of accessibility to higher driving forces prevented further investigation of a potential inverted region for PT. Nonetheless, the unique spectral properties of CF₃-7DMAQ provide an excellent model for studying ESPT and PT, and continued investigations using quinoline motifs should provide further insight into the relationship between PT and driving force.

4.5. Experimental Details

Photoluminescence Measurements

Steady state and time-resolved emission spectra were recorded using a commercially available Edinburgh FLS920 spectrometer. Steady state emission spectra were collected using a 1 nm step size, 5 nm bandwidth, and 0.3 s dwell time; each spectra was collected in triplicate and fully corrected for the spectral response of the instrument. A 330 nm high pass optical filter was used to minimize the amount of stray UV light in the excitation beam. Time-resolved measurements were obtained using time-correlated single photon counting (TCSPC) function of the same instrument. An Edinburgh EPL-445 ps pulsed laser diode (444.2 nm, pulse width = 95 ps, rep rate = 2 MHz) was used to excite CF₃-7DMAQ, and the maximum channel for each measurement set collected 5000 counts. Emission lifetimes were determined by reconvolution fit with the instrument response using Edinburgh FS900 software. Data agreeably fit to a monoexponential function of the equation below, where I is the counts (intensity) and τ is the lifetime of the sample.

$$I_t = I_0 e^{-t/\tau}$$

Förster Cycle Calculations (refer to Figure 4.6)

General Equation used to calculate excited-state pK_a ; determining the ground-state pK_a , and E_{00} for both the basic and acidic species allows for the calculation of pK_a^*

$$pK_a - pK_a^* = \frac{E_{00}(\text{CF}_3 - 7\text{DMAQH}^+) - E_{00}(\text{CF}_3 - 7\text{DMAQ})}{1.37 \text{ kcal/mol}}$$

Conversion of E_{00} for CF₃-7DMAQ from eV to kcal mol⁻¹

$$\Delta G_{E00}^\circ = (23.06 \text{ kcal mol}^{-1} \text{ V}^{-1}) * E_{00} = (23.06 \text{ kcal mol}^{-1} \text{ V}^{-1}) * 2.56 \text{ V}$$

$$\Delta G_{E00}^{\circ} = 59.1 \text{ kcal mol}^{-1}$$

Conversion of E_{00} for $\text{CF}_3\text{-7DMAQH}^+$ from eV to kcal mol^{-1}

$$\Delta G_{E00}^{\circ} = (23.06 \text{ kcal mol}^{-1} \text{ V}^{-1}) * E_{00} = (23.06 \text{ kcal mol}^{-1} \text{ V}^{-1}) * 2.19 \text{ V}$$

$$\Delta G_{E00}^{\circ} = 50.6 \text{ kcal mol}^{-1}$$

Plugging E_{00} values back into Förster cycle equation:

$$11.5 - \text{p}K_{\text{a}}^* = \frac{E_{00}(50.6 \text{ kcal mol}^{-1}) - E_{00}(59.1 \text{ kcal mol}^{-1})}{1.37 \text{ kcal mol}^{-1}}$$

$$\text{p}K_{\text{a}}^* = 17.7$$

NMR Titration Derivation

^1H NMR was used to determine the extent of hydrogen bonding between each acid and either pyridine or dimethylaniline. In the instance that a proton is in rapid exchange with multiple locations, only one peak should appear. The apparent shift is a product of the shift of each pure species, and the extent to which the proton is in each state.

The interaction between base (B) and acid (HA) can be described with the chemical equation (1) and equilibrium expression (2) below:



$$(2) \quad K = \frac{[\text{BHA}]}{[\text{HA}][\text{B}]}$$

The observed peak shift, δ_{obs} , is a function of the peak shift and mole fraction of free acid, and peak shift and mole fraction of hydrogen-bonded species (3):

$$(3) \quad \delta_{\text{obs}} = \delta_{\text{HA}}\chi_{\text{HA}} + \delta_{\text{BHA}}\chi_{\text{BHA}} = \frac{\delta_{\text{HA}}[\text{HA}] + \delta_{\text{BHA}}[\text{BHA}]}{[\text{HA}] + [\text{BHA}]}$$

The initial concentrations of base and acid are defined as B and HA respectively (4):

$$(4) \quad \text{HA} = [\text{HA}]_{\text{init}}, \text{B} = [\text{B}]_{\text{init}}$$

Plugging initial concentrations defined in (4) into (3) gives:

$$(5) \quad \delta_{obs} = \frac{\delta_{HA}(HA - [BHA]) + \delta_{BHA}[BHA]}{HA}$$

Rearranging (2) and plugging in (4) gives:

$$(6) \quad [BHA] = K[B][HA] = K(HA - [BHA])(B - [BHA])$$

Expanding (6) gives the quadratic:

$$(7) \quad [BHA] = \frac{\frac{1}{K} + HA + B - \sqrt{\left(\frac{1}{K} + HA + B\right)^2 - 4HA * B}}{2}$$

Plugging (7) into (5) gives the final equation used to fit the NMR experiments, where two variables float, δ_{BHA} and K :

Equation 4.4

$$f(x) = \delta_{obs} = \delta_{HA} + (\delta_{BHA} - \delta_{HA}) \left(\frac{\frac{1}{K} + HA + B - \sqrt{\left(\frac{1}{K} + HA + B\right)^2 - 4HA * B}}{2HA} \right)$$

Transient Absorption Measurements

Nanosecond to microsecond transient absorption experiments were performed using a custom-build laser flash photolysis system. Laser excitation (5-7 ns FWHM) was provided by a pulsed Nd:YAG laser (Spectra-Physics, Inc., model Quanta-Ray LAB-170-10) / OPO (basiScan) combination (415–800nm range). The laser system operates at 10 Hz. A glass window was used to deflect a small portion of excitation beam to a Si diode detector (DET10A, ThorLabs), triggering the oscilloscope to start data collection. Timing of the laser was controlled by a digital delay generator (9514+ Pulse Generator, Quantum Composers).

For 2–800 us time windows, a 75 watt Xe Arc Lamp white light source (PowerArc, Optical Building Blocks) was used in continuous wave mode. The probe beam was passed through a 375 nm long pass filter before passing through the sample collinear with the pump

beam, neutral density filter, and color filter wheel. Single wavelength kinetics were obtained using a double slit monochromator (Spectral Products CM112) outfitted with a Hamamatsu R928 photomultiplier tube (PMT). The signal is amplified by a 200 MHz wideband voltage amplifier (DHPVA-200, Electro Optical Components), and is processed using a digitizer (CompuScope 12502, GaGeScope) controlled by MatLab software.

REFERENCES

- (1) Peters, K. *Acc. Chem. Res.* **2009**, *42* (1), 89.
- (2) Kiefer, P. M.; Hynes, J. T. *J. Phys. Org. Chem.* **2010**, *23* (7), 632.
- (3) Bell, R. P. *The Proton in Chemistry*; Chapman and Hall: London, 1973.
- (4) Eigen, M. *Angew. Chem. Int. Ed. Engl.* **1964**, *3* (I), 1.
- (5) Silverman, D. N. *Biochim. Biophys. Acta - Bioenerg.* **2000**, *1458* (1), 88.
- (6) Weinberg, D. R.; Gagliardi, C. J.; Hull, J. F.; Murphy, C. F.; Kent, C. a; Westlake, B. C.; Paul, A.; Ess, D. H.; McCafferty, D. G.; Meyer, T. J. *Chem. Rev.* **2012**, *112* (7), 4016.
- (7) Mayer, J. M.; Rhile, I. J.; Larsen, F. B.; Mader, E. A.; Markle, T. F.; DiPasquale, A. G. *Photosynth. Res.* **2006**, *87* (1), 3.
- (8) Wenger, O. S. *Acc. Chem. Res.* **2013**, *46* (7), 1517.
- (9) Dempsey, J. L.; Winkler, J. R.; Gray, H. B. *Chem. Rev.* **2010**, *110* (12), 7024.
- (10) Dempsey, J. L.; Winkler, J. R.; Gray, H. B. *J. Am. Chem. Soc.* **2010**, *132* (47), 16774.
- (11) Rountree, E. S.; McCarthy, B. D.; Eisenhart, T. T.; Dempsey, J. L. *Inorg. Chem.* **2014**, *53* (19), 9983.
- (12) Rountree, E. S.; Dempsey, J. L. *Submitted* **2016**.
- (13) Eisenhart, T. T.; Dempsey, J. L. *J. Am. Chem. Soc.* **2014**, *136* (35), 12221.
- (14) Driscoll, E. W.; Hunt, J. R.; Dawlaty, J. M. *J. Phys. Chem. Lett.* **2016**, 2093.
- (15) Gagliardi, C. J.; Westlake, B. C.; Kent, C. a; Paul, J. J.; Papanikolas, J. M.; Meyer, T. J. *Coord. Chem. Rev.* **2010**, *254* (21-22), 2459.
- (16) Nocera, D. G. *Acc. Chem. Res.* **2012**, *45*, 767-776.
- (17) Arnaut, L. G.; Formosinho, S. J. *J. Photochem. Photobiol. A Chem.* **1993**, *75* (1), 1.
- (18) Ireland, J. F.; Wyatt, P. A. H. *Adv. Phys. Org. Chem.* **1976**, *12*, 131.
- (19) Mohammed, O. F.; Pines, D.; Pines, E.; Nibbering, E. T. J. *Chem. Phys.* **2007**, *341* (1-3), 240.
- (20) Prémont-Schwarz, M.; Xiao, D.; Batista, V. S.; Nibbering, E. T. J. *J. Phys. Chem. A* **2011**, *115* (38), 10511.

- (21) Prémont-Schwarz, M.; Barak, T.; Pines, D.; Nibbering, E. T. J.; Pines, E. *J. Phys. Chem. B* **2013**, *117* (16), 4594.
- (22) Kuss-Petermann, M.; Wolf, H.; Stalke, D.; Wenger, O. S. *J. Am. Chem. Soc.* **2012**, *134* (30), 12844.
- (23) Bronner, C.; Wenger, O. S. *Phys. Chem. Chem. Phys.* **2014**, *16* (8), 3617.
- (24) Kuss-Petermann, M.; Wenger, O. S. *J. Phys. Chem. A* **2013**, *117* (28), 5726.
- (25) Kellmann, A.; Lion, Y. *Photochem. Photobiol.* **1979**, *29* (2), 217.
- (26) Nishida, Y.; Kikuchi, K.; Kokubun, H. *J. Photochem.* **1980**, *13*, 75.
- (27) Kuz'min, V. A.; Levin, P. P.; Belyaev, A. B. *Bull. Acad. Sci. USSR.* **1989**, No. i, 165-167.
- (28) Panda, D.; Datta, A. *J. Chem. Phys.* **2006**, *125* (5).
- (29) Panda, D.; Ghosh, D.; Datta, A. *J. Photochem. Photobiol. A Chem.* **2009**, *207* (2-3), 254.
- (30) Munitz, N.; Avital, Y.; Pines, D.; Nibbering, E. T. J.; Pines, E. *Isr. J. Chem.* **2009**, *49* (2), 261.
- (31) Arbeloa, T. L.; Arbeloa, F. L.; Arbeloa, I. L. *J. Lumin.* **1994**, *59*, 369.
- (32) Barman, N.; Singha, D.; Sahu, K. *J. Phys. Chem. A* **2013**, *117* (19), 3945.
- (33) Eisenhart, T. T.; Howland, W. C.; Dempsey, J. L. *J. Phys. Chem. B* **2016**, *Submitted*.
- (34) Weller, A. *Prog. React. Kinet. Mech.* **1961**, *1*, 187.
- (35) Kaljurand, I.; Ku, A.; Soova, L. *J. Org. Chem.* **2005**, *70* (4), 1019.
- (36) McCarthy, B. D.; Martin, D. J.; Rountree, E. S.; Ullman, A. C.; Dempsey, J. L. *Inorg. Chem.* **2014**, *53* (16), 8350.
- (37) Kütt, A.; Leito, I.; Kaljurand, I.; Sooväli, L.; Vlasov, V. M.; Yagupolskii, L. M.; Koppel, I. a. *J. Org. Chem.* **2006**, *71* (7), 2829.
- (38) Lakowicz, J. R. *Principles of Fluorescence Spectroscopy*, Third.; Springer Science+Business Media: New York, 2006.
- (39) Biczok, L.; Valat, P.; Wintgens, V. *Phys. Chem. Chem. Phys.* **1999**, *1* (20), 4759.
- (40) Rhile, I. J.; Mayer, J. M. *J. Am. Chem. Soc.* **2004**, *126* (40), 12718.
- (41) Biczok, L.; Gupta, N.; Linschitz, H. *J. Am. Chem. Soc.* **1997**, *119* (51), 12601.

- (42) Crooks, J. E.; Robinson, B. H. *Faraday Symp. Chem. Soc.* **1975**, 10, 29.
- (43) Jarczewski, A.; Hubbard, C. D. *J. Mol. Struct.* **2003**, 649 (3), 287.
- (44) Arnaut, L. G.; Formosinho, S. J. *Chem. - A Eur. J.* **2008**, 14 (22), 6578.
- (45) Sen Gupta, S. K.; Arvind, U. *J. Phys. Org. Chem.* **1997**, 10 (6), 466.
- (46) Hojatti, M.; Leffek, K. T. *Can. J. Chem.* **1984**, 62 (12), 2653.
- (47) Martin, D. J.; Rountree, E. S.; McCarthy, B. D.; Dempsey, J. L. *Submitted* **2016**.
- (48) Gamiz-Hernandez, A. P.; Magomedov, A.; Hummer, G.; Kaila, V. R. I. *J. Phys. Chem. B* **2015**, 119 (6), 2611.
- (49) Kaila, V. R. I.; Hummer, G. *J. Am. Chem. Soc.* **2012**, 244, 19040.
- (50) Marcus, R. A. *J. Phys. Chem.* **1968**, 72 (3), 891.
- (51) Andrieux, C. P.; Gamby, J.; Hapiot, P.; Savéant, J. M. *J. Am. Chem. Soc.* **2003**, 125 (33), 10119.
- (52) Peters, K. S.; Cashin, A.; Timbers, P. *J. Am. Chem. Soc.* **2000**, 122, 107-113.